http://researchcommons.waikato.ac.nz/

Research Commons at the University of Waikato

Copyright Statement:

The digital copy of this thesis is protected by the Copyright Act 1994 (New Zealand).

The thesis may be consulted by you, provided you comply with the provisions of the Act and the following conditions of use:

- Any use you make of these documents or images must be for research or private study purposes only, and you may not make them available to any other person.
- Authors control the copyright of their thesis. You will recognise the author's right to be identified as the author of the thesis, and due acknowledgement will be made to the author where appropriate.
- You will obtain the author's permission before publishing any material from the thesis.

Andesite volcanic facies and hydrothermal alteration in the subsurface peripheral to existing Waihi mine workings

A thesis submitted in partial fulfilment

of the requirements for the degree

of

Master of Science (Research)

in Earth Sciences

at

The University of Waikato

by

Billy Bodger

The University of Waikato
2015

THE UNIVERSITY OF
WAIKATO
Te Whare Wānanga o Waikato

Abstract

The Waihi vein system is an andesite-hosted epithermal Au-Ag deposit comprising a series of veins located in the southern Hauraki Goldfield, New Zealand. It includes the Martha Mine which is the largest gold producer in the Hauraki Goldfield. Despite a history of over 127 years of prospecting and mining at Waihi, the Favona Au-Ag deposit was recently discovered in blind quartz veins 2 km to the east of Martha Mine. This highlights that there are still new Au-Ag veins to be found and extensions of existing veins to be explored. Little work has been published on the volcanism of the Waipupu Formation andesites, which host the mineralisation. Secondly, the formation of epithermal mineral deposits is accompanied by various chemical reactions which occur between mineralising fluids and host rock, and commonly produce distinct mineralogical and geochemical halos that overprint the volcanic textures and are generally much larger than the ore bodies themselves. The overall aim of this project is, therefore, to reconstruct the volcanic and hydrothermal setting peripheral to the Martha Hill mine. Two northwest-oriented exploration drill holes that are peripheral to the Martha Hill vein system were logged from a volcanological perspective, sampled and analysed by optical mineralogy, TerraSpec, x-ray diffraction on clay separates and x-ray-fluorescence.

Eight new andesite lava facies have been recognised. Six of the facies were identified based on mineral abundances and the presence of quartz phenocrysts. The crystal abundances within these lava facies ranges from 10 to 60% and are dominated by feldspar and mafic minerals. Quartz phenocrysts are minor but prominent features in the rock. These mineral abundances are near synonymous with other active andesite volcanoes and Late Archean examples. The texture of each of the lava facies is dominantly porphyritic, and phenocrysts are mainly plagioclase + ferromagnesian silicates ± quartz. Quartz phenocrysts are commonly resorbed which reflects different levels of magma mixing within the magma chamber before erupting. The other two facies were andesite lava breccias described as either monolithic (containing one clast type) or heterolithic (containing multiple clast types). The monolithic breccia resembles that of an autobreccia, typically associated with the outer parts of a lava flow.

Using alteration mineralogy data (from shortwave infrared spectroscopy and x-ray diffraction on clay separates) and geochemical data (from x-ray fluorescence), a transition from illite to interstratified illite-smectite to smectite was identified heading northwest from the Martha Mine and major mineralised Au-Ag quartz veins. Based on known thermal stabilities for these minerals, a paleoisotherm model was established peripheral to the Martha Hill mine suggesting a “cooling” of the hydrothermal fluid northwest of Martha Mine. Multiple trace elements such as Tl, Bi and Se strongly correlated to the mineralogy, vectoring towards higher temperature mineralisation.

Acknowledgments

I would like to thank the following people who have made a contribution to this project; it would have not been possible without you:

I first thank my supervisors Dr Adrian Pittari and Dr Shaun Barker for offering unbeatable guidance, support and knowledge. You two were my inspiration throughout this project and I will continue to build my geological proficiency because of it.

Special thanks go to Newmont Waihi Gold Ltd., in particular Lorrance Torckler and the geology team, for providing access to resources, data and core samples. The additional knowledge and support were greatly appreciated and it was a pleasure working alongside you.

Thanks to GNS Science, particularly Mark Simpson, for usage of the TerraSpec and additional knowledge and resources.

I thank technical staff in the Department of Earth and Ocean Sciences, particularly Annette Rodgers, Renat Radosinsky and Janine Ryburn, for the excellent laboratory training and assistance. I thank Roger Briggs for taking the time to assist with petrography and Sydney Wright for times where I needed pointing in the right direction.

I also thank my fellow MSc students and office crew (particularly Kev, Ryan and George) for the support, good discussions, and laughs. I thank Megan Saunders for proof-reading and endless moral support.

To my family who were behind me every step of the way, I cannot thank you enough. Special shout-out to mum for the occasional ginger crunch and to my best mates for being there for me.

Funding was received from the University of Waikato School of Science Masters Research Scholarship, the AusIMM New Zealand Branch Education Endowment Trust Scholarship and a Parininihi ki Waitotara (PKW) tertiary grant.

Table of Contents

List of figures

List of tables

Chapter 1 Introduction

1.1 Introduction

The Coromandel Volcanic Zone (CVZ) is a continental volcanic arc dominated by andesite-dacite-rhyolite volcanism (Brathwaite & Faure 2002). The CVZ is also referred to as the Hauraki Goldfield as it is host to a large number of epithermal Au-Ag deposits (Clarke et al. 1990). The largest of these deposits is the world-class Martha Hill (Waihi) deposit located in the southern part of the CVZ (Brathwaite et al. 2006). Through 2009, total production from open-pit and underground mining was 210,944 kg Au and 1,299,893 kg Ag, which accounts for approximately 66 percent of the total Au and 89 percent of the total Ag production of the Hauraki goldfield (John 2011; Spörli & Cargill 2011). Despite a history of over 127 years of prospecting and mining at Waihi, the Favona Au-Ag deposit was recently discovered in blind quartz veins 2 km to the east of Martha Mine (Brathwaite *et al*. 2006). This highlights that there are still new Au-Ag veins to be found and extensions of existing veins to be explored. In this study, two exploration drill holes orientated northwest peripheral to the Martha Hill vein system (Fig. 1), are logged, sampled and analysed to study the alteration mineralogy and geochemistry. Additionally, volcanic lava facies have been defined according to their primary volcanic textures.

1.2 Research aims, objectives and methodology

The overall aim of this project is to reconstruct the volcanic and hydrothermal setting peripheral to the Martha Hill mine. Firstly, this study will identify and document new volcanic facies for the Waipupu Formation andesite peripheral to the Martha Mine based on recognition of primary volcanic textures and relate these textures to their magmatic origin and emplacement processes. Secondly, the secondary mineralogy and geochemistry of the hydrothermal alteration which overprints the primary volcanic facies will be documented to determine systematic variations in alteration processes and propose potential alteration halos to assist in exploration.

The aim was met by the following objectives:

- Describe the differences in crystal abundances and assemblages via stratigraphic logging in the field.
- Describe the optical mineralogy of each facies.
- Identify mass changes in major and trace elements.
- Identify the distribution of illite, interstratified illite-smectite, and smectite using various techniques. These minerals are important temperature sensitive minerals and their distribution in epithermal environments may indicate directions toward fluid sources and/or potential sites of ore deposition.
- Assess the geochemistry as a proxy for mineral assemblages.

The objectives were met by the following methods:

- Volcanic facies were established from drill core logging and petrography of primary volcanic textures and classified based primarily on the visible crystal abundance and then termed accordingly using crystal abundance classes of Cas *et al*. (2009).
- Alteration minerals were identified by TerraSpec 4 Hi-Res and clay separate X-ray diffraction (XRD). Major and minor geochemistry was determined by laboratory X-ray fluorescence spectrometry.
- Compare the mineralogy to the geochemistry by plotting a feldspar Na-K GER diagram to infer alteration mineral species.

1.3 Thesis outline

Chapter 2 is a comprehensive literature review of the tectonic and geologic setting of the Hauraki Goldfield with attention given to the Waihi geology, structure, mineralisation and alteration. An introductory review to epithermal systems is provided in Chapter 3. The results from 1811.5 m of drill core logging are presented in Chapter 4 from which eight new andesite volcanic facies are described and discussed. Chapter 5 describes the alteration mineralogy and geochemistry and discusses its application in vectoring towards mineralisation. The summary and conclusions of this project are presented in Chapter 6.

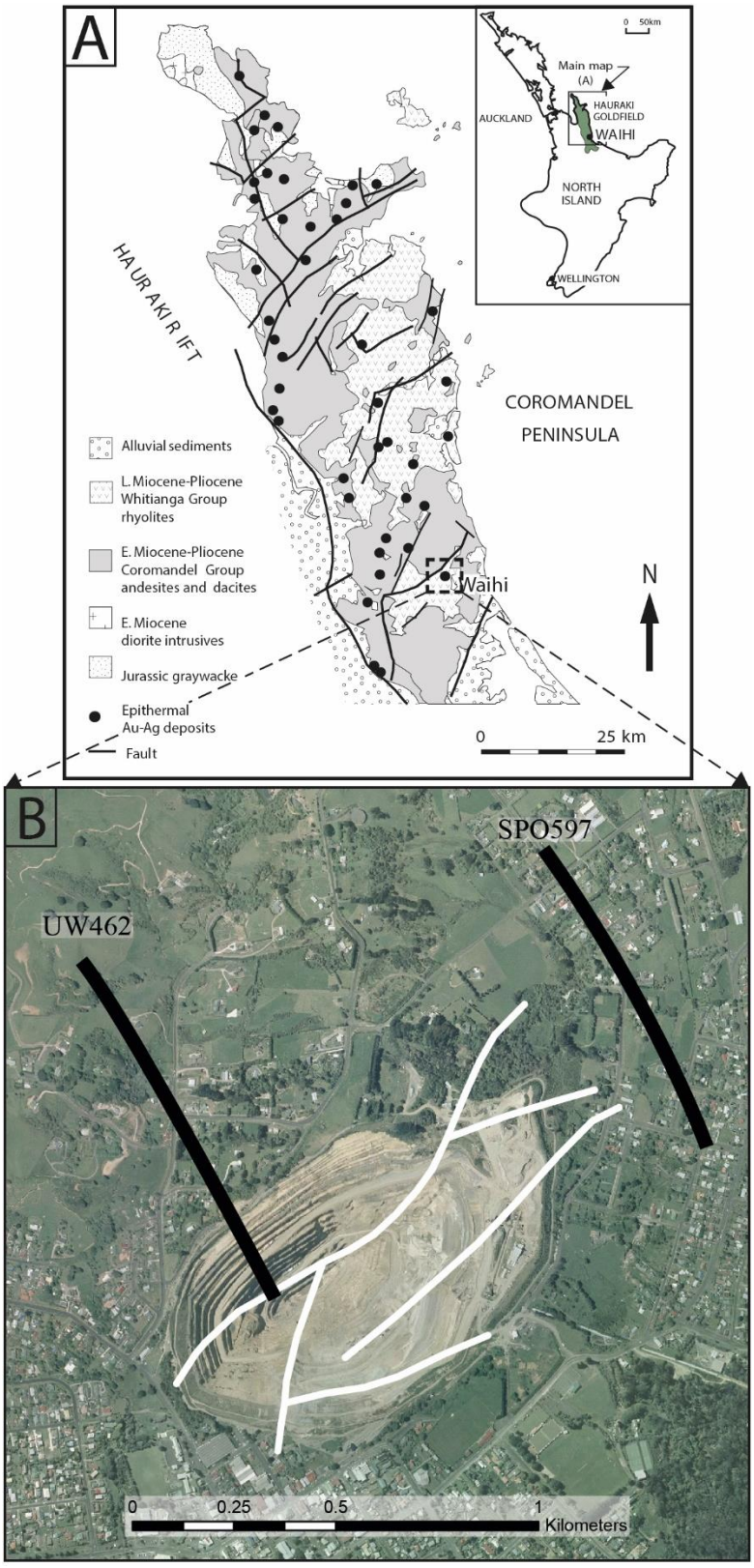

Fig. 1.1. A) Hauraki Goldfield showing geology and distribution of epithermal Au-Ag deposits and the location of the Waihi deposit relative to the North Island, New Zealand (modified after Brathwaite & Faure 2002). B) Martha Pit, Waihi, and location of drill holes studied. Drill hole UW462 (left black solid line) and drill hole SPO597 (right black solid line). White solid lines represent major mineralised veins projected to the surface.

Chapter 2 Tectonic and geologic setting

2.1 Introduction

The Coromandel Volcanic Zone (CVZ), considered a tectonic precursor to the active Taupo Volcanic Zone (TVZ) (Adams *et al.* 1994), comprises a continental volcanic arc constructed under an extensional tectonic regime associated with subduction processes at the Australian-Pacific plate boundary (Clarke *et al*. 1990; Adams *et al.* 1994). The CVZ is part of the greater Hauraki Volcanic Region (HVR) (Skinner 1986), being active between c. 18 Ma and c. 1.9 Ma (Christie *et al.* 2007). The Hauraki goldfield in the CVZ contains approximately 50 epithermal Au-Ag deposits in a north-south-oriented belt, one that extends 200 km in length and by up to 40 km in width. Based on factors such as host rock and geologic setting of the deposits, the goldfield has been divided into three provinces (northern, eastern, and southern) (Christie *et al*. 2007). Rock types within the HVR range from basalt to rhyolite (Clarke *et al*. 1990) with andesite and dacite of the Coromandel Group representing 61% of the rocks exposed in the goldfield. Irrespective of the Coromandel Group's abundance, some 97% of total past gold production was from deposits hosted in these Miocene andesite and dacite Coromandel Group rocks (Christie *et al*. 2007). To date, the largest producer in the Hauraki goldfield is the world-class Martha Hill deposit in Waihi which is part of a series of veins known as the Waihi vein system (John 2011; Simpson *et al*. 2015).

The remainder of this chapter outlines the tectonic and geological context from which these rocks derived, and looks at the spatial distribution and controls of epithermal deposits in the Hauraki goldfield. The stratigraphy, structure, mineralisation and alteration of the Waihi vein system will also be briefly discussed in conjunction with the mining history.

2.2 Tectonic and geological setting

2.2.1 Tectonic setting

The oldest rocks in the CVZ are Late Jurassic (c. 163 Ma – c. 145 Ma) low grade metagreywacke basement sequences of the Manaia Hill Group (Adams *et al.* 1994). These basement rocks which accreted onto the margin of Gondwana during the Mesozoic (Christie *et al.* 2007), presently have limited exposure restricted to the

northern and northwestern areas of Coromandel peninsula (Fig. 2.1; Adams *et al.* 1994). Extension occurred from c. 105 to 82 Ma and culminated with the opening of the Tasman Sea, thus separating the New Zealand microcontinent from Gondwana, which resulted in a prolonged period of extensional faulting and marine sedimentation (Christie *et al*. 2007). Oligocene coal measures and early Miocene sediments overlie folded and faulted basement in this region and document the initiation of volcanism on the peninsula as volcaniclastic mass flow deposits (Colville Formation of the Waitemata Group) (Skinner 1986; Adams et al. 1994). Block faults in the greywacke basement were re-activated in overlying Tertiary rocks (Christie *et al*. 2007).

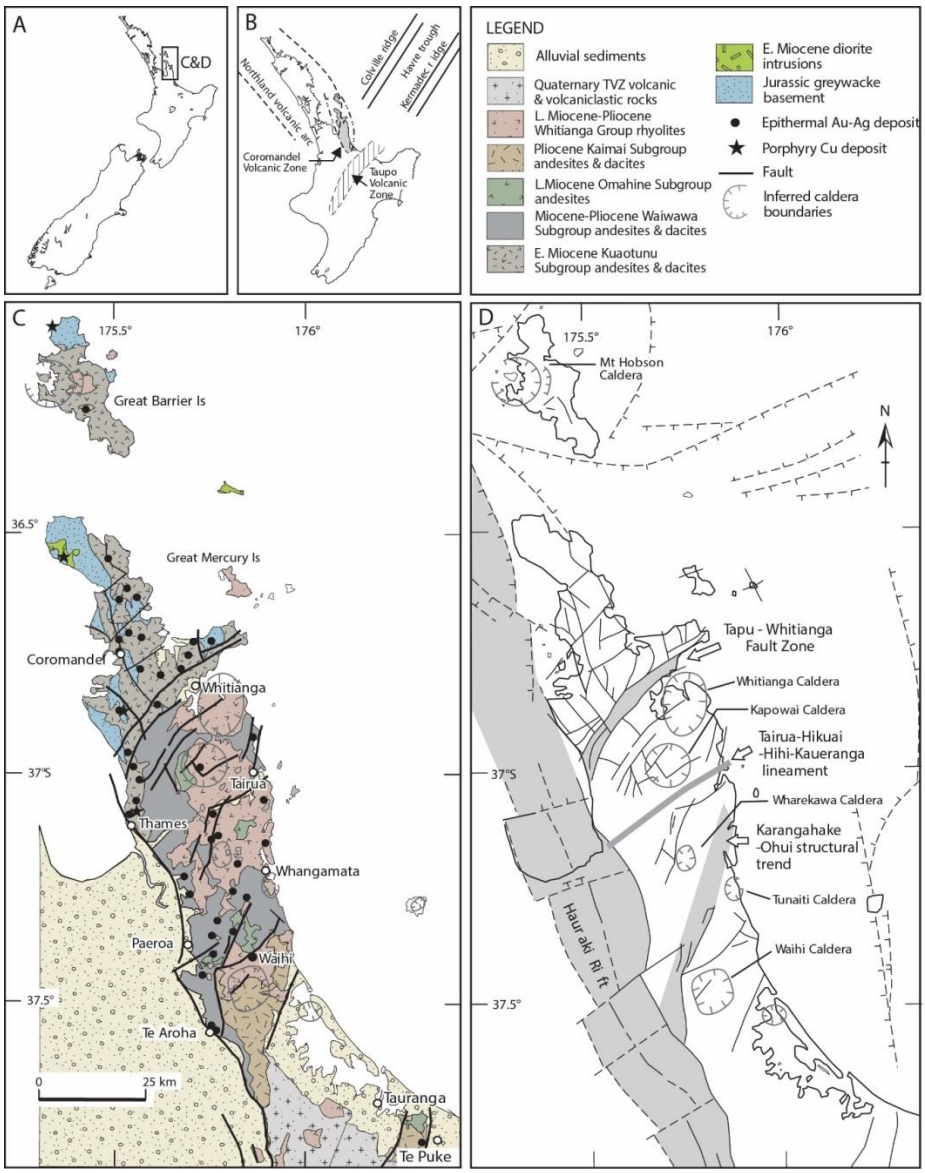

Fig. 2.1. Location of the Hauraki goldfield (A.). Outlined box shows locations of panels C and D. Location of Coromandel Volcanic Zone is outlined in relation to the Taupo Volcanic Zone (B.). Regional geology and mineral deposits (C.). Structural features of the Coromandel Volcanic Zone and Hauraki goldfield (D.). Figure modified from Christie et al. (2007).

A number of different interpretations regarding the Cenozoic tectonic history of the Coromandel volcanic arc have been suggested in numerous papers (Brathwaite & Skinner 1997; Spörli *et al*. 2006; King 2010; Mortimer *et al*. 2010; Mauk *et al*. 2011; Spörli & Cargill 2011), however there is wide agreement that propagation of the Australian-Pacific plate boundary through New Zealand during the Late Oligocene (c. 25 Ma) lead to volcanism (Christie *et al*. 2007; Mauk *et al*. 2011). This profound change in tectonism, following such a long period of volcanic and tectonic quiescence (Ballance 1974), has since developed into a convergent margin similar to its present form (Christie *et al*. 2007).

Subduction of the Pacific plate initiated a series of volcanic arcs in the northern North Island of New Zealand (Christie *et al*. 2007), the locations of which shifted considerably with the locus of volcanism (Mauk *et al.* 2011). From 25 Ma, the north-west trending Northland arc was active until 15 m.y. ago (Mauk *et al.* 2011). During the early Miocene, the continuing change in the alignment and nature of the Australian-Pacific plate boundary (Hayward *et al.* 2001) caused a shift in volcanism from the Northland arc towards the CVZ (Mauk *et al.* 2011). Volcanism in the CVZ began approximately 18 m.y. ago and continued until the late Pliocene (at c. 1.9-1.5 Ma), where volcanic activity shifted to the Taupo Volcanic Zone (TVZ). Unlike the TVZ, which is represented by voluminous eruptions of rhyolite and to a lesser extent andesite and dacite, the CVZ is dominated by andesite and dacite (Fig. 2.1; Christie *et al*. 2007).

2.2.2 Geology

The Coromandel Volcanic Zone is predominantly comprised of calc-alkaline, medium K volcanic rocks (Fig. 2.2). Andesite and dacite Coromandel Group rocks represent approximately 61% of exposed rocks in the CVZ (Christie *et al*. 2007). Dacite, rhyolite, and rhyodacite rocks of the Whitianga Group are the second largest exposed lithological unit in the CVZ forming 30 %, while basalt of the Kerikeri Volcanic Group (Mercury Basalts) make up <0.1 %. Greywacke of the Manaia Hill Group contributes the remaining 9 %. Ages show that the volcanic units become younger towards the south and east along the Coromandel peninsula. Another key trend is that andesitic volcanism was predominant in the western part of the region, whereas rhyolitic calderas were predominant in the eastern part.

Volcanic activity was not continuous in the CVZ. Periods of volcanic quiescence and erosion separated much of the volcanism and as a result the andesites and dacites of the Coromandel Group are subdivided into several subgroups including Kuaotunu (early to middle Miocene), Waiwawa (middle to late Miocene), Omahine (late Miocene to Pliocene), and Kaimai (late Miocene to Pliocene) subgroups (Fig. 2.2; Christie *et al*. 2007). Mineralogy between the Coromandel Group subgroups differ, with the Kuaotunu Subgroup consisting of alternating pyroxene andesite and hornblende-pyroxene andesite to dacite sequences, whereas the Waiwawa and Omahine subgroups are predominantly pyroxene andesite. Subvolcanic dikes, stocks, porphyritic andesite and dacite plugs, and local plutons of quartz diorite to granodiorite (some of which are altered and mineralised) are also included within the Coromandel Group (Christie *et al*. 2006; 2007). These intrusive rocks encroach into basement and volcanic rocks of the northern and central Coromandel peninsula and northern Great Barrier Island (Christie *et al*. 2007). The earlier Kuaotunu and Waiwawa subgroups preceded Whitianga Group rhyolitic volcanism, whereas the Omahine subgroup generally overlies or intrudes the rhyolitic rocks (Fig. 2.2; Christie *et al*. 2006).

Whitianga Group rocks comprise three late Miocene to Pliocene subgroups (Fig. 2.2). Minden Rhyolite Subgroup consists of calc-alkaline to alkaline felsic flow- and dome-forming rhyolites, whereas the Coroglen Subgroup comprises rhyolitic pyroclastic and volcaniclastic sedimentary rocks (Christie *et al*. 2006; 2007). These two subgroups are most abundant in the central and southern parts of the eastern Coromandel peninsula (Fig. 2.1). Pleistocene ignimbrites, which make up the Ohinemuri Subgroup, represent the youngest units of the Whitianga Group and are found in the southern part of the Coromandel Volcanic Zone. The volumetrically smaller Mercury Basalts (Kerikeri Volcanic Group; Fig. 2.2) form a bimodal rhyolite-basalt assemblage with rhyolites of the Whitianga Group found solely in the northeastern part of the Coromandel peninsula and offshore islands (Christie *et al*. 2007).

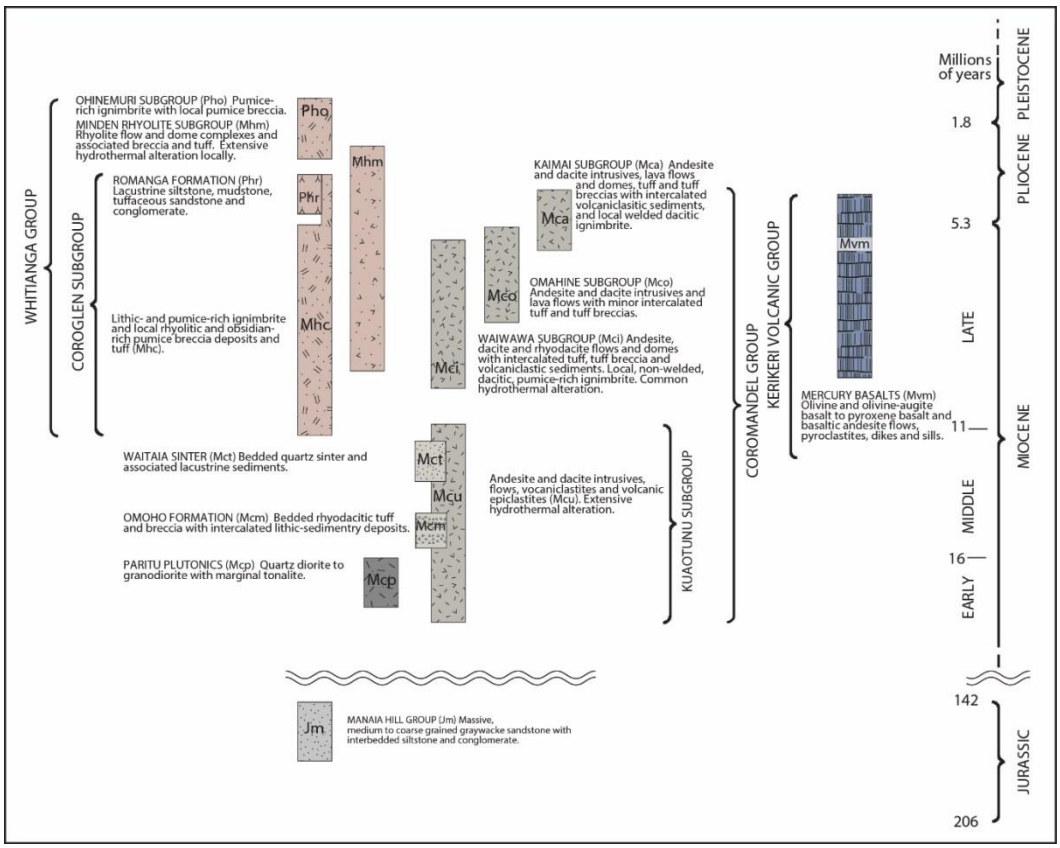

Fig. 2.2. Stratigraphy of the Coromandel volcanic zone (modified from Christie et al. 2007).

2.2.3 Structure

Block faulting during the Cretaceous formed numerous faults in the greywacke basement and presumably reactivated in the CVZ volcanic rocks. Faults throughout the Coromandel peninsula strike NNW and NNE to ENE, some of which include major fault zones transecting the peninsula. There are also individual faults of a few hundred meters to several kilometres in length, including those filled with epithermal quartz veins. The presently active Hauraki rift in the west and the Colville ridge and/or Harve trough system in the east are also considered responsible for faulting (Christie *et al*. 2007).

Displacement from the northeast- and east-northeast-striking faults has resulted in lowering Jurassic basement to the south and the volcanic sequence consequently thickens towards the TVZ. Although north-northwest-striking faults are equally downthrown to the east and west, there is also a gentle eastward tilting of the stratigraphy (Christie *et al*. 2007).

A north-northwest-striking belt of calderas associated with Whitianga Group rhyolites (Fig. 2.1; Spörli & Cargill 2011) occur along the eastern Coromandel peninsula, including the Whitianga, Kapowai, Wharekawa, Tunaiti, and Waihi calderas (Christie *et al*. 2007, and references therein).

The currently active Hauraki rift is a continental rift that extends over 300 km from north of Little Barrier Island to the TVZ in the south, where it is buried under late Pleistocene ignimbrites (Fig. 2.1; Briggs *et al*. 2005). It bounds the Coromandel peninsula to the west (Christie *et al*. 2007) and has downthrown the Miocene to Pliocene volcanic rocks by 1 to 3 km (Hochstein & Balance 1993). Timing of the initial formation of the Hauraki rift is still uncertain, but is considered to be during the Late Miocene (c. 7 Ma), with main subsidence occurring more recently between 1 and 2 Ma (Hochstein and Ballance, 1993; Briggs *et al*., 2005).

2.3 Hauraki goldfield

The Hauraki goldfield is a major gold producing region (Gadsby *et al.* 1990) occurring as a north-south–trending belt along the length of the Coromandel peninsula and is associated with the Miocene-Pliocene volcanics of the CVZ (Mauk *et al.* 2011). Recent work (Christie *et al*. 2007) has broadly subdivided some 50 adularia-sericite epithermal Au-Ag deposits of the Hauraki goldfield into three provinces: northern, eastern and southern (Fig. 2.3) (Christie *et al*. 2007; Mauk *et al.* 2011). This broad grouping of the deposits is based on host rocks, age, variability of vein strike, Au/Ag ratios, occurrence or relative abundance of key minerals such as adularia, calcite, and arsenopyrite, grain size of vein quartz, and differences in vein textures (Table 2.1; Christie *et al*. 2007).

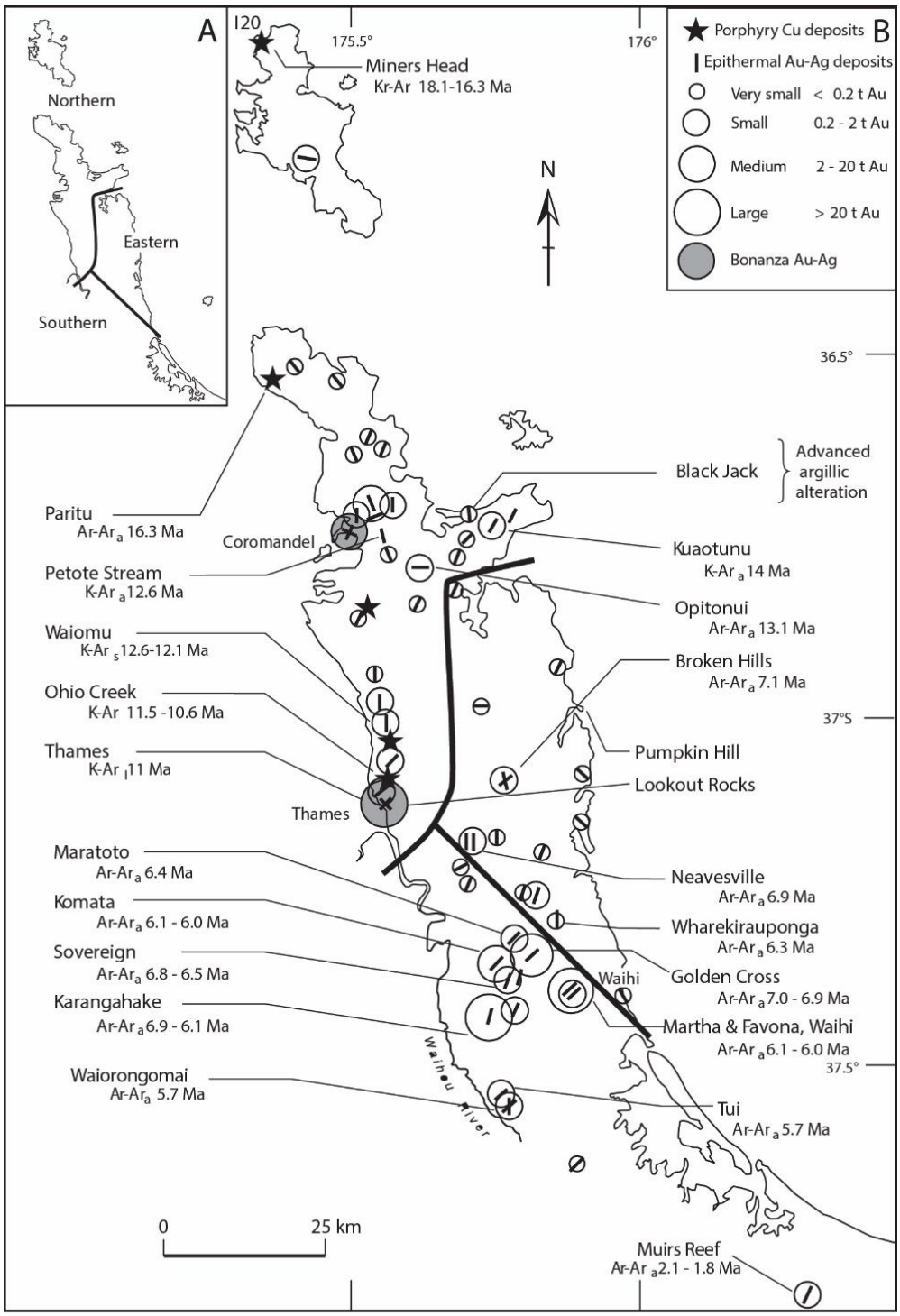

Fig. 2.3. Subdivision of Hauraki goldfield into northern, southern and eastern epithermal provinces (A.). Location of mineral deposits in the Hauraki goldfield, past Au production, and ages of deposits (B.). Bar symbol shows the main strike of veins at each deposit. Subscripts show the type of mineral dated: a = adularia, i = illite, mo = molybdenite, s = sericite (modified from Christie et al 2007; Mauk et al 2011 and references therein).

Table 2.1. Subdivision of the Hauraki goldfield, Coromandel Volcanic Zone deposits into northern, southern and eastern epithermal provinces (from Christie et al. 2007).

	Northern province	Eastern province	Southern province
Production (total)	59,137 kg Au (16%)	1,607 kg Au (0.5%)	307,640 kg Au (83.5 %)
Largest producer	44,847 kg Au, Thames	737 kg Au, Broken Hills-Golden Hills	208,737 kg Au, Martha, Waihi
Kg Au per km ^{2}	61	2.4	530
Au/Ag ratio	Average 1.8, range 0.24 to 3.4	Average 0.7, range 0.49 to 2.0	Average 0.25, range 0.22 to 1.9
Host rock	Kuaotunu Subgroup andesite and Manaia Hill Group graywacke	Whitianga Group rhyolitic rocks, local Waiwawa Subgroup andesite at depth	Waiwawa Subgroup andesite and minor Whitianga Group rhyolitic rocks
Host rock age	19.0 to 9.0 Ma	11.0 to 5.0 Ma	8.0 to 5.5 Ma
Mineralization age	>10 Ma	7.1 to 6.3 Ma	6.9 to 5.7 Ma
Vein orientation	Diverse strike; N, NE, E, and NNW	Diverse strike; N, NE, E, and NNW	Focused, predominately NE striking
Vein style	Veins (bonanzas at Coromandel and Thames)	Stockworks, veins, disseminated, hydrothermal eruption breccias, silica sinter	Veins and stockworks
Vein textures	Massive crystalline and comb quartz	Colloform banded, cryptocrystalline or finely crystalline	Crustiform and colloform banded, cryptocrystalline or finely crystalline quartz, and quartz pseudomorphs after platy calcite
Vein mineralogy	Quartz, minor base metal sulfides	Quartz, minor adularia	Quartz, minor adularia, and calcite
Distinctive minerals	Illite and rare adularia. Arsenopyrite in Coromandel field	Adularia	Adularia, platy calcite, and massive calcite
Level of exposure	Intermediate to deep (>500 to 1,300 m)	Shallow to intermediate (0 to 500 m)	Shallow to intermediate (>50 to 900 m)
Associations	Proximal to porphyry Cu prospects		
Type examples	Coromandel, Thames, Opitonui, Monowai	Kapowai, Broken Hills, Neavesville, Wharekirauponga, Ohui	Martha, Favona, Golden Cross, Karangahake, Maratoto, Muirs Reefs
Atypical example	Kuaotunu (banded veins, adularia, quartz after platy calcite, sinter)		Komata (hosted in rhyolite dike)

2.3.1 Northern province

The deposits located in the northern province of the Hauraki goldfield are hosted in andesite and dacite of the Kuaotunu Subgroup (Coromandel Group) and locally in greywacke basement of the Mania Hill Group, the sole area where mineralisation in the greywacke basement is exposed (Fig. 2.1; (Christie *et al*. 2007). These northern goldfield host rocks are between 19 to 9 Ma (excluding greywacke basement) with limited radiometric dates suggesting they have mineralisation ages of 14 to 10 Ma.

There has been an intermediate to deep level (≥500 m) of erosion in the northern province deposits as indicated by fluid inclusion data (Christie *et al*. 2007). Some of the deposits subjected to deep levels of erosion reveal a close spatial and possible genetic relationship with porphyry Cu deposits (including Sylvia epithermal veins and Ohio Creek porphyry Cu-Mo-Au deposit). At a regional and deposit scale, veins in the northern goldfield have a large range of strike directions, including the Coromandel and Thames deposits which are the main bonanza-style veins in the Hauraki goldfield. As well as relatively high Au/Ag ratios and veins filled with coarse comb or massive quartz, some deposits are characterised by arsenopyrite (found in the Coromandel deposits and in deposits farther north) and absent or rare vein adularia.

2.3.2 Eastern province

The eastern province of the goldfield contains deposits which occur primarily in rhyolite of the Whitianga Group, but in local instances (e.g., Broken Hills and Neavesville) are hosted by, or extend downward into, andesite and dacite of the Waiwawa Subgroup (Christie *et al*. 2007). Host rock ages in the eastern province range from 11 to 5 Ma (Christie *et al*. 2007), with radiometric dates ($^{40}Ar/^{39}Ar$) from vein adularia at Neavesville presenting plateau ages of 6.89 ± 0.02 Ma (Mauk & Hall 2004). Mineralisation ages in this province generally range from 7.1 to 6.3 Ma (Christie *et al*. 2007).

The presence of sinters and hydrothermal eruption breccias indicate that the deposits formed in the shallow epithermal environment and eroded to shallow levels (Christie *et al*. 2007). In some instances epithermal mineralisation is controlled by structures associated with caldera formation (Briggs & Krippner 2006). Similarly to the northern goldfield deposits, veins in the east have a wide range of strike directions (Christie *et al*. 2007). Compared to the andesites of the underlying Coromandel Group, the Whitianga Group rhyolites have greater permeability and lesser structural competence. Mineralised veins are therefore generally thinner, represent a smaller amount of extension by vein opening, but are more tightly clustered (Spörli & Cargill 2011). Host rock is commonly replaced by adularia in veins (Christie *et al*. 2007)

2.3.3 Southern province

Greater than 80 percent of the Au that has been recovered from the goldfield was deposited in the southern province (Mauk *et al.* 2011). These deposits occur in andesites and dacites of the Waiwawa Subgroup, with the exception of some (e.g., Karangahake) extending upward into overlying rhyolitic rocks of the Whitianga Group (Fig. 2.3; Christie *et al*. 2007).). The host rock ages in the southern province are more constrained than other provinces being in the range of 8 Ma to 5.5 Ma. Radiometric dates suggest mineralisation occurred almost simultaneously with host rock formation ages (c. 7 and 6 Ma).

Other than Karangahake and Martha, both of which exhibit large vertical intervals of mineralisation, the deposits are generally eroded to intermediate levels (Christie *et al*. 2007). A common feature with the southern deposits is the relatively narrow

range of vein strike directions, with most veins striking northeast. A large number of veins exhibit colloform and crustiform textures and are filled with cryptocrystalline or finely crystalline quartz. Adularia and calcite are common accessory minerals in veins with adularia commonly replacing the host rocks surrounding these veins. Gold/silver ratios are relatively low in these deposits.

Exceptions include the Kuaotunu and Komata deposits (Fig. 2.3; Christie *et al*. 2007). The Kuaotunu deposit in the northern province has crustiform-banded veins, lattice-bladed quartz textures and adularia occurrences similar to deposits in the southern goldfield. Komata, a southern goldfield deposit, occurs predominantly within a rhyolite dike. Despite this, Komata has all the characteristics of deposits in andesite and dacite of the southern goldfield, including significant Au-Ag production.

2.4 The Waihi vein system

2.4.1 Stratigraphy

The Waihi vein system includes the world-class Martha Hill deposit, an epithermal Au-Ag base metal sulfide-quartz vein system (Brathwaite *et al.* 2006), the nearby Union-Gladstone Hill deposits (Brathwaite & Faure 2002), and the newly discovered Favona deposit (Fig. 2.4; Torckler *et al.* 2006; Simpson & Mauk 2007). These quartz vein systems are hosted by hydrothermally altered andesite of the Waipupu Formation, a Late Miocene formation within the Coromandel Group. The main rock type is plagioclase-porphyritic two-pyroxene andesite, with prominent but minor quartz phenocrysts in the lower part of the sequence. Waipupu Formation andesites have a predominantly high Si composition with SiO_2 contents ranging between 60 and 63% (anhydrous composition). Unaltered andesite contains phenocrysts of plagioclase, augite, hypersthene, minor quartz, and local hornblende, with accessory magnetite, apatite, and zircon. Beds of dacitic lithic and crystal tuffs occur between some flows. The tuffs are composed of lithic clasts (andesite, dacitic tuff, and pyritic siltstone) and broken crystals of plagioclase, quartz, and altered pyroxene or biotite. Thin carbonaceous lake beds are also present at several levels within the sequence and dip at about 40° SE (Brathwaite & Faure 2002; Brathwaite *et al.* 2006). In the northeast part of the deposit, the upper part of the sequence is dominated by dacitic tuffs and tuff breccias with only minor andesite flows

(Brathwaite & Faure 2002). This upper part of the sequence hosts the Favona deposit (Brathwaite *et al.* 2006).

Immediately east of Favona, the andesitic and dacitic host rocks are unconformably overlain by unaltered hornblende dacite of the Uretara Formation, a late Miocene to early Pliocene formation (K-Ar age of 5.1 to 4.9 Ma) within the Kaimai Subgroup (Brathwaite & Faure 2002; Brathwaite *et al.* 2006). About 1 km east, the nearby biotite rhyolite (Homunga Rhyolite) of the Whitianga Group (K-Ar age of 5.5.-5.3 Ma) is overlain and intruded by the hornblende dacite.

The host andesite and overlying dacite and rhyolite are largely covered by unaltered Corbett, Owharoa and Waikino ignimbrites of late Pliocene to early Quaternary age, only a small part of the Waihi quartz vein system originally cropped out on Martha Hill (Brathwaite & Faure 2002; Brathwaite *et al.* 2006). The Owharoa Ignimbrite has been dated at 3.69 Ma (Hoskin *et al.* 1998) and 3.76 Ma (Vincent 2012) by U-Pb dating on zircon. To the south, the ignimbrites are underlain by alluvial-lacustrine carbonaceous beds (Romanga Formation) of late Pliocene age from palynology. The ignimbrite and lake sediment deposits infill what is considered a caldera structure of the Waihi Basin (as defined by decreases in gravity and resistivity) resulting in their increasing thickness towards the south. In the Waihi area, northeasterly trending faults dominate, but north- and northwest-striking faults are also present (Brathwaite & Faure 2002; Brathwaite *et al.* 2006).

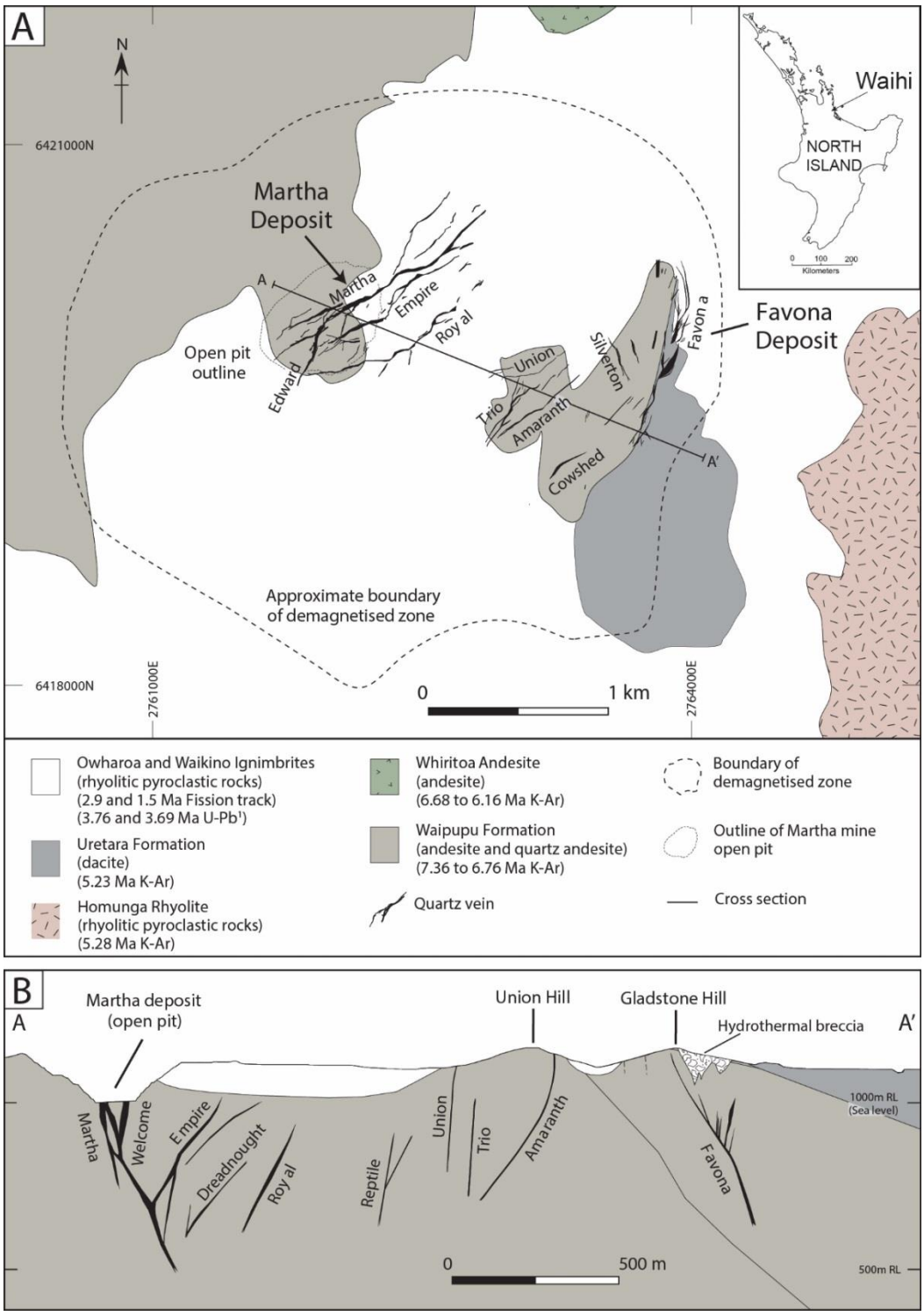

Fig. 2.4. Surface geology map of the Waihi vein system. All veins occur in the Waipupu Formation. The Favona, Trio, Martha, Edward, Empire, and Royal veins are projected to the surface from 850 m RL (A.). Cross section showing the geology and veins of the Waihi vein system (B.) [1] U-Pb age determinations for the Owharoa Ignimbrite are from Vincent (2012) and Hoskin et al. (1998) respectively (image modified from Simpson & Mauk 2007).

2.4.2 Structure

Martha Hill

The Martha Hill deposit consists of five principal quartz lodes or vein zones (Brathwaite *et al.* 2006). Martha, Welcome, Empire and Royal lodes are collectively subparallel with a predominantly northeast strike, while the Edward lode, located further south, strikes NNE (Fig. 2.5). The Martha Lode dips at 70° to 80° SE, whereas most of the other lodes dip near vertically or steeply NW, and converge with the Martha Lode at depth (Fig. 2.6). Sets of less continuous veins, such as Jellicoe, strike east and a few veins are associated with northerly-striking faults. Mapping of the open Martha pit has also revealed a set of en echelon cross veins striking at 100°. The hanging walls of the Martha, Empire and Royal lodes are bounded towards their tops by fault zones.

In the Martha Hill vein system, the Martha lode is the principal fault in an extensional fault-fracture mesh where an anastomosing array of linking and rejoining splays have formed between the Martha lode and the principal hanging wall fault splays hosting the Welcome, Empire, and Royal lodes. Splay faults evident in the footwall commonly loop back on the principal structure (Brathwaite *et al.* 2006). The majority of veins formed in opening faults or fractures and display releasing-restraining bend geometry and little or no lateral movement. Vein formation was broadly synchronous, although NE-striking veins commonly cut E-striking veins (Brathwaite *et al.* 2001; Brathwaite *et al.* 2006).

2.4.3 Mineralisation and alteration

Hydrothermal alteration

The epithermal deposits of the Hauraki goldfield are quartz ± calcite ± adularia ± illite types, although some occurrences of epithermal mineralisation in the Thames area have affinity with hypogene advanced argillic alteration (Christie *et al*. 2007). At Martha, potassic (quartz + adularia + illite + pyrite ± chlorite ± albite), propylitic (quartz + calcite + chlorite + illite + pyrite), and argillic (illite + smectite + chlorite + pyrite) are three main types of alteration recognised (Brathwaite et al. 2006). Proximity to quartz veins has strong control over the extent and intensity of the potassic and propylitic alteration, where a zone of pervasive potassic alteration envelopes the quartz veins and is surrounded by a zone of propylitic alteration. Argillic alteration is largely confined to the upper part of the vein system on the

hanging wall of the Martha Lode at the eastern end of the vein system where it locally overprints other alteration types. Goethite, alunite and kaolinite are found in the eastern and southern walls of the pit as oxidation/weathering products forming a brown oxidised andesite.

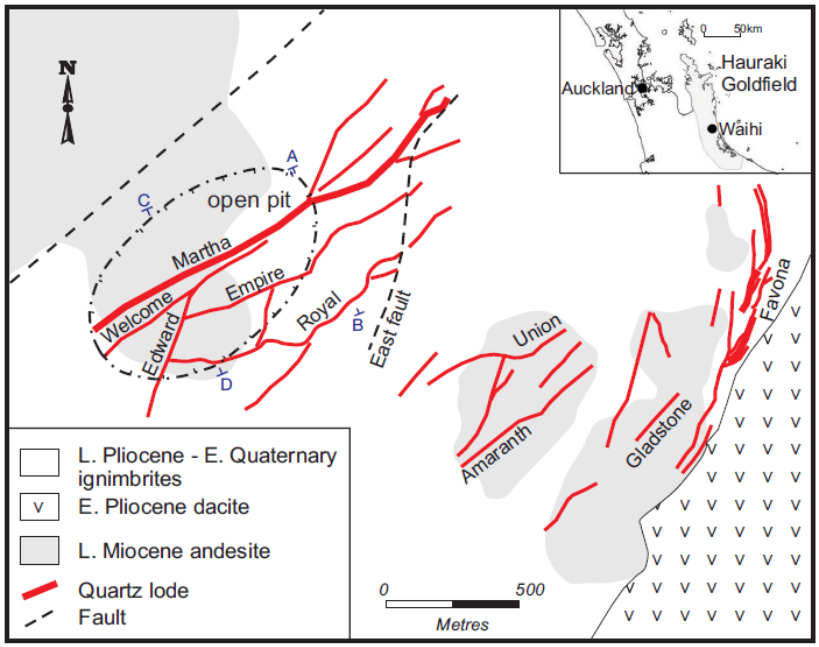

Fig. 2.5. Simplified geology map of the Waihi vein system with traces of the lodes projected to the surface (from Brathwaite et al. 2006).

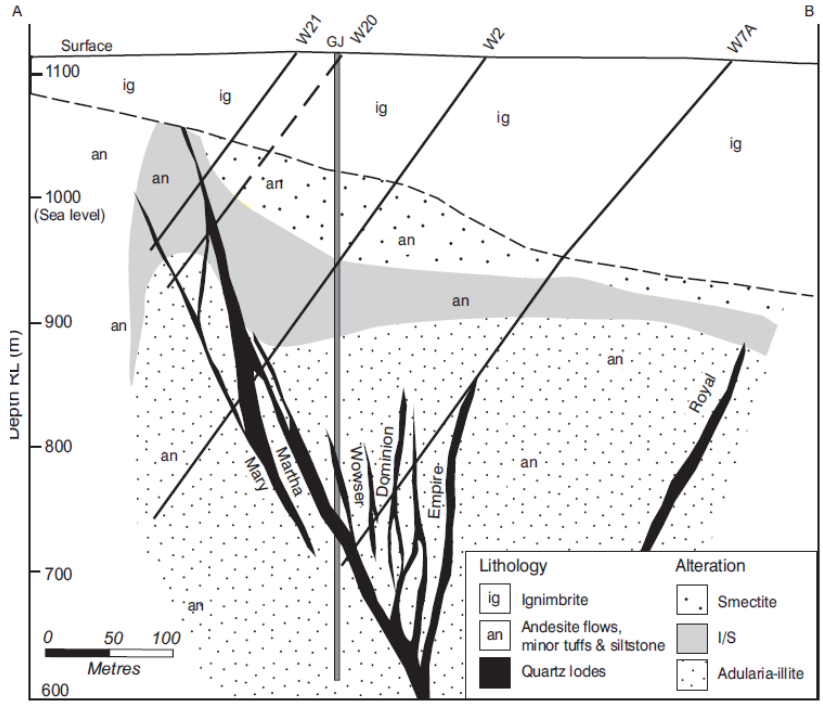

Fig. 2.6. Cross-section A-B at 2160 m E (mine grid), showing the main lithologies, lodes and alteration zones of smectite, interlayered illite-smectite (I/S) and adularia-illite. Also shown are the location of drill holes and the Grand Junction shaft (GJ) for former underground workings (from Brathwaite et al. 2006).

Vein mineralisation

The major lodes at Martha Hill are filled with microcrystalline to medium-grained quartz and quartz vein breccias. Sulfide-bearing bands containing pyrite, sphalerite, galena, chalcopyrite and acanthite occur within fine- to medium-grained quartz. The detailed paragenesis of the veins is complex but multiple phases have been recognised and major lodes consist of an early stage of platy calcite + quartz, a main stage of quartz + sulfides and a late stage amethyst (Brathwaite & Faure 2002; Brathwaite et al. 2006). Although amethyst represents a minor phase, it distinctively marks the last event in the vein deposition sequence. The main quartz stage itself is made up of multiple vein depositional phases which occur over an extended period of time (Brathwaite & Faure 2002).

Vein paragenesis alters with depth at the Martha Hill deposit (Brathwaite & Faure 2002; Brathwaite et al. 2006). In the upper part of the vein system (above about 1070 m RL, 70 m asl), quartz occurs as crustiform to colloform veins consisting of mm-scale bands of microcrystalline and fine-grained crystalline quartz, the latter commonly enclosing small open space cavities as fine comb quartz. Minor adularia, which mainly occurs locally in bands in contact with wall rock, indicates that this adularia was deposited at an early stage of the vein-filling sequence. Minor pyrite, sphalerite, chalcopyrite, tetrahedrite, acanthite, and electrum occur locally within the colloform quartz. Below 1070 m RL, crustiform banding is coarser, consisting of interbanded fine- to medium-grained quartz, with sulfides (pyrite, sphalerite, galena and chalcopyrite) making up 3 to 80% of some bands. Many veins contain hydrothermal breccias composed of angular vein quartz or wallrock fragments in a fine-grained quartz matrix. Quartz and sulfides commonly form cockade overgrowths around the fragments.

2.4.4 Martha mining and production history

From 1882 until 1952, following the discovery of the Martha lode in 1878, the Martha deposit was worked as an underground mine that exploited the extensive system of Au-Ag bearing quartz lodes along a strike length greater than 1500 m and from a vertical extent of up to 575 m (Brathwaite & Faure 2002; Brathwaite *et al*. 2006; Mauk *et al*. 2011). During this period the underground mines produced 1,082,000 kg of Au-Ag bullion from 12 Mt of ore, estimated at 152,800 kg Au (4.9 Moz) and 929,000 kg Ag (29.9 Moz), representing average grades of 12.7 g/t Au

and 77 g/t Ag. The Waihi Gold Mining Company (WGMC) and its successor the Martha Gold Mining Company produced most of the ore from the Martha mine, while some of the ore was also mined by the Waihi Grand Junction Company (GJ) from the eastern end of the lode system. In 1926 the GJ mine was leased to the WGMC and later purchased outright in 1939 (Brathwaite *et al*. 2006). The major period of gold mining ended with the closure of the underground Martha mine at Waihi in 1952 (Christie et al. 2007).

Revival during the 1960s and early 1970s saw a number of companies (South Pacific Mines, Norpac Mining Ltd, Newmont Pty Ltd) carrying out further exploration with encouraging results. Mineral Resources (NZ) Ltd acquired the property in 1974 and subsequent prospecting on Martha Hill led to the concept of an open-pit mineable resource. The open-pit concept was tested in 1979 when Amax entered into a joint venture with Mineral Resources. Detailed drilling from 1980 to 1983 defined an open-pit mineable resource of about 10 Mt grading 2.9 g/t Au and 28.1 g/t Ag. Open-pit mining commenced in 1988 after intensive environmental impact and engineering studies relating the problems of operating a large open pit mine in close proximity to an existing town (Brathwaite et al. 2006). From 1997 it has been worked on as an open-pit mine with a planned length of 840 m, width of 575 m, and depth of 250 m. This new pit design exploits remnants of veins targeted by earlier mining, stope fill, vein breccias and the abundant veins and veinlets that occur between the main veins (Mauk *et al*. 2011).

To date, the largest producer in the Hauraki goldfield is the Martha mine (John 2011). Through 2009, total production from open-pit and underground mining was 210,944 kg Au and 1,299,893 kg Ag, which accounts for approximately 66 percent of the total Au and 89% of the total Ag production of the Hauraki goldfield (John 2011; Spörli & Cargill 2011).

Chapter 3 Epithermal deposits

3.1 Introduction

Epithermal deposits are important sources of gold and silver that are formed in the shallow parts of high-temperature hydrothermal systems (Simmons *et al*. 2005). The term "epithermal" was first derived from Lindgren (1933) who established, using observations of mineralogy and texture, an ore-forming environment with specific temperatures and pressures (depth). Epithermal orebodies display a wide range of characteristic features with over a dozen classification schemes proposed since the late 1970s (Simmons *et al*. 2005).

This chapter provides an introductory review to epithermal systems focusing on the definition and classification, general characteristics, and common settings of mineralisation in epithermal deposits. Differences between low-sulfidation and high-sulfidation styles, the two principal styles of epithermal mineralisation in which gold is the dominant economic metal and, finally, styles of hydrothermal alteration are here discussed in brief.

3.2 Definition and classification

Epithermal deposits develop within large, mainly subaerial, hydrothermal systems under a range of temperature versus depth (pressure) ore-forming conditions (Simmons *et al*. 2005; Fig. 3.1a). In the shallow environment, which is near-hydrostatic (at equilibrium), depth relates directly to pressure, with maximum temperature largely controlled by the boiling-point-for-depth curve (Fig. 3.1b). Ore minerals precipitate at a range of temperatures (from ~150° to ~300° C) and depths (from ~50 to as much as 1500 m below the water table), as a consequence of chemical changes derived from environmentally-influenced sharp pressure and temperature gradients (Simmons *et al.* 2005). The epithermal environment is hence defined by these physical controls. However, ore genesis also relies upon composition of the hydrothermal solutions, which controls metal transport and deposition. Because these metal-transporting solutions vary in composition and differ in origin, they vary in their metal content. As a result, epithermal orebodies

display a wide range of characteristic features with over a dozen classification schemes being proposed since the late 1970s (Table 3.1).

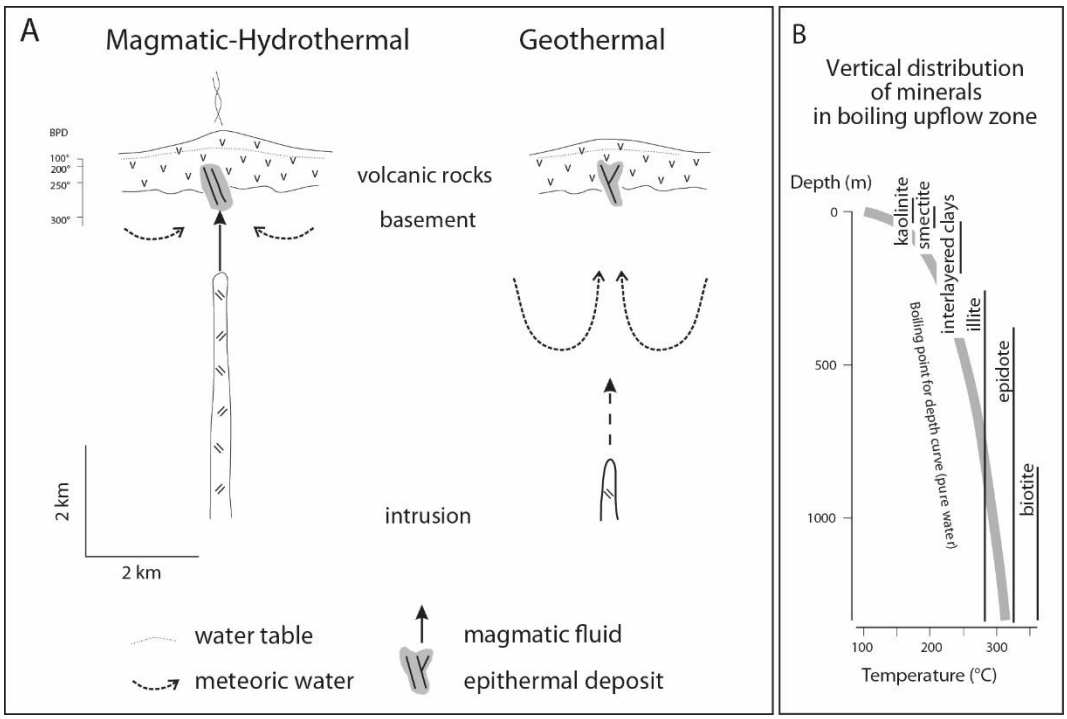

Fig. 3.1. A) Simplified conceptual models of high-temperature hydrothermal systems, showing the relationship between epithermal environments, magmatic intrusions, fluid circulation paths, and volcanic and basement host rocks. The magmatic-hydrothermal epithermal environment is analogous to those existing in modern volcanoes where the system is dominated by acid hydrothermal fluids formed by magmatic liquid and vapour containing H_2O, CO_2, HCl, H_2S, SO_2, with variable input from local meteoric water. The geothermal epithermal environment is analogous to systems exploited for generation of electricity. This system is dominated by deeply circulated, near-neutral pH chloride waters containing CO_2, NaCl, and H_2S, mostly of meteoric origin. The location of the underlying magma chambers in both environments is hypothetical to portray the different path lengths that deep fluids traverse before encountering the ore-forming environment. There is minimal water-rock interaction during ascent in the magmatic-hydrothermal environment compared to considerable water-rock interaction during ascent in the geothermal environment. B) Vertical distributions of common hydrothermal minerals plotted according to depth, using the hydrostatic boiling curve as the reference temperature gradient (modified after Simmons *et al.* 2005).

3.3 General characteristics of epithermal deposits

Epithermal deposits comprise epigenetic ore mostly mined for gold and silver (Simmons *et al*. 2005). The deposits are generally hosted by coeval and older volcanic rocks, but rarely by subvolcanic intrusions. Underlying basement rocks often serve as host rocks. A single deposit can cover areas that range from <10 to >100 km^2 (Simmons *et al*. 2005). In places like the Hauraki Goldfield, New Zealand, more than 50 epithermal Au-Ag deposits occur in a 200-km-long by 40-

km-wide belt (John 2011). Epithermal orebodies are located within shallow parts of fossil hydrothermal systems, representing zones of palaeopermeability (Simmons *et al*. 2005), the permeability of the host rock at the time of hydrothermal activity. The shape of the orebody is influenced by structural and lithological controls which can vary significantly between deposits (Simmons *et al*. 2005). Most epithermal orebodies occur within steeply dipping veins of minor faults (second- or third-order structures) formed through dilation and extension. Veins hosted in major faults are less common. Rock rheology and brittle failure are crucial features when considering the structural development of epithermal deposits. Lithology is also important as it can significantly affect porosity and permeability, which in turn can control fluid flow through specific units, along rock contacts, or through permeable masses of brecciated rock. Factors such as faults and fracture networks, breccias, coarse clastic rocks, and intensely leached rocks, whether they are formed from volcanic or hydrothermal processes, all contribute to the ore-forming process and determine whether ore occurs in veins or is disseminated. The spectrum from vein-related to disseminated ores means orebodies can extend for hundreds to thousands of metres laterally and tens to hundreds of metres vertically. Quartz is the dominant gangue mineral which makes ores hard and generally resistant to weathering. Pyrite is the dominant sulphide mineral, ranging in sulphide content from <1 to >20 volume percent.

Table 3.1. Evolution of classification schemes applied to epithermal deposits (modified after Simmons *et al.* 2005).

Sillitoe (1977)	Acid		Alkaline			
Buchanan (1981)	Epithermal					
Ashley (1982)	Enargite gold					
Giles and Nelson (1982)			Hot-spring type			
Bonham (1986, 1988)	High sulfur		Low sulfur		Alkalic deposits	
Hayba et al. (1985) Heald et al. (1987)	Acid sulfate		Adularia-sericite			
Hedenquist (1987), White and Hedenquist (1990, 1995)	High sulfidation		Low sulfidation			
Berger and Henley (1989)	Alunite-kaolinite		Adularia-sericite			
Albino and Margolis (1991)			Type 1 adularia-sericite		Type 2 adularia-sericite	
Sillitoe (1989, 1993a)	High sulfidation		Low sulfidation			
			High sulfide + base metal		Low sulfide + base metal	
White and Poizat (1995)	High sulfidation		Low sulfidation			
	Au-Ag-Cu deposits with vuggy quartz alteration	Au-Ag-Cu deposits with pyrophyllite-sericite alteration	Sn-Ag-base metal deposits	Ag-Au-base metal deposits	Au-Ag deposits With calc-alkaline volcanic rocks	Au-Ag deposits With alkaline volcanic rocks
Hedenquist et al. (2000), Einaudi et al. (2003), Sillitoe and Hedenquist (2003)	High sulfidation		Intermediate sulfidation		Low sulfidation	Alkalic
Cooke and Deyell (2003)	Descriptive nomenclature based on ore metals, deposit form, diagnostic hypogene gangue and alteration minerals, and dominant Cu-bearing mineral					

3.4 Settings of epithermal mineralisation

Igneous settings

Igneous activity has an important role in the formation of most epithermal deposits because they are spatially and temporally associated with subaerial volcanic rocks and their related subvolcanic intrusions (White & Hedenquist 1990). Igneous activity may provide heat necessary to generate a hydrothermal convection cell or, in some cases, the magma may contribute a component of the total gases to an overlying hydrothermal system.

The volcanic-hosted deposits typically occur within effusive or pyroclastic rocks of intermediate to acid volcanic settings, significant deposits being discovered in calk-alkaline to alkaline suites (White & Hedenquist 1990). They may also occur in bimodal volcanic suites. In rare cases, epithermal deposits are hosted in basic volcanics which have shoshonitic or alkaline affinities.

Hydrothermal activity also occurs in a variety of modern volcanic environments, including calderas or grabens, andesitic stratovolcanoes, cordilleran volcanism, and oceanic islands (White & Hedenquist 1990). The hydrological regime is characteristic to these volcanic environments and controls the discharge and recharge of the hydrothermal system, the distribution of conduits, the types and distribution of hydrothermal alteration products, and the potential sites of deposition or ore minerals.

Tectonic setting

Epithermal mineralisation may occur in a variety of tectonic settings associated with the subaerial volcanism described above, the most common setting being volcanic arcs characteristic of convergent tectonic settings (White & Hedenquist 1990). Back-arc rifting is also common in these settings. If back-arc rifting evolves into a marine back-arc basin, it is characteristically submarine and therefore no longer prospective for epithermal deposits as massive sulfide deposits form in this setting instead.

Not all subaerial volcanic settings appear prospective for epithermal deposits, mostly due to magma chamber dynamics (White & Hedenquist 1990). Examples include regions of continental flood basalts and primitive island-arc settings. The magma chambers of continental flood basalts are deep and/or small, with narrow

conduits. This prevents the development of a major hydrothermal system at shallow depths. In primitive island-arc settings, such as the Tonga-Kermadec chain, large magma chambers have not yet developed. Therefore, the necessary heat-flow conditions required to establish major hydrothermal activity have probably not been met.

Structural setting

Near-surface structures are almost essential in the formation of most gold deposits because it enhances permeability (White & Hedenquist 1990). At a regional scale, many epithermal deposits are associated with volcanic-related structures. In places like the San Juan Mountains of Colorado, and in some parts of Japan and the southwest Pacific, epithermal deposits have a close association with felsic calderas and andesitic vent complexes.

Regional faults play a major role on the localisation of epithermal deposits (White & Hedenquist 1990). They may guide the emplacement of the magmatic heat source by providing a path of least resistance and thus influencing the location of subsequent hydrothermal activity. However, mineralisation is commonly located on subsidiary faults or splays, not the major regional structure. Minor structural features also play a role on the localisation of epithermal deposits, particularly within a prospect area. Permeability and hence the distribution of mineralisation, may be influenced by bedding planes, joints and joint intersections.

3.5 Low-sulfidation versus high-sulfidation

The two principal styles of epithermal mineralisation where gold is the dominant economic metal are low-sulfidation and high-sulfidation styles (White & Hedenquist 1995). Other literature (Heald *et al*. 1987) also refers to these two styles as adularia-sericite and acid-sulfate types, respectively. These terms reflect the two end-member sulfidation states of the sulfide mineral assemblage (Hedenquist *et al*. 2000). The difference between low-sulfidation and high-sulfidation mineralisation styles is discussed, outlining the importance to distinguish between the two for exploration.

One of the main reasons the two deposit styles differ is that they are formed from fluids of contrasting chemistry (White & Hedenquist 1995; Fig. 3.2). The mineralising fluids in the low-sulfidation environment are similar to those from

active geothermal systems. Fluids are reduced and have a near-neutral pH, forming low-sulfidation state sulfide minerals. In high-sulfidation systems, relatively high-sulfidation state minerals are dominant and are linked to acidic and oxidised fluids formed in the magmatic-hydrothermal environment adjacent to young volcanoes.

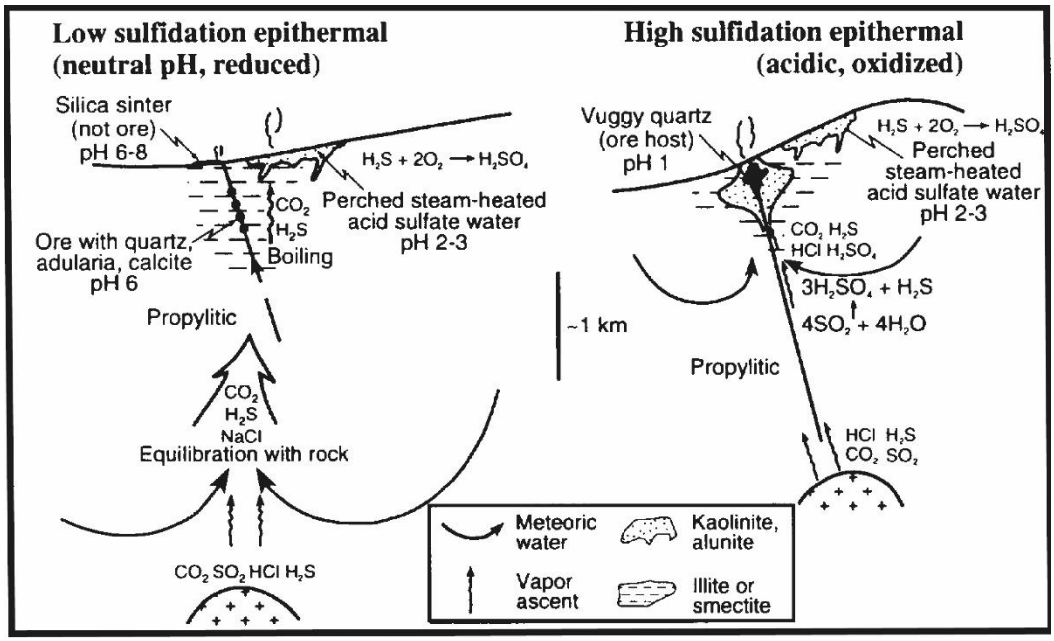

Fig. 3.2. The relationship between fluid types and alteration zoning in low- and high-sulfidation systems (after White & Hedenquist 1995).

The primary reason why the fluids differ between these two styles is the degree to which they have equilibrated with their host rocks below the level of ore deposition. Meteoric water is the dominant hydrothermal fluid in the low-sulfidation environment. In some systems water and reactive gases are of magmatic origin (White & Hedenquist 1995). As fluids ascend from great depths, they essentially equilibrate with the altered host rocks. Resultant liquid is typically low salinity, less than 1 to 2 wt percent NaCl equivalent, and may be gas-rich, with CO_2 and H_2S being the dominant gases (Hedenquist *et al*. 2000; Fig. 3.2).

In high-sulfidation environments (Fig. 3.2), the reactive components are derived from an oxidised magmatic source which ascended to the near surface with little water-rock interaction at depth (White & Hedenquist 1995). At shallow depths, groundwater may absorb HCl- and SO2-rich vapour, transforming it into a hot (200-300 °C), highly acidic (pH 0-2) and oxidized fluid. This fluid reacts extensively with, and leaches, host rock.

Ore deposits of all types can be classified based on basic characteristics such as form, mineralogy, textures, and alteration zoning (White & Hedenquist 1995). When comparing low-sulfidation from high-sulfidation systems, although there is a considerable overlap in characteristics there are many distinctive features. The form of these two styles of epithermal deposits is summarised in Table 3.2. Both styles are typically structurally controlled. In low-sulfidation deposits, ore is generally located within cavity-filling veins with sharp boundaries, or stockworks of small veins. In high-sulfidation deposits, veins can be important, but the majority of ore is disseminated, replacing or impregnating leached country rock. This disseminated form can conceal structures related to mineralisation.

Table 3.2. Characteristic forms of low-sulfidation and high-sulfidation alteration assemblages (after White & Hedenquist 1995).

Low Sulfidation (Adularia-sericite)	**High Sulfidation** (Acid sulfate)
Open-space veins dominant	Veins subordinate, locally dominant
Disseminated ore mostly minor	Disseminated ore dominant
Replacement ore minor	Replacement ore common
Stockwork ore common	Stockwork ore minor

Ore and gangue

The different redox conditions of the hydrothermal fluid between the low- and high-sulfidation styles result in several distinct differences in the ore mineralogy and gangue minerals and, although there are overlaps, these differences are primarily in the sulphide mineralogy (White & Hedenquist 1995; Table 3.3). One example is that sphalerite and arsenopyrite are commonly found in low-sulfidation deposits, but are scarce and rare in high-sulfidation deposits, respectively. Copper minerals, especially the high-sulfidation state sulfosalts enargite-luzonite, are common in high-sulfidation deposits only. Total sulfide mineral abundance (dominantly pyrite) is not significant in either style as it can be high or low.

There is also overlap and differences in gangue minerals for the two styles of epithermal mineralisation (White & Hedenquist 1995; Table 3.4). These differences ultimately arise from the reactivity (pH) of the altering fluid. The most common gangue mineral in both styles is quartz. Adularia and calcite are the next most common (after quartz) in low-sulfidation styles, but are absent from high-sulfidation deposits. In acidic conditions, the formation of minerals such as kaolinite and alunite (among others) are common in high-sulfidation deposits, occurring in minor abundance. Kaolinite and alunite only occur as an overprint in low-sulfidation deposits and not as a primary gangue mineral.

Table 3.3. Ore minerals in epithermal ores shown as frequency of occurrence relative to the abundance (bracketed) (after White & Hedenquist 1995).

	Low Sulfidation	High Sulfidation
Pyrite	Ubiquitous (abundant)	Ubiquitous (abundant)
Sphalerite	Common (variable)	Common (very minor)
Galena	Common (variable)	Common (very minor)
Chalcopyrite	Common (very minor)	Common (minor)
Enargite-luzonite	Rare (very minor)	Ubiquitous (variable)
Tennantite-tetrahedrite	Common (very minor)	Common (variable)
Covellite	Uncommon (very minor)	Common (minor)
Stibnite	Uncommon (very minor)	Rare (very minor)
Orpiment	Rare (very minor)	Rare (very minor)
Realgar	Rare (very minor)	Rare (very minor)
Arsenopyrite	Common (minor)	Rare (very minor)
Cinnabar	Uncommon (minor)	Rare (very minor)
Electrum	Uncommon (variable)	Common (minor)
Native gold	Common (very minor)	Common (minor)
Tellurides-selenides	Common (very minor)	Uncommon (variable)

Table 3.4. Mineralogy of gangue shown as frequency of occurrence relative to the abundance (bracketed) (after White & Hedenquist 1995).

	Low Sulfidation	High Sulfidation
Quartz	Ubiquitous (abundant)	Ubiquitous (abundant)
Chalcedony	Common (variable)	Uncommon (minor)
Calcite	Common (variable)	Absent (except as overprint)
Adularia	Common (variable)	Absent
Illite	Common (abundant)	Uncommon (minor)
Kaolinite	Rare (except as overprint)	Common (minor)
Pyrophyllite-diaspore	Absent (except as overprint)	Common (variable)
Alunite	Absent (except as overprint)	Common (minor)
Barite	Common (very minor)	Common (minor)

Textures

Low-sulfidation deposits are texturally diverse in contrast to high-sulfidation deposits. Textures in low-sulfidation deposits include banded, crustiform quartz and chalcedony veins, druse-lined cavaties, and multiple-episode vein breccias. Multiple-episode vein breccias may reflect hydrothermal eruptions at the surface as a result of explosive pressure release. Boiling in a low-sulfidation deposit can form lattice-textured bladed calcite. Quartz can replace calcite textures as the system cools (White & Hedenquist 1995). If there has been little erosion, the palaeosurface in low-sulfidation deposits may be marked by distinctive silica sinters which form where the boiling, neutral-pH hot-spring water discharges at the surface (White & Hedenquist 1995; Hedenquist *et al*. 2000).

By contrast, there is little variation of textures in high-sulfidation styles (White & Hedenquist 1995). Massive bodies of vuggy quartz typical of Nansatsu-type deposits are characteristic textures. In some cases, local veins and breccias may be important hosts to ore. Vuggy quartz forms as a result of acid leaching at pH <2. This leaching creates open spaces and leaves mainly silica behind. The residue from the acid leaching recrystallises to quartz. Additional quartz and pyrite are also deposited from solution. The vuggy quartz bodies may also be cut by massive to banded sulphide veins consisting of pyrite and enargite. Unlike low-sulfidation deposits, silica sinters never form at the surface in this acidic environment because the polymerisation and precipitation of silica from acidic solutions is inhibited by kinetic factors. These two styles of deposit can be distinguished from one another on textural grounds alone.

Alteration mineralogy and zoning

Low- and high-sulfidation style deposits can also be distinguished by their mineralogy and zonation of hydrothermal alteration assemblages (White & Hedenquist 1995). Thermal and geochemical structures of hydrothermal systems can be reconstructed using alteration minerals because many hydrothermal minerals are stable over limited temperature and/or pH ranges. Because epithermal deposits occur at shallow depths and generally within a dynamic environment which is vulnerable to significant erosion during hydrothermal activity, it is necessary to distinguish alteration that overprints the system from that associated with ore.

Temperatures of near-neutral pH thermal waters in low-sulfidation deposits decrease with decreasing depth and with increasing distance from the conduit of the fluid flow (White & Hedenquist 1995). Direct measurement of the alteration mineralogy and temperature in active geothermal systems can provide an indication of the range of thermal stability of temperature-dependent minerals. This information is useful when it comes to exploration of epithermal prospects because, by establishing the distribution of alteration minerals, a palaeoisotherm can be deduced. In turn, this helps to locate conduits of palaeoflow, and to determine the level of erosion. The significance of locating conduits of palaeoflow is that major ore accumulates in conduit zones. Knowing the level of erosion is important for exploration because most epithermal ore is deposited over the range of 180 to 280 °C, equivalent to a depth below the palaeowater table from about 100 m to 800-1500 m. An indication of palaeotemperatures low in that range is encouraging for

prospects. Palaeotemperatures >280 °C suggests the prime epithermal potential has been eroded.

Low-sulfidation environments are dominated by clay minerals that have variations in their basal spacing – one of the best indicators of palaeotemperature (White & Hedenquist 1995). Smectite, which is stable at <160 °C, will give way to interstratified illite-smectite with increasing temperature. Illite by itself is generally stable at >220 °C. This progression in thermal stability is common in low-sulfidation ore bodies where there is a clear upward and outward zonation of minerals. Adularia and calcite are common minerals in the ore zone of low-sulfidation deposits. Although these minerals are relatively insensitive to temperature (Fig. 3.3), they form from boiling in the conduits which causes CO_2 loss and consequent increase in pH. Zeolites (most stable at <220 °C, except for wairakite) and Ca-silicates such as epidote (stable above 200-240 °C) are among other temperature-sensitive minerals. Near the base of the epithermal environment, hydrothermal biotite and amphibole are minerals that commonly indicate temperatures above about 280 °C.

Under high-sulfidation, acidic conditions, stable minerals include kaolinite, dickite, pyrophyllite, diaspore and alunite (White & Hedenquist 1995). Several of these minerals are also temperature sensitive (Fig. 3.3). At a temperature <160 °C, pyrophyllite may form if the silica concentration is high (i.e., forming chalcedony or amorphous silica). If pyrophyllite coexists with dickite, illite or diaspore, it infers palaeotemperatures >200 °C. Minerals such as zunyite, topaz and andalusite comprise the advanced argillic alteration assemblage formed by high-temperature (>260 °C) acidic fluids in high-sulfidation deposits. The host rock in high-sulfidation deposits will commonly consist of leached silicic alteration with advanced argillic alteration grading outward to argillic alteration halos. Away from the conduit, the acidic water is progressively neutralised by reaction with the host rock which allows illite or smectite to become stable.

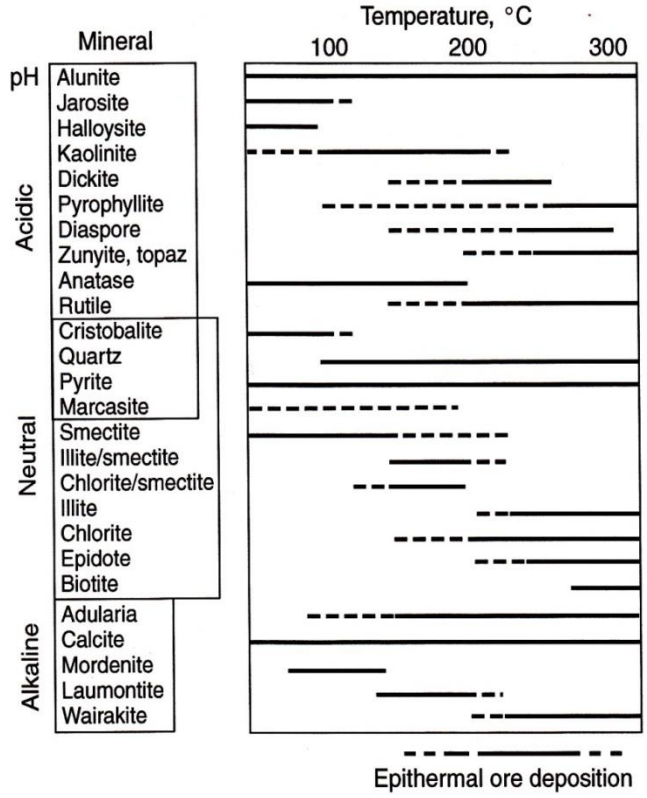

Fig. 3.3. Thermal stability of various hydrothermal minerals that occur in the epithermal environment under acid and neutral-pH conditions, and the typical temperature range for deposition of epithermal ore (after Hedenquist *et al.* 2000).

Even though kaolinite and alunite are acid-stable minerals at lower temperatures, they can also occur in low-sulfidation systems by near-surface steam-heated waters (White & Hedenquist 1995). Typically forming around 100 °C, these acid-sulfate waters may be further heated at depth if they flow downwards along fractures. Where hydrothermal kaolinite and alunite occur in these deposits they overprint ore or overlay ore, marking the top of a low-sulfidation deposit. A similar alteration overprint can occur when sulfides are weathered.

In summary, it is essential to distinguish these two styles of mineralisation during exploration because 1) they have a different distribution of the alteration zones and 2) the economic potential is associated with different parts of the system (Macdonald 2007). Ore in a high-sulfidation deposit is typically associated with, and usually in, the zone of most acid alteration (White & Hedenquist 1995). Mineral assemblages which indicate less acidic conditions typically surround the high-sulfidation ore. Ore within a low-sulfidation deposit will be associated with the least acidic alteration, containing minerals such as adularia and calcite or illite. Acid-

stable minerals (kaolinite and alunite only) typical of advanced argillic alteration may occur within a low-sulfidation deposit as an overprint and are not related directly to ore mineralisation.

Chapter 4 Volcanic facies

4.1 Introduction

Drill core offers one of the most continuous sampling of rock encountered in the subsurface. The aim of this chapter is to undertake a facies analysis approach to identify the original rock types based on recognition of primary volcanic textures through strong and variable overprints of hydrothermal alteration and to establish new volcanic facies for the Waipupu Formation andesite. Eight new volcanic facies were identified and described from drill holes 844SPO597 and UW462 (Fig. 4.1), as an outcome of 1811.5 m of drill core logging. These eight facies were defined based on visible mineralogy and texture, excluding alteration mineralogy (e.g. chlorite, pyrite), and using terminology from Cas *et al.* (2009).

In the remainder of this chapter, each facies and its petrographic characteristics are described as well as their distribution downhole. Because of the orientation and limited number of drill holes used, no attempt was made to reconstruct the vertical volcanic stratigraphy, nor correlate between drill holes. However, based on textural and optical properties there is significant evidence towards magma mixing. The Waipupu Formation andesite is also texturally similar to other national and international examples.

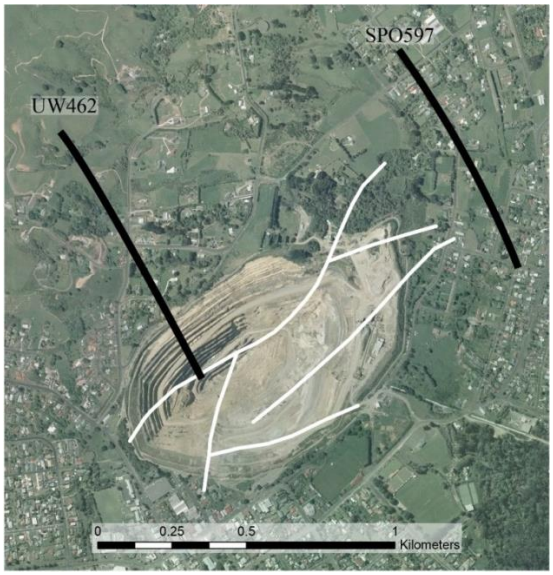

Fig. 4.1. Martha Pit, Waihi, and location of drill holes UW462 (left black solid line) and SPO597 (right black solid line). White solid lines represent major mineralised veins projected to the surface.

4.2 Sampling and analytical techniques

Lithologic description of the core was undertaken at Newmont Waihi Gold's head office located in Waihi, New Zealand. The onsite core description included physical appearance, hardness, mineralogy, texture, structure/fabric, contacts, alteration, and nature of the veins, which are further described in the following paragraphs. Samples were taken at approximate 20 m intervals, or where there were major differences or features in the core. The first 30 m of core SPO597 is shown in Figure 4.2 to illustrate the logging methodology. Remaining core logs are located in Appendix A.

Physical appearance

Colour of the core was a useful feature for differentiating between units, but was sometimes misleading or uninformative due to alteration. Colours were described here using basic hues (i.e., grey, green, blue, black), supplemented with modifying hues (i.e., greenish grey), or combinations (i.e., green-grey) as required. When describing the physical appearance fresh core was used if it had begun to oxidise, and the surface was wetted before describing. Colour intensity was also recorded as light, medium, or dark.

Hardness

Hardness was ranked based on the appearance and response of the core when hit with a geological hammer and ranked on an informal scale of 1 through to 5. A hardness of 1 represented a very soft or plastic rock which could be deformed by hand. A hardness of 2 represented a soft rock which could be scratched by a fingernail but did not crumble between the fingers, as soft rock easily pits with light blows of a geological hammer. A moderately hard rock was ranked as 3 as it scratched easy with a steel scribe and can be pitted with moderate blows of a geology hammer. A hardness of 4 represented a hard rock which was difficult to scratch with a steel scribe and could not be pitted with a geology hammer but was chipped with moderate blows of the hammer. A very hard rock was ranked as a 5. It was seldom scratched with a steel scribe and chips could be broken off only with heavy blows.

Mineralogy

Mineralogy included identifying phenocrysts and noting their shape where possible. Because of the degree of alteration in most of the core, if the correct mineral species could not be identified it was logged as a mafic or non-mafic mineral to avoid inaccurate logging. Further analysis, such as microscopic petrography and x-ray diffractometry (XRD), will be used to identify correct mineralogy.

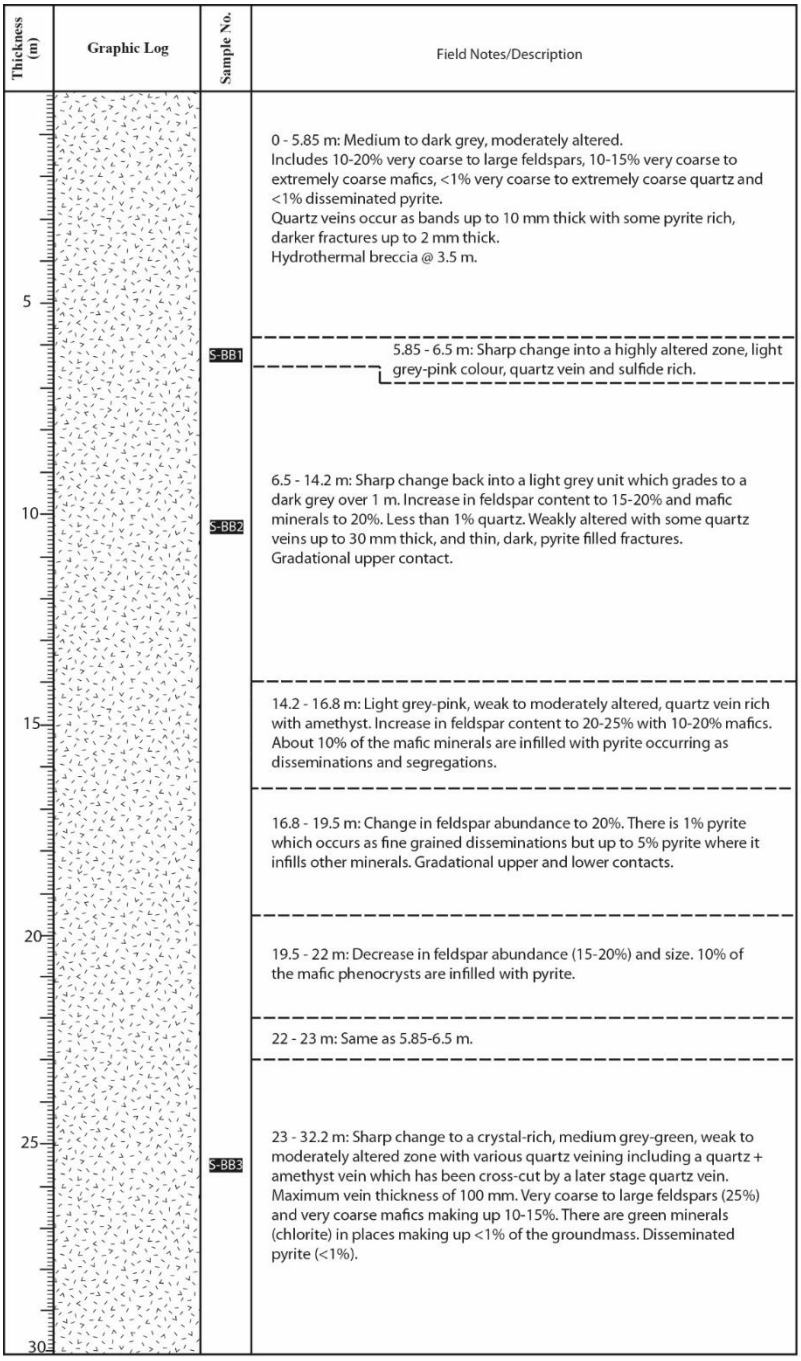

Fig. 4.2. Core log sheet for the first 30 m from drillhole SPO597, illustrating logging methodology of this study.

Texture

Grainsize (average phenocryst) and phenocryst percentage of each mineral species and percentage of groundmass were recorded under texture. Estimating the percentage of phenocryst to groundmass was done visually using a template (Fig. 4.3) and classified using abundance classes from Cas *et al.* (2009) (Table 4.1). A ruler was used for identifying the average grainsize and classified using nomenclature from Cas *et al.* (2009) (Table 4.2).

Structure/fabric

The overall structure of the core was logged noting whether it was massive, bedded, or brecciated. If layered, the layering type and thickness was logged and, if brecciated, the lithologies of the clasts were recorded together with clast size (average and range), abundance, and shape.

Contacts

Contacts between flow units were logged as sharp or gradational, but, because of the degree of alteration, many of the contacts were overprinted and not identifiable. Contacts between facies were mostly gradational.

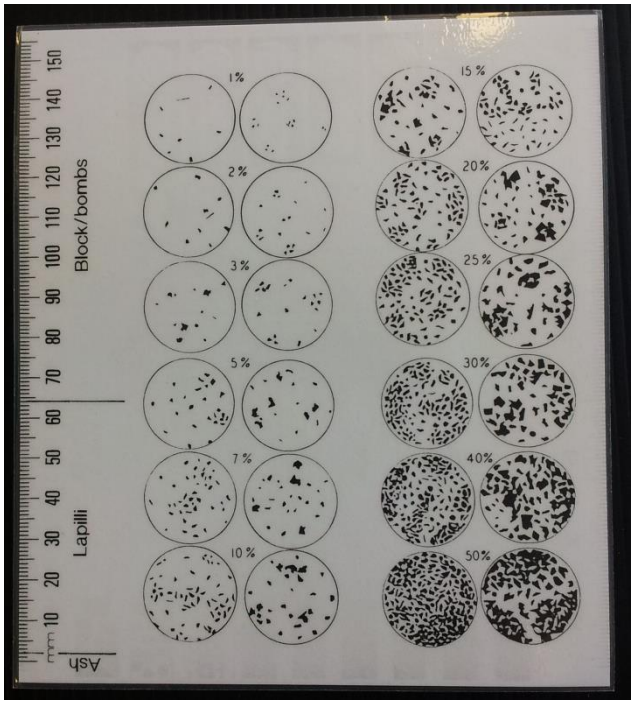

Fig. 4.3. Template used for estimating the percentage of phenocryst to groundmass.

Table 4.1. Crystal (phenocryst and xenocryst) abundance classes for coherent rocks used in this study (from Cas et al. 2009).

Crystal content	Terminology
0%	Aphyric/crystal free
<10%	Crystal-poor
10 - 25%	Moderately crystal-rich
25 - 50%	Crystal-rich
50 - 80%	Very crystal-rich
>80%	Extremely crystal-rich

Table 4.2. Crystal size nomenclature for coherent rocks used in this study (from Cas *et al.* 2009).

Grainsize	Terminology
<0.0625 mm	Microlites, microcrystals
0.0625 - 0.25 mm	Fine crystals
0.25 - 0.5 mm	Medium crystals
0.5 - 1 mm	Coarse crystals
1 - 2 mm	Very coarse crystals
2 - 4 mm	Extremely coarse crystals
4 - 8 mm	Large crystals
8 - 16 mm	Very large crystals
16 - 32 mm	Extremely large crystals
>32 mm	Extraordinary large crystals (e.g. spinifex, pegmatite crystals)

Alteration

Alteration was logged as being weakly-, moderately-, or strongly-altered on the basis of variations in colour, how well the primary volcanic textures were preserved, and the nature of the veins. The mineralogy of the vein was recorded, along with the thickness, abundance, and style (i.e. crustifrom, colloform, comb, stringers, or bands). Alteration style (mineralogy) was also recorded where known. Alteration characteristics are the focus of chapter 5.

Other

All inclusions were described, noting mineralogy, texture and appearance. Hydrochloric acid was also applied to most veins/veinlets and host rocks to identify carbonate minerals; the reaction being described as weak, moderate, or strong.

4.3 Facies types

Facies are classified below primarily on the visible crystal abundance and termed accordingly using abundance classes of Cas *et al.* (2009; Table 4.1). Facies were also classified based on the presence or absence of quartz phenocryst in the drillcore, this being a significant variation noted during the logging process.

4.3.1 Very crystal rich andesite lava (VCR)

Light to dark grey, to light to dark grey-green, very crystal rich andesite lava (Fig. 4.4 A). Phenocrysts are predominantly very coarse to extremely coarse feldspar (20-40%) and mafic minerals (15-40%). These lavas have 50-60% crystal content with no visible quartz. Average feldspar size is extremely coarse (2-4 mm) compared to the very coarse mafic minerals (1-2 mm). This facies is locally xenolithic and variably altered.

4.3.2 Very crystal rich quartz-bearing andesite lava (VCRQB)

Light to dark grey, to light to dark grey-green, very crystal rich, quartz-bearing andesite lava (Fig. 4.4 B). The crystal content ranges between 50-60% and includes quartz in the mineral assemblage. The phenocrysts include 20-50% feldspars, with 15-30% mafic minerals, and rare quartz ≤1-2%. The phenocrysts are set in a fine grained groundmass comprised predominantly of feldspars. These lavas contain larger feldspar phenocrysts compared to the very crystal rich lavas which lack

quartz. Feldspar phenocrysts are, on average extremely coarse, 2-4 mm in size, but range from very coarse to large (1-5 mm). Mafic minerals are finer grained, ranging in size from very coarse to extremely coarse (1-4 mm), but are, on average, very coarse crystals (1-2 mm). This facies is locally xenolithic and variably altered.

4.3.3 Crystal rich andesite lava (CR)

Light to medium grey-green, to light to medium grey-brown, crystal rich andesite lava (Fig. 4.4 C). The phenocrysts include 5-30% feldspars and 5-40% finer grained mafic minerals. The total mineral assemblage in these lavas range between 25-50%. There is no quartz in the mineral assemblage. The phenocrysts are set in a fine grained groundmass comprised predominantly of feldspars and mafic minerals. Feldspar phenocrysts are, on average, very coarse (1-2 mm) in size but range from very coarse to large (1-8 mm). Mafic minerals are finer grained, ranging in size from coarse to extremely coarse (0.5-4 mm), but are, on average, coarse to very coarse crystals (0.5-2 mm). This facies is locally xenolithic and variably altered.

4.3.4 Crystal rich quartz-bearing andesite lava (CRQB)

Light to dark green-grey, to light to dark grey-brown, to light to medium grey-pink, crystal rich, quartz-bearing andesite lava (Fig. 4.4 D). The presence of prominent quartz phenocrysts differentiates these lavas from the crystal rich andesite. The mineral assemblage varies between 25-50% phenocrysts, 0.5-2 mm in size and set in a fine grained groundmass. Phenocrysts are predominantly very coarse feldspars (5-30%), with coarse to very coarse mafic (1-26%) minerals, and very coarse to extremely coarse crystals of quartz (≤1-10%). This facies is locally xenolithic and variably altered.

4.3.5 Moderately crystal rich andesite lava (MCR)

Light to dark grey-green, to light to dark brown-grey-red, moderately crystal rich andesite lava (Fig. 4.4 E). Moderately crystal rich lavas are comprised of 10-25% minerals, compared to the crystal rich lavas comprised of 25-50% crystal content. The phenocrysts include feldspars and mafic minerals varying from 1-20% and 1-10%, respectively. Groundmass is fine grained. Feldspars range in size from very coarse to large crystals, with an average crystal size of 1-2 mm. Mafic minerals are

finer grained ranging in size from coarse to extremely coarse crystals, with an average size of 1 mm. This facies is locally xenolithic and variably altered.

4.3.6 Moderately crystal rich quartz-bearing andesite lava (MCRQB)

Colours vary between light to dark green-grey, to light to dark grey-brown to dark grey-blue (Fig. 4.4 F). These lavas are moderately crystal rich andesite with quartz. These lavas have a total crystal content of 10-25%. The phenocrysts include 1-20% feldspars, 1-20% mafic minerals and, ≤1-10% quartz. Feldspars range in size from coarse to large crystals, with an average crystal size of 1-2 mm. Mafic minerals are finer grained ranging in size from coarse to extremely coarse crystals, with an average size of 1 mm. Quartz crystals range in size from coarse to large crystals, with an average crystal size of 2-4 mm. This facies is locally xenolithic and variably altered.

4.3.7 Monolithic andesite lava breccia

Light to dark grey-green, to light grey-brown-pink, coarsely brecciated, moderately sorted, monolithic andesite lava breccia (Fig. 4.4 G). Brecciated clasts are angular to round and range in size from 9-150 mm, with an average clast size of 45 mm. Clasts are porphyritic andesite predominantly comprised of coarse feldspars and minor mafic minerals. An example monolithic clast is in Figure 4.5.

4.3.8 Heterolithic andesite lava breccia

Light to medium grey-green, coarsely brecciated, moderately to well sorted, heterolithic andesite lava breccia (Fig. 4.4 H). Brecciated clasts are angular to round and range in size from 15-135 mm, with an average clast size of 65 mm. Clasts are predominantly comprised of porphyritic andesite (with a variable mineral assemblage of medium to coarse feldspars, quartz, and mafic minerals). A brief description of all clast types are given in Table 4.3 with photo examples in Figure 4.6.

Table 4.3. Description of clast types in the heterolithic breccia.

Clast type	Description
Type 1	Light grey andesite with 5-10% feldspars, 5-10% mafic minerals, and 5% quartz (most abundant clast type)
Type 2	Medium green andesite with 1-5% mafic minerals, <1% feldspars, and <1% quartz
Type 3	Dark green andesite with 1% mineral content made up of feldspars, mafic minerals, and disseminated pyrite
Type 4	Light red-grey, fine grained clasts with <1% mafic minerals
Type 5	Fine grained brown clasts
Type 6	Light green, fine grained clasts
Type 7	Medium grey, porphyritic andesite
Type 8	Red crystalline clasts (red vitreous crystals)

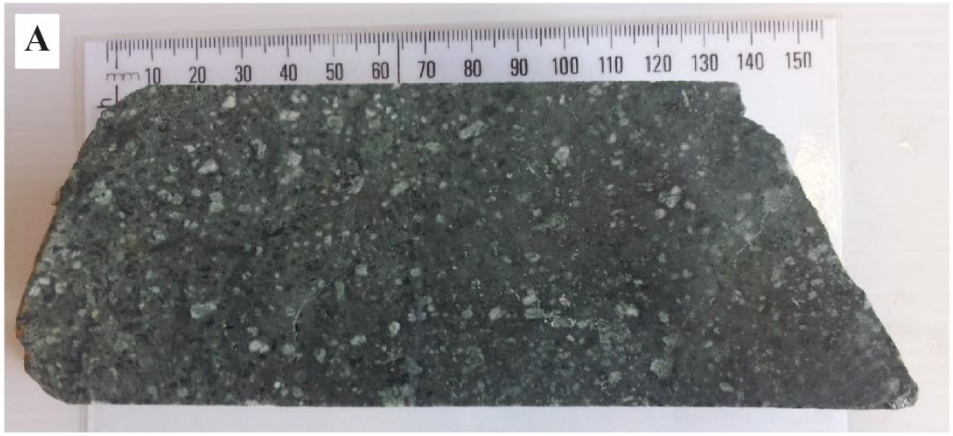
A


B
Ash
Lapilli
Block/bombs

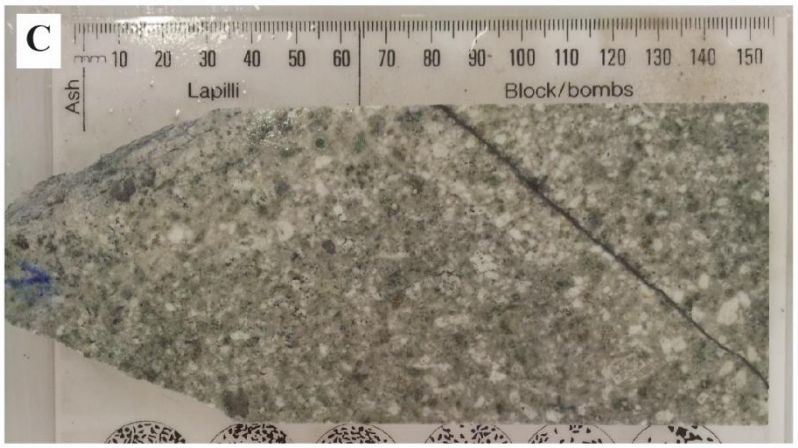
C
Ash
Lapilli
Block/bombs


D
Ash
Lapilli
Block/bombs

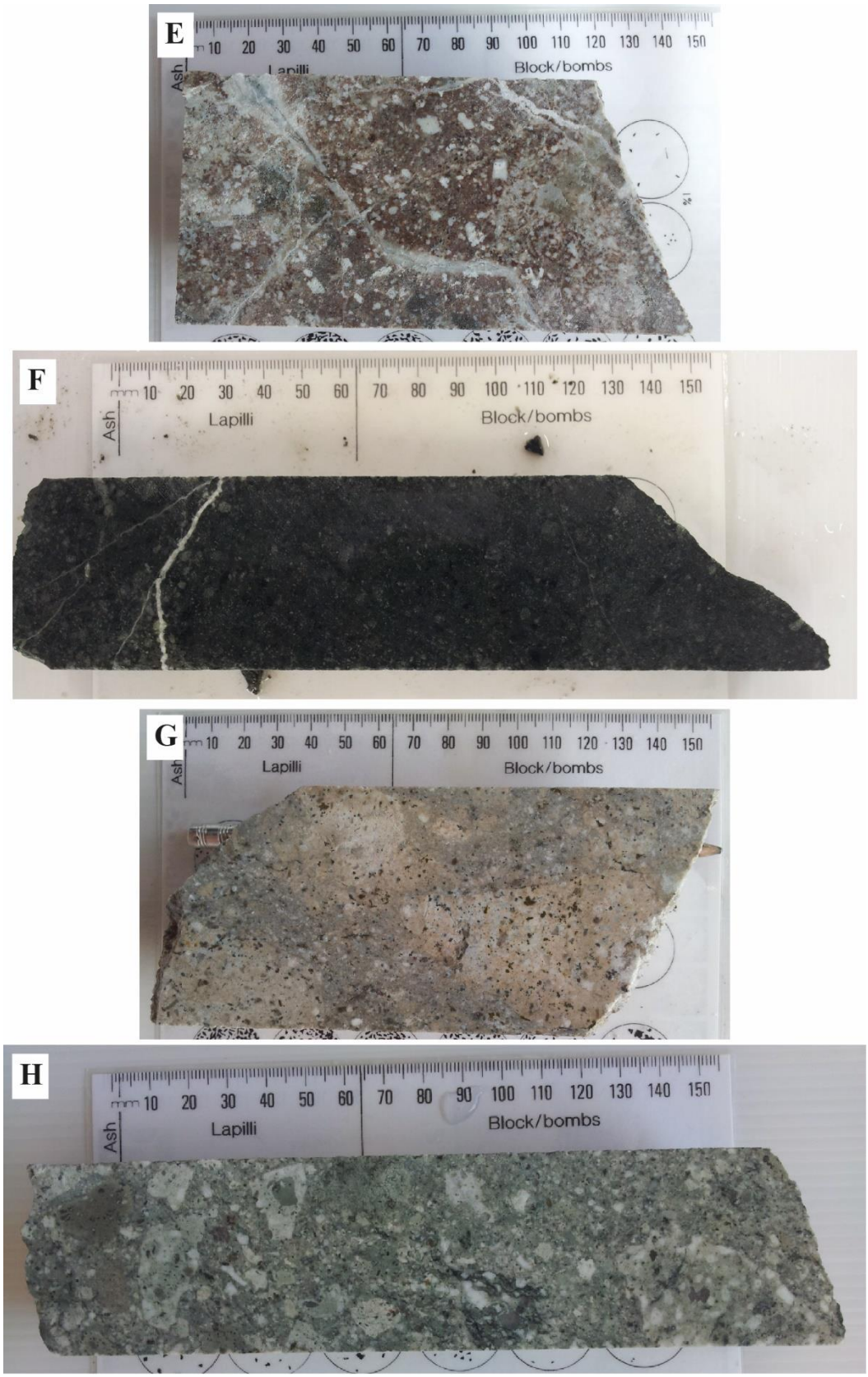

Fig. 4.4. Representative photos of each facies. A) VRC facies, sample U-BB01. B) VCRQB facies, sample U-BB18. C) CR facies, sample U-BB28. D) CRQB facies, sample S-BB32. E) MCR facies, sample, S-BB27. F) MCRQB facies, sample U-BB58. G) Monolithic andesite lava breccia, sample S-BB38. H) Heterolithic andesite lava breccia, sample S-BB12.

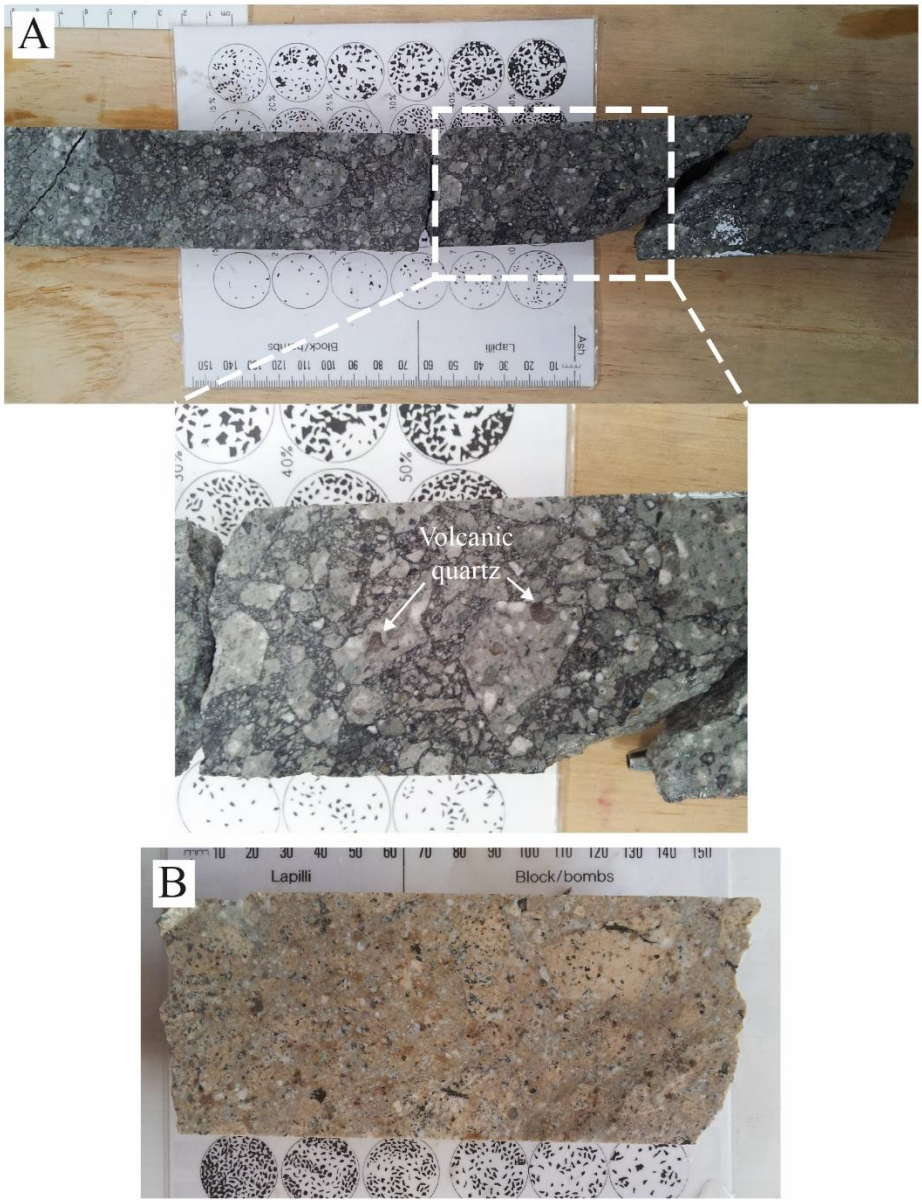

Fig. 4.5. Further examples of the various monolithic andesite lava breccias. Note the prominent quartz phenocrysts labelled in A. Resorbed textures can be seen in larger quartz phenocrysts in hand specimen. B) Light grey-pink, monolithic, andesite breccia.

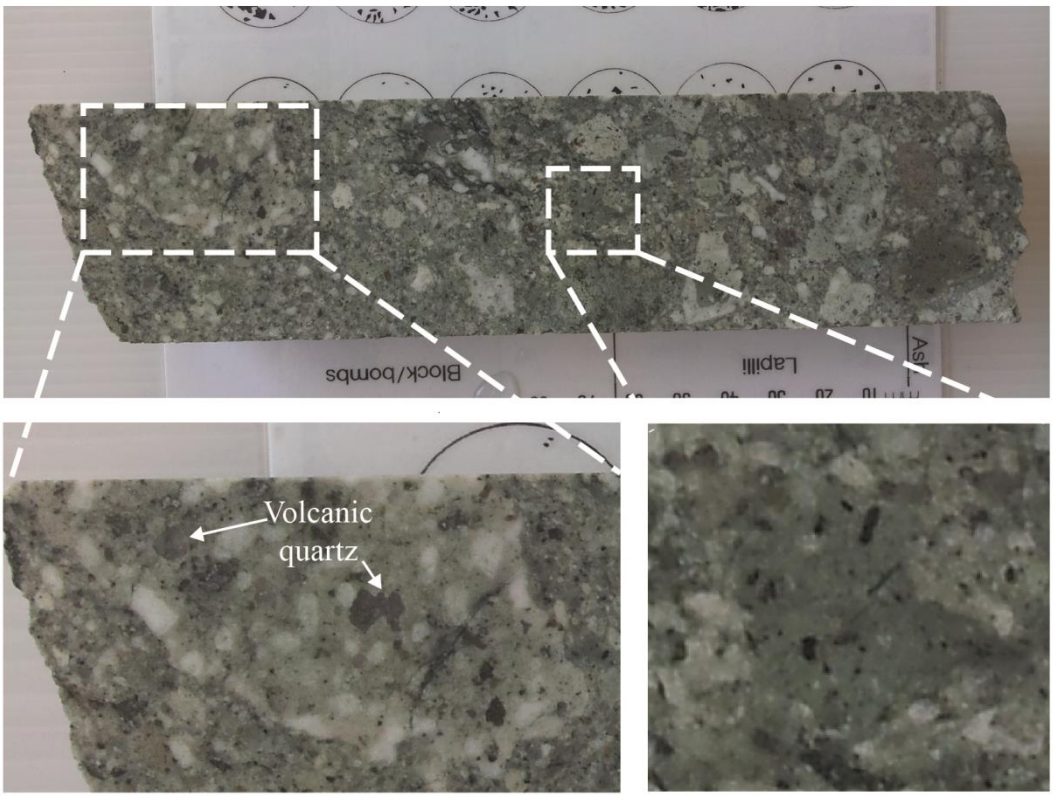

Fig. 4.6. Heterolithic andesite lava breccia with close-up examples of a Type 1 (lower left) and Type 2 (lower right) clast (refer to Table 4.3). Prominent quartz phenocrysts labelled.

4.4 Componentry of lava facies

Although alteration has largely affected the phenocrysts and groundmass within these andesite lavas, the preserved texture is generally porphyritic, dominated by plagioclase + ferromagnesian siliates ± quartz. Variably amounts of glomeroporphyritic aggregates are present and few samples display seriate texture. Groundmass textures are typically intersertal (or hyalopilitic) or cryptocrystalline.

4.4.1 Phenocrysts

Quartz

Quartz phenocrysts are ubiquitous in all quartz-bearing facies and generally resistant to hydrothermal alteration. Under thin section they are typically 0.5 to 3 mm in diameter, but can be <0.5 mm and up to 5 mm (Fig. 4.7 A). Quartz is typically euhedral to subhedral. Minor anhedral forms occur. Quartz commonly display resorbed or embayed textures (Fig. 4.7 B). Quartz does not vary texturally

between facies. Very minor quartz phenocrysts can be seen optically in facies which have no visible quartz in hand specimen (Fig. 4.7 C).

Plagioclase

Plagioclase is the most common phenocryst in all samples, but do not show textural variations between facies. Unlike quartz, plagioclase crystals show variably amounts of alteration, from minor to complete replacement. They are largely altered to calcite ± sericite. Plagioclase occurs mostly as irregular to tabular euhedral phenocrysts up to 3 mm long (Fig. 4.7 D). Some plagioclase crystals are prismatic (Fig. 4.7 E) and anhedral in shape. Most of the plagioclase crystals display polysynthetic twining (Fig. 4.7 D); simple twinning also occurs but is less common. Many of the plagioclase crystals display zoning, notably normal and oscillatory zoning. Phenocrysts of plagioclase can be seen grouped in clusters in some samples (Fig. 4.7 F).

Ferromagnesian silicates

Pseudomorphs of relict ferromagnesian silicates occur in most samples and have been largely altered to chlorite (Fig. 4.7 G and H). They are anhedral to subhedral and up to 2 mm in length. The unaltered andesite contains augite and hypersthene (Brathwaite *et al*. 2005).

4.4.2 Groundmass mineralogy

The groundmass is typically intersertal (or hyalopilitic) or cryptocrystalline (Fig. 4.8 A and B). Relict feldspar laths are common within a homogenous, fine grained altered groundmass. There are no relict phenocrysts in the samples which are glassy with cryptocrystalline texture. The cryptocrystalline samples are also variably altered. More strongly altered samples have a silicified groundmass made up of finely crystalline quartz and calcite pseudomorphs after plagioclase (Fig. 4.8 C). Other strongly altered samples have a fine grained groundmass but the phenocrysts and textures are unresolvable (Fig. 4.8 D). In some less altered samples, the groundmass is weakly to moderately trachytic with relict microlites (Fig. 4.8 E). There is no clear variation in groundmass textures between facies.

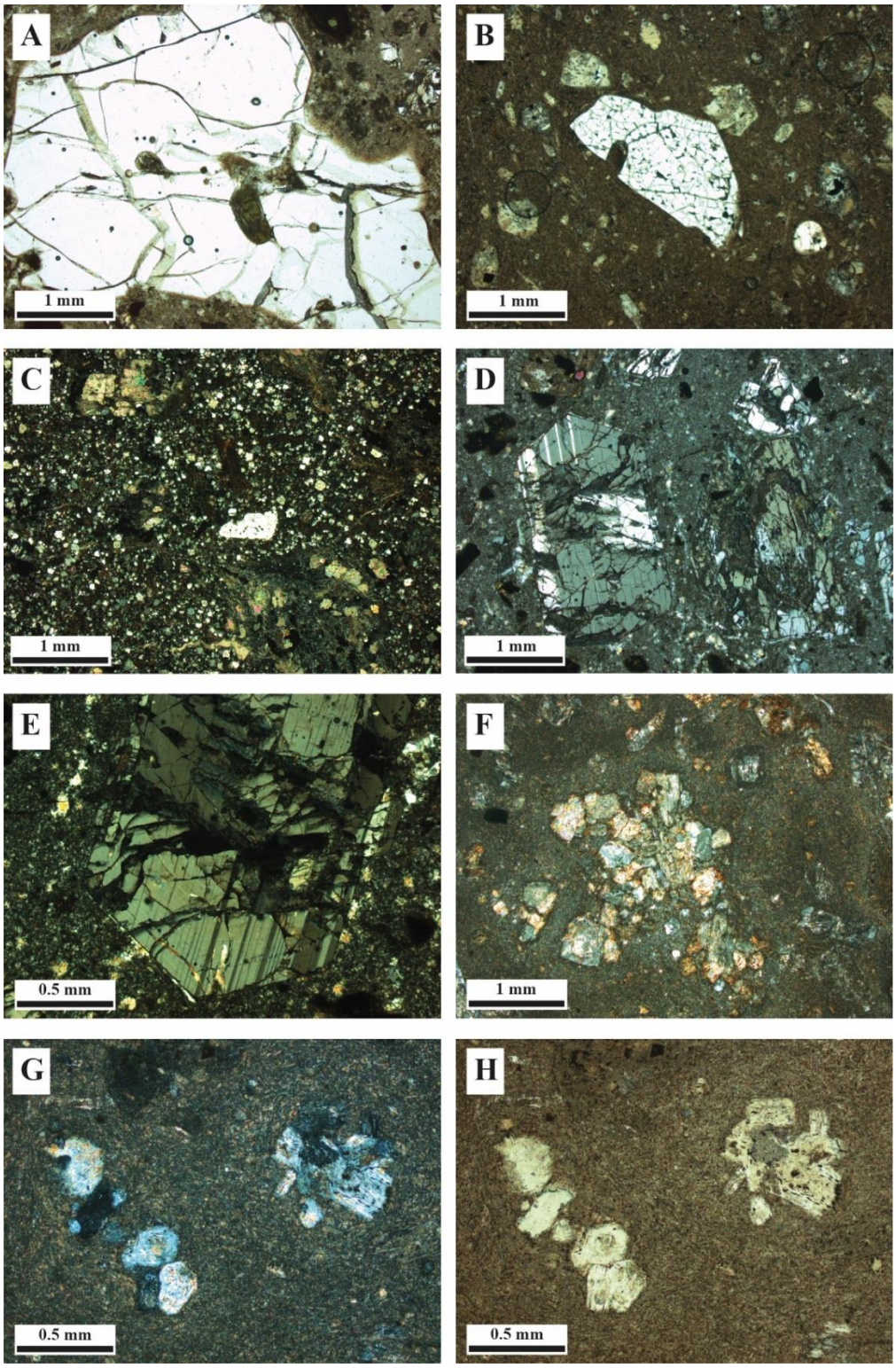

Fig. 4.7. Photomicrographs of the main phenocrysts observed and their textures. A) Large, embayed quartz, sample U-BB58, plane-polarised light. B) Euhedral, partially resorbed quartz, sample S-BB44, plane-polarised light. C) Small, single quartz crystal occurring in a facies logged as having no visible quartz in hand specimen, sample S-BB27, cross-polarised light. D) Plagioclase with polysynthetic twinning, sample U-BB58, cross-polarised light. E) Prismatic plagioclase, sample U-BB58, cross-polarised light. F) A clot or cluster of dominantly plagioclase altered to sericite, sample S-BB07, cross-polarised light. G) Small clot of augite crystals altered to chlorite displaying typical Prussian blue or Berlin blue colour, sample S-BB07, cross-polarised light, and H) plane-polarised light.

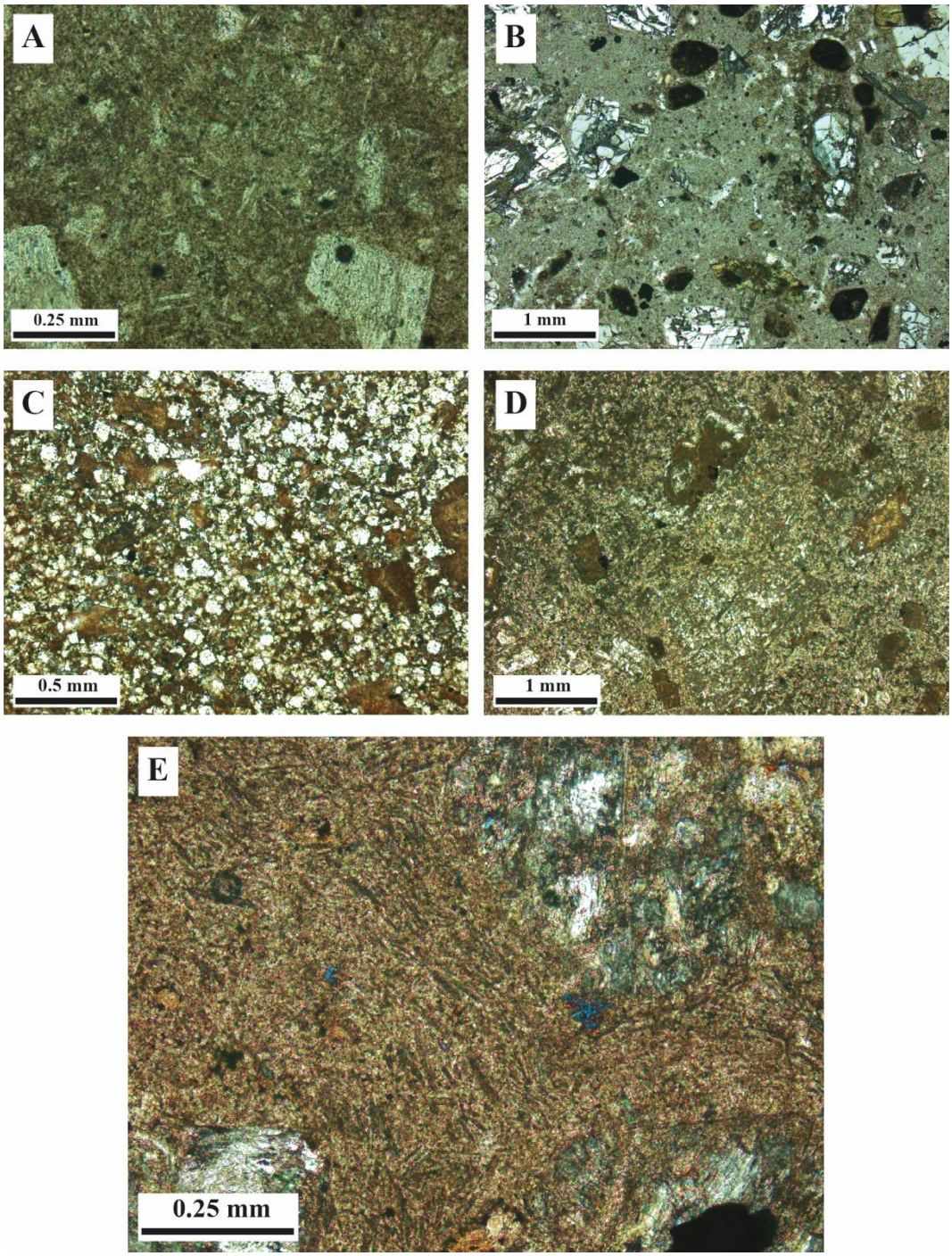

Fig. 4.8. Photomicrographs of the various groundmass textures observed. A) Homogenous, fine grained, groundmass with relict plagioclase laths, sample S-BB44, plane-polarised light. B) Phenocrysts (mostly quartz and plagioclase) set in a cryptocrystalline groundmass, sample U-BB58, cross-polarised light. C) Finely crystalline, quartz and calcite rich, altered groundmass, sample S-BB27, plane-polarised light. D) Unresolvable, fine grained groundmass due to alteration, sample U-BB18, plane-polarised light. E) Weakly trachytic, very fine grained groundmass with small relict microlites, sample S-BB07, cross-polarised light.

4.5 Facies distribution

The down-hole distribution of the above facies is illustrated here in Figure 4.9. It is important to note that this is a generalised figure because some facies change over small thicknesses (e.g. <1 m). Where this occurs, the facies which is dominant over a 10 m interval is represented. Detailed descriptions can be found in the primary logs (Appendix A). Also, the colours used to represent each facies is not a representation of the actual rock colour, but is used to help differentiate between each facies. Missing core or other logged features such as alteration/mineralisation is not illustrated unless it represents a significant section of the core. It is instead illustrated by the most dominant facies to occur on either side of that particular section. Refer to Appendix A for full descriptions.

4.5.1 SPO597

The dominant facies of SPO597 are MCRQB andesite flows, occurring over a collective 310.85 m. This is followed by the CRQB flows for 191.25 m and MCR flows for 139 m (Fig. 4.9).

The first 105 m of SPO597 is represented by the CRQB andesite flow. This changes to a ~27 m quartz vein rich/strongly altered section. Between 132.1 to 222.9 m, a range of facies occur which are between 7 to 25 m thick, before another highly mineralised section to 233.6 m. This is followed by ~25 m of MCR andesite and ~10 m of CR andesite. At 266.8 m is the first major occurrence of the monolithic breccia at 4.2 m thick. This grades into 15 m of MRCQB andesite. A 32.6 m thick section of monolithic breccia occurs from 286 to 318.6 m. The next 118.9 m is dominated by MCR andesite with thin occurrences of MCRQB andesite and monolithic breccia. The first major occurrence of heterolithic breccia occurs from 437.5 to 459.6 m. The last 394 m is dominated by thick sequences of MCRQB and CRQB andesite and occurrences of monolithic and heterolithic breccias.

4.5.2 UW462

The most dominant facies of UW462 includes the MCRQB andesite flows, occurring over a collective 283.95 m. This is followed by the VCRQB andesite for 218.9 m and VCR andesite for 110.8 m (Fig. 4.9).

The first 316.8 m of UW462 is represented by thick, alternating sequences of VCR and VCRQB andesite. From 316.8 m to 433 m the CRQB andesite dominates which alternates between thinner CR, VCRQB and MCR andesites. From 433 to 479 m, thin sequences of CR, strongly altered rock and MCRQB andesites occur. A thick, 45.5 m slab of MCRQB andesite occurs to 524.5 m, followed by ~22 m of CRQB andesite and ~30.5 m of monolithic breccia to 579.15 m. The MCRQB andesite dominates the last 378.75 m, occurring in thick sequences from 579.15 to 657.5 m, 746 to 875.5 m, 895.1 m to 948.6 m, with some thinner occurrences in between. In the last 378.75 m there are also thin (<6 m), monolithic breccias, MCR andesites <20 m thick, and crystal poor lavas <8 m thick.

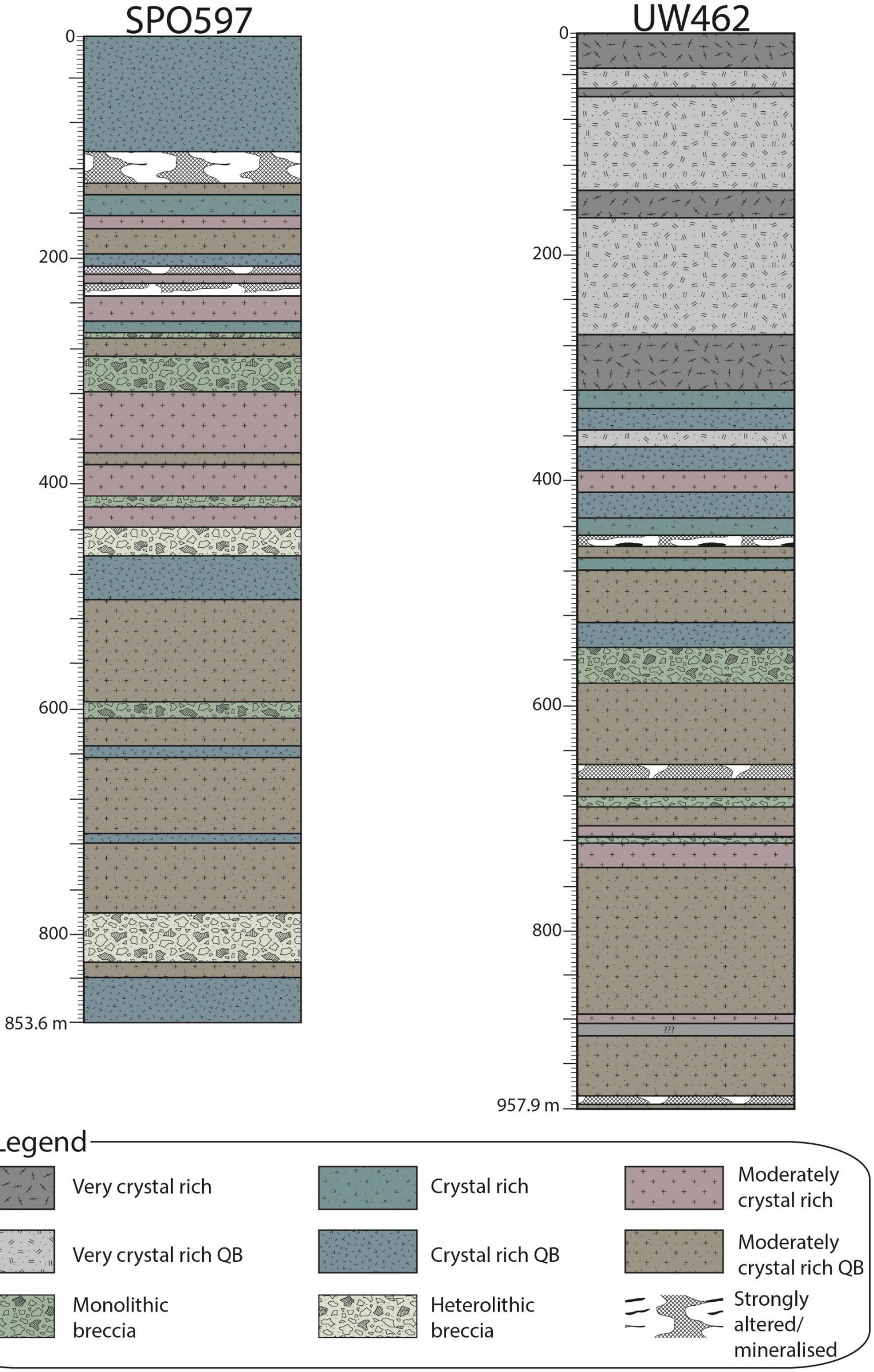

Fig. 4.9. Generalised distribution of the different facies types down hole.

4.6 Discussion

The observations outlined previously in this chapter will be discussed here. The lava textures will be compared to other andesites both regionally and globally. The petrography will be compared to known literature as to its magmatic origin. The flows will be discussed as to their emplacement processes.

4.6.1 Origin of crystal-rich lava facies

The crystal abundances observed for the Waipupu Formation andesite, in this study, are similar to those of andesites studied elsewhere, both regionally and globally. The Waihianoa Formation is a 60-120 ka cone-building andesite within the volcanic succession of Mount Ruapehu, a well-characterised, active andesitic volcano located at the southern end of the TVZ, New Zealand (Waight et al. 1999). These lavas are generally porphyritic plagioclase-two pyroxene andesites with 15-40% phenocrysts, which, are comparable to the MCR (10-25% crystal content) and CR (25-50% crystal content) facies described in this study. The MCR facies is the most frequently occurring facies down both the drill holes, while the CR facies is the second most occurring facies down drill hole SPO597 in particular. The least altered zones of the Waipupu Formation lavas and the Waihianoa Formation andesites, which are generally unaltered, both have light grey groundmasses (Fig. 4.6 B; Waight et al. 1999).

Various andesitic flow units around the Turoa ski-field area at Mount Ruapehu, also identified by Waight et al. (1999), also share similar textural characteristics to the MCR and CR facies. The Turoa lavas are considered part of the Mangaturuturu Formation and are texturally variable with between 7 to 51% phenocryst abundance. Waight et al. (1999) confirmed by geochemistry, that the more phenocryst-rich lavas represent crystal accumulation, either within individual flows (post-eruptive), or within a magma chamber (pre-eruptive). This is a similar feature to the clot of phenocrysts described previously in sample S-BB07 (Fig. 4.5 F). Many of these Turoa lavas show flow alignment of microlites (trachytic texture) also observed in the Waipupu Formation lavas.

A more recent study by Streck et al. (2005) describes phenocryst abundances of younger basaltic andesites at Arenal volcano, Costa Rica, noting two distinct textures. The Arenal volcano is one of the few arc volcanoes that have undergone

multi-decade, continuous eruptive activity of basaltic andesite. The lavas which have continuously erupted since March 1969 are compositionally monotonous and are characterised by ~35% phenocrysts, composed of glomerocrystic aggregates, and microphenocrysts of plagioclase, orthopyroxene and rarer clinopyroxene, some oxides, and the occasional olivine. The lavas which followed the initial plinian eruption phase in July of 1968 consisted of 20% phenocrysts and microphenocrysts, with the other 80% a mixed groundmass of rapidly quenched microlites and residual glass. Both the lavas of the initial eruption, and ongoing lavas after March 1969 have phenocryst abundance values comparable to those described here in this study. Although Streck et al. (2005) also undertook detailed textural and compositional analyses of not only phenocrysts but mineral inclusions and microlites, they identified at least four crystallisation environments which reflect mafic magmas developing to basaltic andesite through mixing, fractionation and assimilation during their ascent from the crustal level to subvolcanic depths. The compositional monotony is inferred to represent increments of new basaltic andesite supplying the subvolcanic reservoir concurrently to the current eruption. These new increments are blended into the residing, subvolcanic magma.

There are also Late Archean andesites-dacites that have similar crystal abundances to those described here in this study. The volcanic rocks of the Kurnalpi Terrane, Eastern Goldfield Superterrane, Western Australia, are calk-alkaline, dominantly andesitic complexes with an age of 2720-2700 Ma (Barley et al. 2008). One of the four main facies recognised is a variably porphyritic and amygdaloidal, coherent andesite-dacite (facies 3). These lavas range from weakly porphyritic andesite (5-10% phenocrysts) to relatively crystal-rich andesite to dacite (25-30% phenocrysts), the latter being similar to the MCR and CR facies.

4.6.2 Magmatic origin

Thin section petrography can provide information on magmatic processes before and during eruption (Gill 2010). There is petrographic evidence that the phenocrysts described above have undergone partial resorption. Resorption can occur for many reasons as outlined in Gill (2010), including a drop in pressure owing to adiabatic ascent, which can bring the temperature of a water-undersaturated magma closer to its liquidus temperature. Resorption may also occur if phenocrysts in equilibrium with host magma mix with a more primitive (higher-temperature) magma,

sometimes leading to reverse zoning. The internal and external corrosion of phenocrysts is common as a result of resorption. It can lead to deep embayments and channels as observed in Figure 4.5 B. Pockets of melt may also occur in voids if there is subsequent rapid overgrowth.

Another distinction which can be made based on petrography is the presence of quartz phenocrysts. In the next chapter, an Nb/Y versus Zr/Ti plot indicates that the lithology of the Waipupu Formation is consistently andesitic, but Gill (2010) notes that the petrographic distinction between dacite and andesite is the presence of abundant quartz in dacite. The International Union of Geological Sciences also recommends classifying quartz andesites as dacite (Le Maitre *et al*. 2002). Considering the quartz-bearing facies described above were the most common containing ubiquitous crystals of quartz, are they then technically dacite? The lack of hornblende and/or biotite crystals, which is commonly the dominant mafic minerals of dacites (Gill 2010), and the Nb/Y versus Zr/Ti plot suggests they are more andesitic than dacitic.

Some samples described above also display seriate texture. Seriate texture is an inequigranular texture displaying a continuum of crystal sizes from the largest phenocryst to the finest groundmass crystal (Gill 2010). It suggests polybaric crystallisation during magma accent, described in Figure 4.10 C.

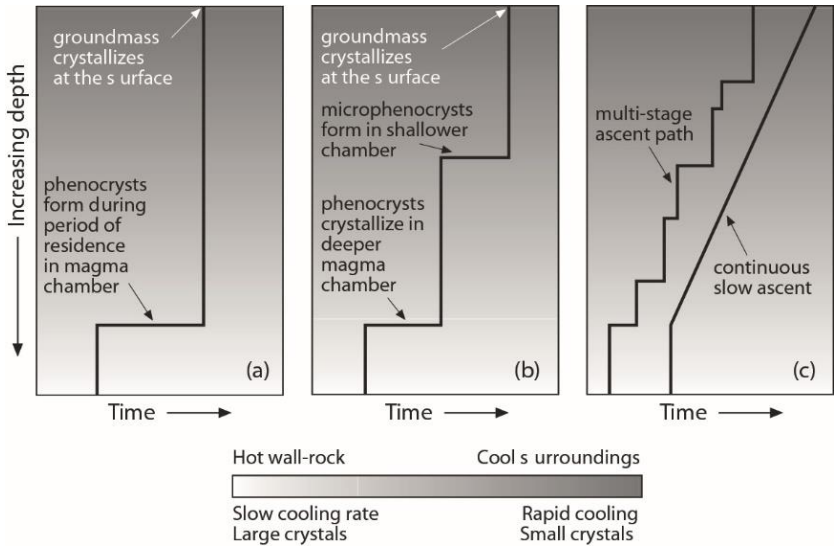

Fig. 4.10. Hypothetical magma ascent versus time paths to explain (a) porphyritic basalt and (b) the presence of two distinct generations of phenocrysts; (c) two alternative ascent paths to explain seriate texture. Real ascent paths are probably more complex than those shown (after Gill 2010).

Volcanic rocks are not only made up solely of individual crystals but contain mixtures of both individual crystals and clusters of touching crystals referred to as clumps, clots or glomerocrysts (Jerram *et* al. 2003). One of the most common inclusions in andesite are coarse-grained glomeroporphyritic clots, as noted previously in Figure 4.5 F, G and H. Glomeroporphyritic clots contain a cluster of phenocrysts 1 to 10 mm in size (Gill 1981). Jerram *et al.* (2003) attribute the likely origin of crystal clusters to involve either (or a combination of) heterogeneous nucleation, remobilisation of cumulate mushes or crystals sticking together during settling and/or flow. Stewart (1975) interpreted glomeroporphyritic clots as decompression break-down products of amphibole. This is an unlikely suggestion which does not apply to most glomeroporphyritic clots (Gill 1981).

These crystal clusters are important because they are the basic unit 'building blocks' from which many igneous textures develop (Jerram *et al.* 2003). Jerram *et al*. (2003) further note that the porosity of a melt is affected by the crystal framework. If a framework is produced from a mixed population of irregular-shaped clusters or clumps of crystals, the resulting framework will contain a high melt porosity and be loosely packed (Fig. 4.11 A). Conversely, frameworks that are constructed from individual crystals will have a more tightly packed arrangement of crystals with lower melt porosity (Fig. 4.11 B). As the modal abundance of the framework-building phase is reduced a more intricate clustered or chained network is required to remain touching in three dimensions (Fig. 4.11 C). Having glomeroporphyritic clots associated with higher melt porosity may provide insight as to why 97% of total past gold production in the Hauraki Goldfield is from deposits hosted in andesite and dacite Coromandel Group rocks.

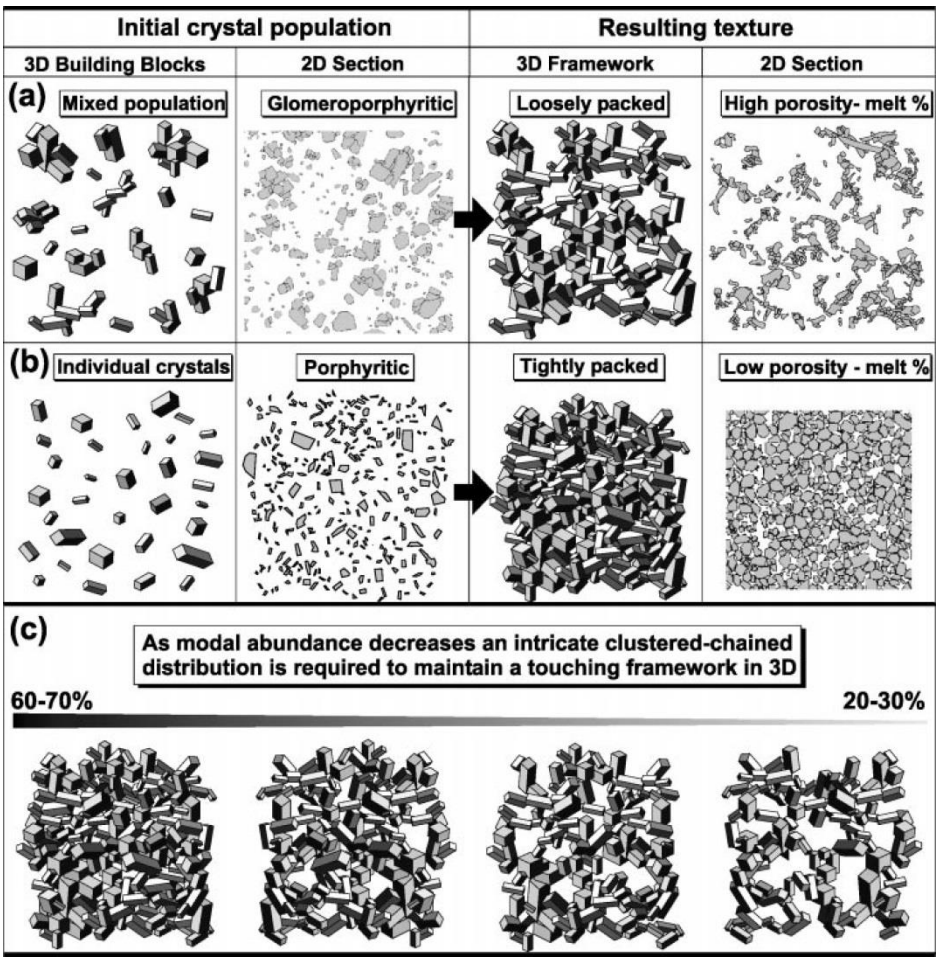

Fig. 4.11. The development of crystal frameworks using phenocryst populations as initial `building blocks' and the resulting texture. A) The initial `building blocks' consist of a mixed population of clustered (clumped) and individual crystals. B) The initial `building blocks' consist of a population of individual crystals. C) Touching crystals show markedly different spatial packing arrangements in order to maintain their frameworks at different modal abundance (after Jerram *et al.* 2003).

4.6.3Flow emplacement processes

The monolithic andesite lava breccia facies described in this chapter (section 4.3.7) resembles that of an autobreccia. Autobrecciation is a primary volcanic process (Cas & Wright 1987) involving the non-explosive fragmentation of flowing lava (Mcphie *et al*. 1993). When lava flows are cooler, more viscous, or subject to locally higher strain rates than the rest, the flow, especially the outer surfaces, respond to stress in a brittle manner, generating a layer of rigid blocks, plates and spines (Mcphie *et al*. 1993). The blocks typically cascade down the flow front (sometimes tens of metres high) and become re-incorporated in the base of the flow as the lava advances over them (Gill 2010). A coherent interior enclosed by a carapace and floor of autobreccia is typically observed. Parts of the brecciated surface are

sometimes incorporated into the flow interior where they are preserved as irregular pockets of autobreccia within otherwise coherent lava. Subsequent hydrothermal alteration can significantly modify textures characteristic of autobreccias by affecting clast margins and fractures within clasts, transforming the original clast-supported or in situ jigsaw-fit breccia into an apparent matrix-supported breccia (Mcphie *et al*. 1993).

4.7 Summary

Logging of primary volcanic textures made it possible to distinguish between separate flow events and assign new facies types based on primary mineralogy. Petrography was useful to further analyse and describe the petrographic characteristics of these lavas. The moderately crystal rich quartz bearing andesite flows were the most common facies consisting of 10-25% mineral content made up of 1-20% feldspars, 1-20% mafic minerals and, ≤1-10% quartz; these values are very similar to other andesite examples. There was also significant petrographic evidence (i.e. embayment textures in quartz crystals) that would suggest that these lavas underwent different levels of magma mixing within the magma chamber before erupting. An important finding suggests that some of these lavas have high melt porosity which may provide insight to why andesite is a preferred host rock in the Hauraki Goldfield.

Although this chapter provides a starting foundation, it was not possible to interpret or construct the volcanic structure of the Waihi area. It would be beneficial to incorporate the facies approach used here with vertically orientated holes for a better understanding of the volcanic history.

Chapter 5 Alteration mineralogy and geochemistry

5.1 Introduction

The formation of hydrothermal mineral deposits is accompanied by various chemical reactions which occur between mineralising fluids and host rock. These reactions commonly produce distinct mineralogical and geochemical halos (Stanley & Madeisky 1994). These alteration halos are generally very much larger than the metal deposits themselves (i.e. the ore bodies) and can provide information about the geohydrologic structure (i.e. up flow, outflow, influx zones) of active and extinct geothermal systems as they are commonly zoned about the hydrothermal fluid conduits (Stanley & Madeisky 1994; Simpson *et al*. 2013).

In this chapter I report and compare alteration mineralogy results produced by a variety of techniques (TerraSpec 4 Hi-Res shortwave infrared red spectroscopy, and x-ray diffraction on clay separates) with major and minor geochemistry. The aim of this chapter is to locate the occurrence and distribution of illite, interstratified illite-smectite and smectite to infer formation temperatures, which is particularly useful in exploration as they may indicate directions toward fluid sources and/or potential sites of ore deposition (Chang & Yang 2012; Simpson *et al*. 2013). I also describe the distribution of certain pathfinder elements and discuss their usefulness for identifying broader alteration halos at Waihi.

5.2 About the TerraSpec:

Compact and field portable, the TerraSpec is a device which uses non-destructive near infrar-red reflectance spectroscopy for mineral identification (Simpson *et al*. 2006). The benefits to using the TerraSpec are no sample preparation is required and data is produced by a single scan in 10 seconds. When a sample is scanned by the TerraSpec, visible (350-700 nm) and infrared (700-2500 nm) light is reflected off the surface of the sample with certain wavelengths absorbed by minerals crystal lattice as a result of sub-molecular vibrations associated with covalent and molecular bonds (AlOH, FeOH, MgOH, OH, H_2O, CO_3^{2-}, and NH_4). The absorptions are presented in the reflectance spectrum as minima below the baseline

of the spectra (Fig. 5.1). Minerals can therefore be identified by simple pattern recognition as the absorption features for most minerals form a distinctive pattern characteristic of a particular mineral group known as the mineral's "spectral signature". The TerraSpec detects a range of mineral species including clays, micas, carbonates, and hydroxides as well as certain sulfates and silicates (Table 5.1). Mineral species such as quartz and feldspar and minerals which lack the above covalent or molecular bonds are not detectable via the TerraSpec. Also, depending on the sharpness or wavelength position of absorption features, the crystallinity (i.e. illite and kaolinite) and qualitative chemistry (i.e. chlorite and carbonates) of certain minerals can be determined, respectively. An important aspect to note is that the quality of the spectral profile is influenced by rock colour, so dark rocks will absorb both infrared and visible light resulting in flat noisy spectra due to poor reflection (a common problem most associated with weakly altered rocks as many hydrothermally altered rocks are pale in colour).

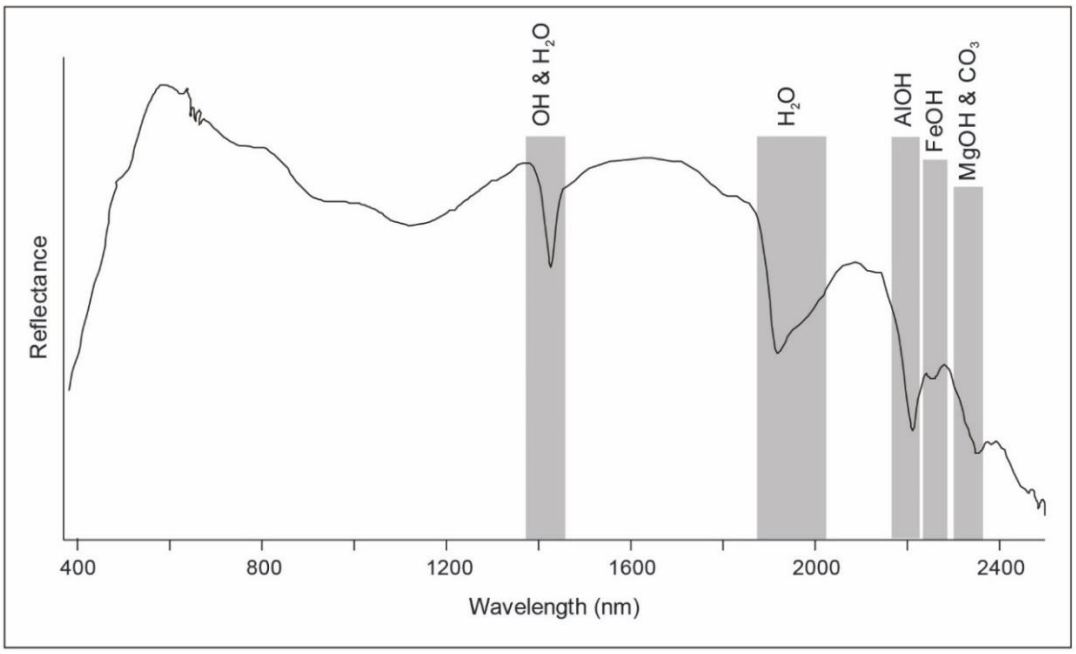

Fig. 5.1. Example spectra profile produced from a TerraSpec showing the wavelength positions of the main absorption features: OH, H_2O, AlOH, FeOH, CO_3^{2-}, and MgOH (after Simpson et al. 2006).

Table 5.1. Mineral groups and mineral species that can be detected using the TerraSpec (after Simpson et al. 2006).

Mineral Group	Minerals
Amphiboles	Actinolite, Termolite, Hornblende, Edenite
Carbonates	Calcite, Dolomite, Rhodochrosite, Magesite, Siderite, Azurite, Malachite
Clays	Chlorite, Illite, Interstratified illite-smectite, Smectites (montmorillonite, beidellite, hectorite, saponite, nontronite), Kaolinite, Dickite, Halloysite, Palygorskite, Sepiolite
Epidote	Clinozoisite, Zoisite
Hydroxides	Brucite, Diaspore, Gibbsite
Micas	Biotite, Muscovite, Lepidolite, Paragonite, Phogopite, Roscolite
Phosphates	Apatite, Turquoise
Phyllosilicates (selected)	Pyrophyllite, Talc, Serpentines (antigorite, chrysotile)
Silicate (selected)	Beryl, Buddingtonite, Topaz, Tourmaline, Zircon
Sulfates (selected)	Alunite, Jarosite, Gypsum

5.3 Methods:

5.3.1 TerraSpec analysis

A mixture of whole rock, rock chips and powders were selected for short wave infrared spectroscopy using a TerraSpec 4 Hi-Res. Three spectra were acquired for each sample. For all scans, a white reference of 400, a dark current of 25, and scan duration of 10 seconds were used. Because the TerraSpec only measures a small area each scan (2.5 cm diameter circle), three different spots were measured for each sample to account for any heterogeneity. The instrument was calibrated every hour using a white disc until a flat spectrum with 100% reflectance was obtained. A total of 73 samples (52 from SPO597 and 21 from UW462) were analysed. The spectral patterns were viewed and interpreted using The Spectral Geologist solftware (TSG) equipped with a TSG spectral database of reference minerals and visually analysed with the assistance of Mark Simpson (Geothermal Geologist, GNS Science) using reference spectra (AusSpec 2010).

5.3.2 Clay XRD

Laboratory procedure:

Based on the results from the TerraSpec, samples which indicated an interstratification of illite-smectite were chosen for further analysis by clay separate XRD to help confine/define the boundary between illite to smectite. Other samples were chosen at random to get an even distribution downhole, focus being more towards the end of the hole. All samples could not be analysis by clay separate XRD because of time constraints involved with sample preparation.

The procedure involved preparing visually homogenous areas of the sample and breaking off a subsample using a hydraulic splitter. Veins and veinlets were avoided where possible. The subsample was then crushed to a fine powder using an agate mortar and pestle. Two millilitres of the crushed sample were then placed into a 10 mL test tube along with 8 mL of distilled water with sodium hexametaphosphate (deflocculent). The rock solution was then agitated by hand and placed in an ultrasonic bath for five minutes.

Following the ultrasound, the samples were agitated and then spun in a centrifuge for two minutes at 1500 rpm to separate the <2 µm fraction. The clay-water mixture was pipetted onto glass slides and left to air dry overnight. The air dried samples were then analysed by X-ray diffraction (XRD) using a Panalytical Emperan instrument equipped with a 256 channel "2D" detector, in the Faculty of Science and Engineering, University of Waikato. The samples were x-rayed from 2 to 28° using Cu radiation.

After the air dried samples were analysed, they were treated with ethylene glycol to expand the swelling clays and then re-analysed using the same machine specifications. To glycolate, samples were placed on a platform in a sealed desiccator containing ethylene glycol at the base, so the samples can glycolate by absorption of the ethylene glycol vapour. Samples were left to glycolate for 36 hours at room temperature.

Glycolation is a process used to expand swelling clays. For example, smectite minerals are able to expand and contract their structures while maintaining two-dimensional crystallographic integrity. Thus, when a smectite expands, the

interlayer cation may be replaced by some other cation. When a sample containing smectite is treated with a polar organic compound (i.e. ethylene glycol), the compound is able to enter the interlayer space causing the mineral to swell. Compared to other clay minerals, smectite have a high cation-exchange capacity which produces a distinct change in diffraction patterns when glycolated (Moore & Reynolds 1997). Whether or not a mineral expands and the amount of expansion can provide essential supplementary information aiding clay-mineral identification (Poppe *et al*. 2001).

Clay mineral identification:

Clay XRD raw data were loaded onto HighScore Plus and used in conjunction with mineral data from PDF-4/Minerals 2014. HighScore Plus is an analysis software package which combines phase identification, Rietveld refinements, and crystallographic analyses for powder diffraction measurements. PDF-4/Minerals 2014 is a database containing 97% (41,423) of all known mineral types, as defined by the International Mineralogical Association, as well as many unclassified minerals.

All samples were also identified manually using their peak positons measured in degrees two-theta (°Th). Illite was identified by its strong basal 001 reflection at about 8.8 °2Th and smaller 002 and 003 reflections at 17.7 and 26.3 °2Th, respectively (Moore & Reynolds 1997). Smectite was easily identified by comparing diffraction patterns of air-dried samples to ethylene glycol treated samples. A glycol-treated sample containing smectite will have a very strong 001 reflection at about 5.2 °2Th (Moore & Reynolds 1997). Before treatment, the 001 peak shifts to between 5.8 and 7.3 °2Th (Hume & Nelson 1982). The determination of illite percentages in interstratified samples containing a smectitic component was calculated based on the difference in °2Th of the 002 and 003 peaks (Moore & Reynolds 1997). Chlorite (clinochlore) was usually identified by the software but can be identified manually. It has a characteristic 002 peak at ~12.6 °2Th and a 004 peak at ~25.1 °2Th (Hume & Nelson 1982; Moore & Reynolds 1997). These should not be confused with kaolinite which has a 001 peak also at ~12.6 °2Th and a 002 peak at 24.9 °2Th. Positive identification of chlorite is provided by peaks at 6.2 and 18.8 °2Th (Moore & Reynolds 1997).

5.3.3 XRF

A total of 111 samples were initially prepared for XRF analysis using a tungsten-carbide ring-mill. Because this study is concerned with the mass changes associated with the andesite host rock, samples were chosen carefully so minimal veins and veinlets were incorporated. Pressed pellets for all 111 samples were made for trace element analysis by mixing approximately 5 g of sample with 8 to 10 drops of PVA binder. The mixture was then pressed into an aluminium cap using a hydraulic press. The pressed pellet was then oven dried overnight at 70 °C to evaporate off the binder.

In order to assess the quality and validity of using the major element geochemical data produced by the pressed powder pellets, 13 samples were selected which covered a range of K/Al vs Na/Al ratios. Glass fusion beads were made for each of those selected samples and new major element data was generated. Only 13 samples were used because of the intensive sample preparation required for making Glass fusion beads. By plotting the major element data produced by the fusion beads and pressed pellets against each other, the slope of a linear trendline was used as a correction factor to correct the trace element major elements.

Glass fusion beads were made by fusing 0.28-0.30 g of powdered sample with 2.50-2.55 g LM100 flux (pure 100% Li-metaborate) in Pt/Au crucibles in a Bradway Fusion Furnace at progressive heating steps (650, 720, 780, 825 °C) for 15 minutes at each stage and at 1000 °C for 15 minutes with the shaker on. A few grains of NH_4I were added to each sample before turning on the shaker. Each crucible was then poured onto a graphite disc individually and pressed to make a glass disc. Samples were left to anneal on a hot plate at 230 °C for at least 1-2 hours before being transferred to a cooler hot plate were it was left for a further 2 hours. The hot plate was turned off and the samples left to slowly cool overnight. Loss on ignition was determined by placing 1-2 g of powdered sample in a Bradway Fusion Furnace at 1100 °C for about an hour and calculating weight lost as a percent.

Both the fusion beads and pressed pellets were analysed by X-ray fluorescence (XRF) using a SPECTRO X-LAB 2000 equipped with a polarising EDS spectrometer in the Faculty of Science and Engineering, University of Waikato.

5.4 Results

5.4.1 TerraSpec results

The TerraSpec results for 73 samples (52 from SPO597 and 21 from UW462) are summarised in Table 5.2. Illite and chlorite are the dominant minerals identified in most samples. Calcite is also largely present. Interstratified illite-smectite is first identified at 601.6 m down hole SPO597, occurring more frequently thereafter, and identified at 100.7 m down hole UW462.

Table 5.2. TerraSpec results. X = mineral identified. ? Low = low signature identification.

Hole ID	Sample ID	Down hole depth (m)	Minerals				
			Illite	Illite-smectite	Smectite	Chlorite	Calcite
SPO597	S-BB2	10.27	? Low			X	X
	S-BB3	25.5	? Low			X	X
	S-BB4	38.85	X				
	S-BB5	53	X			X	?
	S-BB6	70.4	X			X	
	S-BB7	91.6	X			X	X
	S-BB10	128.7	X				
	S-BB11	141	X			X	?
	S-BB12	158.4	X			X	X
	S-BB13	171.3	X			X	X
	S-BB14	184	X			X	X
	S-BB15	204.35	X			?	
	S-BB16	216.1				X	

S-BB17	223.4				
S-BB18	249.4	? Low		X	
S-BB19	275	X		X	
S-BB20	297.5	X		?	
S-BB21	316.8	X		?	
S-BB22	323.8	? Low		X	?
S-BB23	348.85	X		X	X
S-BB24	360.2	X			
S-BB26	379.8	X		X	
S-BB27	399.55	X		?	
S-BB28	408.5	X			
S-BB29	434.6	X		X	X
S-BB30	452.85	X		?	
S-BB31	472.5	X			
S-BB32	494.7	X			
S-BB33	505.75	X		?	
S-BB34	514.3	X		?	
S-BB35	537.85	X		X	?
S-BB36	557.35	? Low		?	
S-BB37	566.4	X		?	
S-BB38	601.6		?		
S-BB39	612.74	X		X	

	S-BB40	630.88	?		X	X
	S-BB41	645.85	X		X	X
	S-BB42	661.8	? Low		X	?
	S-BB43	679.7		?	X	
	S-BB44	702.18	X		X	X
	S-BB45	717.25		?	X	?
	S-BB46	718.4		?	X	
	S-BB47	737		?	X	
	S-BB48	761		?	X	
	S-BB49	779.2		?		
	S-BB50	785.2	X		X	
	S-BB51	796.75		?	X	?
	S-BB52	808.1	X		?	
	S-BB53	822.2	X		?	
	S-BB54	833.25		?	X	
	S-BB55	837.4	X		?	
	S-BB56	852	X		?	
UW462	U-BB1	0.9	? Low		X	X
	U-BB2	24	? Low		X	X
	U-BB3	37	X		X	
	U-BB4	50.8	X		X	?

U-BB5	66.6	? Low			
U-BB6	82.6	? Low		X	X
U-BB7	100.7		?		
U-BB8	123.8	? Low		X	X
U-BB9	134.5			X	X
U-BB10	145.6	X			
U-BB11	152.6	X		X	X
U-BB12	173	X			
U-BB13	188.5	? Low		X	?
U-BB14	201	? Low		X	
U-BB15	219	? Low		X	?
U-BB16	233.8	X			
U-BB17	253.6	X		X	?
U-BB18	270.5	X		X	
U-BB19	283.2	X		?	
U-BB20	300.7	?	?		
U-BB21	318.4	X		X	X

5.4.2 Clay separate XRD

A summary of results from the XRD clay mineral separation analysis is given in Table 5.3 for drill hole SPO597 and Table 5.4 for drill hole UW462. Drill hole SPO597 shows fairly consistent mineralogy, grading from illite to illite-smectite + chlorite. Illite-smectite has very high illite content of ≥90 %. An example spectrum of interstratified illite-smectite with ≥90 % illite is illustrated in Figure 5.3A, showing the characteristic 001, 002, and 003 reflections at ~8.8, ~17.7 and ~26.3 °2Th, respectively, in the unglycolated sample. Drill hole UW462 shows more varied mineralogy with a general zonation of clays from illite, through illite-smectite to smectite with some overlap. Illite-smectite in drill hole UW462 ranges in illite content from 50 to ≥90%. Figures 5.3B and 5.3C are example spectra of smectite + chlorite and interstratified illite-smectite with 50 % illite + chlorite, respectively. Note the characteristic shift in the 001 peak position in Figure 5.3B from 6.1 to 5.4 °2Th clearly showing the swelling of smectite following glycolation. Occurrences of kaolinite and gypsum are also identified in certain samples (Table 5.4). Each individual clay XRD spectra can be found in Appendix B.

Table 5.3. Clay mineral results from clay separate XRD analysis for drill hole SPO597.

Sample	Down hole depth	Minerals
S-BB07	91.6	Illite, chlorite, possible
S-BB22	323.8	IS >90% illite, chlorite
S-BB36	557.35	IS >90% illite, chlorite
S-BB43	679.7	IS 90% illite, chlorite
S-BB46	718.4	IS 90% illite, chlorite
S-BB47	737	IS 90% illite, chlorite
S-BB49	779.2	Illite, chlorite
S-BB51	796.75	IS, chlorite
S-BB53	822.2	Illite, chlorite
S-BB54	833.25	IS >90% illite, chlorite
S-BB56	852	IS 90% illite, chlorite

Table 5.4. Clay mineral results from clay separate XRD analysis for drill hole UW462.

Sample	Down hole depth	Minerals
U-BB07	100.7	Illite, chlorite
U-BB20	300.7	Illite, gypsum
U-BB27	393.7	IS >90% illite, chlorite
U-BB31	491	Smectite, kaolinite
U-BB37	576.6	Illite and IS, gypsum
U-BB47	740.5	Smectite, kaolinite
U-BB51	821.1	IS 50 % illite (super ordered; rectorite), chlorite
U-BB55	902.3	Smectite, trace kaolinite
U-BB58	956.9	Smectite, chlorite

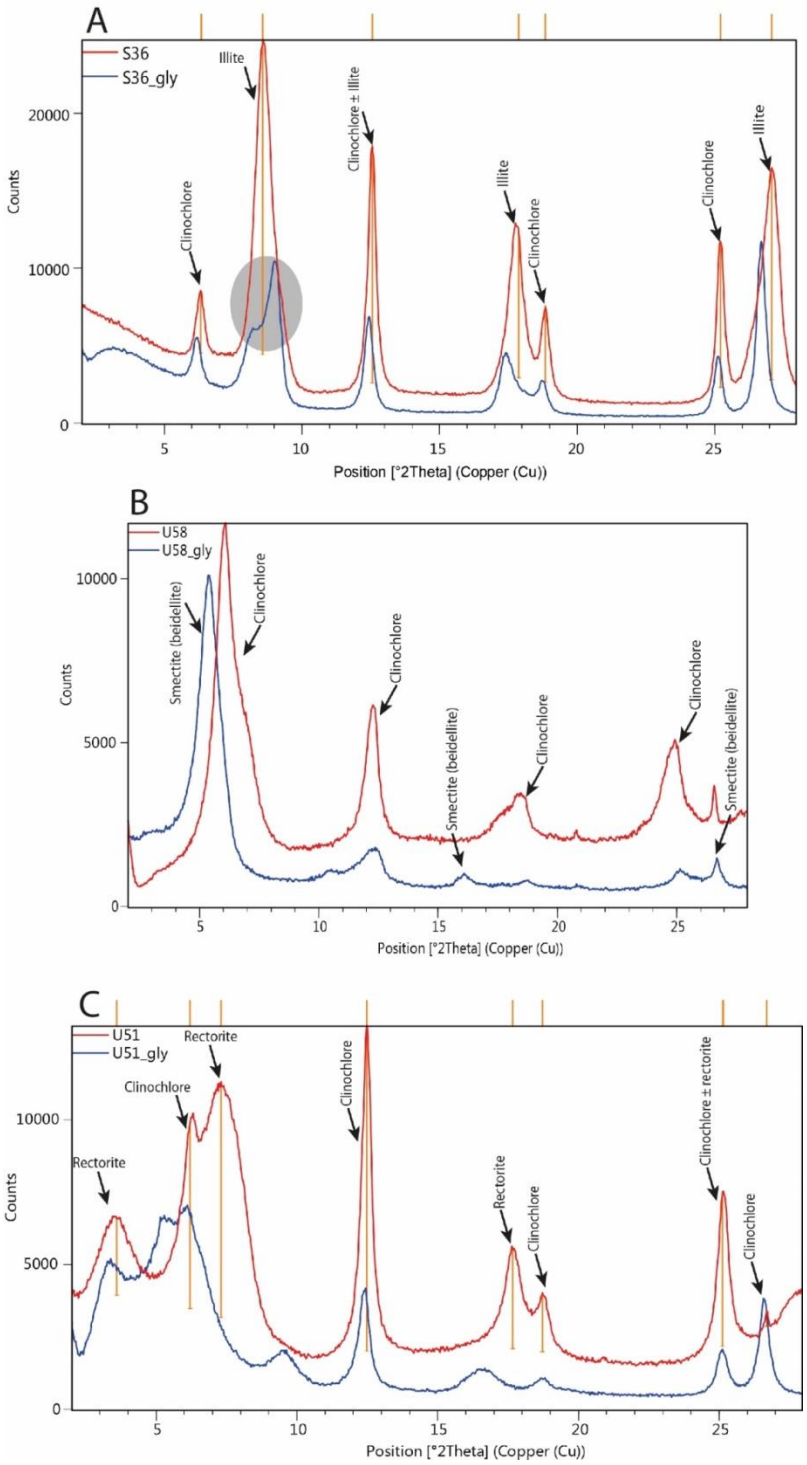

Fig. 5.3. Example clay XRD spectra. A) An example of interstratified illite-smectite with ≥90 % illite from sample S-BB36. Note the shoulder which develops when the sample is glycolated (grey circle). Red line: unglycolated. Blue line: glycolated. B) An example of smectite + chlorite from sample U-BB588. Red line: unglycolated. Blue line: glycolated. C) An example of interstratified illite-smectite with 50 % illite + chlorite from sample U-BB51. HighScore Plus indicated rectorite. Red line: unglycolated. Blue line: glycolated.Figures from HighScore Plus and further annotated in Adobe Illustrator.

5.4.3 XRF

As previously mentioned, analysing major elements via glass fusion beads involves intensive sample preparation. For this reason, only 13 samples were selected to be analysed for their major elements via this method. Subsequently, these values are used to calibrate and correct the major element data collected on the pressed powder pellets. The 13 samples selected were distributed over the extent of a K/Al vs Na/Al plot (Fig. 5.4). The glass fusion bead results was plotted against the pressed pellet results in scatter plots to determine whether a linear relationship between the concentration of major elements measured on glass fusion beads and on pressed powder pellets by a simple regression analysis (Fig. 5.5). Simple linear regression fits a straight line (trendline) through a set of points in order to minimise the sum of squared residuals of the linear regression model. The sum of squared residuals is the vertical distance between the data points and the fitted line. The slope of the linear trendline (Fig. 5.5) was used as a correction factor to correct the major element results determined on the pressed powder discs. Each major element has its own correction factor (Table 5.5). Full XRF analytical results can be found in Appendix C.

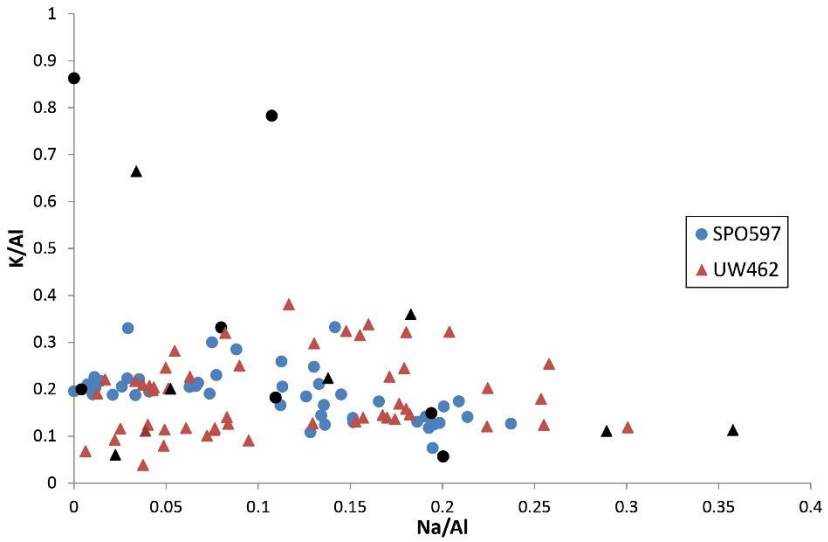

Fig. 5.4. K/Al vs Na/Al plot using major elements produced by the pressed pellet technique. Black symbols represent samples chosen for major element analysis via glass fusion beads.

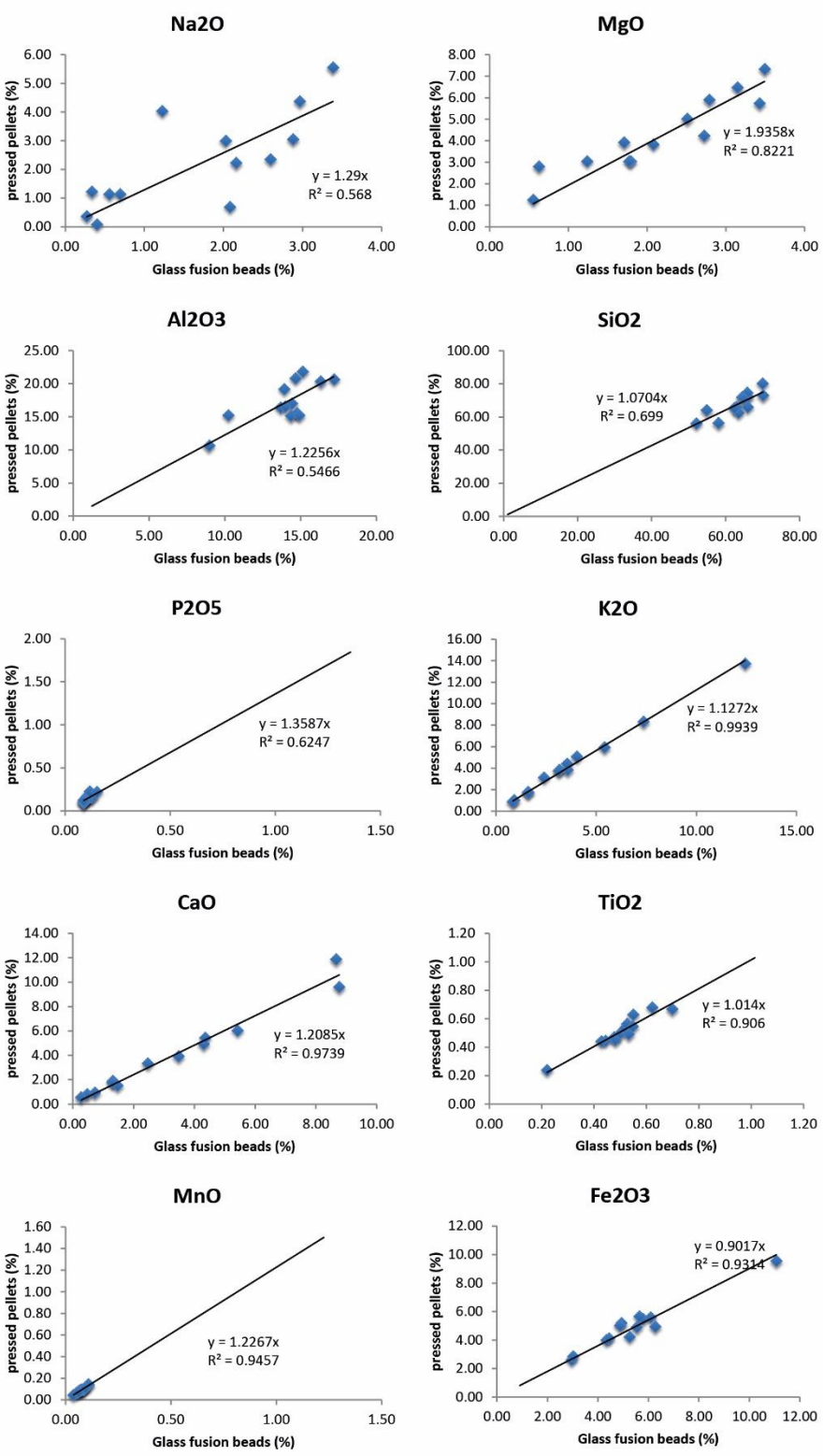

Fig. 5.5. Correlation plots of the major elements from the glass fusion beads plotted against the pressed pellets to determine the slope of the line as a correction factor.

Table 5.5. Correction factors used to correct the major elements detected via the pressed pellet technique.

Element	Correction factor
Na	1.28995
Mg	1.93580
Al	1.22556
Si	1.07036
P	1.35871
K	1.12721
Ca	1.20852
Ti	1.01400
Mn	1.22667
Fe	0.90170

5.5 Rock composition and classification

The total alkalis-silica diagram (TAS) is one of the most useful classification schemes available for volcanic rocks (Rollinson 1993). However, the TAS classification scheme is unsuitable for altered volcanic rocks because of how readily the alkalis are mobilised in aqueous solutions, often leading to misleading results (Rollinson 1993; Le Maitre *et al*. 2002). Considering the local Waihi geology encountered in this study (andesite and quartz andesite), a simple TAS diagram using geochemical data from this study illustrates this effect of mobilisation clearly, plotting as a range of volcanic rock types (Fig. 5.6). There is significant Si loss and gain in many samples. Diagrams based on elements or element ratios that are insensitive to secondary processes (such as hydrothermal alteration) are more successful (Pearce 1996).

It is important to choose immobile elements or element ratios that are alteration-insensitive equivalents to the TAS diagram (Pearce 1996). Based on observational and theoretical criteria (Pearce 1996), Ti, Zr, Hf, Nb, Ta, Cr, Th, Al Ga, and rare earth elements (excluding La) are usually immobile during weathering and metamorphism up to and including greenschist facies conditions, so are therefore suitable for use in this study.

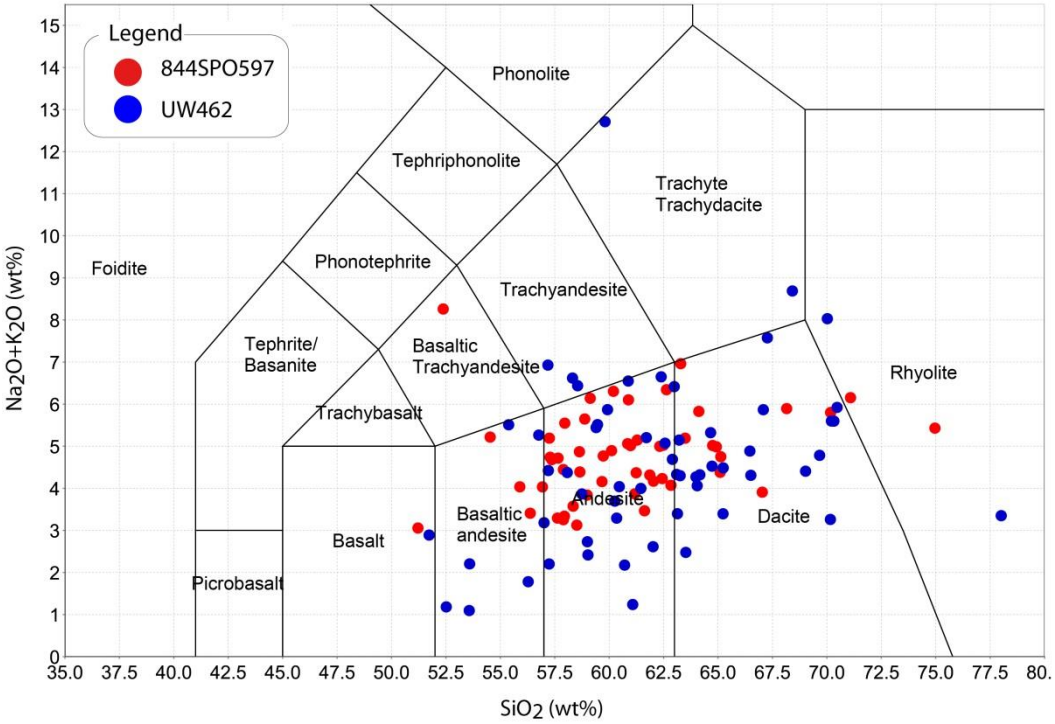

Fig. 5.6. Total alkalis-silica diagram (wt%) of all samples (after Le Maitre et al. 1989).

To find a suitable immobile element substitute for alkalinity, Pearce (1996) compared geochemical patterns of selective immobile elements in basalts. He demonstrated that there was a trend from tholeiitic to alkali basalt showing a strong enrichment in Th and Nb, a moderate enrichment in Ce, a slight enrichment in Zr, and no significant enrichment in Ti and Y. The degree of alkalinity could therefore be indicated by the magnitude of the ratio:

$$M_1/M_2$$

$where\ M_1$ is a strongly enriched element

$and\ M_2$ is a less strongly enriched element

An effective ratio to use in this situation is the Nb/Y ratio of Pearce & Cann (1973) and Floyd & Winchester (1978). It incorporates the two immobile elements that are at either extreme of the enrichment spectrum and is less sensitive to fractional crystallisation or alteration (Pearce 1996).

To account for fractionation, Ti, which is highly incompatible during mantle melting and fractional crystallisation of basic magma becoming compatible with the addition of an oxide during the crystallising phase, shows an increasing negative anomaly, responsible for the principal variation in the immobile elements (Pearce 1996). Therefore, the extent of fractionation should be indicated by the magnitude of the ratio:

$$M_1/Ti$$

$$where\ M_1 is\ an\ element\ that\ is\ incompatible\ throughout\ fractionation$$

The most effective ratio is the Zr/Ti ratio because it is less affected by alkalinity and calc-alkalinity than Nb, Th, or Ce, and less affected by garnet than Y. With that being said, the Zr/Ti-Nb/Y plot of Winchester & Floyd (1977) provides a sound empirical and petrogenetic case to recognise altered rocks (Pearce 1996).

Before the publication of the TAS classification diagram, the Zr/Ti-Nb/Y diagram of Winchester & Floyd (1977) was an early discrimination diagram for indicating rock type. This original projection was, however, based off few trace element data of the required quality. The field boundaries have since been modified by Pearce (1996), incorporating around 8000 data points. Although the modified Zr/Ti-Nb/Y diagram is not perfect and omits some rock types for convenience, it does provide a rigid basis in which to distinguish between basic, intermediate and evolved rock types. It has been used here in this study (Fig. 5.7) for quality assurance to test both the reliability of the Faculty of Science and Engineering, University of Waikato SPECTRO X-LAB 2000 XRF and, considering the length of the drill holes in this study, that drilling did intercept new or unknown lithologies to those previously recognised and described at Waihi by Newmont Waihi geologists and various associated studies.

The Zr/Ti-Nb/Y diagram (Fig. 5.7) is well suited for the altered Waihi andesites. All but two samples plot well inside the andesite boundary. Sample S-BB08, plotting above the lithology field boundaries, is predominantly a quartz vein sample whereas sample S-BB10 plots as basalt; this could be attributed to minor quartz and sulfide veinlets which were incorporated into the sample when prepared for XRF analyses.

The two holes plot up as two distinct clouds (Fig. 5.7). Samples from drill hole UW462 are concentrated, while drill hole SPO597 varies. This variability in the geochemistry could be attributed to different lava flows and may imply different eruption episodes resembling magma mingling processes, given the distance between the drill holes. Disequilibrium features, such as the resorbed and embayed quartz phenocrysts, described in Chapter 4, are evidence supporting the involvement of magma mingling processes (Kuşcu & Floyd 2001; Müller *et al*. 2005).

5.6 Geochemistry

The distribution of the corrected pressed pellet major elements for each drill hole is discussed here. The corrected major elements (Fig. 5.9) are compared to a plot of molar K/Al against molar Na/Al, which is used for the geochemical identification of important temperature dependent hydrothermal minerals (Fig. 5.9). The spatial distribution of the minerals identified by the molar K/Al versus molar Na/Al plot is also shown for comparison (fig. 5.9).

Subsequently, the downhole spatial concentrations of selected pathfinder elements associated with gold deposits (S, As, Cl, Bi, Se, Mo, U, Tl; Fig. 5.10 A) are discussed and also compared to the K-Na-Al feldspar control diagram (Fig. 5.10 B and C).

5.6.1 K-Na-Al feldspar control diagram

In shallow hydrothermal systems the gain of K and the loss of Na and Ca account for much of the mass transfer (Booden *et al*. 2011). Mass changes associated with K metasomatism can be evaluated graphically using molar element ratios such as the feldspar Na-K GER diagram of Stanley & Madeisky (1996) which plots molar K/Al against molar Na/Al. The benefit to plotting molar values is that compositions

of altered rocks can be compared to the compositions of primary and secondary K-, Na-, Ca-, and Al-bearing minerals that are located in the same compositional space, thus allowing identification of important hydrothermal minerals (e.g., illite, smectite) and alteration processes that are reflected in trends from fresh-rock compositions toward the compositions of hydrothermal minerals (Warren *et al*. 2007).

When plotted on the feldspar Na-K GER diagram, we see the samples clustered into three distinct arrays (Fig. 5.9 B). The first array is associated with illite as it reflects a gain in Al and K and a loss of Na. The second array is associated with smectite as it reflects a loss in K. The third array is considered less altered because there is no significant gain and/or loss in K, Al, or Na to suggest otherwise. No adularia was detected via this plot.

5.6.2 Major element concentrations downhole

Drill hole UW462

Potassium remains fairly constant with an average 4.24 wt% from the start of the hole to 482.5 m (Fig. 5.9 A). This is relatively enriched compared to the rest of the hole which abruptly drops to an average of 2.46 wt% from 491 to the end of the drill hole at 956.1 m. Aluminium shows enriched concentrations in two pockets (Fig. 5.9 A). Between 145.6 to 173 m, Al levels ranges between 15.85 to 17.79 wt%. Between 336.9 and 503.7 m, Al ranges between 12.40 to 20.55 wt%, with an average of 16.29 wt%. From 522.4 to the end of the drill hole, the average Al levels decrease to 13.97 wt%. The higher concentrations of K and Al, particularly between 336.9 and 503.7 m, indicate that the rock contains illite (Poppe *et al*. 2001). While K is required for the formation of illite, the formation of smectite is consistent with a paucity of K. Smectite is also associated with Ca (Poppe *et al*. 2001). Calcium shows a slight overall increase towards the end of the drill hole (Fig. 5.9 A). This transition from K-Al enrichment to K depletion, accompanied by an increase in Ca, would suggest, although erratic, an overall gradation from illite to smectite. This can be confirmed using the feldspar Na-K GER diagram (Fig. 5.9 B) to determine illite and smectite. The corresponding gains and losses of K, Al, and Ca can be seen spatially associated with the identified illite and smectite zone (Fig. 5.9 C). It shows

an abrupt change from illite-bearing to less altered/smectitic bearing rock at the same position that there are losses in K and Al and gains in Ca.

Pyrite is ubiquitous in low sulfidation epithermal Au-Ag deposits (Christie & Barker 2007). How much pyrite has been added to the rocks, or degree of pyritisation, can be assessed using a Fe-S plot (Fig. 5.11). The Fe-S plot is a PER molar ratio plot of Fe/Zr versus S/Zr. The theoretical basis for PER diagrams is described in Stanley & Madeisky (1996). Essentially, gains in S and Fe are associated with the formation of pyrite. Down drill hole UW462, most samples are not fully sulfidised (Fig. 5.11). The diagram suggests the formation of pyrrhotite in some samples, mostly those that are identified as illite from the feldspar Na-K GER diagram. Most of the smectite inferred samples are weakly sulfidised. However, there are two samples that are strongly sulfidised; it is possible that those samples contained sulfide veinlets; a common alteration texture noted in the logging from Chapter 4 and sometimes unavoidable during crushing of bulk rock samples for XRF.

Drill hole SPO597

Potassium content is highest between 0 and 557.35 m with an average of 3.7wt% (Fig. 5.9 A). From 566.4 m to the end of the drill hole at 852 m the average K content suddenly decreases to 2.42 wt%. Aluminium contents vary throughout this drill hole with an average of 15.03 wt% (Fig. 5.9 A). There is a small increase in Al between 316.8 to 612.74 m and 718.4 to 808.1 m, with an average Al content of 16.24 and 16.03 wt%, respectively. Similar to drill hole UW462, the elevations of K and Al, particularly up to 557.35 m, are consistent with the formation of illite. The abrupt drop in K is also accompanied by an increase in Ca (Fig. 5.9 A), which, as previously outlined, is consistent with the formation of smectite. However, unlike drill hole UW462, Al remains relatively elevated which might suggest a gradation from illite to interlayered illite-smectite rather than to smectite. Looking at the inferred illite and smectite zones for this drill hole (Fig. 5.9 B) the gains and losses of K, Al, and Ca are also spatially associated with the distribution of illite and smectite (Fig. 5.9 C). At the exact positon that illite changes to less altered andesite, K also decreases in wt%. A similar pattern exists for Ca, which shows enrichment in less altered zones and depletions in illite inferred zones. What is

interesting about this hole is that no smectite was inferred from the feldspar Na-K GER diagram. Compared to drill hole UW462, Al (and more or less K) does not decrease so drastically after the illite zone, suggesting the least altered samples could be interstratified illite-smectite, but the diagram is not able to yet pick it out. This will be evaluated later.

The degree of pyritisation down SPO597 is similar to UW462 in the respect that most samples are not fully sulfidised (Fig. 5.11). The more sulfidised samples are mostly those that are identified as illite from the feldspar Na-K GER diagram. The less altered samples, which generally have low S contents are still relatively enriched in Fe. Iron could be associated with chlorite rather than pyrite, as chlorite is the principal alteration mineral that hosts Fe and Mg (Booden *et al*. 2011). Elevated concentrations do correspond to elevated Fe (Fig. 5.9 A).

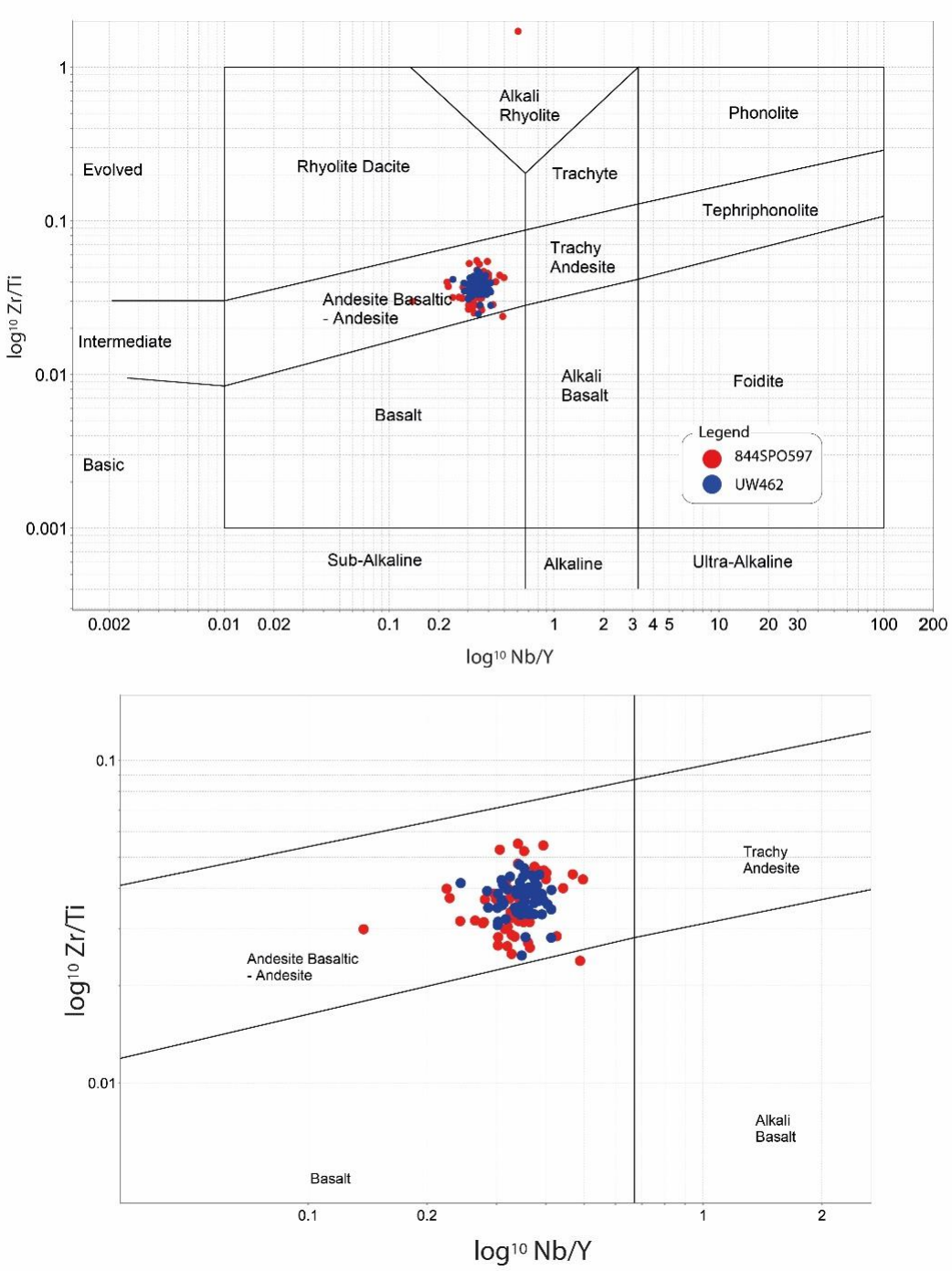

Fig. 5.7. Rock classifications plot of Zr/Ti vs. Nb/Y for all samples after Pearce (1996).

Fig. 5.9. Left: Ranked variable maps of selected pathfinder elements plotted downhole. Left drillhole = UW462. Right drillhole = SPO597. Top right: Feldspar Na-K GER diagram with reference rock and mineral data plotted (large grey circles). Bottom right: Attribute map showing the distribution of minerals inferred from B plotted spatially.

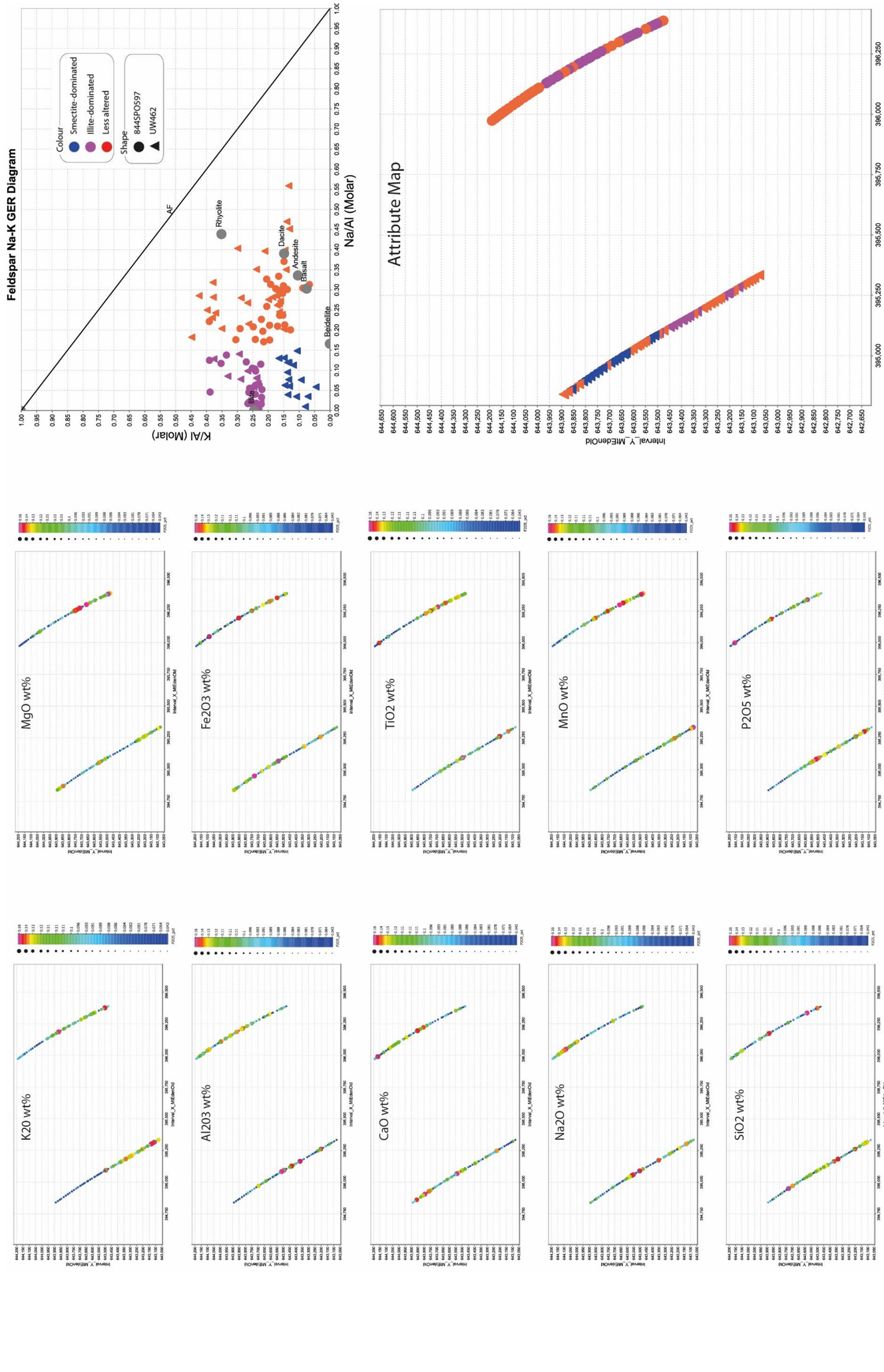

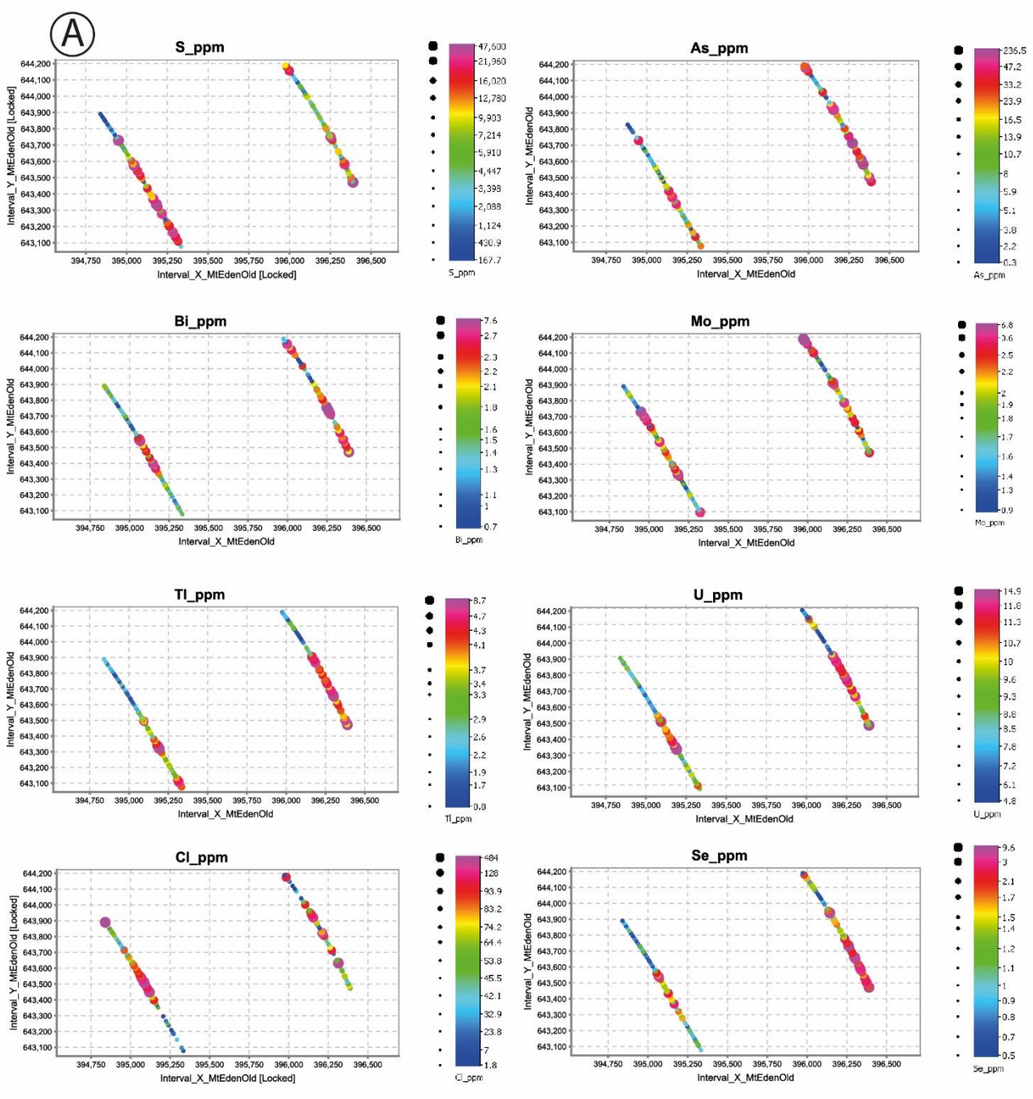

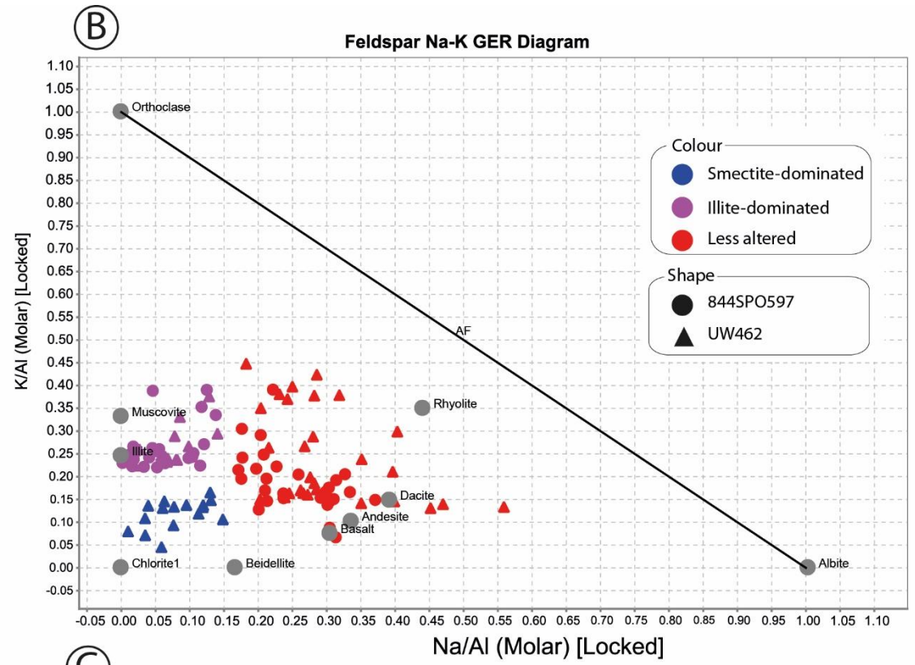

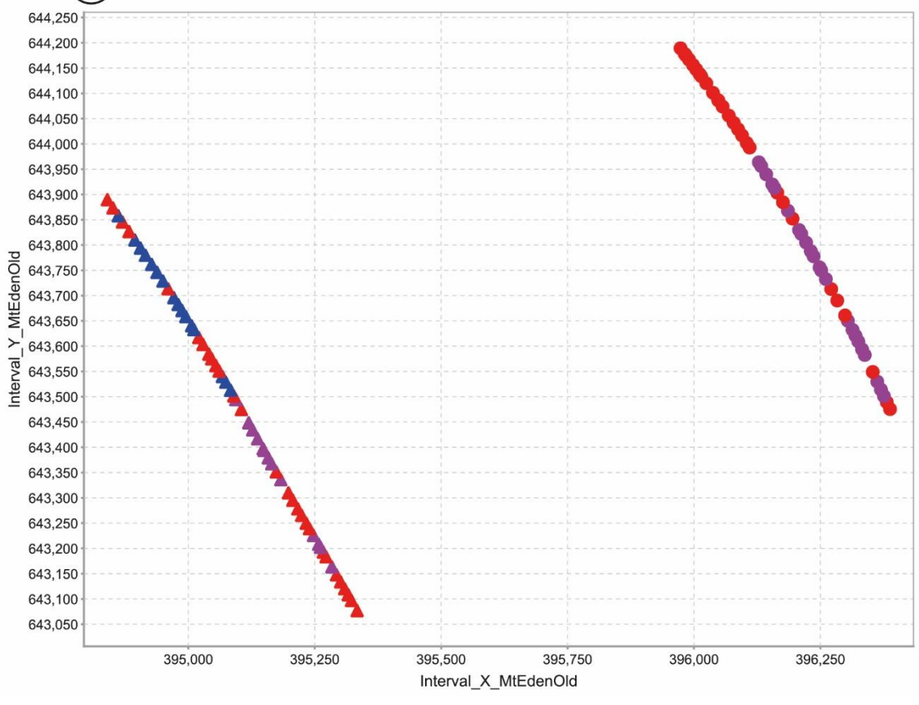

Fig. 5.10. A) Ranked variable maps of selected pathfinder elements plotted downhole. Left drillhole = UW462. Right drillhole = SPO597. B) Feldspar Na-K GER diagram with reference rock and mineral data plotted (large grey circles). C) Attribute map showing the distribution of minerals inferred from B plotted spatially.

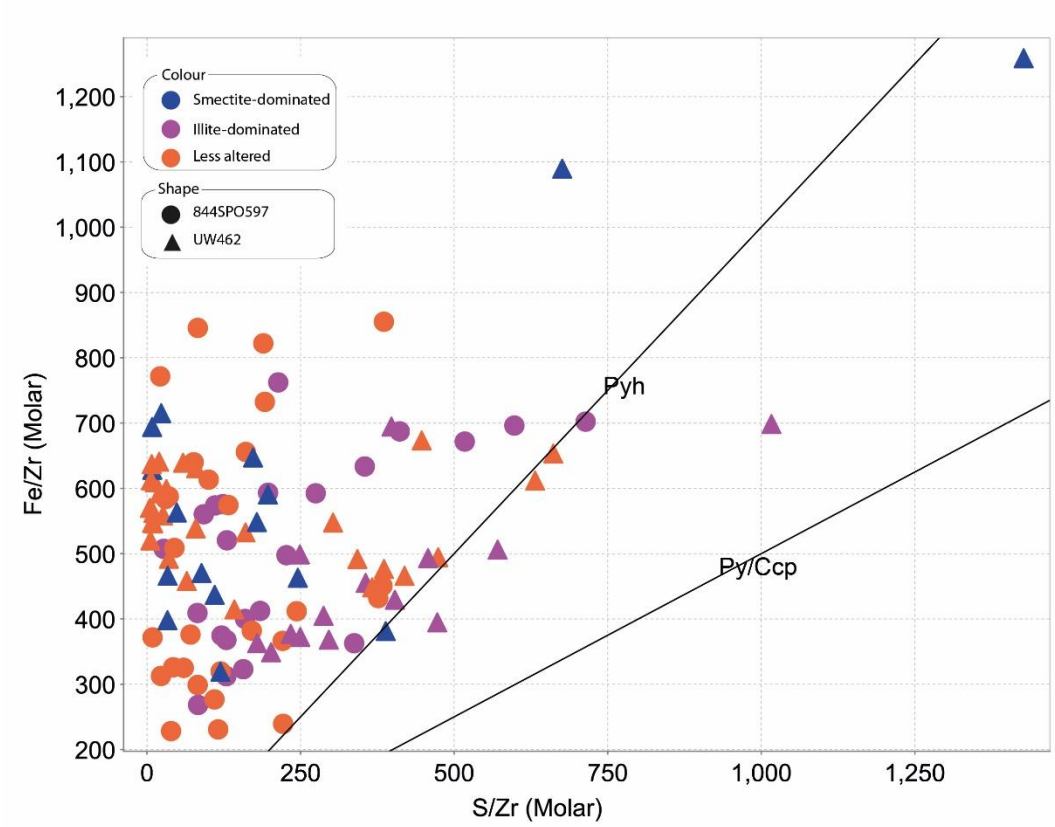

Fig. 5.11. Sulfide Fe vs S plot with "Pyh" pyrrhotite and "Py/Ccp" pyrite-chalcopyrite control lines.

5.6.3 Trace element pathfinders

Arsenic

Arsenic has been recognised as being an excellent pathfinder element in mineral exploration. It is widely distributed in geological materials as well as being geochemically relatively mobile (Parker & Nicholson 1990). Arsenic is linked to more than 20 economically important elements (Boyle & Jonasson 1973), including precious metals (Au, Ag, Pt) and base metals (e.g. Cu,Zn, Pb, and Co). Arsenic concentrations are notably elevated in mineral deposits and commonly form halos around ore bodies (Parker & Nicholson 1990). Arsenic is also detected in trace amounts in electrum, the main ore mineral in Waihi (Brathwaite & Faure 2002). My results show a large variation in As concentrations (Fig. 5.10 A). Down drill hole SPO597, the average As level is 29 ppm, with a max of 237 ppm and a minimum of 1 ppm. There are distinct elevations in As which correlate with a zone of illite (Fig. 5.10 C), determined by the feldspar Na-K GER diagram. For drill hole

UW462, the average level of As is 12 ppm, with a max of 49 ppm and a minimum of <0.3 ppm (Fig. 5.10 A). Anomalous levels of As down drill hole UW462, between 300.7 and 393.7 m, also correlates with the illite zone (Fig. 5.10 C).

Chlorine

Chlorine is a useful pathfinder element for hydrothermal mineralisation because of its broad dispersion pattern in mineral deposits (Fuge *et al.* 1986). Chlorine levels range from 1.8 to 160.9 ppm down SPO597 and 3.1 to 484 ppm down UW462 (Fig. 4. 5.10 A). Down both drill holes there Cl is weakly correlated with the inferred illite (Fig. 5.10 C).

Bismuth

In many quartz-sulfide systems, Bi levels are anomalous making it useful as a pathfinder element (Corbett 2002). Minerals from the large group of bismuth-chalcogenides also act as 'gold carriers', containing 'invisible' gold (Ciobanu *et al*. 2009). In my samples, Bi is enriched throughout most of SPO597, reaching 7.6 ppm at 323.8 m (Fig. 5.10 A). There is a clear increase in Bi concentrations from 300.7 to 560.7 m down UW462, with up to 3.7 ppm Bi. This increase of Bi down UW462 correlates with the feldspar Na-K GER diagram where illite is indicated (Fig. 5.10 C). Similarly for drill hole SPO597, the higher levels of Bi are also occurring where illite is indicated (Fig. 5.10 C).

Selenium

Selenium is also a very useful pathfinder element for precious metals, particularly in epithermal Au-Ag deposits that contain gold and silver selenides (Budyak & Bryukhanova 2012). Selenium displays almost identical patterns to Bi, with highest Se levels occurring in the illite dominated sections for both SPO597 and UW462 (Fig. 5.10 A and C).

Molybdenum

Molybdenum is a characteristic pathfinder element in epithermal systems. In the Hauraki Goldfield, elevated contents of Mo are reported to occur at deeper levels of epithermal systems (Clarke & Govett 1990). Here, Mo ranges between 0.9 and 6.9 ppm down drillhole SPO597 and between 1.2 and 5.1 ppm down drill hole UW462 (Fig5.10 A). Unlike most of the other pathfinder elements, Mo does not

show any zones which are particularly elevated and shows no correlation to the illite zones Fig. 5.10 C).

Uranium

Although uranium is not generally affected by epithermal alteration (sometimes even showing a depletion; Morrell *et al*. 2011), there is a clear elevation in U concentrations in similar locations to the other pathfinders (Fig. 5.10 A). Uranium for both drill holes correlate near perfectly with the illite zones (Fig. 5.10 C).

Thallium

Thallium has been proposed as a potential guide for mineral exploration (Ikramuddin *et al.* 1986). It is concentrated in altered rocks and known to form extensive halos surrounding particular types of vein- and massive sulfide-style deposits, including epithermal vein deposits (Large *et al.* 2001; Gemmell 2007). Thallium has a high affinity for phyllosilicates (micas and clays), tectosilicates (feldspars), and sulfides (galena, pyrite, and Tl sulfides and Tl sulfosalts), substituting for K in phyllosilicate and tectosilicate structures and Pb among sulfides. The concentrations of thallium in phyllosilicates and tectosilicates generally are in the 1 to 10s of ppm range (Shah *et al.* 1994; Gemmell 2007).

The distribution of Tl using data from this study is shown in Figure 5.10 A. Thallium levels are elevated for the first 505.75 m down drillhole SPO597, while in drillhole UW462 Tl is elevated in three distinct pockets (from 0 to 66.6 m, 253.6 to 350.5 m, and at 482.5 m). Like the other pathfinders, Tl enrichments occur in the illite zones (Fig. 5.10 C).

Gemmell (2007) noted that at the Gosowong epithermal Au-Ag deposit, Halmahera, Indonesia, high K_20 concentrations in the deposit, alteration halo and upflow zone were related to the distribution of adularia. Both K_20 and Tl concentrations were elevated in the areas of greatest adularia abundance. The study recognised a strong positive correlation between K and Tl, while there was no correlation between S and Tl. Thus, leading to the conclusion that adularia, not sulfide minerals, contain the Tl in the hydrothermal alerted rocks surrounding the Gosowong deposit. These patterns are also recognised here in Figures 5.12 A and B. However, adularia was

not inferred from the feldspar Na-K GER diagram. Therefore, Tl is substituting for K in the illite, a known behaviour during metasomatism (Booden *et al*. 2011).

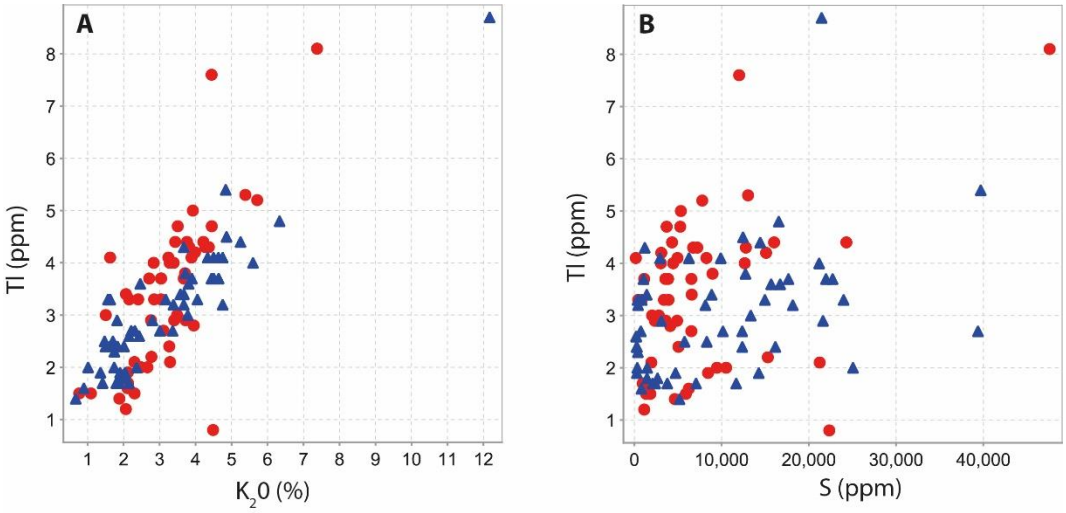

Fig. 5.12. Relationship between whole-rock Tl, K_2O, and S content. A) Positive correlation between K_2O and Tl suggests that Tl is associated with illite. B) A lack of correlation between S and Tl suggests that Tl is not as strongly associated with sulfur-bearing minerals as it is with K-bearing minerals. Red circles = 844SPO597. Blue triangles = UW462.

5.7 Alteration mineralogy

Here I discuss the suitability of the feldspar Na-K GER diagram for mineral identification by comparing the inferred mineral species to those identified by clay separate XRD and TerraSpec analysis. For the feldspar Na-K GER diagram, the minerals approximated are classified as illite-dominated, smectite-dominated or less altered. The TerraSpec results are classified as illite, low illite or illite-smectite. The clay XRD results are classified as illite, illite-smectite with ≥90 % illite, illite-smectite with 50 % illite, and smectite.

Figure 5.13 compares the TerraSpec results to the feldspar Na-K GER diagram. The samples which are classified as less altered by the geochemistry are generally identified as containing low illite content or illite by the TerraSpec, and in some cases, illite-smectite. Where the geochemistry identifies illite, we see a strong correlation. However, illite appears to be more widespread than indicated by the whole rock geochemistry. The smectitic samples approximated by the geochemistry were not analysed by TerraSpec so the ability to correctly identify smectite

geochemically cannot be confirmed, but it can be noted that none of the samples analysed via TerraSpec identified pure smectite.

In Figure 5.14, the feldspar Na-K GER diagram results are compared to the clay XRD results. The benefit of the clay XRD is that the illite content within the interstratified samples can be easily distinguished as previously described in the results section in this chapter. The illite and interstratified illite-smectite with ≥90 % illite determined by the clay XRD correlates with the geochemically identified illite. Down drill hole SPO597, majority of the samples classified as less altered are identified as ≥90 % illite by clay XRD. Pure smectite was not identified by clay XRD down drill hole SPO597. In contrast, clay XRD identified smectite in four samples down drill hole UW462. While all four samples are geochemically considered less altered, they occur proximal to the smectite zone.

Overall, the geochemistry is a good proxy for K and Al rich illite. Higher concentrations of Na in some samples appear to mask the illite. Although the smectitic samples identified by clay XRD do not plot geochemically as smectite, they occur adjacent to the zone of smectite. Because of limited clay XRD results due to the extensive sample preparation involved, a larger data set utilising more clay XRD results may aid in evaluating the potential of the feldspar Na-K GER diagram for identifying interstratified illite-smectite and determining illite content.

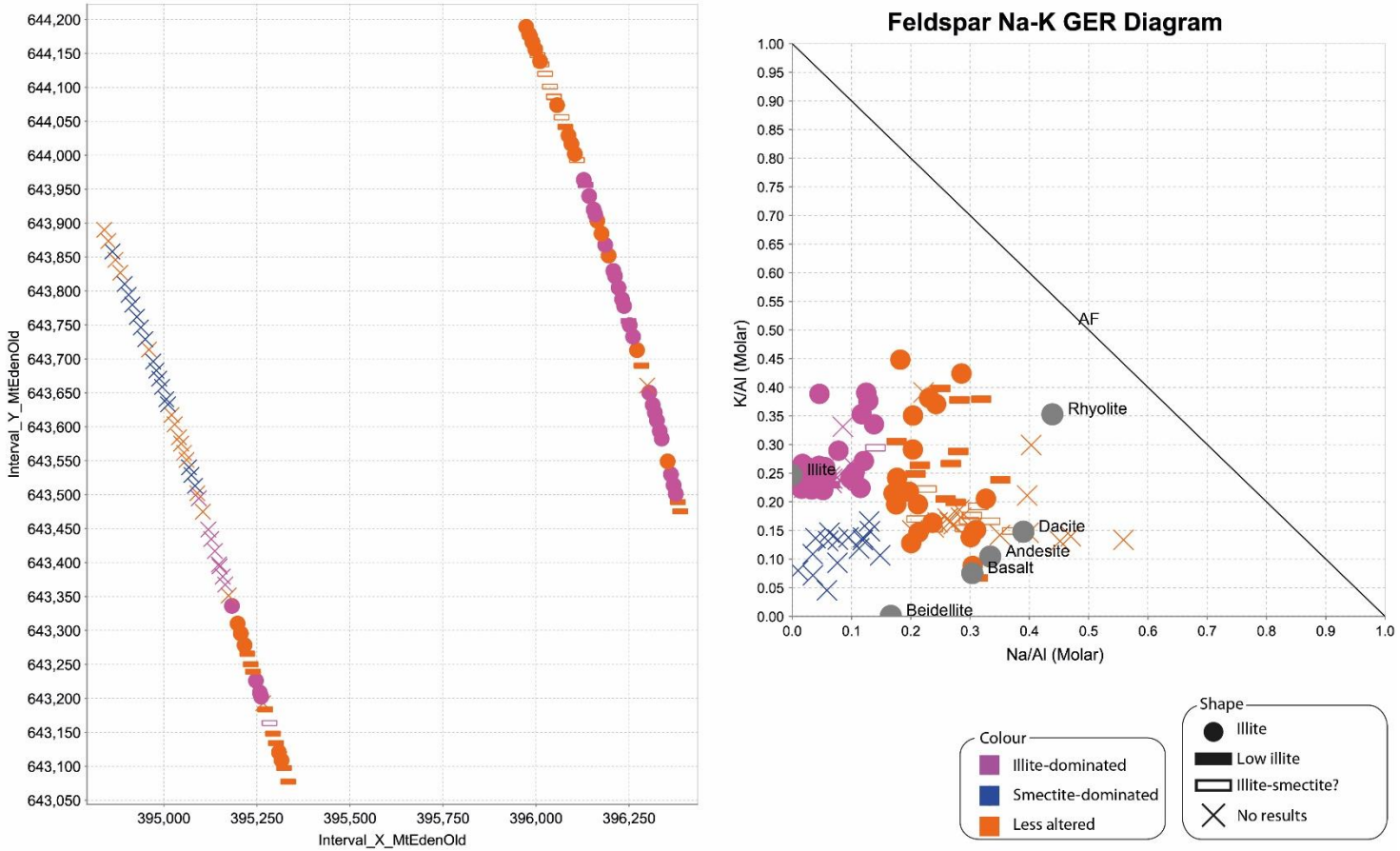

Fig. 5.13. The comparison between TerraSpec results and geochemically inferred minerals using the feldspar Na-K GER diagram. Left: spatial distribution of mineral species down hole. Right: the minerals approximated using the feldspar Na-K GER diagram. . Colours defined on basis of geochemistry, shapes defined on the basis of TerraSpec. Large grey circles represent reference minerals and rock types.

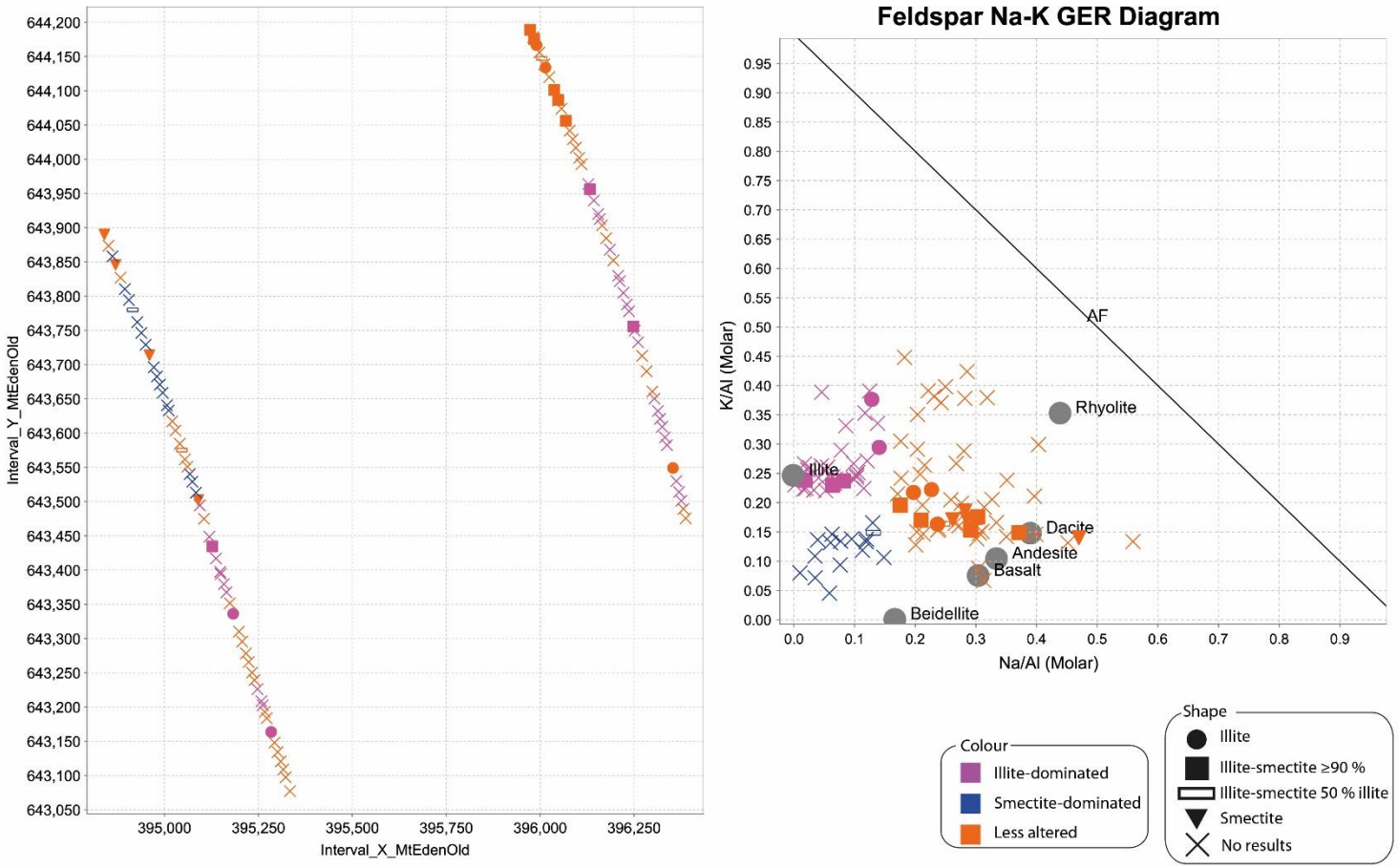

Fig. 5.14. The comparison between clay XRD results and geochemically inferred minerals using the feldspar Na-K GER diagram. Left: spatial distribution of mineral species down hole. Right: the minerals approximated using the feldspar Na-K GER diagram classified by colour. . Colours defined on basis of geochemistry, shapes defined on the basis of XRD. Large grey circles represent reference minerals and rock types.

5.8 Interpretation

As discussed in Chapter 3, Au ore in low-sulfidation deposits can vary from vein to stockwork to disseminated forms. In vein-controlled mineralisation, alteration halos will include a variety of temperature-sensitive clay minerals (Fig. 5.15) that can lead to the zone of mineralisation. The areal extent of such clay alteration may be two orders of magnitude larger than the actual ore deposit (Hedenquist *et al*. 2000).

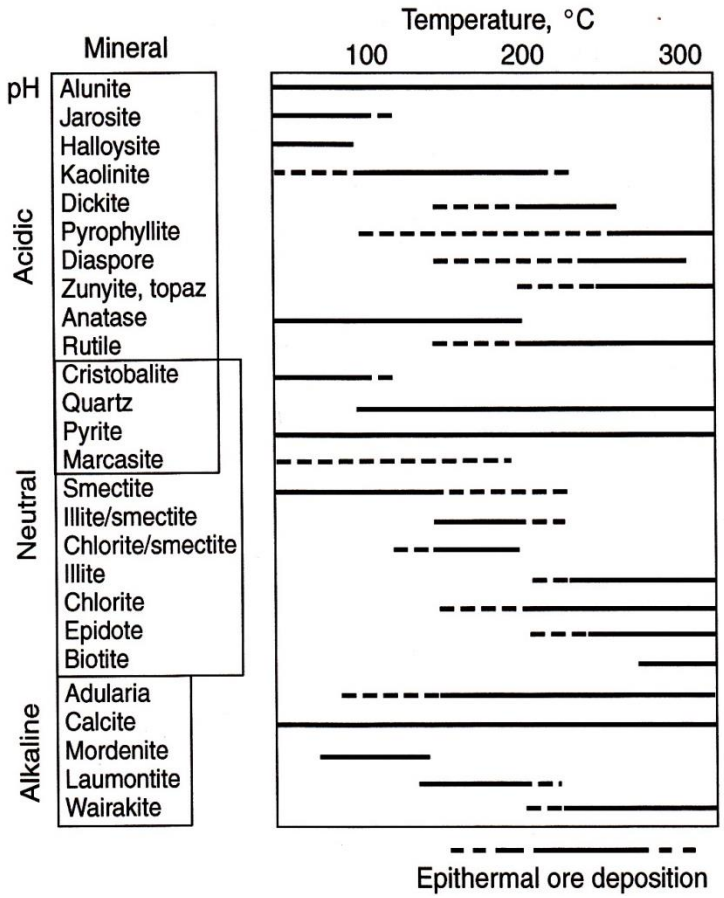

Fig. 5.15. Thermal stability of various hydrothermal minerals that occur in the epithermal environment under acid and neutral-pH conditions, and the typical temperature range for deposition of epithermal ore (after Hedenquist et al. 2000).

Rather than trying to group my alteration mineralogy and geochemistry results discussed above into an alteration assemblage, specific mineral distributions can provide the adequate information to establish the paleoisotherms, and thus, paleofluid flow directions which lumping into a broad caterory would lose (Hedenquist *et al*. 2000). For example, the zonation of hydrothermal clays from smectite to interstratified illie-smectite to illite matches an increasing thermal gradient (Fig. 5.15) and can be used to estimate isotherms (Hedenquist *et al*. 2000).

In Figure 5.16 the TerraSpec 4 Hi-Res, clay separate XRD, and geochemistry results are combined with known thermal stabilities of certain minerals to create a simplified schematic paleoisotherm model in the main study area peripheral to Martha Mine. Down drill hole SPO597, illite is largely dominant, transitioning to interstratified illite-smectite with >90% illite content. In contrast, illite occurs for approximately the first half of drill hole UW462 before there is an abrupt change to smectite. This feature is inferred to here as a "hard-bar" or lens of less permeable/altered rock. These hard-bars have been noted throughout the Hauraki Goldfield (Stuart *et* al. n.d.; Simpson & Mauk 2000; Simpson *et* al. 2001; Mauk & Simpson 2007) occurring exclusively in lava flows of the Waipupu Formation and the Waiharakeke Dacite (Simpson *et* al. 2001). There is a small zone of interstratified illite-smectite north of the hard-bar, followed by a zone largely dominated by smectite.

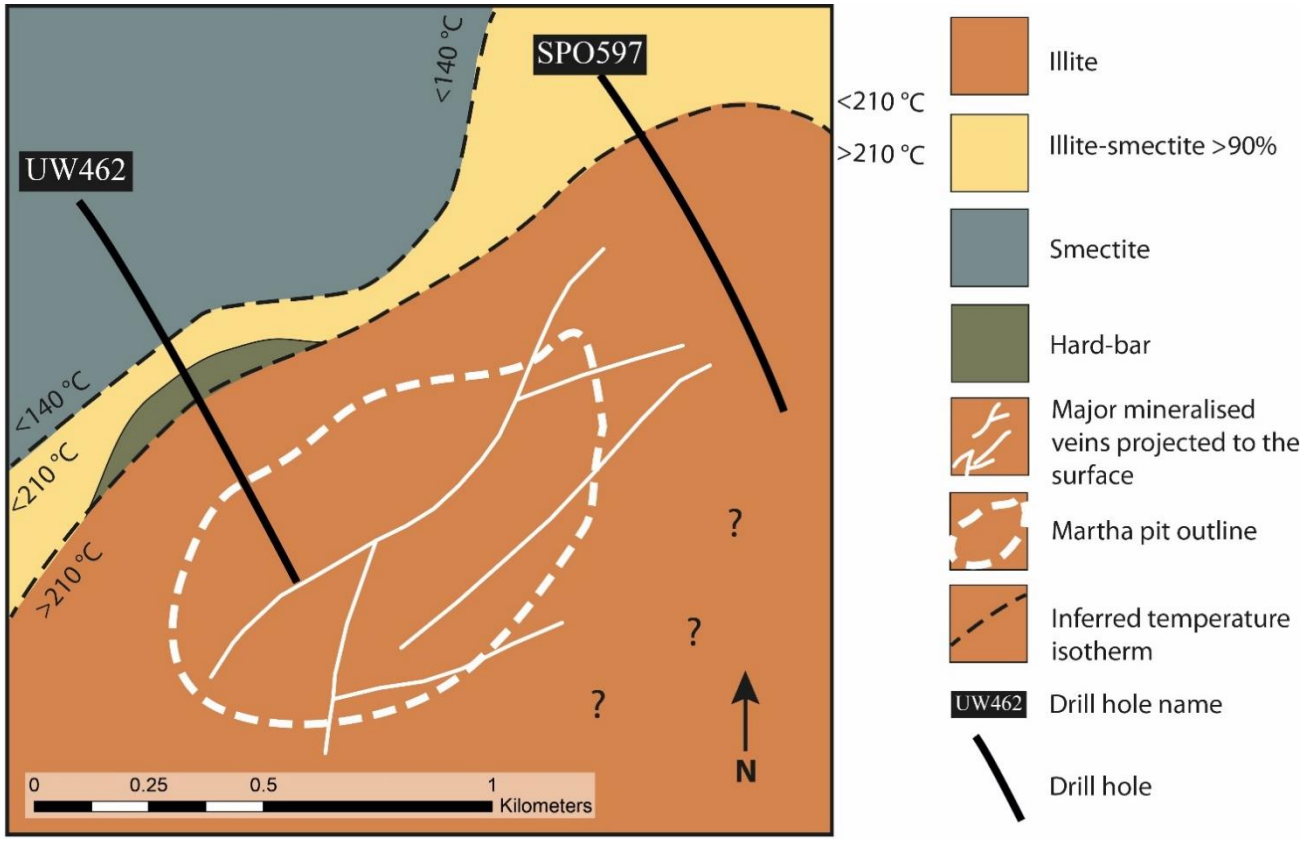

Figure 5.16.Simplified schematic paleoisotherm model showing the transition from illite to smectite based on TerraSpec, clay XRD and geochemical results. Inferred temperatures (black isotherm) based on the mineral assemblage and their corresponding thermal stability ranges. The question mark symbol (?) represents inferred illite as there is no data.

5.9 Summary

Short wave infrared spectroscopy provided cost effective and rapid data acquisition of mineral assemblages. Used in conjunction with x-ray diffraction on clay separates, the occurrence and distribution of temperature-sensitive illite, interstratified illite-smectite, and smectite was accurately identified peripheral to existing Waihi mine workings and major mineralised Au-Ag quartz veins. The thermal gradient associated with the transition from illite through to smectite suggests a "cooling" of the hydrothermal fluid northwest of Martha Mine. An abrupt change from illite-bearing rock to smectite-bearing rock down drill hole UW462 could be associated with a "hard-bar". The feldspar Na-K GER molar element ratio diagram provided an additional method to identify alteration mineralogy by geochemically identifying mineral species, particularly K- and Al-rich illite.

Variations in the concentration of known pathfinder elements showed strong correlation to mineralogy, demonstrating their potential as vectors for exploration. Thallium was identified as having a high affinity with illite. Other elements such as Bi and Se were also vectoring towards illite-bearing rocks. The Nb/Y versus Zr/Ti molar element ratio plot of Pearce (1996) provided a reliable substitution for the TAS diagram for rock classification of altered volcanic rocks.

Chapter 6 Summary and conclusions

6.1 Introduction

Epithermal deposits in New Zealand are predominantly located in subaerial calc-alkaline volcanic rocks. Within the Coromandel Volcanic Zone, the Hauraki Goldfield consists of approximately 50 separate epithermal Au-Ag deposits associated with calc-alkaline volcanic rocks of Miocene-Pliocene age. The location of such orebodies is strongly controlled by lithology. Greater than 95 percent of the Hauraki Goldfield production has been derived from veins hosted by andesite and dacite of the Coromandel Group, despite other lithologies (e.g. rhyolite, ignimbrite) forming nearly 40 percent of the rocks in the goldfield. The Waihi vein system is located at the southern margin of the Hauraki Goldfield and includes deposits such as the world-class Martha Mine in Waihi. The Waihi vein system deposits are hosted by hydrothermally-altered andesite of the Waipupu Formation, a Late Miocene formation within the Coromandel Group. Little work has been published on the volcanism of the Waipupu Formation andesites. Despite over 127 years of prospecting and mining at Waihi, new Au-Ag veins and extensions of existing veins are being discovered. Newmont Waihi Gold is currently drill testing for extensions of the Martha Hill vein system at depth. This research was conducted to reconstruct the volcanic and hydrothermal setting peripheral to the Martha Hill mine.

This study has involved detailed logging and sampling of 1811.5 m of drill core from two subsurface drill holes located peripheral to existing Waihi mine workings. The focus of the logging was to characterise volcanic facies. As an outcome, eight new volcanic facies were identified based on visible crystal abundances. This study also involved analysing the associated hydrothermal mineralogy and geochemistry that overprints the primary volcanic textures. Correct identification of thermally sensitive hydrothermal minerals (e.g. illite and smectite) has applications to exploration as they can provide vectors towards Au-Ag mineralisation. The results show a decreasing thermal gradient away from the major mineralised veins.

6.2 Key findings

Eight new facies were identified based on mineral abundances and the presence of quartz phenocrysts. Crystal abundances within the Waipupu Formation andesite ranged from 10 to 60% and are dominated by feldspar and mafic minerals, which

are usually difficult to identify behind the overprinting alteration. Quartz phenocrysts are scarce but prominent. The moderately crystal rich quartz-bearing andesite facies was the most dominant facies in both drill holes. These lavas have a total crystal content of 10-25%, comprising 1-20% feldspars, 1-20% mafic minerals, and <1-10% quartz. These values are similar to other volcanic successions of modern active andesite volcanoes (Mount Ruapehu, New Zealand), as well as Late Archean andesites-dacites (Kurnalpi Terrance, Western Australia).

The texture of each of the lava facies is dominantly porphyritic, dominated by plagioclase + ferromagnesian silicates ± quartz. Variable amounts of glomeroporphyritic aggregates are present. Groundmass textures are typically intersertal or cryptocrystalline. The feldspar crystals typically display polysynthetic twinning while the quartz was commonly resorbed. The resorbed quartz suggests these lavas underwent different levels of magma mixing within the magma chamber before erupting.

Due to hydrothermal alteration, major element compositions are not representative of the primary igneous geochemistry. The Nb/Y versus Zr/Ti plot, modified by Pearce (1996), was useful as an immobile trace element proxy for the total alkalis versus silica (TAS) diagram that is normally used for the classification of unaltered volcanic rocks. Trace elements are consistent with an andesite composition.

The feldspar Na-K GER diagram, which plots molar K/Al against molar Na/Al, can be used as a proxy for some mineral assemblages. This was confirmed by comparing the geochemically inferred mineral species to those identified by the TerraSpec and clay separate XRD. Potassium and Al rich illite, indicated by the feldspar Na-K GER diagram, correlates well with the mineralogy identifying techniques. Those samples which are interstratified with a smectitic component were not able to be resolved geochemically possibly due to higher concentrations of Na.

Short wave infrared spectroscopy provided cost effective and rapid data acquisition of mineral assemblages. The illite content within mixed-layer clays was efficiently identified by clay XRD. Smectite within mixed-layer clays responded particularly well to ethylene glycol treatment and was easily identified by comparing diffraction patterns of air-dried samples to ethylene glycol treated samples.

Paleoisotherms were established peripheral to the Martha Hill mine based on the identification of illite, interstratified illite-smectite and smectite. Drill hole SPO597 shows a clear transition from illite (>210 °C) to illite-smectite (<210 °C) with >90 % illite content. In contrast, an abrupt change from illite to smectite down drill hole UW462 is associated with a "hard-bar" or lens of less permeable/altered rock which are known to occur exclusively in lava flows of the Waipupu Formation and the Waiharakeke Dacite. The distal part of drill hole UW462 is dominated by smectite which is commonly stable at <140 °C. This thermal gradient suggests a "cooling" of the hydrothermal fluid northwest of Martha Mine.

6.3 Further work

- The horizontal orientation and limited number of drill holes used, prevented attempts to reconstruct the vertical volcanic stratigraphy, nor correlate between drill holes. It would be beneficial to incorporate the facies approach used here with vertically orientated holes for a better understanding of the volcanic history and structure.
- The illite-rich content noted at the distal end of drill hole SPO597 may be vectoring towards more mineralised veins, may indicate an up flow, outflow or influx zone of the past hydrothermal activity, or may indicate more permeable rock. Drill testing in this location in conjunction with techniques such as those used in this study would be needed to investigate this further.
- The "hard-bar" was associated with an abrupt change in mineralogy from illite to smectite. Because it is a common feature of the Waipupu Formation and other volcanic units within the Coromandel Volcanic Zone, further work detailing how it affects hydrothermal fluid flow would be advantageous for mineral exploration.
- More developed testing of the feldspar Na-K GER diagram using a larger dataset containing accurate measurements of illite content in interstratified illite-smectite would be immensely useful to see if geochemistry can better indicate mixed-layer clays.

References

Adams, C. J., Graham, I. J., Seward, D. & Skinner, D. N. B. (1994). 'Geochronological and geochemical evolution of late Cenozoic volcanism in the Coromandel peninsula, New Zealand', *New Zealand Journal of Geology and Geophysics*, *37*(3), pp. 359-379.

AusSpec. (2010). *AusSpec manual*. AusSpec International Ltd, Australia.

Ballance, P. F. (1974). An inter-arc flysch basin in northern New Zeland: Waitemata Group (Upper Oligocene to Lower Miocene). *Journal of Geology*, *82*, 439-471.

Barley, M. E., Brown, S. J., Krapež, B., & Kositcin, N. (2008). Physical volcanology and geochemistry of a Late Archaean volcanic arc: Kurnalpi and Gindalbie Terranes, Eastern Goldfields Superterrane, Western Australia.*Precambrian Research*, *161*(1), 53-76.

Booden, M. A., Mauk, J. L., & Simpson, M. P. (2011). Quantifying metasomatism in epithermal Au-Ag deposits: A case study from the Waitekauri area, New Zealand. *Economic Geology*, *106*(6), 999-1030.

Boyle, R. W., & Jonasson, I. R. (1973). The geochemistry of arsenic and its use as an indicator element in geochemical prospecting. *Journal of Geochemical Exploration*, *2*(3), 251-296.

Brathwaite, R. L., & Skinner, D. N. B. (1997). The Coromandel epithermal gold-silver province: A result of collision of the Northland and Colville volcanic arcs in northern New Zealand. 1997 New Zealand Minerals and Mining Conference, Publicity Units, Crown Minerals, Ministry of Commerce, Wellington, Proceedings, pp. 111-117.

Brathwaite, R. L., & Cargill, H. J., & Christie, A. B., & Swain, A. (2001). Lithological and spatial controls on the distribution of quartz veins in andesite- and rhyolite-hosted epithermal Au-Ag deposits of the Hauraki Goldfield, New Zealand. *Mineralium Deposita*, *36*, pp. 1-12.

Brathwaite, R. L., & Faure, K. (2002). The Waihi epithermal gold-silver-base metal sulfide-quartz vein system, New Zealand: Temperature and salinity controls on electrum and sulfide deposition. *Economic Geology*, *97*, pp. 269-290.

Brathwaite, R. L., Torckler, L. K., & Jones, P. K. (2006). The Martha Hill epithermal Au-Ag deposit, Waihi – geology and mining history. . *Geology and Exploration of New Zealand Mineral Deposits*. Australasian Institute of Mining and Metallurgy Monograph 25, pp. 171-178.

Briggs, R. M., Houghton, B. F., McWilliams, M. & Wilson, C. J. N. (2005). 40Ar/39Ar ages of silicic volcanic rocks in the Tauranga-Kaimai area, New Zealand: dating the transition between volcanism in the Coromandel Arc and the Taupo Volcanic Zone, *New Zealand Journal of Geology and Geophysics*, *48*(3), pp. 459-469.

Briggs, R. M., & Krippner, S. J. P. (2006). The control by caldera structures on epithermal Au-Ag mineralization and hydrothermal alteration at Kapowai, central Coromandel volcanic zone. . *Geology and Exploration of New Zealand Mineral Deposits*. Australasian Institute of Mining and Metallurgy Monograph 25, pp. 101-107.

Browne, P. R. L. (1978). Hydrothermal alteration in active geothermal fields. *Annual Review of Earth and Planetary Sciences, 6,* pp. 229-250.

Budyak, A. E., & Bryukhanova, N. N. (2012). Selenium, bismuth, and mercury in black shale-hosted gold deposits of different genetic types. *Geochemistry International*, *50*(9), 791-797.

Cas, R. A., & Wright, J. V. (1987). *Volcanic successions: modern and ancient*. Springer Science & Business Media.

Cas, R. A. F., Porritt, L., Pittari, A., & Hayman, P. C. (2009). A practical guide to terminology for kimerlite facies: A systematic progression from descriptive to genetic, including a pocket guide. *Lithos, 112*, 183-190.

Chang, Z., & Yang, Z. (2012). Evaluation of inter-instrument variations among short wavelength infrared (SWIR) devices. *Economic Geology, 107,* pp. 1479-1488.

Christie, A. B., & Brathwaite, R. L. (1997). Epithermal gold-silver deposits in New Zealand: a new wall poster. GNS Science; Christie, A. B., & Brathwaite, R. L. (1997). Mineral commodity report 14-gold. New Zealand Mining, 21, 21-40.

Christie, A. B., Rabone, S. D .C., Barker, R. G., & Merchant, R. J. (2006). Exploration of the Wharekirauponga epithermal Au-Ag deposit, Hauraki Goldfield. *Geology and Exploration of New Zealand Mineral Deposits*. Australasian Institute of Mining and Metallurgy Monograph 25, pp. 137-144.

Christie, A. B., & Barker, R. G. (2007). *Mineral resource assessment of the Northland region, New Zealand* (Vol. 2007). GNS Science.

Christie, A. B., Simpson, M. P., Brathwaite, R. L., Mauk. J. L., & Simmons, S. F. (2007). Epithermal Au-Ag and related deposits of the Hauraki Goldfield, Coromandel Volcanic Zone, New Zealand. *Economic Geology*, *102*, pp. 785-816.

Ciobanu, C. L., Cook, N. J., Pring, A., Brugger, J., Danyushevsky, L. V., & Shimizu, M. (2009). 'Invisible gold'in bismuth chalcogenides. *Geochimica et Cosmochimica Acta*, *73*(7), 1970-1999.

Clarke, D. S., & Govett, G. J. S. (1990). Southwest Pacific epithermal gold: a rock-geochemistry perspective. *Journal of Geochemical Exploration*, *35*(1), 225-240.

Clarke, D. S., Spörli, K. B., Smith, I. E. M., Locke, C. A., Kobe, H. W., Black, P.M., & Ballance, P.F. (1990). The geological setting of gold deposits in the Coromandel volcanic zone, New Zealand. Pacific Rim 90 Congress, 2nd, Queensland, Australia, May 9–13, 1990, Proceedings, pp. 337–349.

Coombs, D. S., Ellis, A. J., Fyfe, W. S., & Taylor, A. M. (1959). The zeolite facies, with comments on the interpretation of hydrothermal syntheses.*Geochimica et cosmochimica acta*, *17*(1), 53-107.

Corbett, G. (2002). Epithermal gold for explorationists. *AIG Journal – Applied geoscientific practive and research in Australia.*

Floyd, P. A., & Winchester, J. A. (1978). Identification and discrimination of altered and metamorphosed volcanic rocks using immobile elemetns. *Chemical Geology, 21*(3), 291-306.

Fuge, R., Andrews, M. J., & Johnson, C. C. (1986). Chlorine and iodine, potential pathfinder elements in exploration geochemistry. *Applied geochemistry, 1*(1), 111-116.

Gadsby, M. R., Spörli, K. B., & Clarke, D. S. (1990). Structural elements in epithermal gold deposits of the Coromandel peninsula, New Zealand. Australasian Institute of Mining and Metallurgy Annual Conferecne, Rotorua, Proceedings, pp. 145-151.

Gemmell, J. B. (2007). Hydrothermal alteration associated with the Gosowong epithermal Au-Ag deposit, Halmahera, Indonesia: Mineralogy, geochemistry, and exploration implications. *Economic Geology, 102*(5), 893-922.

Gill, J. B. (1981). *Orogenic andesites and plate tectonics*. New York;Berlin;: Springer-Verlag.

Gill, R. (2010). *Igneous rocks and processes: a practical guide*. John Wiley & Sons.

Hayward, B. W., Black, P. M., Smith, I. E. M., Ballance, P. F., Itaya, T., Doi, M., … Robertson, D.J. (2001). K-Ar ages of early Miocene arc-type volcanoes in northern New Zealand. *New Zealand Journal of Geology and Geophysics*, *44*(2), pp. 285-311.

Heald, P., Foley, N. K., & Hayba, D. O. (1987). Comparative anatomy of volcanic-hosted epithermal deposits; acid-sulfate and adularia-sericite types.*Economic Geology*, *82*(1), 1-26.

Hedenquist, J. W., & Browne, P. R. (1989). The evolution of the Waiotapu geothermal system, New Zealand, based on the chemical and isotopic composition of its fluids, minerals and rocks. *Geochimica et Cosmochimica Acta, 53*(9), 2235-2257.

Hedenquist, J. W., Arribas, A., & Gonzalez-Urien, E. (2000). Exploration for epithermal gold deposits. *Reviews in Economic Geology, 13*, 245-277.

Hochstein, M. P., & Balance, P. F. (1993). Hauraki rift: A young, active, intra-continental rift in a back-arc setting. In P. F. Balance (Ed.), *South Pacific Sedimentary Basins, Sedimentary Basins of the World 2* (pp. 295-305). Amsterdam; New York: Elsevier.

Hoskin, P. W. O., Wysoczanski, R. J., & Briggs, R. M. (1998). U-Pb age determination of 'lenticulite' (Owharoa Ignimbrite) at Waikino, Waihi Area, Coromandel peninsula, and implications. *Geological Society of New Zealand & New Zealand Geophysical Society Joint Annual Conference*, University of Canterbury, Christchurch, pp. 123.

Hume, T. M., & Nelson, C. S. (1982). *X-ray diffraction analytical procedures and some mineralogical characteristics for South Auckland region sediments and sedimentary rocks, with special reference to their clay fraction*. University of Waikato, Department of Earth Sciences.

Ikramuddin, M., Besse, L., & Nordstrom, P. M. (1986). Thallium in the Carlin-type gold deposits. *Applied Geochemistry*, *1*(4), 493-502.

Jerram, D. A., Cheadle, M. J., & Philpotts, A. R. (2003). Quantifying the building blocks of igneous rocks: are clustered crystal frameworks the foundation? *Journal of Petrology*, *44*(11), 2033-2051.

Jakeš, P., & WHITE, A. R. (1972). Major and trace element abundances in volcanic rocks of orogenic areas. *Geological Society of America Bulletin*, *83*(1), 29-40.

John, D. A. (2011). Epithermal gold-silver deposits of the Hauraki Goldfield, New Zealand: An introduction. *Economic Geology*, vol. 106, no. 6, pp. 915-919.

King, P. R. (2000). Tectonic reconstructions of New Zealand: 40 Ma to the Present, *New Zealand Journal of Geology and Geophysics*, *43*(4), pp. 611-638.

Kuşcu, G. G., & Floyd, P. A. (2001). Mineral compositional and textural evidence for magma mingling in the Saraykent volcanics. *Lithos*, *56*(2), 207-230.

Large, R. R., McPhie, J., Gemmell, J. B., Herrmann, W., & Davidson, G. J. (2001). The spectrum of ore deposit types, volcanic environments, alteration halos,

and related exploration vectors in submarine volcanic successions: some examples from Australia. *Economic Geology*, *96*(5), 913-938.

Le Maitre, R. W., Bateman, P., Dudek, A., Keller, J., Lameyre, M., Le Bas, M. J., … ZANETTIN, B. (1989). *A Classification of Igneous Rocks and a Glossary of Terms*. *Recommendations of the International Union of Geological Sciences Subcommission on the Systematics of Igneous Rocks. Blackwell Scientific Publications*. Oxford: Blackwell

Le Maitre, R. W., Streckeisen, A., Zanettin, B., Le Bas, M. J., Bonin, B., & Bateman, P. (Eds.). (2002). *Igneous rocks: a classification and glossary of terms: recommendations of the International Union of Geological Sciences Subcommission on the Systematics of Igneous Rocks*. Cambridge University Press.

Lindgren, W. (1933). Mineral deposits, 930 p. *New York and London, McGraw-HillBook Co*.

Macdonald, E. (2007). *Handbook of gold exploration and evaluation*. Elsevier.

Mauk, J. L., & Hall, C. M. (2004). $^{40}Ar/^{39}Ar$ ages of adularia from the Golden Cross, Neavesville, and Komata epithermal deposits, Hauraki Goldfield, New Zealand. *New Zealand Jornal of Geology and Geophysics*, *47*, pp. 227-231.

Mauk, J. L., & Simpson, M. P. (2007). Geochemistry and stable isotope composition of altered rocks at the Golden Cross epithermal Au-Ag deposit, New Zealand. *Economic Geology*, *102*(5), 841-871.

Mauk, J. L., Hall, C. M., Chesley, J. T., & Barra, F. (2011). Punctuated evolution of a large epithermal province: The Hauraki Goldfield, New Zealand. *Economic Geology*, *106*, pp. 921-943.

McPhie, J., Doyle, M., Allen, R. L., & Allen, R. (1993). *Volcanic textures: A guide to the interpretation of textures in volcanic rocks*. CODES-University of Tasmania.

Moore, D. M. & Reynolds, R. C. (1997). *X-Ray diffraction and the identification and analysis of clay minerals* (2nd ed.).Oxford; New York: Oxford University Press.

Morrell, A. E., Locke, C. A., Cassidy, J., & Mauk, J. L. (2011). Geophysical characteristics of adularia-sericite epithermal gold-silver deposits in the Waihi-Waitekauri region, New Zealand. *Economic Geology*, *106*(6), 1031-1041.

Mortimer, N., Gans, P. B., Palin, J. M., Meffre, S., Herzer, R. H., & Skinner, D. N. B. (2010). Location and migration of Miocene-Quaternary volcanic arcs in the SW Pacific region. *Journal of Volcanology and Geothermal Research*, *190*, pp. 1-10.

Müller, A., Breiter, K., Seltmann, R., & Pécskay, Z. (2005). Quartz and feldspar zoning in the eastern Erzgebirge volcano-plutonic complex (Germany, Czech Republic): evidence of multiple magma mixing. *Lithos*, *80*(1), 201-227.

Parker, R. J., & Nicholson, K. (1990). Arsenic in geothermal sinters: determination and implications for mineral exploration. In *12th NZ Geothermal Workshop, Auckland University, Auckland* (pp. 35-39).

Pearce, J. A., & Cann, J. R. (1973). Tectonic setting of basic volcanic rocks determined using trace element analyses. *Earth and Planetary Letters, 19*(2), 290-300.

Pearce, J. (1996). A user's guide to basalt discrimination diagrams. In Wyman, D. A., (Eds.), Trace element geochemistry of volcanic rocks: Applications for massive sulphide exploration. Geological Association of Canada, Short Course Notes, 12, pp. 79-113.

Poppe, L. J., Paskevich, V. F., Hathaway, J. C., & Blackwood, D. S. (2001). A laboratory manual for X-ray powder diffraction. *US Geological Survey Open-File Report*, *1*(041), 1-88.

Rollinson, H. (1993). *Using geochemical data: Evaluation, presentation, interpretation.* Harlow, Essex, England; New York: Longman Scientific & Technical.

Shah, M. T., Ikramuddin, M., & Shervais, J. W. (1994). Behaviour of Tl relative to K, Rb, Sr and Ba in mineralized and unmineralized metavolcanics from the Dir area, northern Pakistan. *Mineralium Deposita*, *29*(5), 422-426.

Simmons, S. F., White, N. C., & John, D. A. (2005). Geological characteristics of epithermal precious and base metal deposits. *Economic Geology 100th anniversary volume*, *29*, 485-522.

Simpson, M. P., & Mauk, J. L. (2000). Geochemistry of wall rock alteration at the Golden Cross deposit, New Zealand: New Zealand Minerals and Mining Conference, 2000. In *Proceedings* (pp. 197-208).

Simpson, M. P., Mauk, J. L., & Simmons, S. F. (2001). Hydrothermal alteration and hydrologic evolution of the Golden Cross epithermal Au-Ag deposit, New Zealand. *Economic Geology*, *96*(4), 773-796.

Simpson, M.P., Mauk, J.L., Bowyer, D., & Worland, R.J. (2006). Alteration mineral studies of an epithermal prospect and a geothermal field using the TerraSpec. In Australasian Institute of Mining and Metallurgy, *39th NZ Branch annual conference*. p. 247–256. (2006).

Simpson, M. P., & Mauk, J. L. (2007). The Favona epithermal gold-silver deposit, Waihi, New Zealand. *Economic Geology*, *102*, pp. 817-839.

Simpson, M.P., Rae, A.J., Ganefianto, N., & Sepulveda, F. (2013). Short wavelength infrared (SWIR) spectral characterisation of smectite, illite-smectite and illite for geothermal fields of the Taupo Volcanic Zone, New Zealand. In *35th New Zealand Geothermal Workshop proceedings. 35th New Zealand Geothermal Workshop, Rotorua, New Zealand* (pp. 17-20).

Simpson, M. P., Palinkas, S. S., Mauk, J. L., & Bodnar, R. J. (2015). Fluid inclusion chemistry of adularia-sericite epithermal Au-Ag deposits of the southern Hauraki Goldfield, New Zealand. *Economic Geology*, *110*(3), 763-786.

Skinner, D. N. B. (1986). Neogene Volcanism of the Hauraki Volcanic Region', in I. E. M. Smith (ed.), *Late Cenozoic Volcanism in New Zealand*, The Royal Society of New Zealand, Wellington, pp. 21-47.

Spörli, K. B., Begbie, M. J., Irwin, M. R., & Rowland, J. V. (2006). Structural processes and tectonic controls on the epithermal Au-Ag deposits of the Hauraki Goldfield. *Geology and Exploration of New Zealand Mineral Deposits*. Australasian Institute of Mining and Metallurgy Monograph 25, pp. 85-94.

Spörli, K. B., & Cargill, H. (2011). Structural evolution of a world-class epithermal orebody: The Martha hill deposit, Waihi, New Zealand. *Economic Geology*, *106*(6), pp. 975-998.

Stanley, C. R., & Madeisky, H. E. (1994). Lithogeochemical exploration for hydrothermal ore deposits using Pearce element ratio analysis. In Lentz, D (Eds.), *Alteration and alteration processes associated with ore forming systems, Geological Association of Canada Short Course Notes*, (11), 193-211.

Stanley, C. R., & Madeisky, H. E. (1996). Lithogeochemical exploration for metasomatic zones associated with hydrothermal mineral deposits using Pearce Element Ratio Analysis. *Short Course Notes on Pearce Element Ratio Analysis*.

Stewart, D. C. (1975). Crystal clots in calc-alkaline andesites as breakdown products of high-Al amphiboles. *Contributions to Mineralogy and Petrology*, *53*(3), 195-204.

Streck, M. J., Dungan, M. A., Bussy, F., & Malavassi, E. (2005). Mineral inventory of continuously erupting basaltic andesites at Arenal volcano, Costa Rica: implications for interpreting monotonous, crystal-rich, mafic arc stratigraphies. *Journal of Volcanology and Geothermal Research*, *140*(1), 133-155.

Stuart, A. G. J., Simpson, M. P., Mauk, J. L., & Stevens, M. (n.d.). Geology and alteration mineralogy of the Karangahake adularia-sericite epithermal deposit, Hauraki Goldfield, New Zealand.

Torckler, L. K., McKay, D., & Hobbins, J. (2006). Geology and exploration of the Favona Au-Ag deposit, Waihi, Hauraki Goldfield. *Geology and Exploration*

of New Zealand Mineral Deposits. Monograph 25. Australasian Institute of Mining and Metallurgy.

Waight, T. E., Price, R. C., Stewart, R. B., Smith, I. E. M., & Gamble, J. (1999). Stratigraphy and geochemistry of the Turoa area, with implications for andesite petrogenesis at Mt Ruapehu, Taupo Volcanic Zone, New Zealand. *New Zealand Journal of Geology and Geophysics*, *42*(4), 513-532.

Walker, G. P. L., Huntingdon, A. T., Sanders, A. T., & Dinsdale, J. L. (1973). Lengths of lava flows [and discussion]. *Philosophical Transactions of the Royal Society of London A: Mathematical, Physical and Engineering Sciences*, *274*(1238), 107-118.

Warren, I., Simmons, S. F., & Mauk, J. L. (2007). Whole-rock geochemical techniques for evaluating hydrothermal alteration, mass changes, and compositional gradients associated with epithermal Au-Ag mineralization.*Economic Geology*, *102*(5), 923-948.

White, N. C., & Hedenquist, J. W. (1990). Epithermal environments and styles of mineralization: variations and their causes, and guidelines for exploration. *Journal of Geochemical Exploration*, *36*(1), 445-474.

White, N. C., & Hedenquist, J. W. (1995). Epithermal gold deposits: styles, characteristics and exploration. *SEG newsletter*, *23*(1), 9-13.

Winchester, J. A., & Floyd, P. A. (1977). Geochemical discrimination of different magma series and their differentiation products using immobile elements. *Chemical Geology*, *20*, 325-343.

Appendices

Appendix A: Stratigraphic logs

Appendix B: XRD processed spectra

Appendix C: X-ray-fluorescence results

Appendix A – Stratigraphic logs

Drill hole UW462 stratigraphic logs

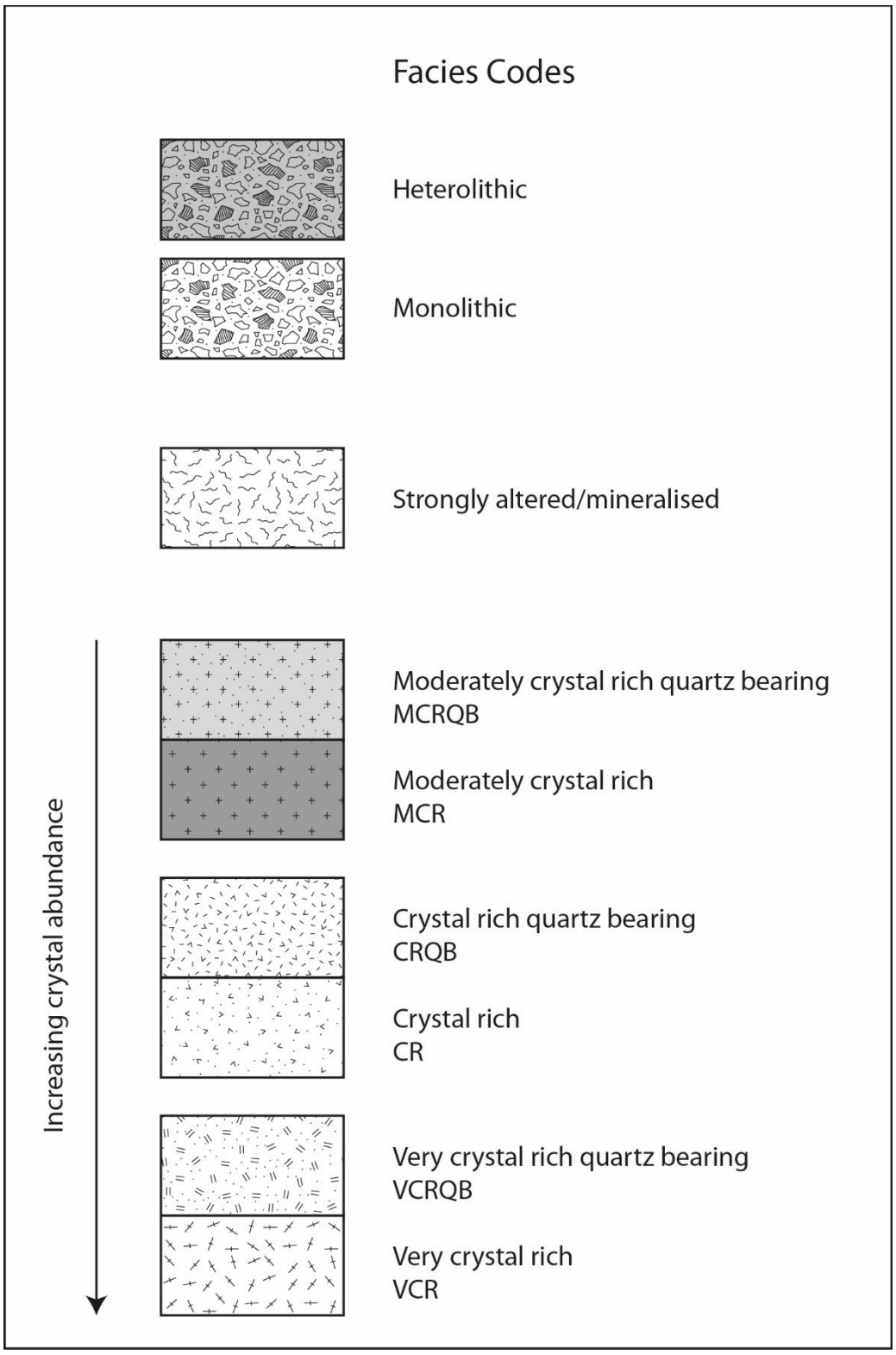

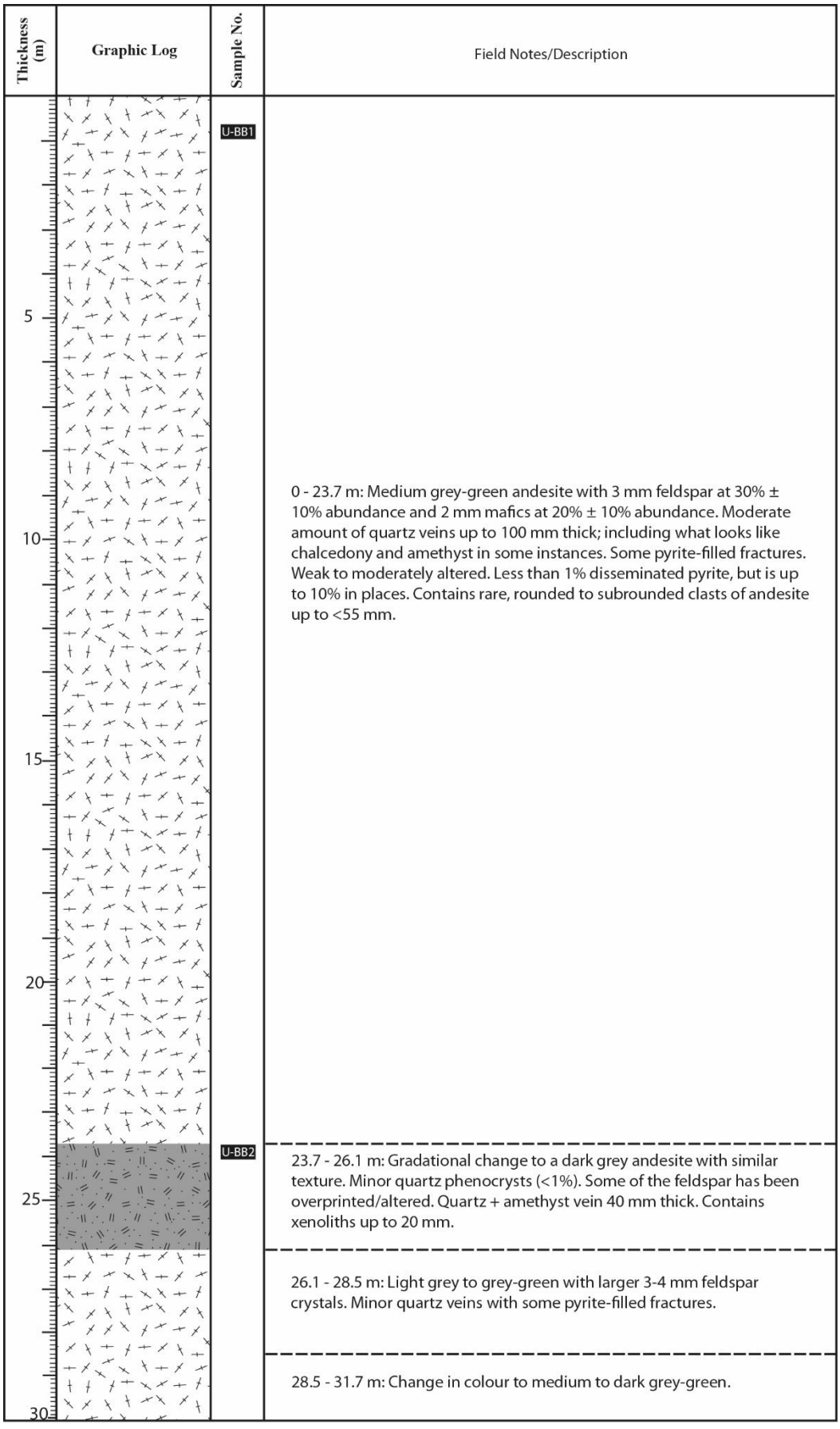
Thickness (m)
Graphic Log
Sample No.
Field Notes/Description
U-BB1
U-BB2
5
10
15
20
25
30
0 - 23.7 m: Medium grey-green andesite with 3 mm feldspar at 30% ± 10% abundance and 2 mm mafics at 20% ± 10% abundance. Moderate amount of quartz veins up to 100 mm thick; including what looks like chalcedony and amethyst in some instances. Some pyrite-filled fractures. Weak to moderately altered. Less than 1% disseminated pyrite, but is up to 10% in places. Contains rare, rounded to subrounded clasts of andesite up to <55 mm.
23.7 - 26.1 m: Gradational change to a dark grey andesite with similar texture. Minor quartz phenocrysts (<1%). Some of the feldspar has been overprinted/altered. Quartz + amethyst vein 40 mm thick. Contains xenoliths up to 20 mm.
26.1 - 28.5 m: Light grey to grey-green with larger 3-4 mm feldspar crystals. Minor quartz veins with some pyrite-filled fractures.
28.5 - 31.7 m: Change in colour to medium to dark grey-green.

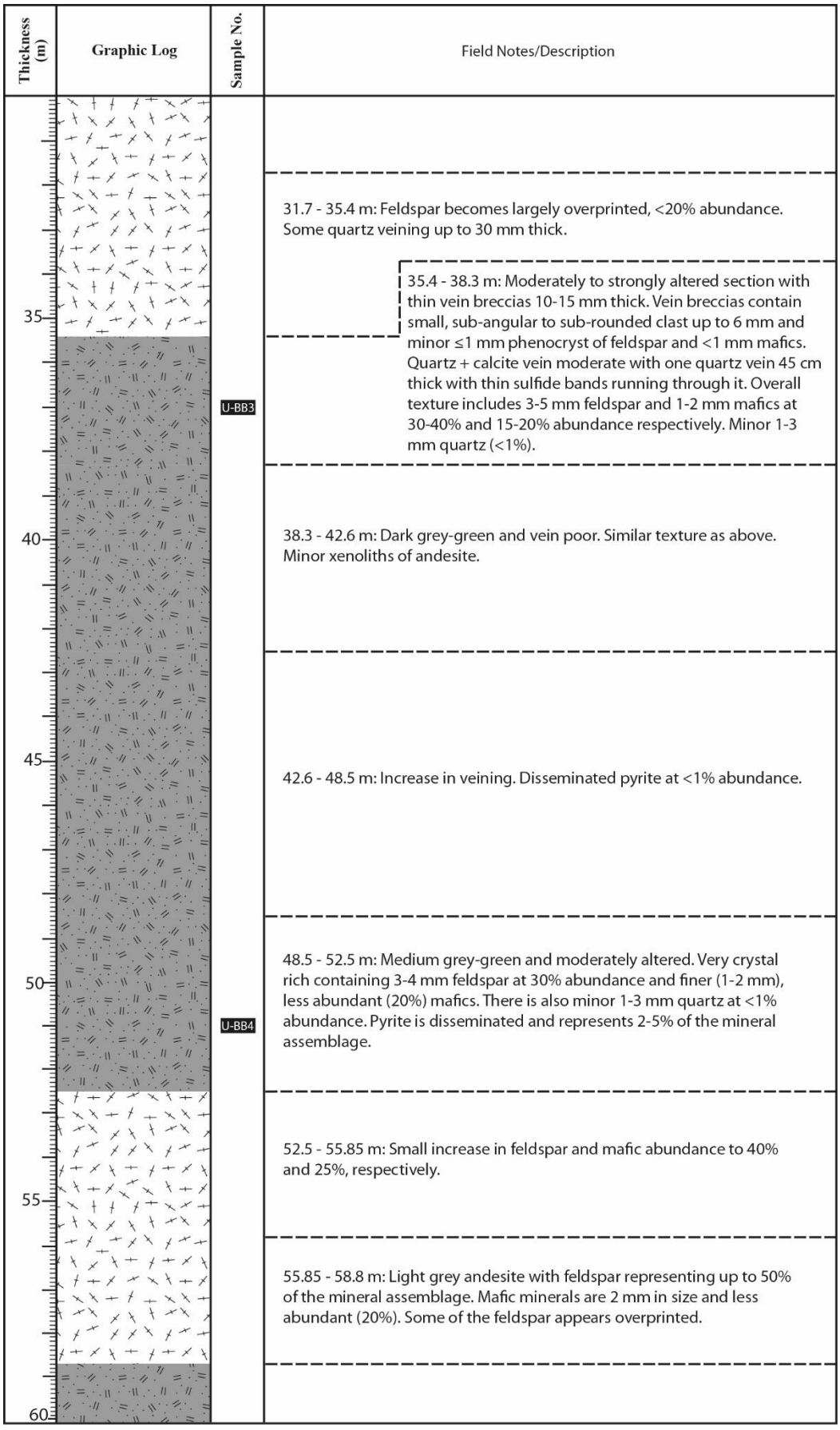
Thickness (m)
Graphic Log
Sample No.
Field Notes/Description
35
40
45
50
55
60
U-BB3
U-BB4
31.7 - 35.4 m: Feldspar becomes largely overprinted, <20% abundance. Some quartz veining up to 30 mm thick.
35.4 - 38.3 m: Moderately to strongly altered section with thin vein breccias 10-15 mm thick. Vein breccias contain small, sub-angular to sub-rounded clast up to 6 mm and minor ≤1 mm phenocryst of feldspar and <1 mm mafics. Quartz + calcite vein moderate with one quartz vein 45 cm thick with thin sulfide bands running through it. Overall texture includes 3-5 mm feldspar and 1-2 mm mafics at 30-40% and 15-20% abundance respectively. Minor 1-3 mm quartz (<1%).
38.3 - 42.6 m: Dark grey-green and vein poor. Similar texture as above. Minor xenoliths of andesite.
42.6 - 48.5 m: Increase in veining. Disseminated pyrite at <1% abundance.
48.5 - 52.5 m: Medium grey-green and moderately altered. Very crystal rich containing 3-4 mm feldspar at 30% abundance and finer (1-2 mm), less abundant (20%) mafics. There is also minor 1-3 mm quartz at <1% abundance. Pyrite is disseminated and represents 2-5% of the mineral assemblage.
52.5 - 55.85 m: Small increase in feldspar and mafic abundance to 40% and 25%, respectively.
55.85 - 58.8 m: Light grey andesite with feldspar representing up to 50% of the mineral assemblage. Mafic minerals are 2 mm in size and less abundant (20%). Some of the feldspar appears overprinted.

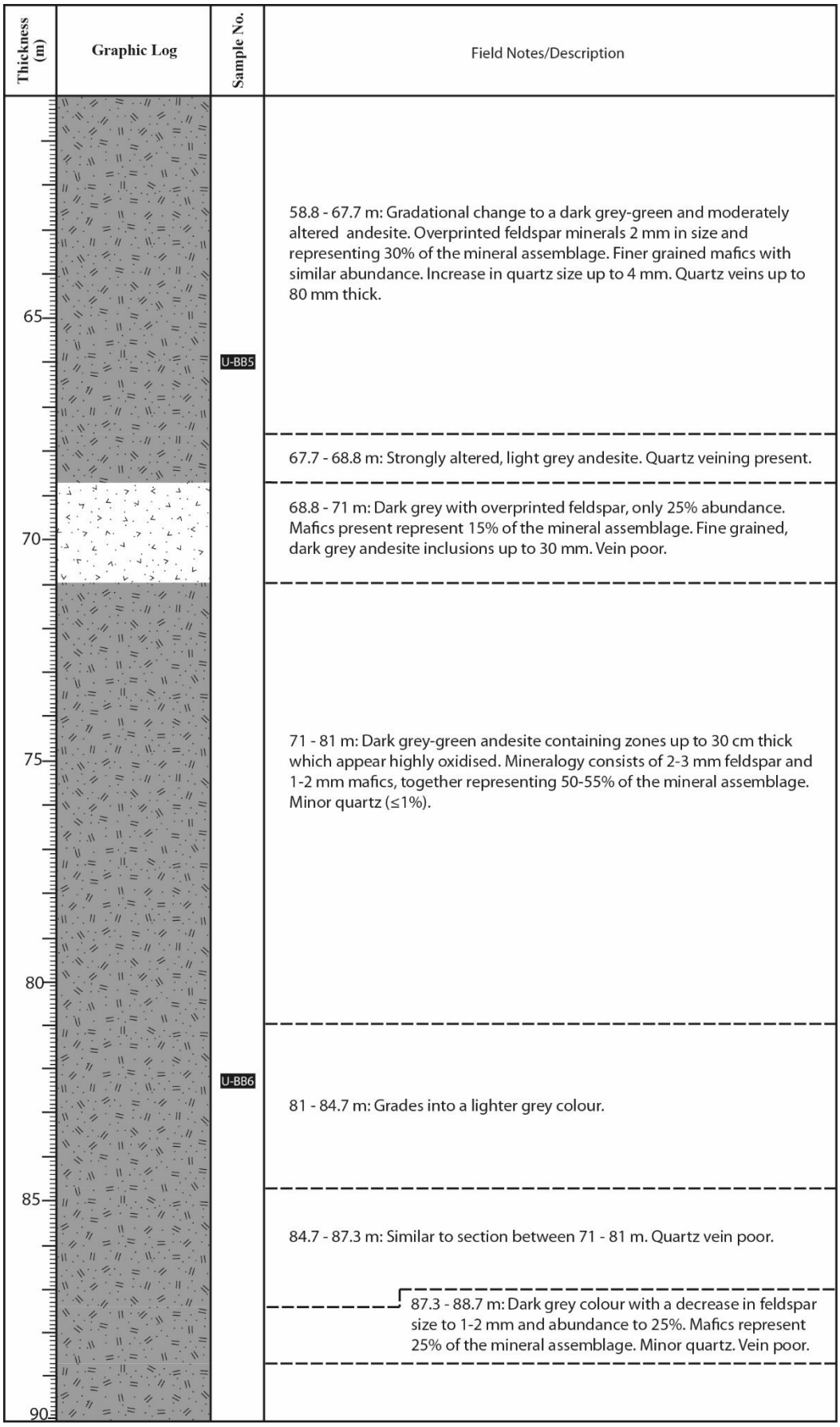
Thickness (m)
Graphic Log
Sample No.
Field Notes/Description
65
70
75
80
85
90
U-BB5
U-BB6
58.8 - 67.7 m: Gradational change to a dark grey-green and moderately altered andesite. Overprinted feldspar minerals 2 mm in size and representing 30% of the mineral assemblage. Finer grained mafics with similar abundance. Increase in quartz size up to 4 mm. Quartz veins up to 80 mm thick.
67.7 - 68.8 m: Strongly altered, light grey andesite. Quartz veining present.
68.8 - 71 m: Dark grey with overprinted feldspar, only 25% abundance. Mafics present represent 15% of the mineral assemblage. Fine grained, dark grey andesite inclusions up to 30 mm. Vein poor.
71 - 81 m: Dark grey-green andesite containing zones up to 30 cm thick which appear highly oxidised. Mineralogy consists of 2-3 mm feldspar and 1-2 mm mafics, together representing 50-55% of the mineral assemblage. Minor quartz (≤1%).
81 - 84.7 m: Grades into a lighter grey colour.
84.7 - 87.3 m: Similar to section between 71 - 81 m. Quartz vein poor.
87.3 - 88.7 m: Dark grey colour with a decrease in feldspar size to 1-2 mm and abundance to 25%. Mafics represent 25% of the mineral assemblage. Minor quartz. Vein poor.

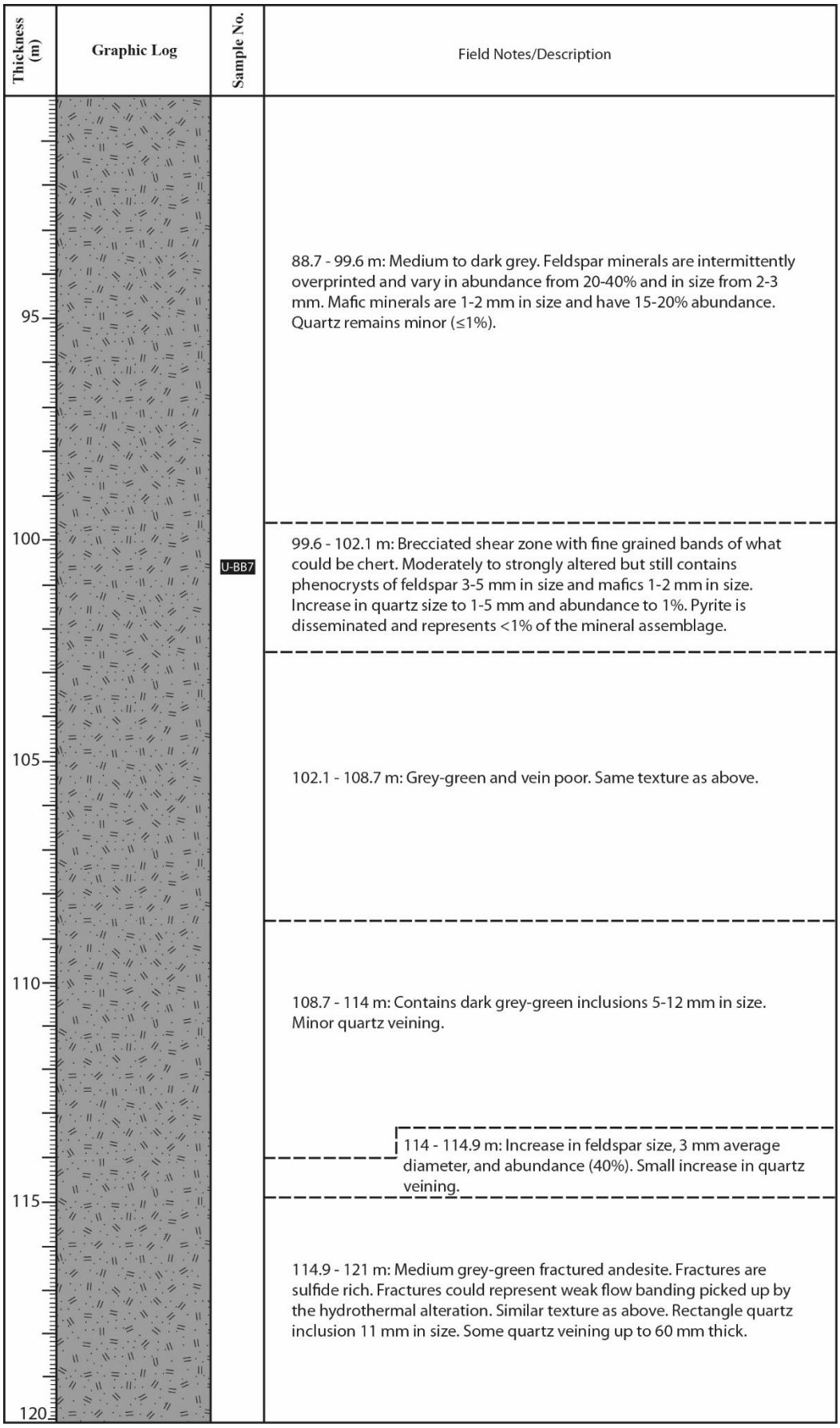
Thickness (m)
Graphic Log
Sample No.
Field Notes/Description
95
100
105
110
115
120
U-BB7
88.7 - 99.6 m: Medium to dark grey. Feldspar minerals are intermittently overprinted and vary in abundance from 20-40% and in size from 2-3 mm. Mafic minerals are 1-2 mm in size and have 15-20% abundance. Quartz remains minor (≤1%).
99.6 - 102.1 m: Brecciated shear zone with fine grained bands of what could be chert. Moderately to strongly altered but still contains phenocrysts of feldspar 3-5 mm in size and mafics 1-2 mm in size. Increase in quartz size to 1-5 mm and abundance to 1%. Pyrite is disseminated and represents <1% of the mineral assemblage.
102.1 - 108.7 m: Grey-green and vein poor. Same texture as above.
108.7 - 114 m: Contains dark grey-green inclusions 5-12 mm in size. Minor quartz veining.
114 - 114.9 m: Increase in feldspar size, 3 mm average diameter, and abundance (40%). Small increase in quartz veining.
114.9 - 121 m: Medium grey-green fractured andesite. Fractures are sulfide rich. Fractures could represent weak flow banding picked up by the hydrothermal alteration. Similar texture as above. Rectangle quartz inclusion 11 mm in size. Some quartz veining up to 60 mm thick.

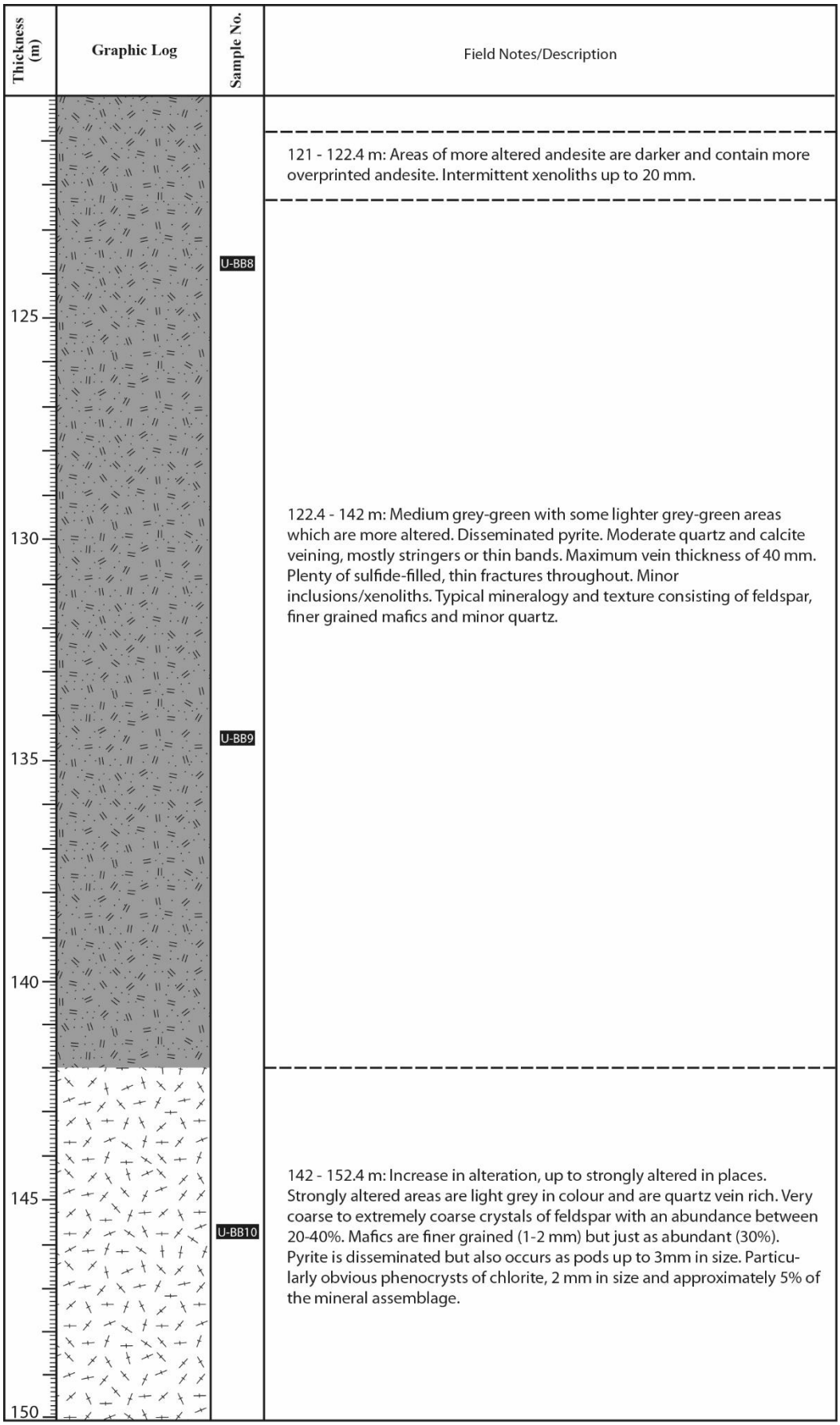
Thickness (m)
Graphic Log
Sample No.
Field Notes/Description
121 - 122.4 m: Areas of more altered andesite are darker and contain more overprinted andesite. Intermittent xenoliths up to 20 mm.
U-BB8
125
122.4 - 142 m: Medium grey-green with some lighter grey-green areas which are more altered. Disseminated pyrite. Moderate quartz and calcite veining, mostly stringers or thin bands. Maximum vein thickness of 40 mm. Plenty of sulfide-filled, thin fractures throughout. Minor inclusions/xenoliths. Typical mineralogy and texture consisting of feldspar, finer grained mafics and minor quartz.
130
U-BB9
135
140
142 - 152.4 m: Increase in alteration, up to strongly altered in places. Strongly altered areas are light grey in colour and are quartz vein rich. Very coarse to extremely coarse crystals of feldspar with an abundance between 20-40%. Mafics are finer grained (1-2 mm) but just as abundant (30%). Pyrite is disseminated but also occurs as pods up to 3mm in size. Particularly obvious phenocrysts of chlorite, 2 mm in size and approximately 5% of the mineral assemblage.
145
U-BB10
150

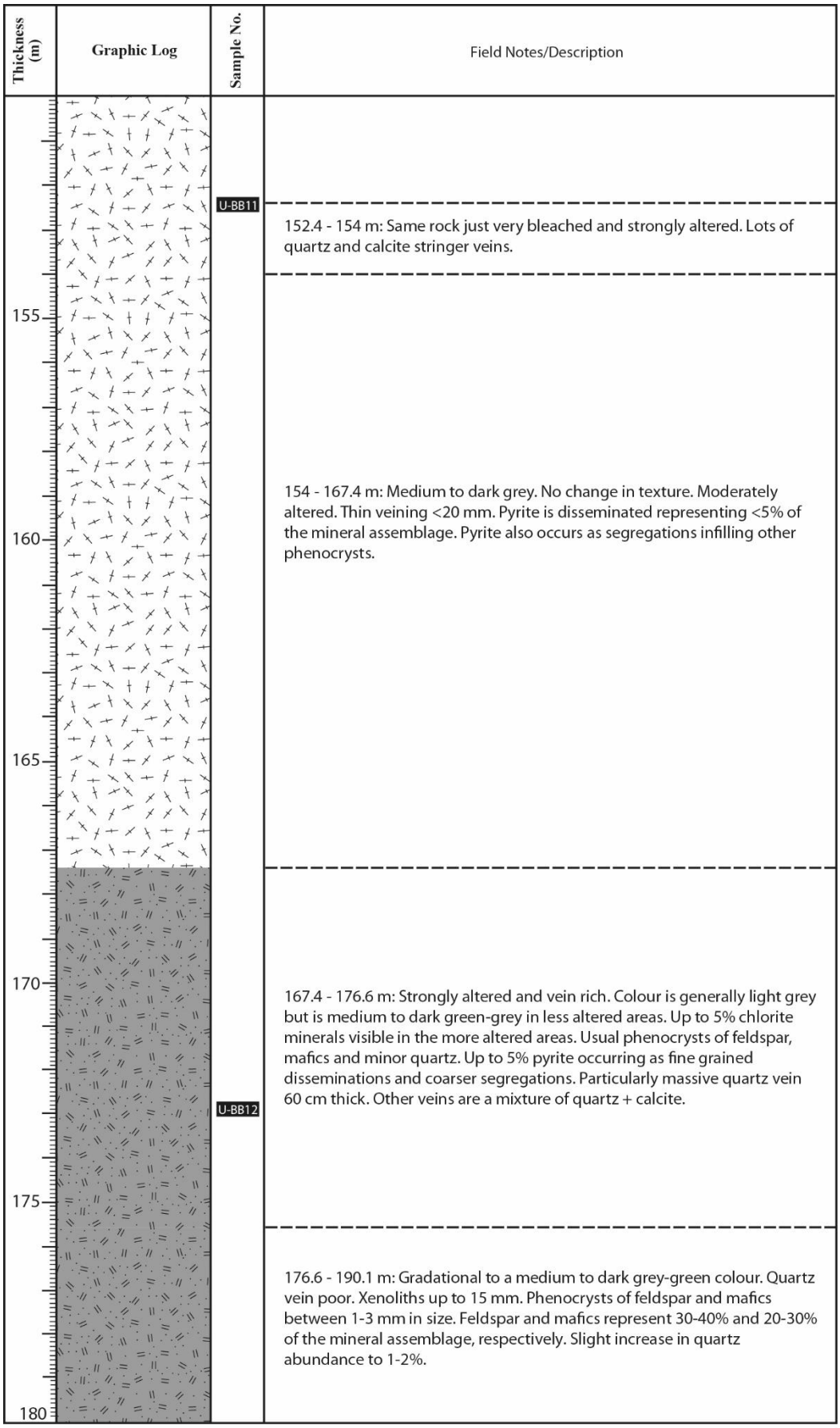
Thickness (m)
Graphic Log
Sample No.
Field Notes/Description
U-BB11
152.4 - 154 m: Same rock just very bleached and strongly altered. Lots of quartz and calcite stringer veins.
154 - 167.4 m: Medium to dark grey. No change in texture. Moderately altered. Thin veining <20 mm. Pyrite is disseminated representing <5% of the mineral assemblage. Pyrite also occurs as segregations infilling other phenocrysts.
167.4 - 176.6 m: Strongly altered and vein rich. Colour is generally light grey but is medium to dark green-grey in less altered areas. Up to 5% chlorite minerals visible in the more altered areas. Usual phenocrysts of feldspar, mafics and minor quartz. Up to 5% pyrite occurring as fine grained disseminations and coarser segregations. Particularly massive quartz vein 60 cm thick. Other veins are a mixture of quartz + calcite.
U-BB12
176.6 - 190.1 m: Gradational to a medium to dark grey-green colour. Quartz vein poor. Xenoliths up to 15 mm. Phenocrysts of feldspar and mafics between 1-3 mm in size. Feldspar and mafics represent 30-40% and 20-30% of the mineral assemblage, respectively. Slight increase in quartz abundance to 1-2%.
155
160
165
170
175
180

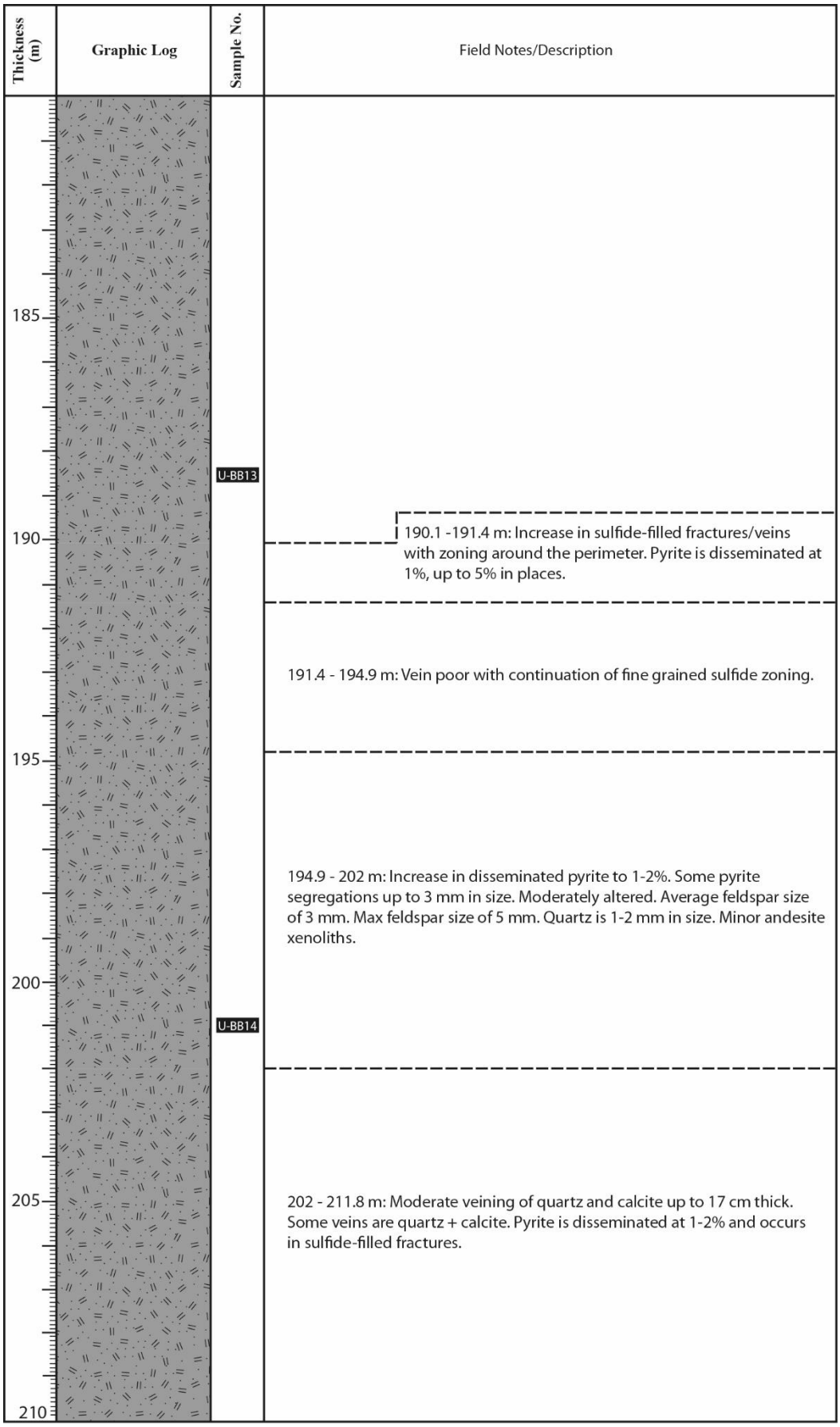
Thickness (m)
Graphic Log
Sample No.
Field Notes/Description
185
190
195
200
205
210
U-BB13
U-BB14
190.1 -191.4 m: Increase in sulfide-filled fractures/veins with zoning around the perimeter. Pyrite is disseminated at 1%, up to 5% in places.
191.4 - 194.9 m: Vein poor with continuation of fine grained sulfide zoning.
194.9 - 202 m: Increase in disseminated pyrite to 1-2%. Some pyrite segregations up to 3 mm in size. Moderately altered. Average feldspar size of 3 mm. Max feldspar size of 5 mm. Quartz is 1-2 mm in size. Minor andesite xenoliths.
202 - 211.8 m: Moderate veining of quartz and calcite up to 17 cm thick. Some veins are quartz + calcite. Pyrite is disseminated at 1-2% and occurs in sulfide-filled fractures.

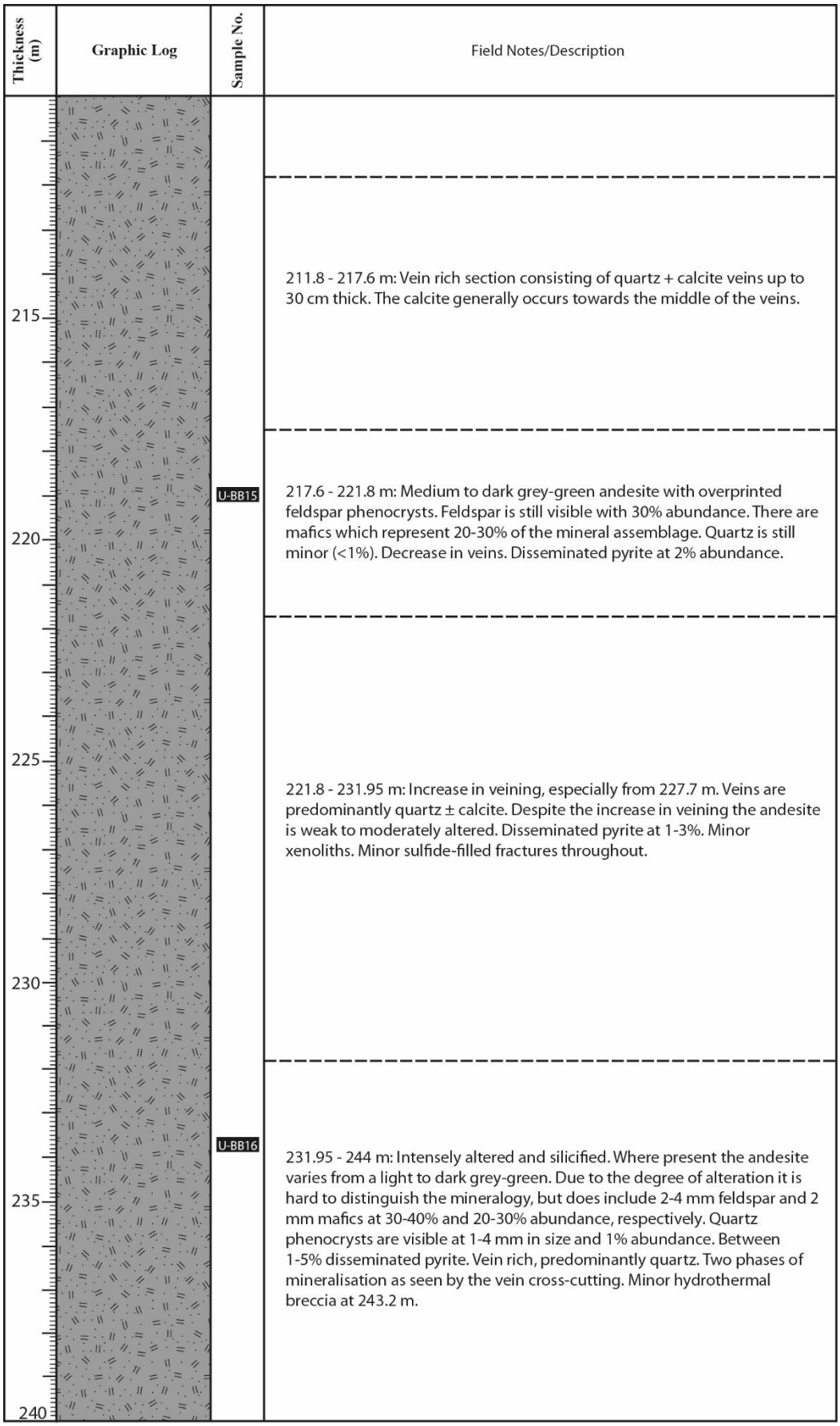
Thickness (m)
Graphic Log
Sample No.
Field Notes/Description
215
220
225
230
235
240
U-BB15
U-BB16
211.8 - 217.6 m: Vein rich section consisting of quartz + calcite veins up to 30 cm thick. The calcite generally occurs towards the middle of the veins.
217.6 - 221.8 m: Medium to dark grey-green andesite with overprinted feldspar phenocrysts. Feldspar is still visible with 30% abundance. There are mafics which represent 20-30% of the mineral assemblage. Quartz is still minor (<1%). Decrease in veins. Disseminated pyrite at 2% abundance.
221.8 - 231.95 m: Increase in veining, especially from 227.7 m. Veins are predominantly quartz ± calcite. Despite the increase in veining the andesite is weak to moderately altered. Disseminated pyrite at 1-3%. Minor xenoliths. Minor sulfide-filled fractures throughout.
231.95 - 244 m: Intensely altered and silicified. Where present the andesite varies from a light to dark grey-green. Due to the degree of alteration it is hard to distinguish the mineralogy, but does include 2-4 mm feldspar and 2 mm mafics at 30-40% and 20-30% abundance, respectively. Quartz phenocrysts are visible at 1-4 mm in size and 1% abundance. Between 1-5% disseminated pyrite. Vein rich, predominantly quartz. Two phases of mineralisation as seen by the vein cross-cutting. Minor hydrothermal breccia at 243.2 m.

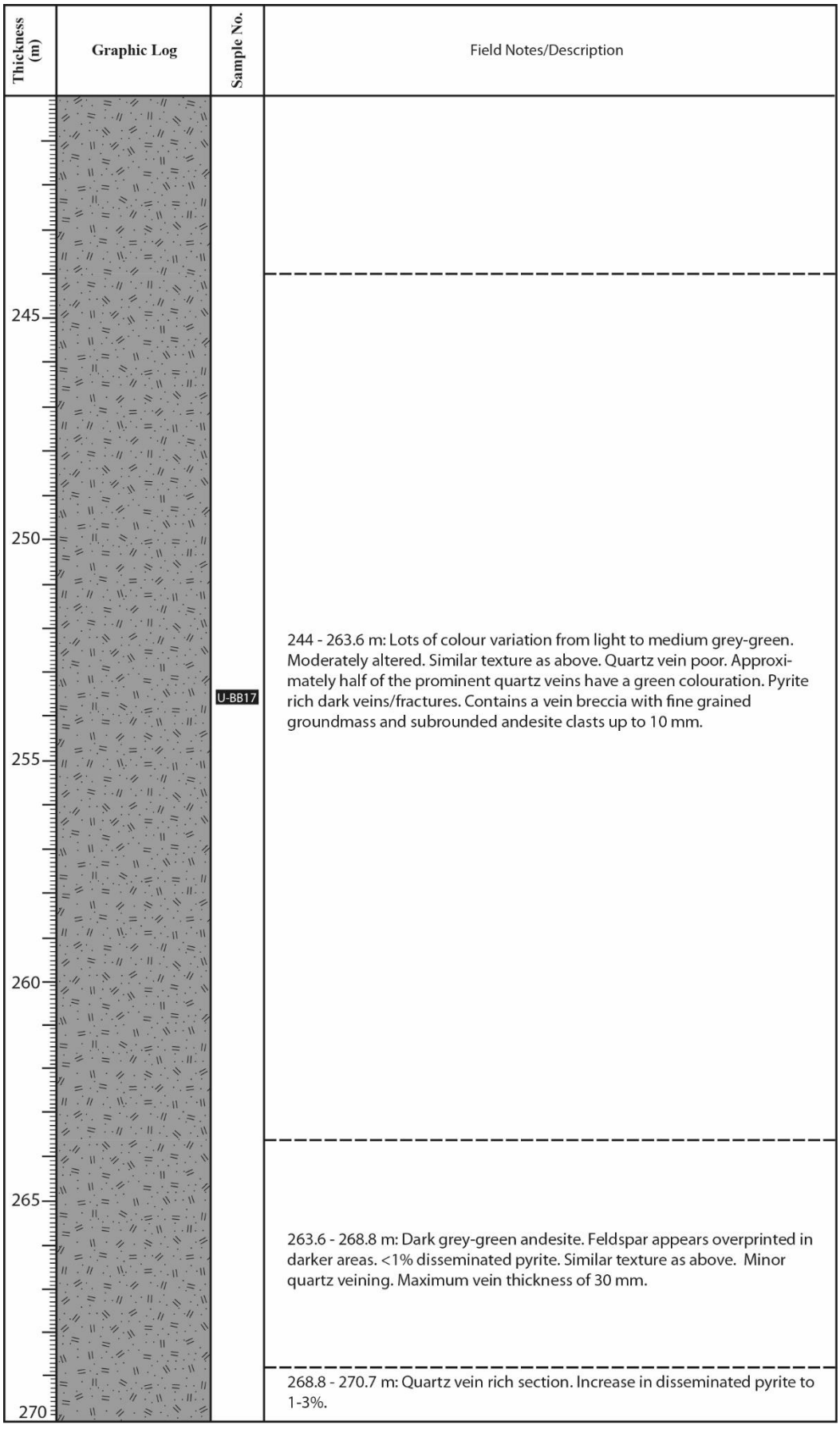
Thickness (m)
Graphic Log
Sample No.
Field Notes/Description
245
250
255
260
265
270
U-BB17
244 - 263.6 m: Lots of colour variation from light to medium grey-green. Moderately altered. Similar texture as above. Quartz vein poor. Approximately half of the prominent quartz veins have a green colouration. Pyrite rich dark veins/fractures. Contains a vein breccia with fine grained groundmass and subrounded andesite clasts up to 10 mm.
263.6 - 268.8 m: Dark grey-green andesite. Feldspar appears overprinted in darker areas. <1% disseminated pyrite. Similar texture as above. Minor quartz veining. Maximum vein thickness of 30 mm.
268.8 - 270.7 m: Quartz vein rich section. Increase in disseminated pyrite to 1-3%.

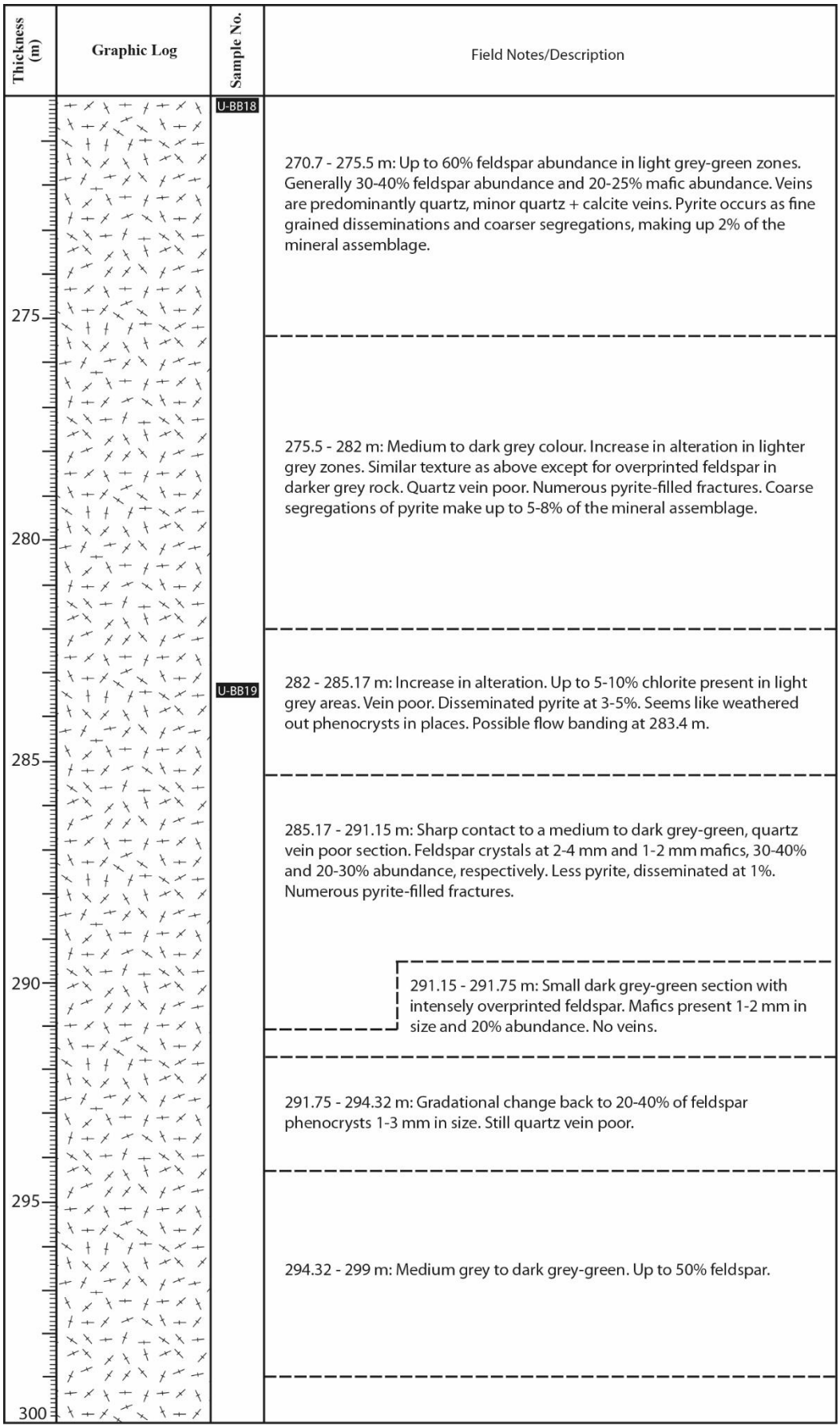
Thickness (m)
Graphic Log
Sample No.
Field Notes/Description
U-BB18
U-BB19
275
280
285
290
295
300
270.7 - 275.5 m: Up to 60% feldspar abundance in light grey-green zones. Generally 30-40% feldspar abundance and 20-25% mafic abundance. Veins are predominantly quartz, minor quartz + calcite veins. Pyrite occurs as fine grained disseminations and coarser segregations, making up 2% of the mineral assemblage.
275.5 - 282 m: Medium to dark grey colour. Increase in alteration in lighter grey zones. Similar texture as above except for overprinted feldspar in darker grey rock. Quartz vein poor. Numerous pyrite-filled fractures. Coarse segregations of pyrite make up to 5-8% of the mineral assemblage.
282 - 285.17 m: Increase in alteration. Up to 5-10% chlorite present in light grey areas. Vein poor. Disseminated pyrite at 3-5%. Seems like weathered out phenocrysts in places. Possible flow banding at 283.4 m.
285.17 - 291.15 m: Sharp contact to a medium to dark grey-green, quartz vein poor section. Feldspar crystals at 2-4 mm and 1-2 mm mafics, 30-40% and 20-30% abundance, respectively. Less pyrite, disseminated at 1%. Numerous pyrite-filled fractures.
291.15 - 291.75 m: Small dark grey-green section with intensely overprinted feldspar. Mafics present 1-2 mm in size and 20% abundance. No veins.
291.75 - 294.32 m: Gradational change back to 20-40% of feldspar phenocrysts 1-3 mm in size. Still quartz vein poor.
294.32 - 299 m: Medium grey to dark grey-green. Up to 50% feldspar.

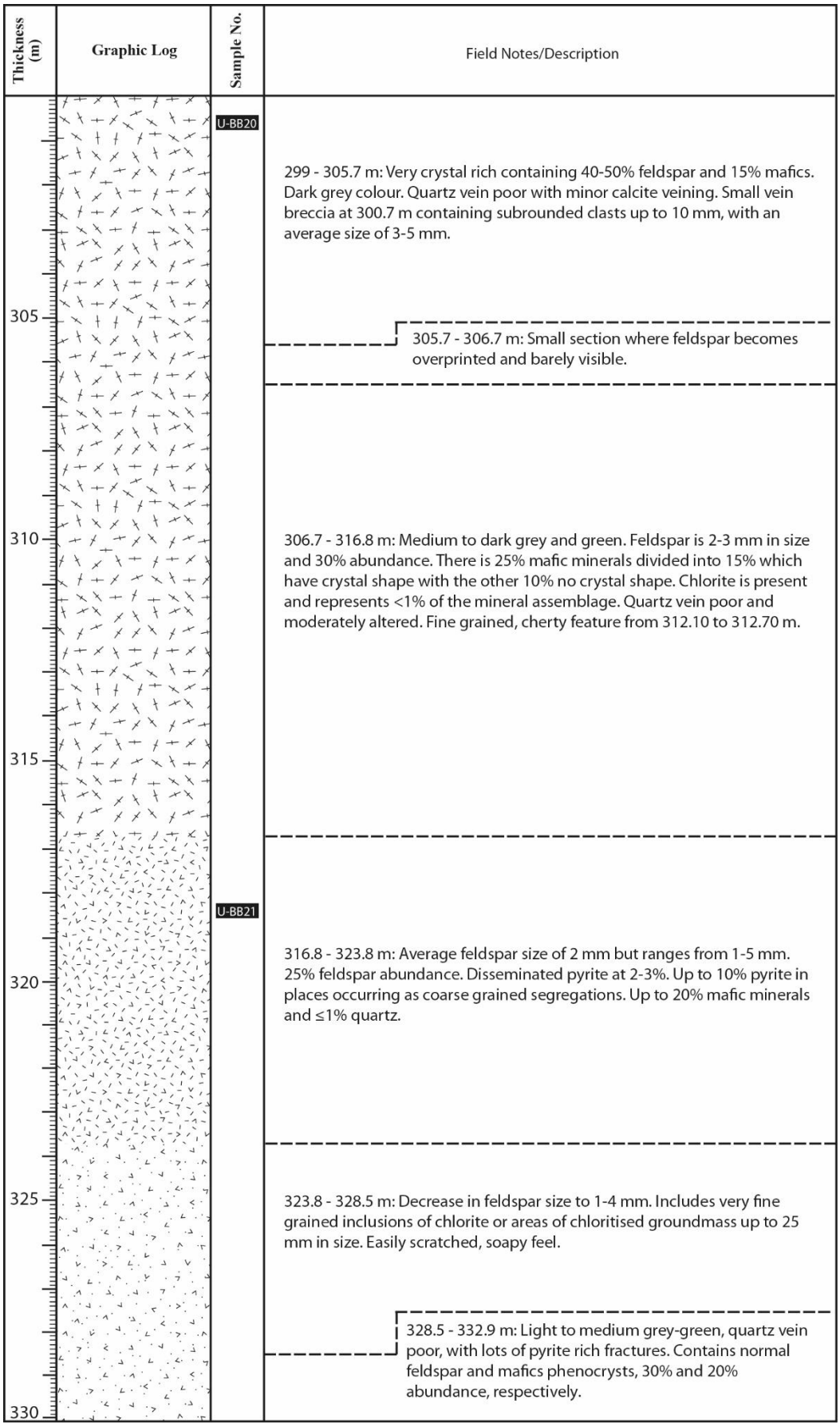
Thickness (m)
Graphic Log
Sample No.
Field Notes/Description
U-BB20
299 - 305.7 m: Very crystal rich containing 40-50% feldspar and 15% mafics. Dark grey colour. Quartz vein poor with minor calcite veining. Small vein breccia at 300.7 m containing subrounded clasts up to 10 mm, with an average size of 3-5 mm.
305
305.7 - 306.7 m: Small section where feldspar becomes overprinted and barely visible.
306.7 - 316.8 m: Medium to dark grey and green. Feldspar is 2-3 mm in size and 30% abundance. There is 25% mafic minerals divided into 15% which have crystal shape with the other 10% no crystal shape. Chlorite is present and represents <1% of the mineral assemblage. Quartz vein poor and moderately altered. Fine grained, cherty feature from 312.10 to 312.70 m.
310
315
U-BB21
316.8 - 323.8 m: Average feldspar size of 2 mm but ranges from 1-5 mm. 25% feldspar abundance. Disseminated pyrite at 2-3%. Up to 10% pyrite in places occurring as coarse grained segregations. Up to 20% mafic minerals and ≤1% quartz.
320
323.8 - 328.5 m: Decrease in feldspar size to 1-4 mm. Includes very fine grained inclusions of chlorite or areas of chloritised groundmass up to 25 mm in size. Easily scratched, soapy feel.
325
328.5 - 332.9 m: Light to medium grey-green, quartz vein poor, with lots of pyrite rich fractures. Contains normal feldspar and mafics phenocrysts, 30% and 20% abundance, respectively.
330

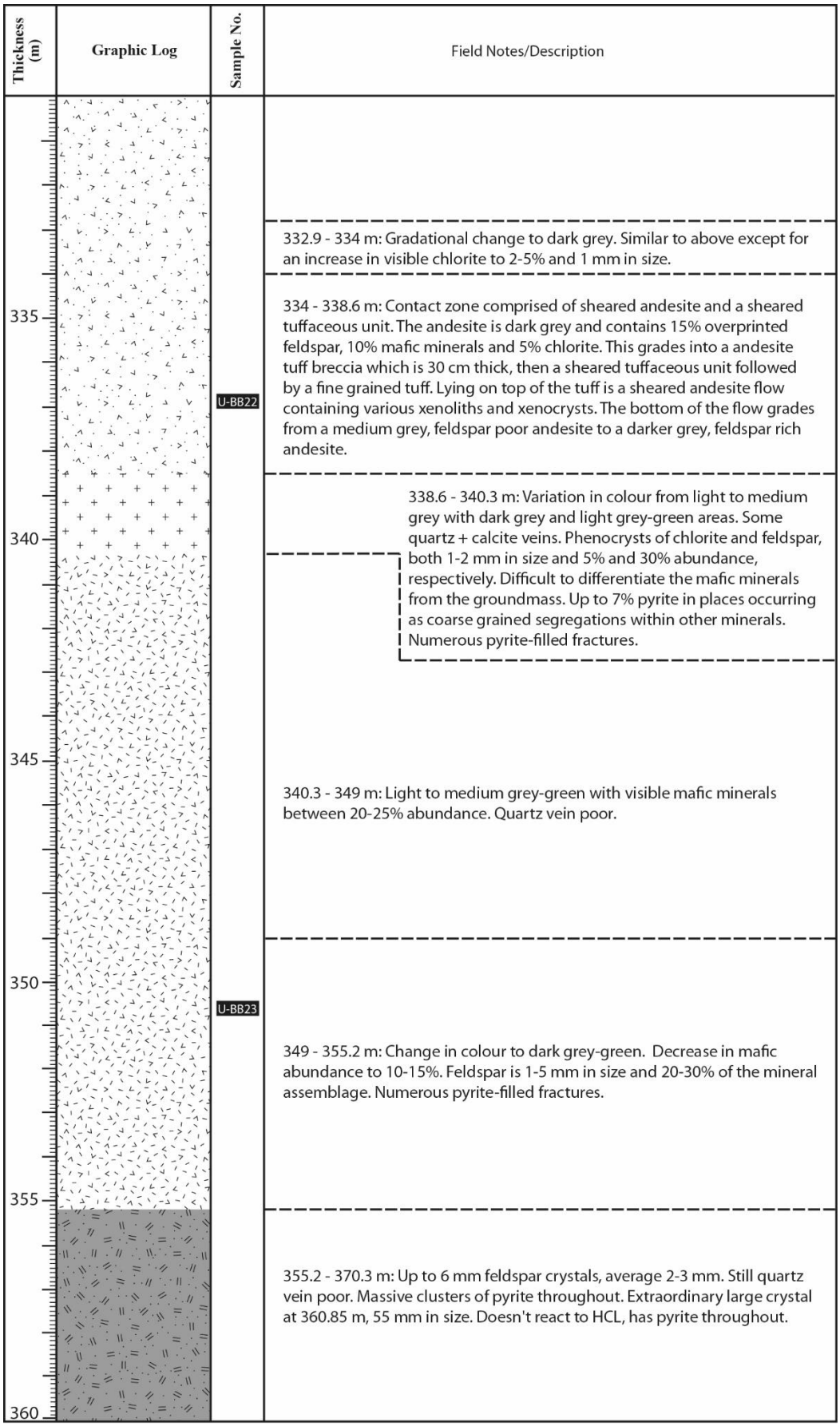
Thickness (m)
Graphic Log
Sample No.
Field Notes/Description
335
340
345
350
355
360
U-BB22
U-BB23
332.9 - 334 m: Gradational change to dark grey. Similar to above except for an increase in visible chlorite to 2-5% and 1 mm in size.
334 - 338.6 m: Contact zone comprised of sheared andesite and a sheared tuffaceous unit. The andesite is dark grey and contains 15% overprinted feldspar, 10% mafic minerals and 5% chlorite. This grades into a andesite tuff breccia which is 30 cm thick, then a sheared tuffaceous unit followed by a fine grained tuff. Lying on top of the tuff is a sheared andesite flow containing various xenoliths and xenocrysts. The bottom of the flow grades from a medium grey, feldspar poor andesite to a darker grey, feldspar rich andesite.
338.6 - 340.3 m: Variation in colour from light to medium grey with dark grey and light grey-green areas. Some quartz + calcite veins. Phenocrysts of chlorite and feldspar, both 1-2 mm in size and 5% and 30% abundance, respectively. Difficult to differentiate the mafic minerals from the groundmass. Up to 7% pyrite in places occurring as coarse grained segregations within other minerals. Numerous pyrite-filled fractures.
340.3 - 349 m: Light to medium grey-green with visible mafic minerals between 20-25% abundance. Quartz vein poor.
349 - 355.2 m: Change in colour to dark grey-green. Decrease in mafic abundance to 10-15%. Feldspar is 1-5 mm in size and 20-30% of the mineral assemblage. Numerous pyrite-filled fractures.
355.2 - 370.3 m: Up to 6 mm feldspar crystals, average 2-3 mm. Still quartz vein poor. Massive clusters of pyrite throughout. Extraordinary large crystal at 360.85 m, 55 mm in size. Doesn't react to HCL, has pyrite throughout.

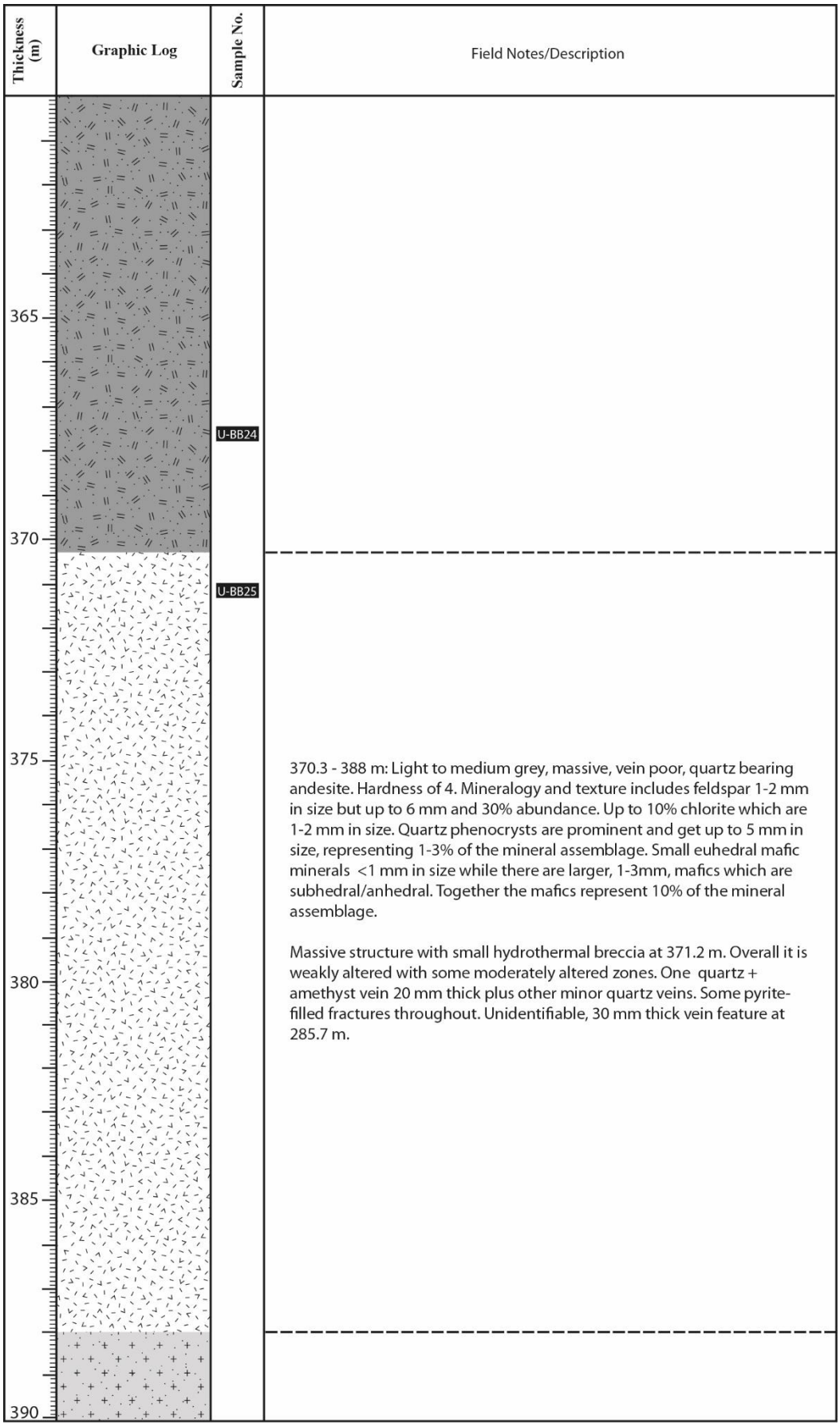
Thickness (m)
Graphic Log
Sample No.
Field Notes/Description
365
370
375
380
385
390
U-BB24
U-BB25
370.3 - 388 m: Light to medium grey, massive, vein poor, quartz bearing andesite. Hardness of 4. Mineralogy and texture includes feldspar 1-2 mm in size but up to 6 mm and 30% abundance. Up to 10% chlorite which are 1-2 mm in size. Quartz phenocrysts are prominent and get up to 5 mm in size, representing 1-3% of the mineral assemblage. Small euhedral mafic minerals <1 mm in size while there are larger, 1-3mm, mafics which are subhedral/anhedral. Together the mafics represent 10% of the mineral assemblage.
Massive structure with small hydrothermal breccia at 371.2 m. Overall it is weakly altered with some moderately altered zones. One quartz + amethyst vein 20 mm thick plus other minor quartz veins. Some pyrite-filled fractures throughout. Unidentifiable, 30 mm thick vein feature at 285.7 m.

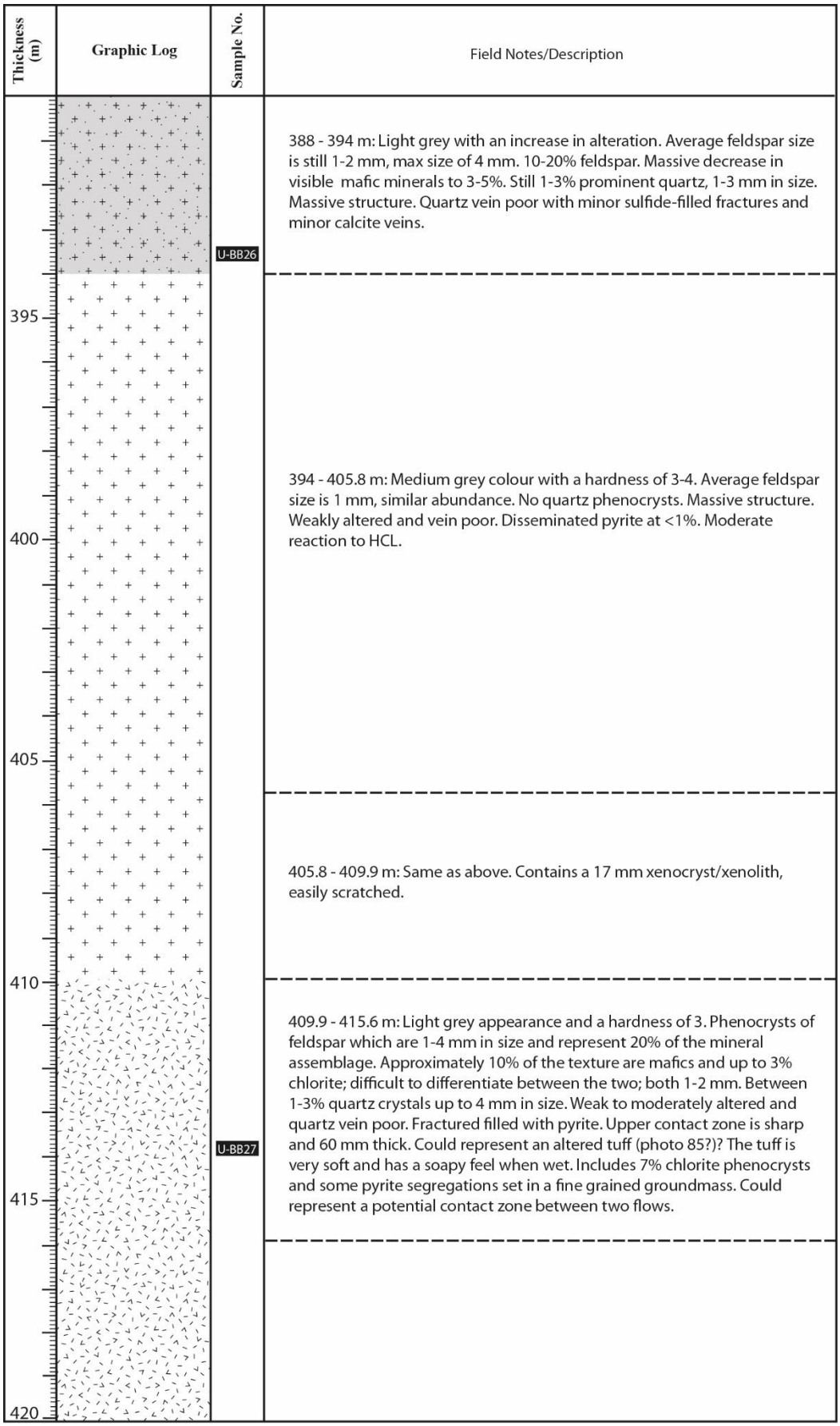
Thickness (m)
Graphic Log
Sample No.
Field Notes/Description
U-BB26
U-BB27
395
400
405
410
415
420
388 - 394 m: Light grey with an increase in alteration. Average feldspar size is still 1-2 mm, max size of 4 mm. 10-20% feldspar. Massive decrease in visible mafic minerals to 3-5%. Still 1-3% prominent quartz, 1-3 mm in size. Massive structure. Quartz vein poor with minor sulfide-filled fractures and minor calcite veins.
394 - 405.8 m: Medium grey colour with a hardness of 3-4. Average feldspar size is 1 mm, similar abundance. No quartz phenocrysts. Massive structure. Weakly altered and vein poor. Disseminated pyrite at <1%. Moderate reaction to HCL.
405.8 - 409.9 m: Same as above. Contains a 17 mm xenocryst/xenolith, easily scratched.
409.9 - 415.6 m: Light grey appearance and a hardness of 3. Phenocrysts of feldspar which are 1-4 mm in size and represent 20% of the mineral assemblage. Approximately 10% of the texture are mafics and up to 3% chlorite; difficult to differentiate between the two; both 1-2 mm. Between 1-3% quartz crystals up to 4 mm in size. Weak to moderately altered and quartz vein poor. Fractured filled with pyrite. Upper contact zone is sharp and 60 mm thick. Could represent an altered tuff (photo 85?)? The tuff is very soft and has a soapy feel when wet. Includes 7% chlorite phenocrysts and some pyrite segregations set in a fine grained groundmass. Could represent a potential contact zone between two flows.

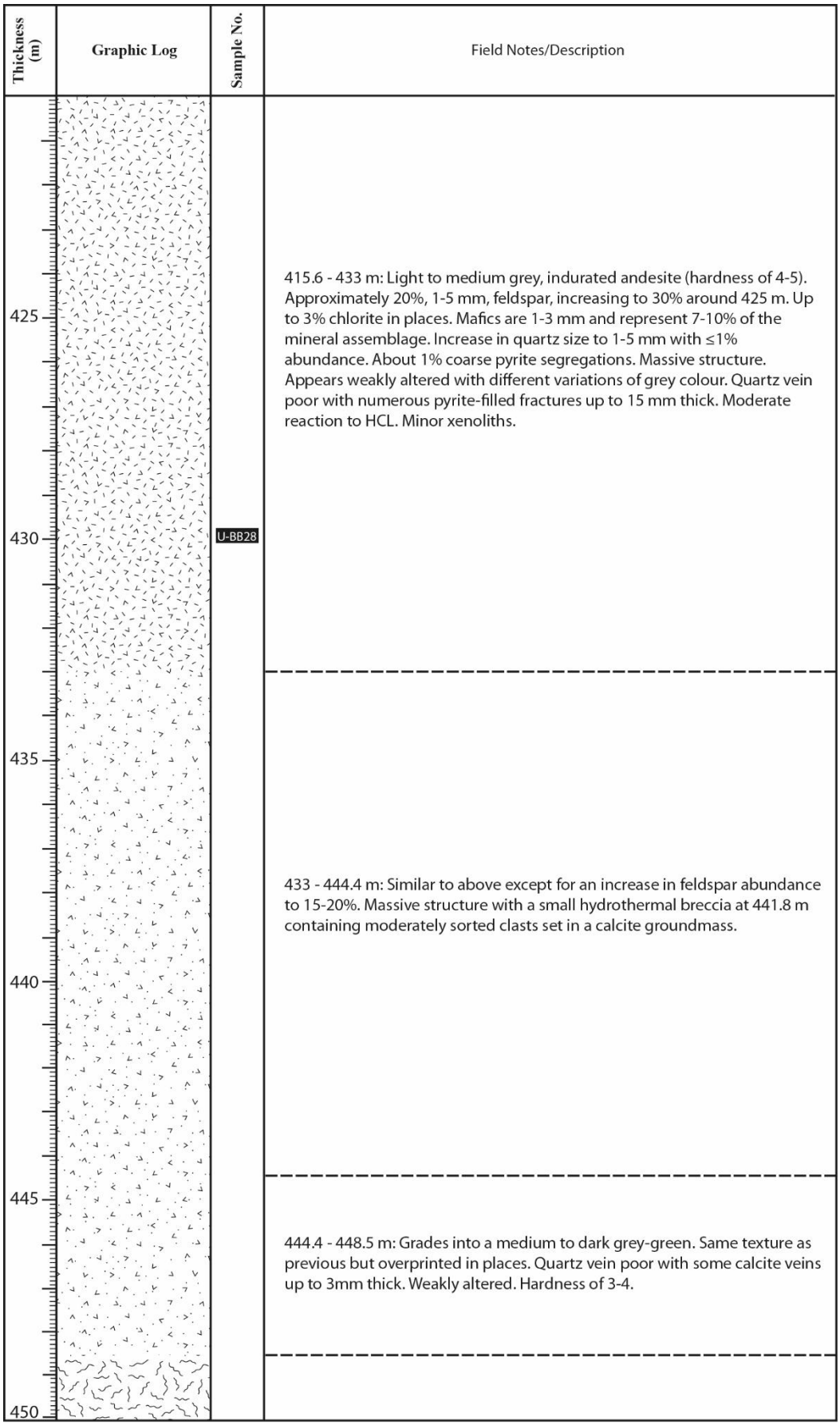
Thickness (m)
Graphic Log
Sample No.
Field Notes/Description
425
430
435
440
445
450
U-BB28
415.6 - 433 m: Light to medium grey, indurated andesite (hardness of 4-5). Approximately 20%, 1-5 mm, feldspar, increasing to 30% around 425 m. Up to 3% chlorite in places. Mafics are 1-3 mm and represent 7-10% of the mineral assemblage. Increase in quartz size to 1-5 mm with ≤1% abundance. About 1% coarse pyrite segregations. Massive structure. Appears weakly altered with different variations of grey colour. Quartz vein poor with numerous pyrite-filled fractures up to 15 mm thick. Moderate reaction to HCL. Minor xenoliths.
433 - 444.4 m: Similar to above except for an increase in feldspar abundance to 15-20%. Massive structure with a small hydrothermal breccia at 441.8 m containing moderately sorted clasts set in a calcite groundmass.
444.4 - 448.5 m: Grades into a medium to dark grey-green. Same texture as previous but overprinted in places. Quartz vein poor with some calcite veins up to 3mm thick. Weakly altered. Hardness of 3-4.

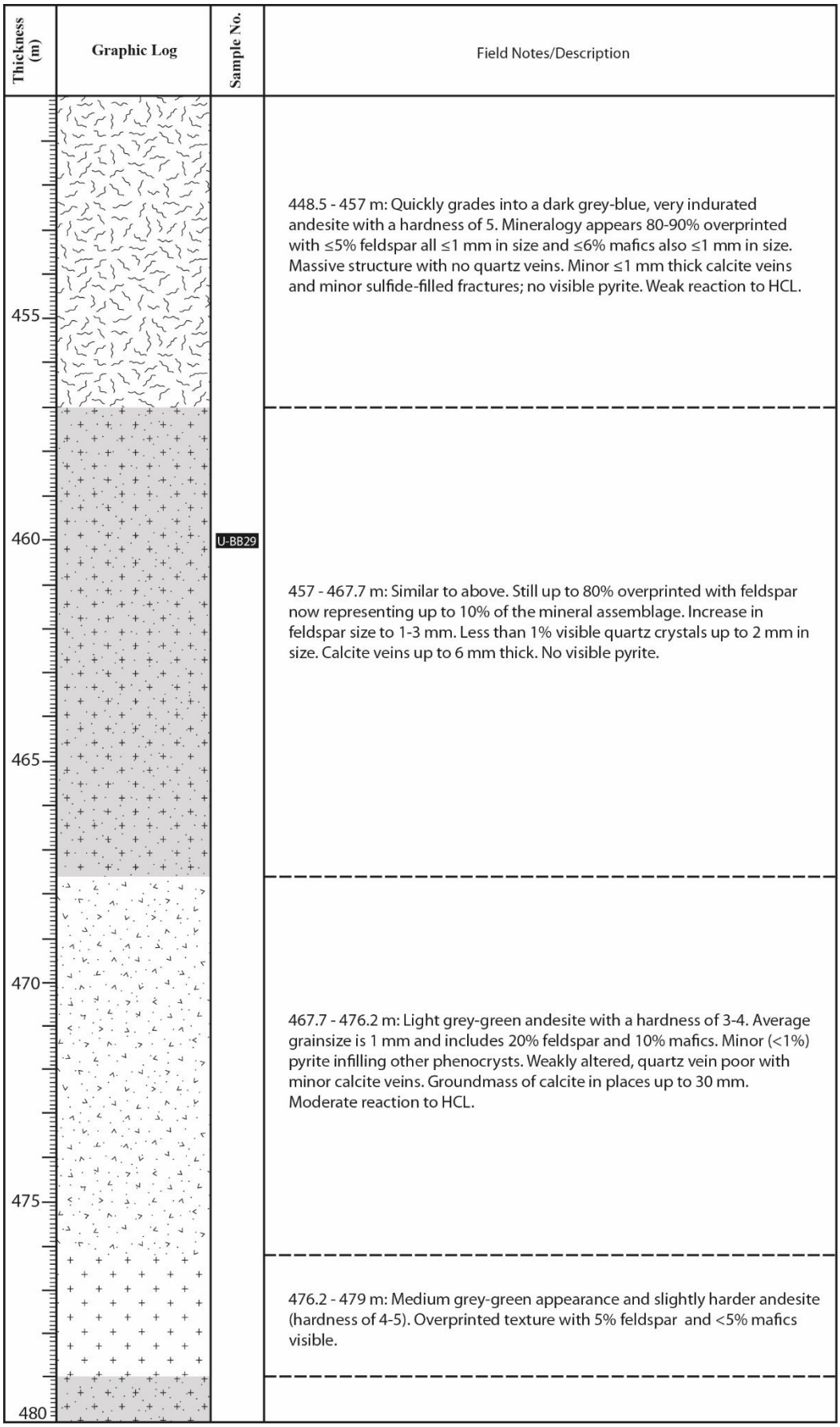
Thickness (m)
Graphic Log
Sample No.
Field Notes/Description
455
460
465
470
475
480
U-BB29
448.5 - 457 m: Quickly grades into a dark grey-blue, very indurated andesite with a hardness of 5. Mineralogy appears 80-90% overprinted with ≤5% feldspar all ≤1 mm in size and ≤6% mafics also ≤1 mm in size. Massive structure with no quartz veins. Minor ≤1 mm thick calcite veins and minor sulfide-filled fractures; no visible pyrite. Weak reaction to HCL.
457 - 467.7 m: Similar to above. Still up to 80% overprinted with feldspar now representing up to 10% of the mineral assemblage. Increase in feldspar size to 1-3 mm. Less than 1% visible quartz crystals up to 2 mm in size. Calcite veins up to 6 mm thick. No visible pyrite.
467.7 - 476.2 m: Light grey-green andesite with a hardness of 3-4. Average grainsize is 1 mm and includes 20% feldspar and 10% mafics. Minor (<1%) pyrite infilling other phenocrysts. Weakly altered, quartz vein poor with minor calcite veins. Groundmass of calcite in places up to 30 mm. Moderate reaction to HCL.
476.2 - 479 m: Medium grey-green appearance and slightly harder andesite (hardness of 4-5). Overprinted texture with 5% feldspar and <5% mafics visible.

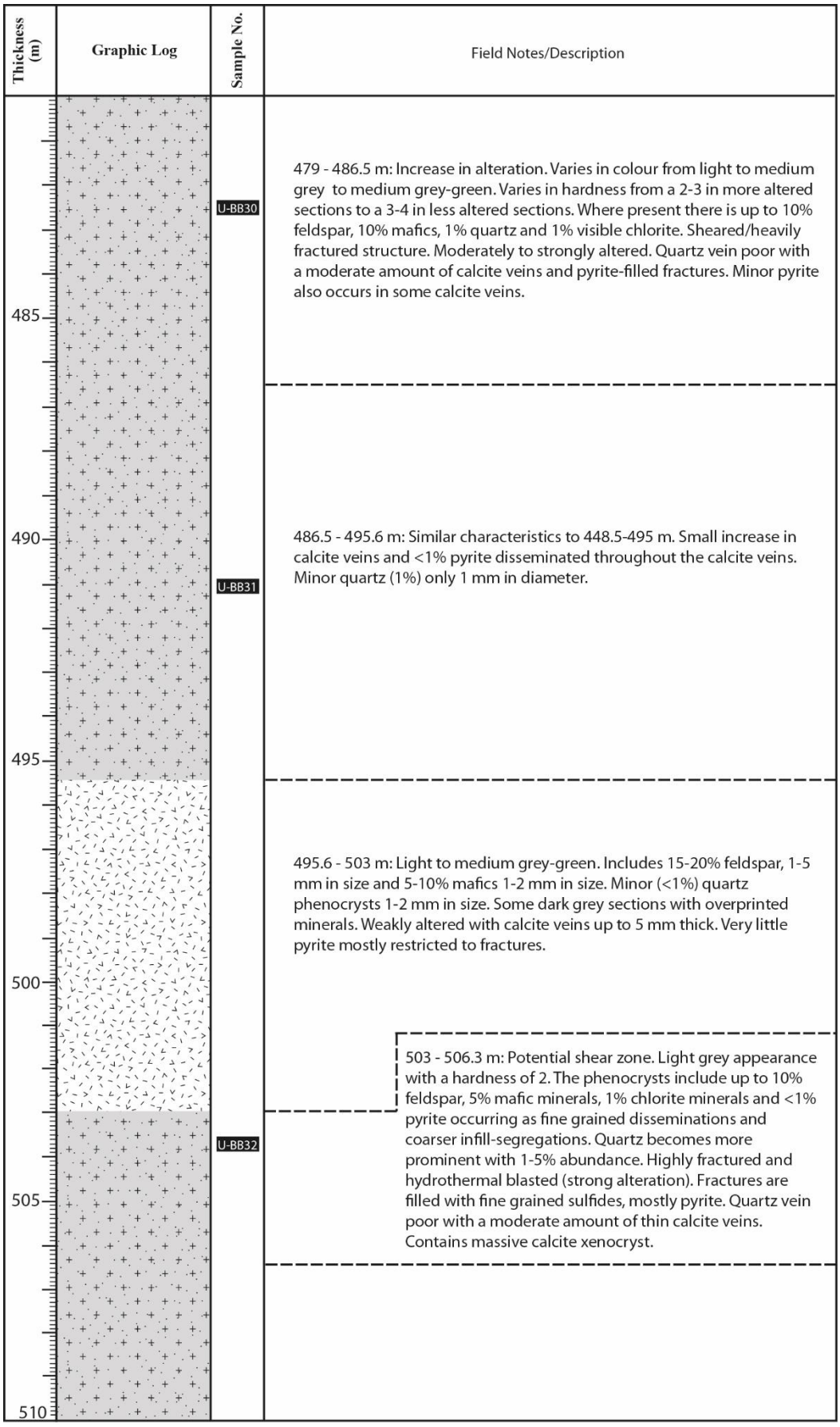
Thickness (m)
Graphic Log
Sample No.
Field Notes/Description
U-BB30
U-BB31
U-BB32
485
490
495
500
505
510
479 - 486.5 m: Increase in alteration. Varies in colour from light to medium grey to medium grey-green. Varies in hardness from a 2-3 in more altered sections to a 3-4 in less altered sections. Where present there is up to 10% feldspar, 10% mafics, 1% quartz and 1% visible chlorite. Sheared/heavily fractured structure. Moderately to strongly altered. Quartz vein poor with a moderate amount of calcite veins and pyrite-filled fractures. Minor pyrite also occurs in some calcite veins.
486.5 - 495.6 m: Similar characteristics to 448.5-495 m. Small increase in calcite veins and <1% pyrite disseminated throughout the calcite veins. Minor quartz (1%) only 1 mm in diameter.
495.6 - 503 m: Light to medium grey-green. Includes 15-20% feldspar, 1-5 mm in size and 5-10% mafics 1-2 mm in size. Minor (<1%) quartz phenocrysts 1-2 mm in size. Some dark grey sections with overprinted minerals. Weakly altered with calcite veins up to 5 mm thick. Very little pyrite mostly restricted to fractures.
503 - 506.3 m: Potential shear zone. Light grey appearance with a hardness of 2. The phenocrysts include up to 10% feldspar, 5% mafic minerals, 1% chlorite minerals and <1% pyrite occurring as fine grained disseminations and coarser infill-segregations. Quartz becomes more prominent with 1-5% abundance. Highly fractured and hydrothermal blasted (strong alteration). Fractures are filled with fine grained sulfides, mostly pyrite. Quartz vein poor with a moderate amount of thin calcite veins. Contains massive calcite xenocryst.

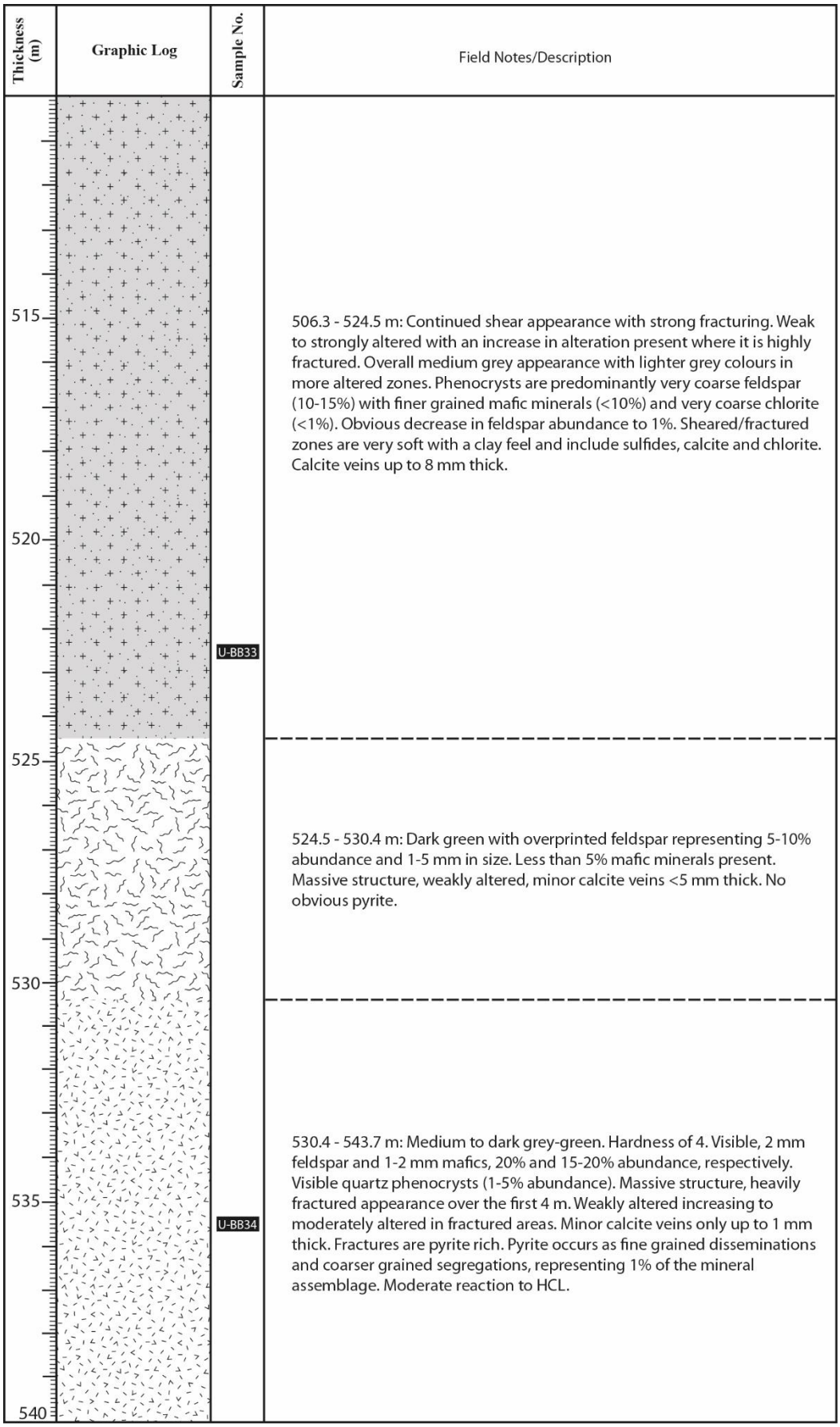
Thickness (m)
Graphic Log
Sample No.
Field Notes/Description
515
520
525
530
535
540
U-BB33
U-BB34
506.3 - 524.5 m: Continued shear appearance with strong fracturing. Weak to strongly altered with an increase in alteration present where it is highly fractured. Overall medium grey appearance with lighter grey colours in more altered zones. Phenocrysts are predominantly very coarse feldspar (10-15%) with finer grained mafic minerals (<10%) and very coarse chlorite (<1%). Obvious decrease in feldspar abundance to 1%. Sheared/fractured zones are very soft with a clay feel and include sulfides, calcite and chlorite. Calcite veins up to 8 mm thick.
524.5 - 530.4 m: Dark green with overprinted feldspar representing 5-10% abundance and 1-5 mm in size. Less than 5% mafic minerals present. Massive structure, weakly altered, minor calcite veins <5 mm thick. No obvious pyrite.
530.4 - 543.7 m: Medium to dark grey-green. Hardness of 4. Visible, 2 mm feldspar and 1-2 mm mafics, 20% and 15-20% abundance, respectively. Visible quartz phenocrysts (1-5% abundance). Massive structure, heavily fractured appearance over the first 4 m. Weakly altered increasing to moderately altered in fractured areas. Minor calcite veins only up to 1 mm thick. Fractures are pyrite rich. Pyrite occurs as fine grained disseminations and coarser grained segregations, representing 1% of the mineral assemblage. Moderate reaction to HCL.

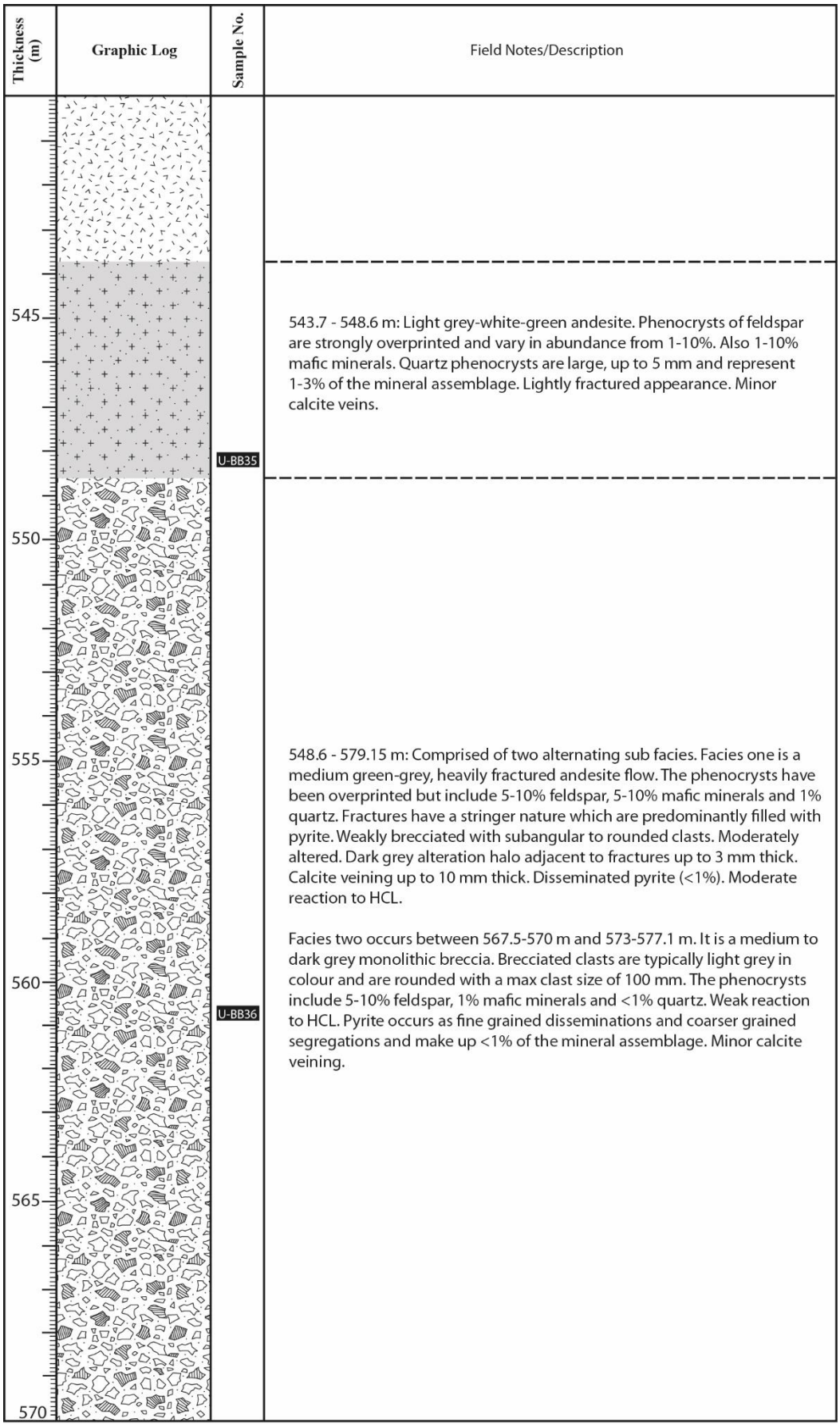
Thickness (m)
Graphic Log
Sample No.
Field Notes/Description
545
550
555
560
565
570
U-BB35
U-BB36
543.7 - 548.6 m: Light grey-white-green andesite. Phenocrysts of feldspar are strongly overprinted and vary in abundance from 1-10%. Also 1-10% mafic minerals. Quartz phenocrysts are large, up to 5 mm and represent 1-3% of the mineral assemblage. Lightly fractured appearance. Minor calcite veins.
548.6 - 579.15 m: Comprised of two alternating sub facies. Facies one is a medium green-grey, heavily fractured andesite flow. The phenocrysts have been overprinted but include 5-10% feldspar, 5-10% mafic minerals and 1% quartz. Fractures have a stringer nature which are predominantly filled with pyrite. Weakly brecciated with subangular to rounded clasts. Moderately altered. Dark grey alteration halo adjacent to fractures up to 3 mm thick. Calcite veining up to 10 mm thick. Disseminated pyrite (<1%). Moderate reaction to HCL.
Facies two occurs between 567.5-570 m and 573-577.1 m. It is a medium to dark grey monolithic breccia. Brecciated clasts are typically light grey in colour and are rounded with a max clast size of 100 mm. The phenocrysts include 5-10% feldspar, 1% mafic minerals and <1% quartz. Weak reaction to HCL. Pyrite occurs as fine grained disseminations and coarser grained segregations and make up <1% of the mineral assemblage. Minor calcite veining.

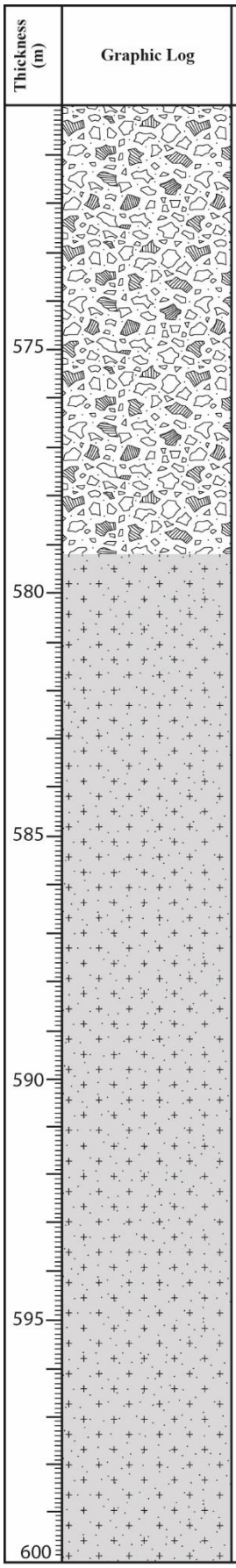

Sample No.	Field Notes/Description
U-BB37	
	579.15 - 589 m: Medium green to medium green-grey. Hardness of 3-4. Overprinted feldspar with 5-10% abundance. Mafics are 1-4 mm in size and have 10% abundance. Increase in quartz abundance to 1-3%. Mostly massive structure with small fractured zones. Weakly altered with minor calcite veins less than 2 mm thick. Fractures have disseminated pyrite. Pyrite is also disseminated in the groundmass and occurs as pods. Moderate reaction to HCL. Contains dark green, irregular shaped areas of groundmass ≤10 mm in size and ≤1% of the andesite.
U-BB38	
	589 - 594 m: Similar to sub-facies one which occurs between 548.6-579.15 m. Increase in quartz abundance to ≤5%. Vein poor.
	594 - 597.6 m: Medium to dark grey-green with minor quartz. Quartz phenocrysts are 1-3 mm and represent <1% of the mineral assemblage. Other phenocrysts include 1mm mafics and 1-3 mm feldspar, 1% and 5-10% abundance, respectively. Weakly altered. Minor calcite veins ≤7 mm thick. Moderate reaction to HCL. Disseminated pyrite and numerous pyrite-filled fractures.
	597.6 - 601.7 m: Increase in feldspar size to 1-6 mm, with an average size of 1 mm, and an increase in quartz size to 1-5 mm. Slight increase in alteration in light grey-green areas. Minor quartz veins with regular calcite veins up to 4 mm thick. Less than 1% disseminated pyrite.

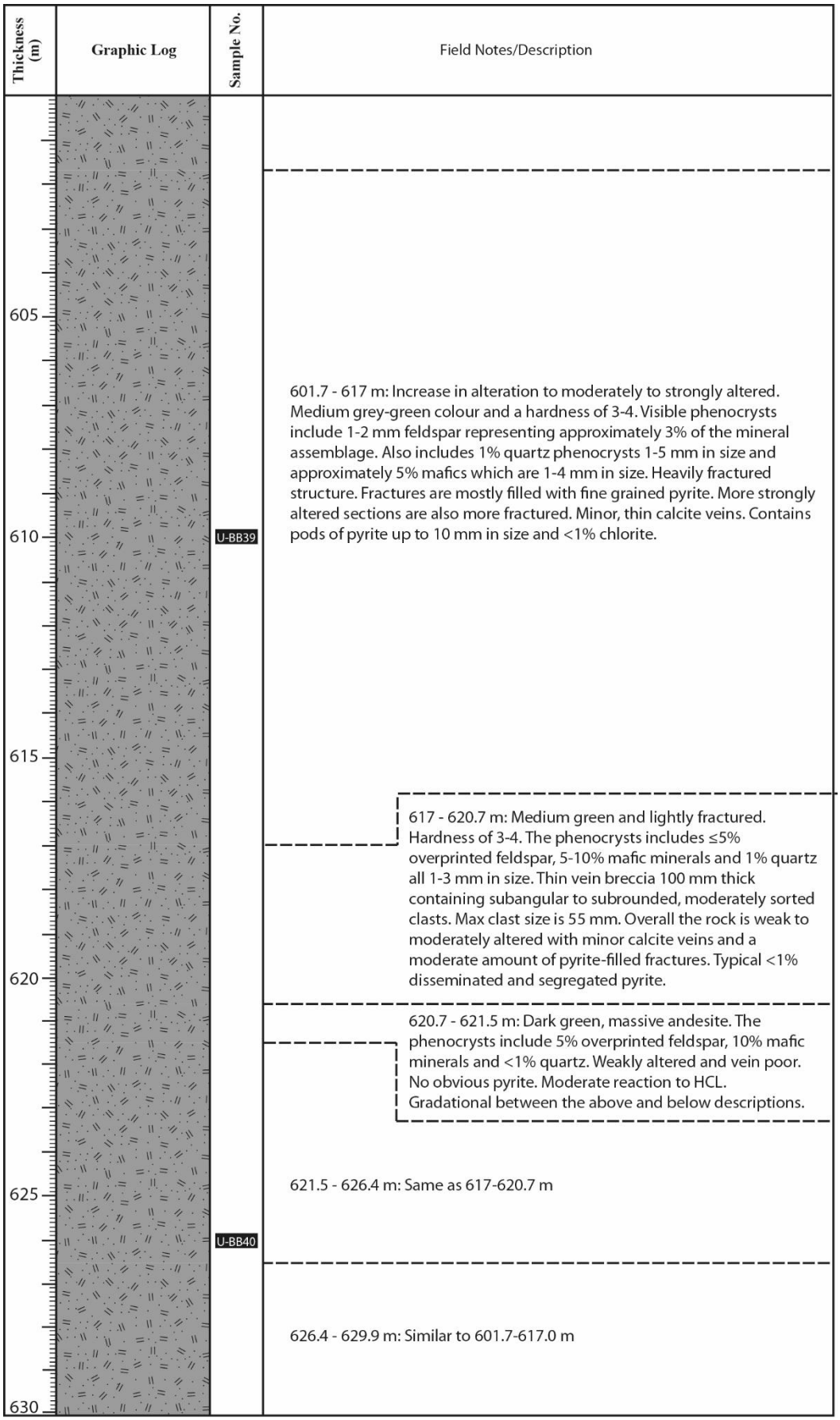
Thickness (m)
Graphic Log
Sample No.
Field Notes/Description
605
610
615
620
625
630
U-BB39
U-BB40
601.7 - 617 m: Increase in alteration to moderately to strongly altered. Medium grey-green colour and a hardness of 3-4. Visible phenocrysts include 1-2 mm feldspar representing approximately 3% of the mineral assemblage. Also includes 1% quartz phenocrysts 1-5 mm in size and approximately 5% mafics which are 1-4 mm in size. Heavily fractured structure. Fractures are mostly filled with fine grained pyrite. More strongly altered sections are also more fractured. Minor, thin calcite veins. Contains pods of pyrite up to 10 mm in size and <1% chlorite.
617 - 620.7 m: Medium green and lightly fractured. Hardness of 3-4. The phenocrysts includes ≤5% overprinted feldspar, 5-10% mafic minerals and 1% quartz all 1-3 mm in size. Thin vein breccia 100 mm thick containing subangular to subrounded, moderately sorted clasts. Max clast size is 55 mm. Overall the rock is weak to moderately altered with minor calcite veins and a moderate amount of pyrite-filled fractures. Typical <1% disseminated and segregated pyrite.
620.7 - 621.5 m: Dark green, massive andesite. The phenocrysts include 5% overprinted feldspar, 10% mafic minerals and <1% quartz. Weakly altered and vein poor. No obvious pyrite. Moderate reaction to HCL. Gradational between the above and below descriptions.
621.5 - 626.4 m: Same as 617-620.7 m
626.4 - 629.9 m: Similar to 601.7-617.0 m

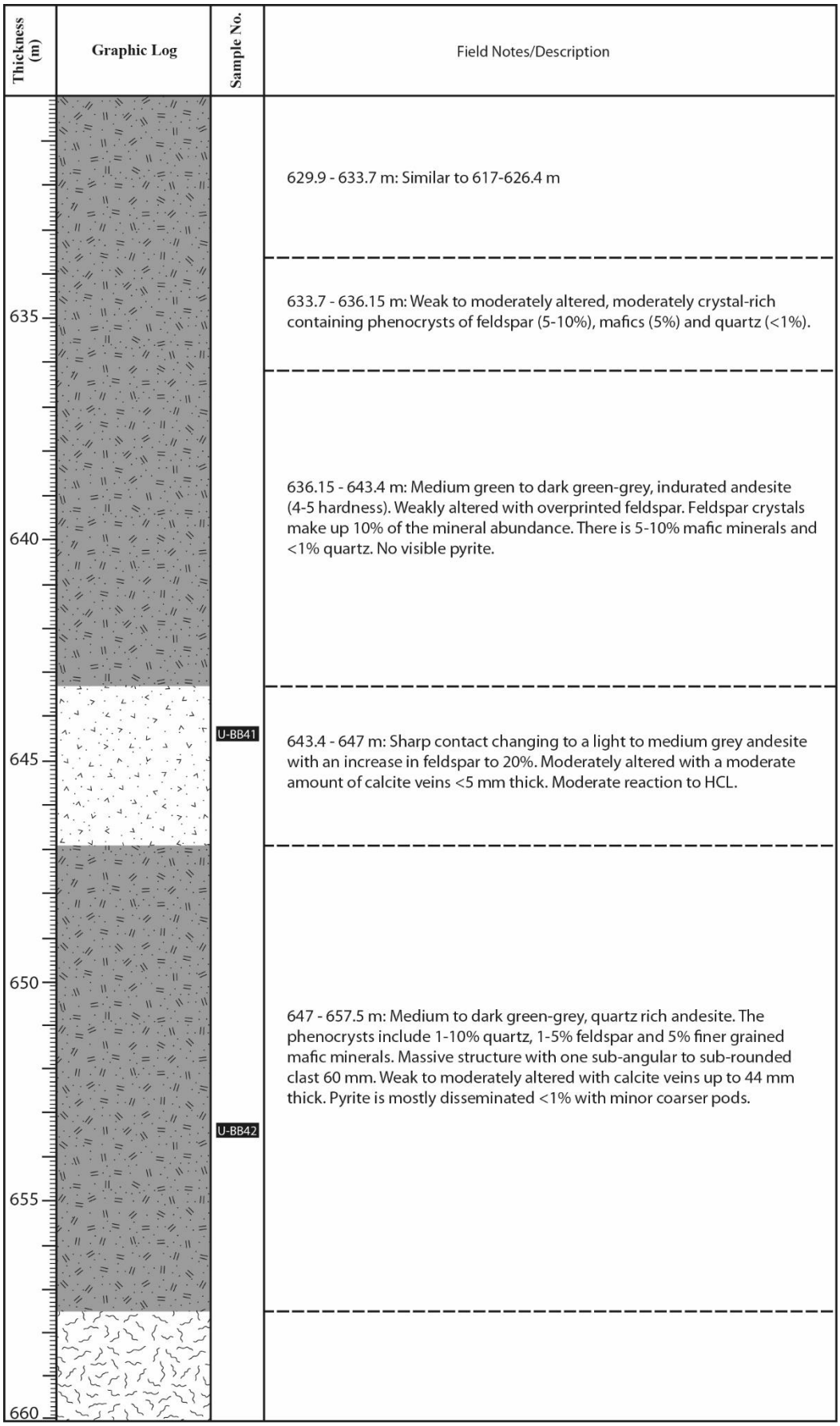
Thickness (m)
Graphic Log
Sample No.
Field Notes/Description
635
640
645
650
655
660
U-BB41
U-BB42
629.9 - 633.7 m: Similar to 617-626.4 m
633.7 - 636.15 m: Weak to moderately altered, moderately crystal-rich containing phenocrysts of feldspar (5-10%), mafics (5%) and quartz (<1%).
636.15 - 643.4 m: Medium green to dark green-grey, indurated andesite (4-5 hardness). Weakly altered with overprinted feldspar. Feldspar crystals make up 10% of the mineral abundance. There is 5-10% mafic minerals and <1% quartz. No visible pyrite.
643.4 - 647 m: Sharp contact changing to a light to medium grey andesite with an increase in feldspar to 20%. Moderately altered with a moderate amount of calcite veins <5 mm thick. Moderate reaction to HCL.
647 - 657.5 m: Medium to dark green-grey, quartz rich andesite. The phenocrysts include 1-10% quartz, 1-5% feldspar and 5% finer grained mafic minerals. Massive structure with one sub-angular to sub-rounded clast 60 mm. Weak to moderately altered with calcite veins up to 44 mm thick. Pyrite is mostly disseminated <1% with minor coarser pods.

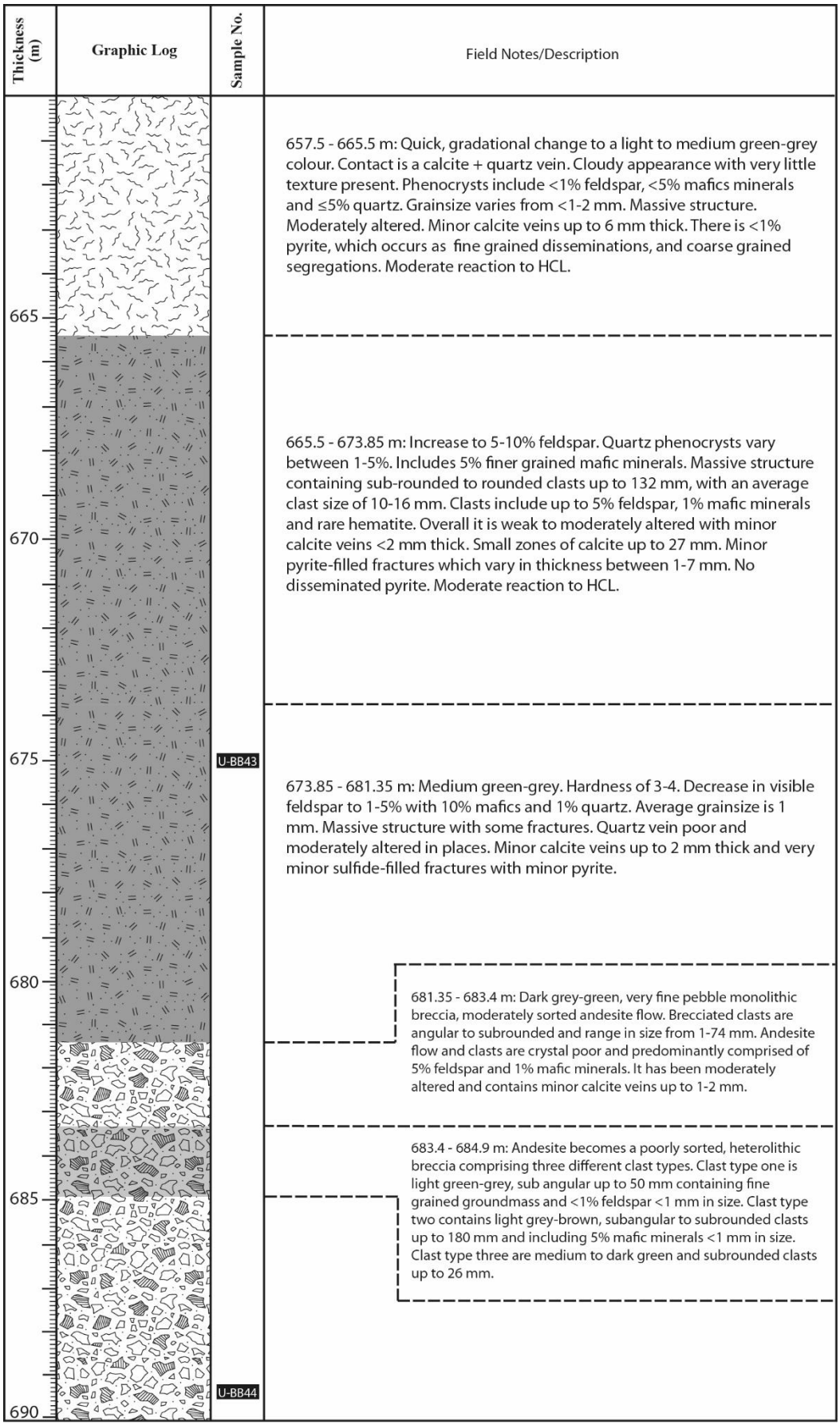
Thickness (m)
Graphic Log
Sample No.
Field Notes/Description
665
670
675
680
685
690
U-BB43
U-BB44
657.5 - 665.5 m: Quick, gradational change to a light to medium green-grey colour. Contact is a calcite + quartz vein. Cloudy appearance with very little texture present. Phenocrysts include <1% feldspar, <5% mafics minerals and ≤5% quartz. Grainsize varies from <1-2 mm. Massive structure. Moderately altered. Minor calcite veins up to 6 mm thick. There is <1% pyrite, which occurs as fine grained disseminations, and coarse grained segregations. Moderate reaction to HCL.
665.5 - 673.85 m: Increase to 5-10% feldspar. Quartz phenocrysts vary between 1-5%. Includes 5% finer grained mafic minerals. Massive structure containing sub-rounded to rounded clasts up to 132 mm, with an average clast size of 10-16 mm. Clasts include up to 5% feldspar, 1% mafic minerals and rare hematite. Overall it is weak to moderately altered with minor calcite veins <2 mm thick. Small zones of calcite up to 27 mm. Minor pyrite-filled fractures which vary in thickness between 1-7 mm. No disseminated pyrite. Moderate reaction to HCL.
673.85 - 681.35 m: Medium green-grey. Hardness of 3-4. Decrease in visible feldspar to 1-5% with 10% mafics and 1% quartz. Average grainsize is 1 mm. Massive structure with some fractures. Quartz vein poor and moderately altered in places. Minor calcite veins up to 2 mm thick and very minor sulfide-filled fractures with minor pyrite.
681.35 - 683.4 m: Dark grey-green, very fine pebble monolithic breccia, moderately sorted andesite flow. Brecciated clasts are angular to subrounded and range in size from 1-74 mm. Andesite flow and clasts are crystal poor and predominantly comprised of 5% feldspar and 1% mafic minerals. It has been moderately altered and contains minor calcite veins up to 1-2 mm.
683.4 - 684.9 m: Andesite becomes a poorly sorted, heterolithic breccia comprising three different clast types. Clast type one is light green-grey, sub angular up to 50 mm containing fine grained groundmass and <1% feldspar <1 mm in size. Clast type two contains light grey-brown, subangular to subrounded clasts up to 180 mm and including 5% mafic minerals <1 mm in size. Clast type three are medium to dark green and subrounded clasts up to 26 mm.

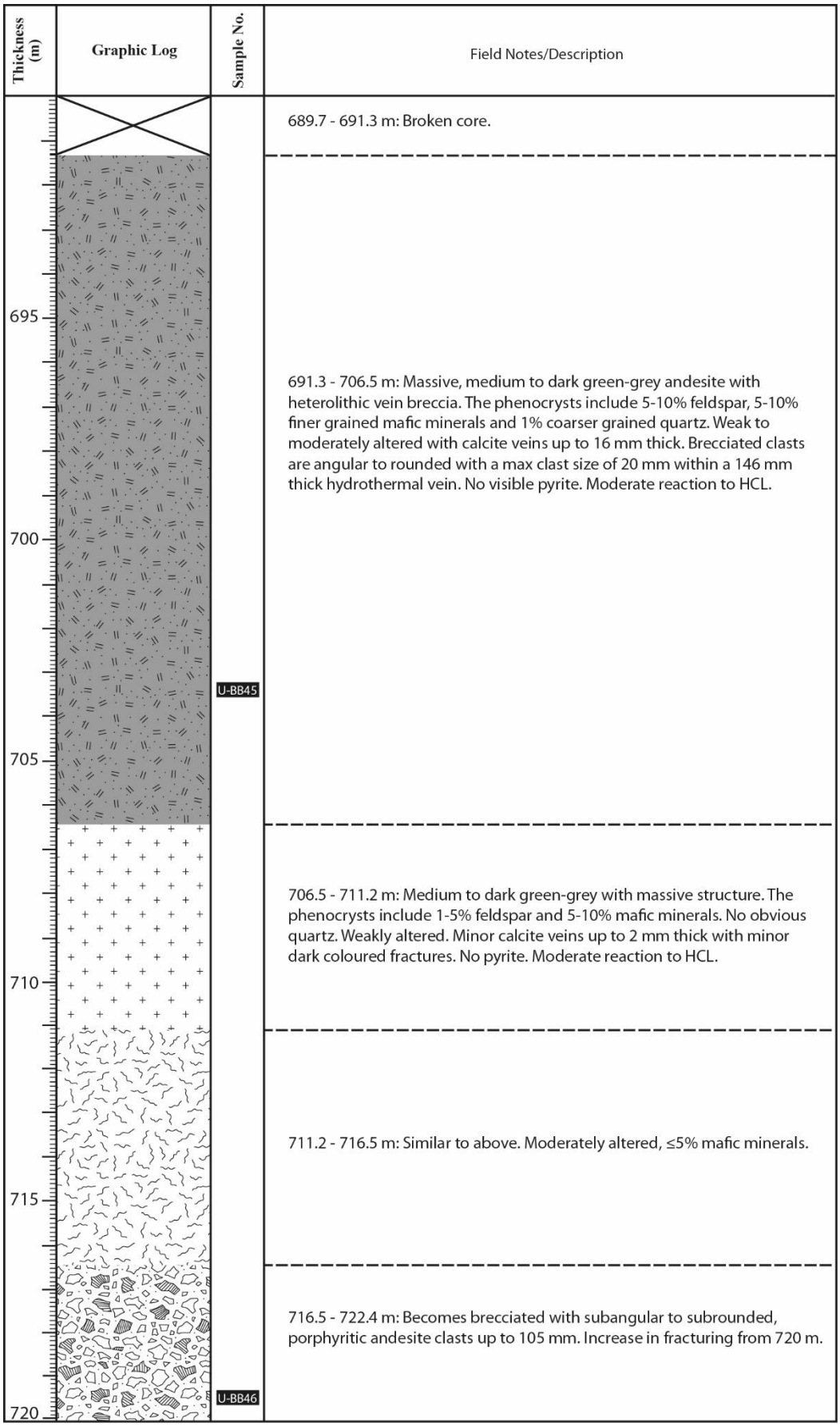
Thickness (m)
Graphic Log
Sample No.
Field Notes/Description
695
700
705
710
715
720
U-BB45
U-BB46
689.7 - 691.3 m: Broken core.
691.3 - 706.5 m: Massive, medium to dark green-grey andesite with heterolithic vein breccia. The phenocrysts include 5-10% feldspar, 5-10% finer grained mafic minerals and 1% coarser grained quartz. Weak to moderately altered with calcite veins up to 16 mm thick. Brecciated clasts are angular to rounded with a max clast size of 20 mm within a 146 mm thick hydrothermal vein. No visible pyrite. Moderate reaction to HCL.
706.5 - 711.2 m: Medium to dark green-grey with massive structure. The phenocrysts include 1-5% feldspar and 5-10% mafic minerals. No obvious quartz. Weakly altered. Minor calcite veins up to 2 mm thick with minor dark coloured fractures. No pyrite. Moderate reaction to HCL.
711.2 - 716.5 m: Similar to above. Moderately altered, ≤5% mafic minerals.
716.5 - 722.4 m: Becomes brecciated with subangular to subrounded, porphyritic andesite clasts up to 105 mm. Increase in fracturing from 720 m.

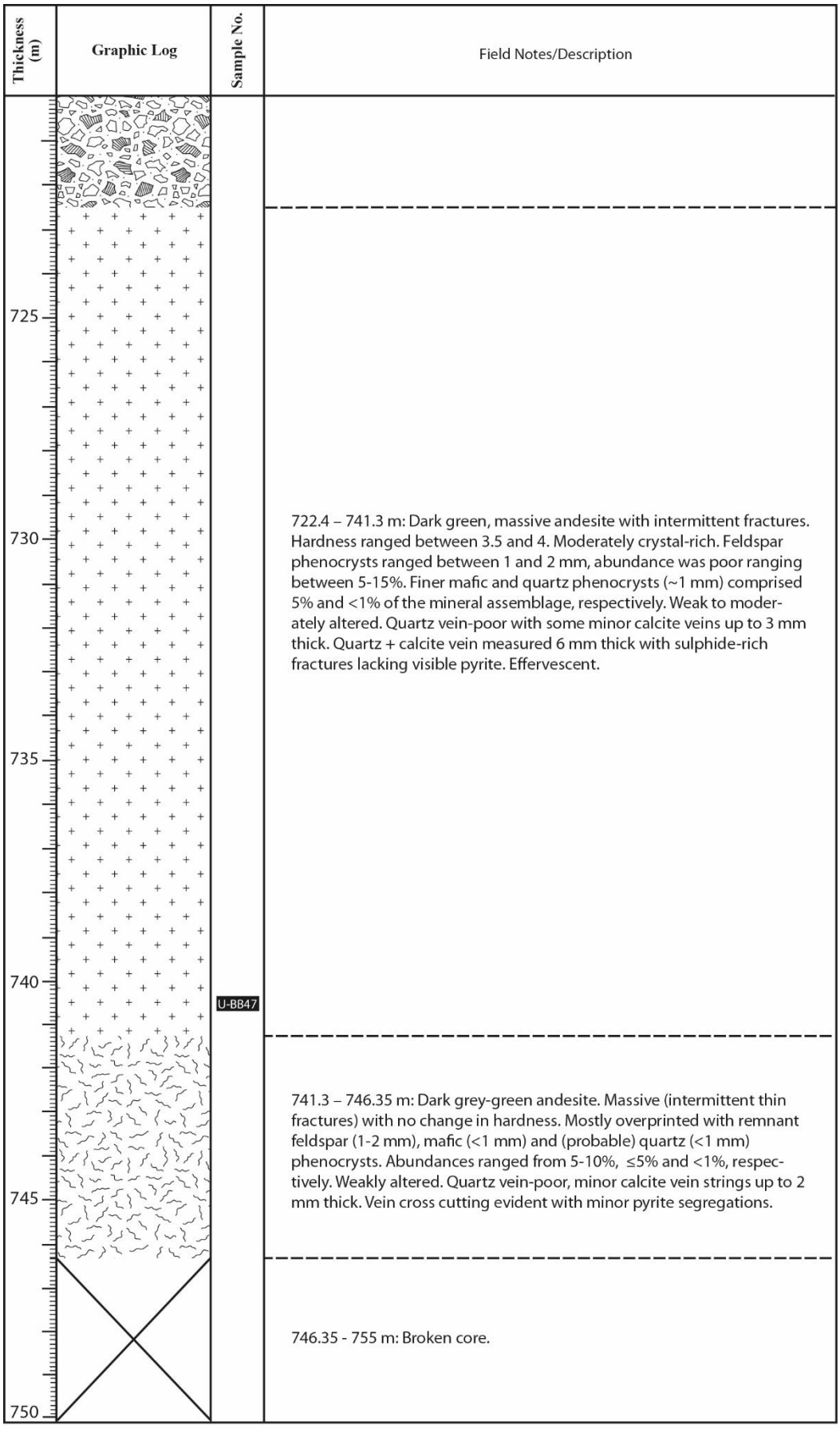
Thickness (m)
Graphic Log
Sample No.
Field Notes/Description
725
730
735
740
745
750
U-BB47
722.4 – 741.3 m: Dark green, massive andesite with intermittent fractures. Hardness ranged between 3.5 and 4. Moderately crystal-rich. Feldspar phenocrysts ranged between 1 and 2 mm, abundance was poor ranging between 5-15%. Finer mafic and quartz phenocrysts (~1 mm) comprised 5% and <1% of the mineral assemblage, respectively. Weak to moderately altered. Quartz vein-poor with some minor calcite veins up to 3 mm thick. Quartz + calcite vein measured 6 mm thick with sulphide-rich fractures lacking visible pyrite. Effervescent.
741.3 – 746.35 m: Dark grey-green andesite. Massive (intermittent thin fractures) with no change in hardness. Mostly overprinted with remnant feldspar (1-2 mm), mafic (<1 mm) and (probable) quartz (<1 mm) phenocrysts. Abundances ranged from 5-10%, ≤5% and <1%, respectively. Weakly altered. Quartz vein-poor, minor calcite vein strings up to 2 mm thick. Vein cross cutting evident with minor pyrite segregations.
746.35 - 755 m: Broken core.

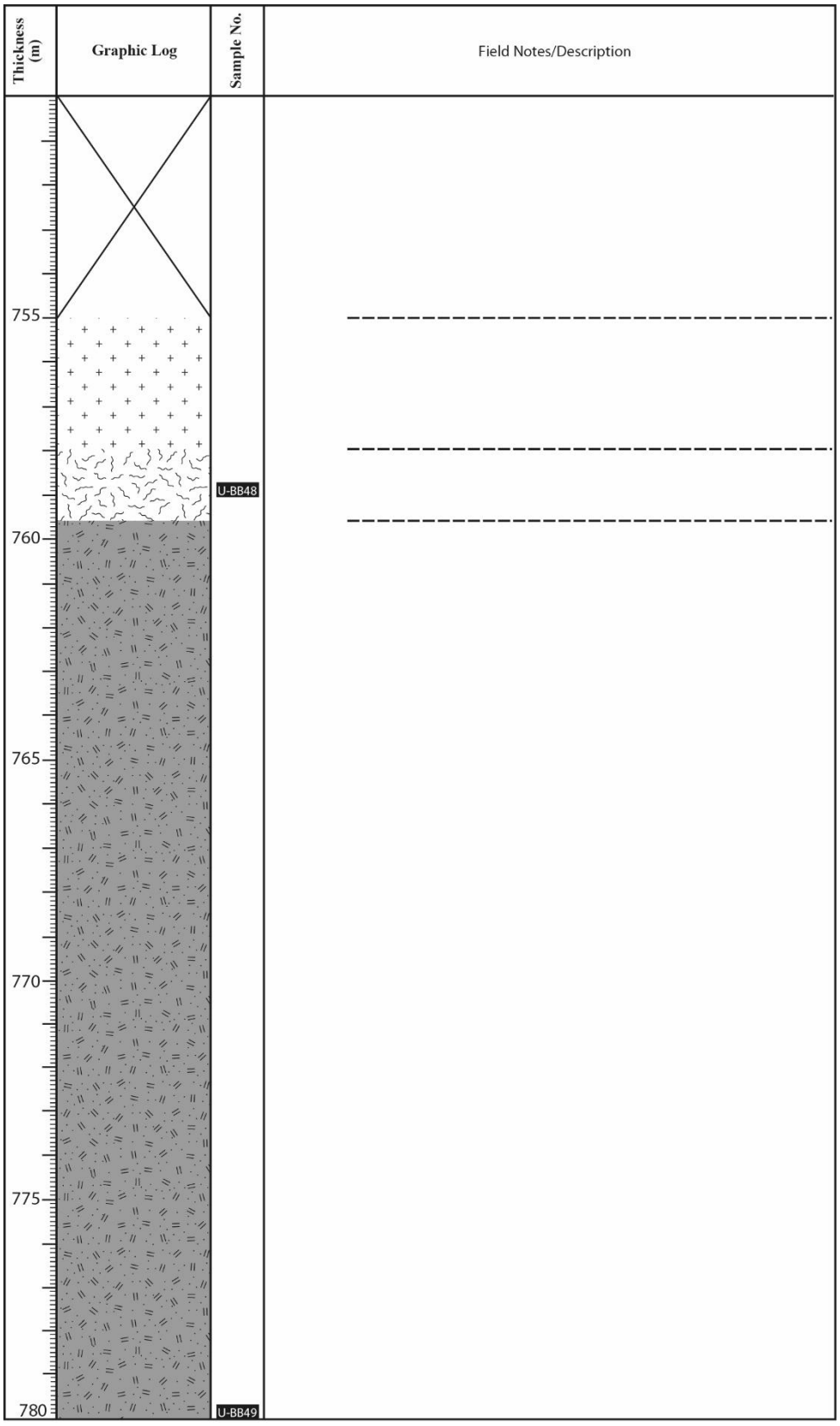

Core descriptions missing from 755 m to 780 m. Graphic log texture is correct – see legend for details.

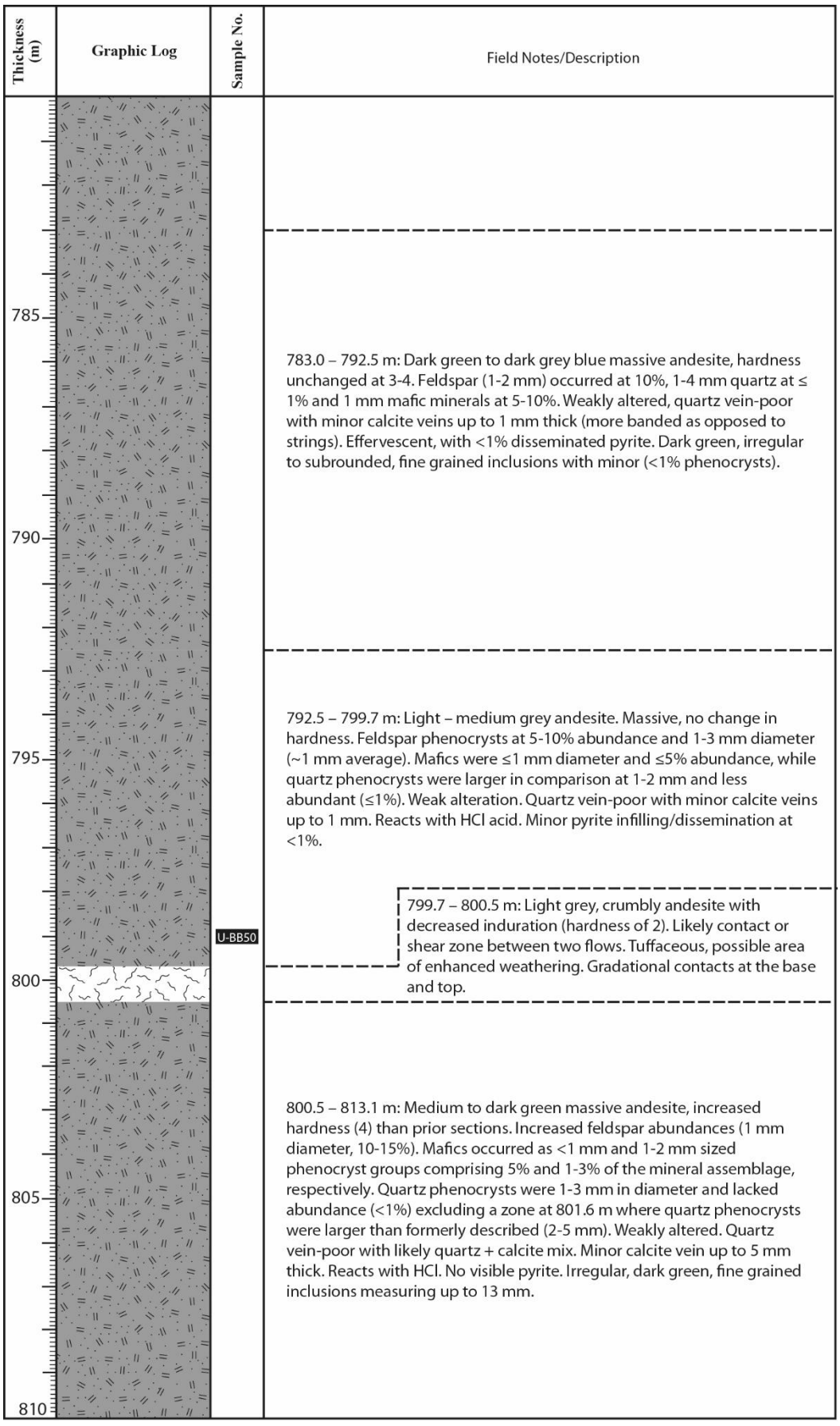
Thickness (m)
Graphic Log
Sample No.
Field Notes/Description
785
790
795
800
805
810
U-BB50
783.0 – 792.5 m: Dark green to dark grey blue massive andesite, hardness unchanged at 3-4. Feldspar (1-2 mm) occurred at 10%, 1-4 mm quartz at ≤ 1% and 1 mm mafic minerals at 5-10%. Weakly altered, quartz vein-poor with minor calcite veins up to 1 mm thick (more banded as opposed to strings). Effervescent, with <1% disseminated pyrite. Dark green, irregular to subrounded, fine grained inclusions with minor (<1% phenocrysts).
792.5 – 799.7 m: Light – medium grey andesite. Massive, no change in hardness. Feldspar phenocrysts at 5-10% abundance and 1-3 mm diameter (~1 mm average). Mafics were ≤1 mm diameter and ≤5% abundance, while quartz phenocrysts were larger in comparison at 1-2 mm and less abundant (≤1%). Weak alteration. Quartz vein-poor with minor calcite veins up to 1 mm. Reacts with HCl acid. Minor pyrite infilling/dissemination at <1%.
799.7 – 800.5 m: Light grey, crumbly andesite with decreased induration (hardness of 2). Likely contact or shear zone between two flows. Tuffaceous, possible area of enhanced weathering. Gradational contacts at the base and top.
800.5 – 813.1 m: Medium to dark green massive andesite, increased hardness (4) than prior sections. Increased feldspar abundances (1 mm diameter, 10-15%). Mafics occurred as <1 mm and 1-2 mm sized phenocryst groups comprising 5% and 1-3% of the mineral assemblage, respectively. Quartz phenocrysts were 1-3 mm in diameter and lacked abundance (<1%) excluding a zone at 801.6 m where quartz phenocrysts were larger than formerly described (2-5 mm). Weakly altered. Quartz vein-poor with likely quartz + calcite mix. Minor calcite vein up to 5 mm thick. Reacts with HCl. No visible pyrite. Irregular, dark green, fine grained inclusions measuring up to 13 mm.

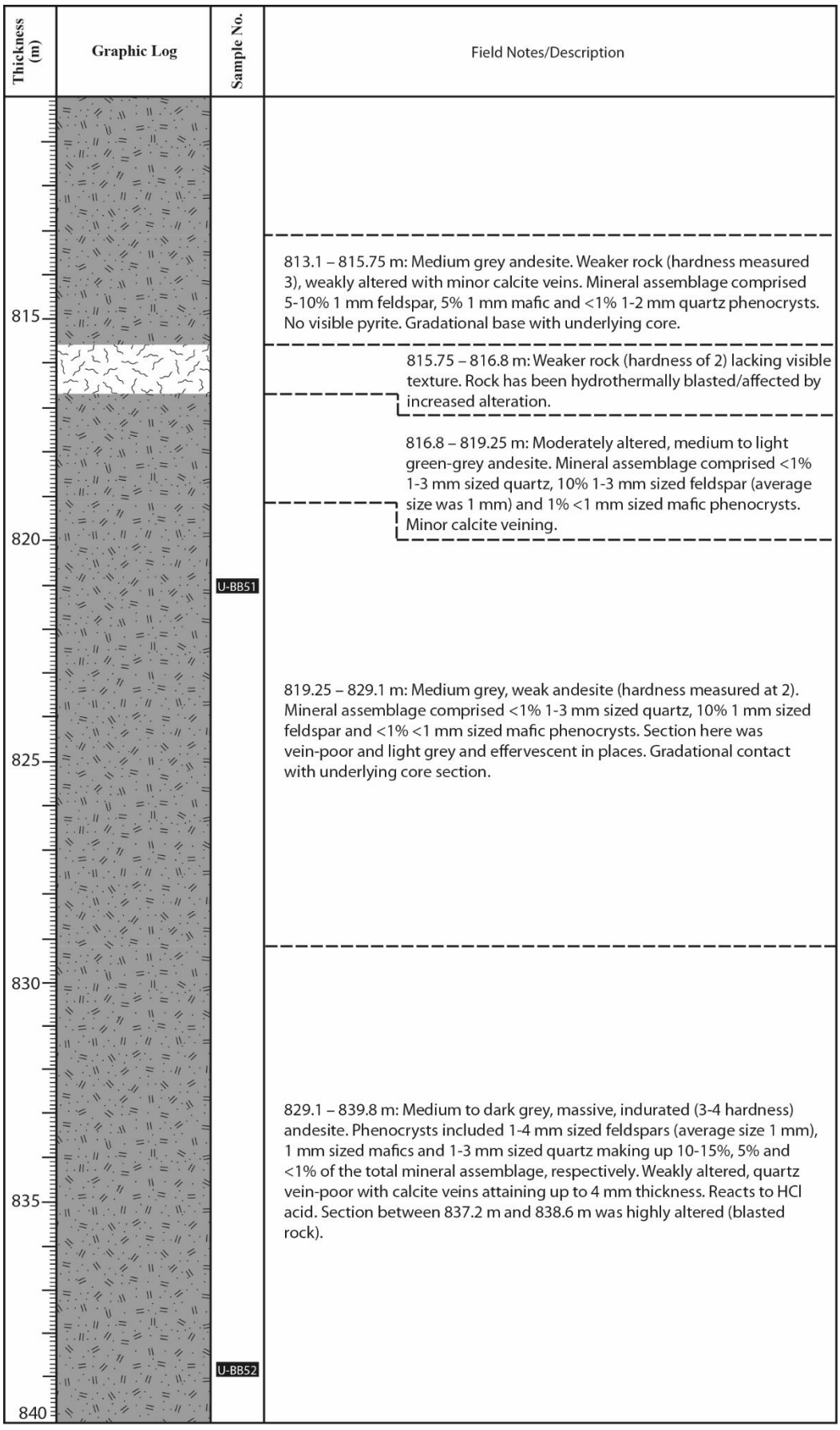
Thickness (m)
Graphic Log
Sample No.
Field Notes/Description
815
820
825
830
835
840
U-BB51
U-BB52
813.1 – 815.75 m: Medium grey andesite. Weaker rock (hardness measured 3), weakly altered with minor calcite veins. Mineral assemblage comprised 5-10% 1 mm feldspar, 5% 1 mm mafic and <1% 1-2 mm quartz phenocrysts. No visible pyrite. Gradational base with underlying core.
815.75 – 816.8 m: Weaker rock (hardness of 2) lacking visible texture. Rock has been hydrothermally blasted/affected by increased alteration.
816.8 – 819.25 m: Moderately altered, medium to light green-grey andesite. Mineral assemblage comprised <1% 1-3 mm sized quartz, 10% 1-3 mm sized feldspar (average size was 1 mm) and 1% <1 mm sized mafic phenocrysts. Minor calcite veining.
819.25 – 829.1 m: Medium grey, weak andesite (hardness measured at 2). Mineral assemblage comprised <1% 1-3 mm sized quartz, 10% 1 mm sized feldspar and <1% <1 mm sized mafic phenocrysts. Section here was vein-poor and light grey and effervescent in places. Gradational contact with underlying core section.
829.1 – 839.8 m: Medium to dark grey, massive, indurated (3-4 hardness) andesite. Phenocrysts included 1-4 mm sized feldspars (average size 1 mm), 1 mm sized mafics and 1-3 mm sized quartz making up 10-15%, 5% and <1% of the total mineral assemblage, respectively. Weakly altered, quartz vein-poor with calcite veins attaining up to 4 mm thickness. Reacts to HCl acid. Section between 837.2 m and 838.6 m was highly altered (blasted rock).

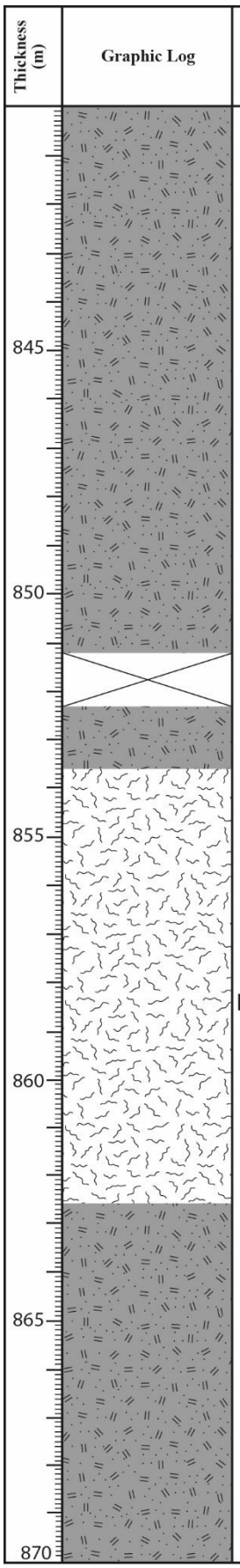

Field Notes/Description
839.8 – 851.2 m: Gradational contact with overlying unit, yielded medium grey to medium green-grey massive andesite. Contains likely shear zones, evidenced through more weakened rock, at several intervals: 844.8 m (20 cm thick), 844.3 m (12 cm), 845.7 m (13 cm), 846.2 m (20 cm) and 846.8 m (12 cm). Rock texture is visible in these weakened zones albeit more altered because of shear movement. In shear parts alteration ranges from weak to strong. Calcite veins measure up to 11 cm thick. Feldspar phenocrysts comprised 10% of the total mineral assemblage and ranged between 1 mm and 6 mm in diameter (average diameter was 1 mm). Mafic phenocrysts yielded two groups, including those <1 mm and those between 1 mm and 2 mm (1 mm average), each comprising ≤5% of the total mineral assemblage. Quartz phenocryst diameters ranged between 1 mm and 4 mm (increased from overlying section). HCl effervescent and contained very fine-grained, disseminated pyrite.
851.2 – 852.3 m: Core section missing.
852.3 – 853.6 m: Same as section 839.8 – 851.2 m, with most of the section containing broken rock rubble (from 852.3 – 852.5 m).
853.6 – 855.3 m: Weakly indurated andesite (hardness of 2), light to medium grey in places. Highly altered section of core attributed to shearing.
855.3 – 860.55 m: Medium to dark grey-green, massive, indurated (measured at 4) andesite. Total mineral assemblage was <1% 1 mm-sized feldspars, 1% 1-3 mm quartz and 3% 1 mm (very faint) green phenocrysts. Weakly to moderately altered. Quartz vein-poor, with minor calcite veins occurring as (up to) 2 mm thick bands. HCl effervescent. Gradational contact with underlying section.
862.7 – 875.5 m: Medium to dark green-grey andesite. Indurated where core is intact (hardness of 3-4). Massive structure containing more altered or shear zones of light grey, friable rock at the 863.8 – 864.1 m, 869.9 – 871.2 m and 872.5 – 873.3 m intervals. Comprises 1 mm-sized feldspars, 1-3 mm-sized quartz and 1 mm-sized mafics, collectively representing <1%, ≤1% and 5-10% of the total mineral assemblage, respectively. Mafics appeared softer and clearer than previously described in overlying core. Weakly altered where core is intact, moderately to highly altered elsewhere (weak/shear zones). Quartz vein-poor, moderate calcite veins (bands + strings) measure up to 2 mm thick. Single, subrounded, light grey, porphyritic xenolith with 10% phenocrysts made up of feldspar, quartz and mafic minerals. There is 1% pyrite which occurs as fine grained disseminations and coarser grained segregations. Moderate reaction to HCL.

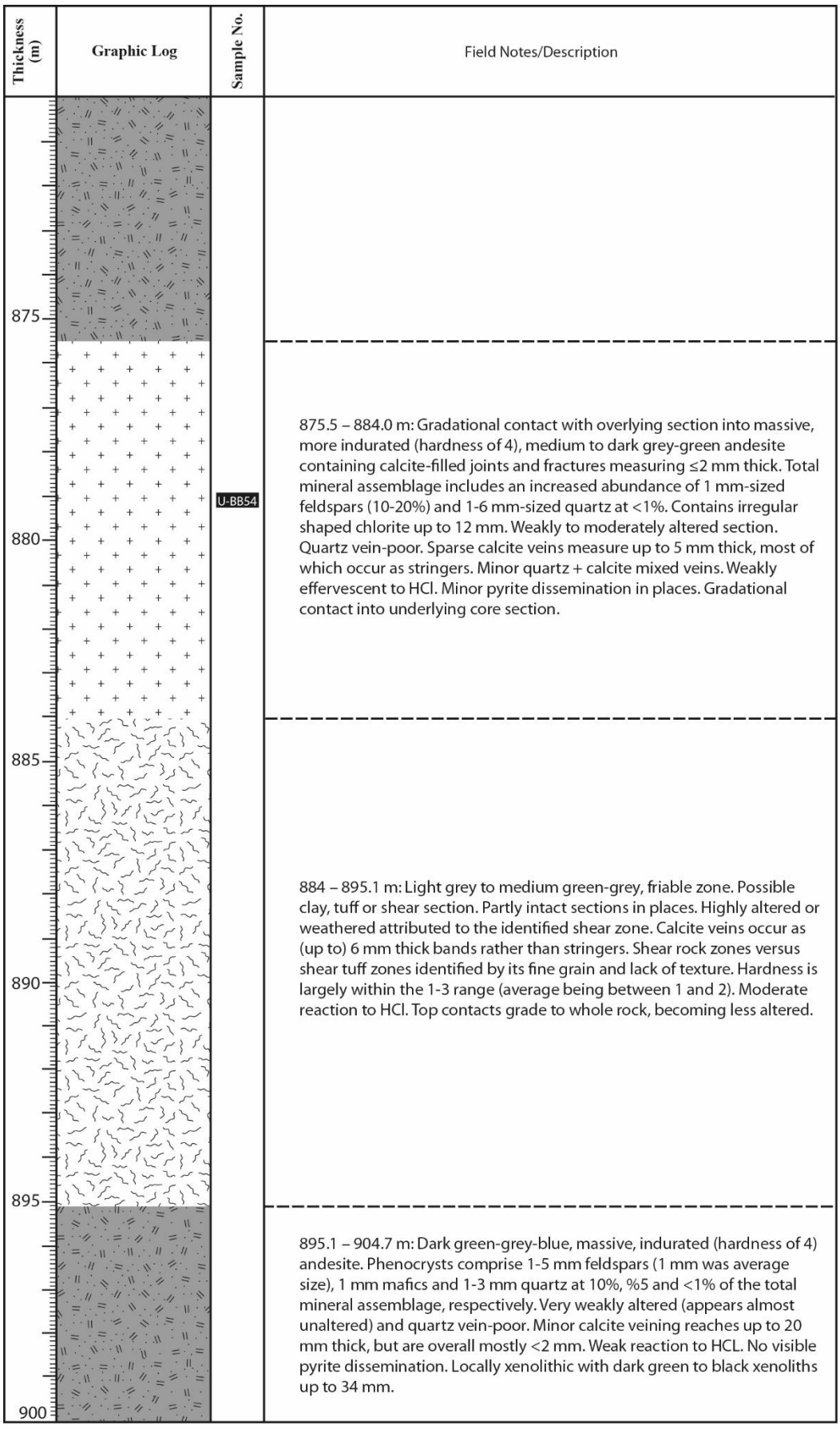
Thickness (m)
Graphic Log
Sample No.
Field Notes/Description
875
880
885
890
895
900
U-BB54
875.5 – 884.0 m: Gradational contact with overlying section into massive, more indurated (hardness of 4), medium to dark grey-green andesite containing calcite-filled joints and fractures measuring ≤2 mm thick. Total mineral assemblage includes an increased abundance of 1 mm-sized feldspars (10-20%) and 1-6 mm-sized quartz at <1%. Contains irregular shaped chlorite up to 12 mm. Weakly to moderately altered section. Quartz vein-poor. Sparse calcite veins measure up to 5 mm thick, most of which occur as stringers. Minor quartz + calcite mixed veins. Weakly effervescent to HCl. Minor pyrite dissemination in places. Gradational contact into underlying core section.
884 – 895.1 m: Light grey to medium green-grey, friable zone. Possible clay, tuff or shear section. Partly intact sections in places. Highly altered or weathered attributed to the identified shear zone. Calcite veins occur as (up to) 6 mm thick bands rather than stringers. Shear rock zones versus shear tuff zones identified by its fine grain and lack of texture. Hardness is largely within the 1-3 range (average being between 1 and 2). Moderate reaction to HCl. Top contacts grade to whole rock, becoming less altered.
895.1 – 904.7 m: Dark green-grey-blue, massive, indurated (hardness of 4) andesite. Phenocrysts comprise 1-5 mm feldspars (1 mm was average size), 1 mm mafics and 1-3 mm quartz at 10%, %5 and <1% of the total mineral assemblage, respectively. Very weakly altered (appears almost unaltered) and quartz vein-poor. Minor calcite veining reaches up to 20 mm thick, but are overall mostly <2 mm. Weak reaction to HCL. No visible pyrite dissemination. Locally xenolithic with dark green to black xenoliths up to 34 mm.

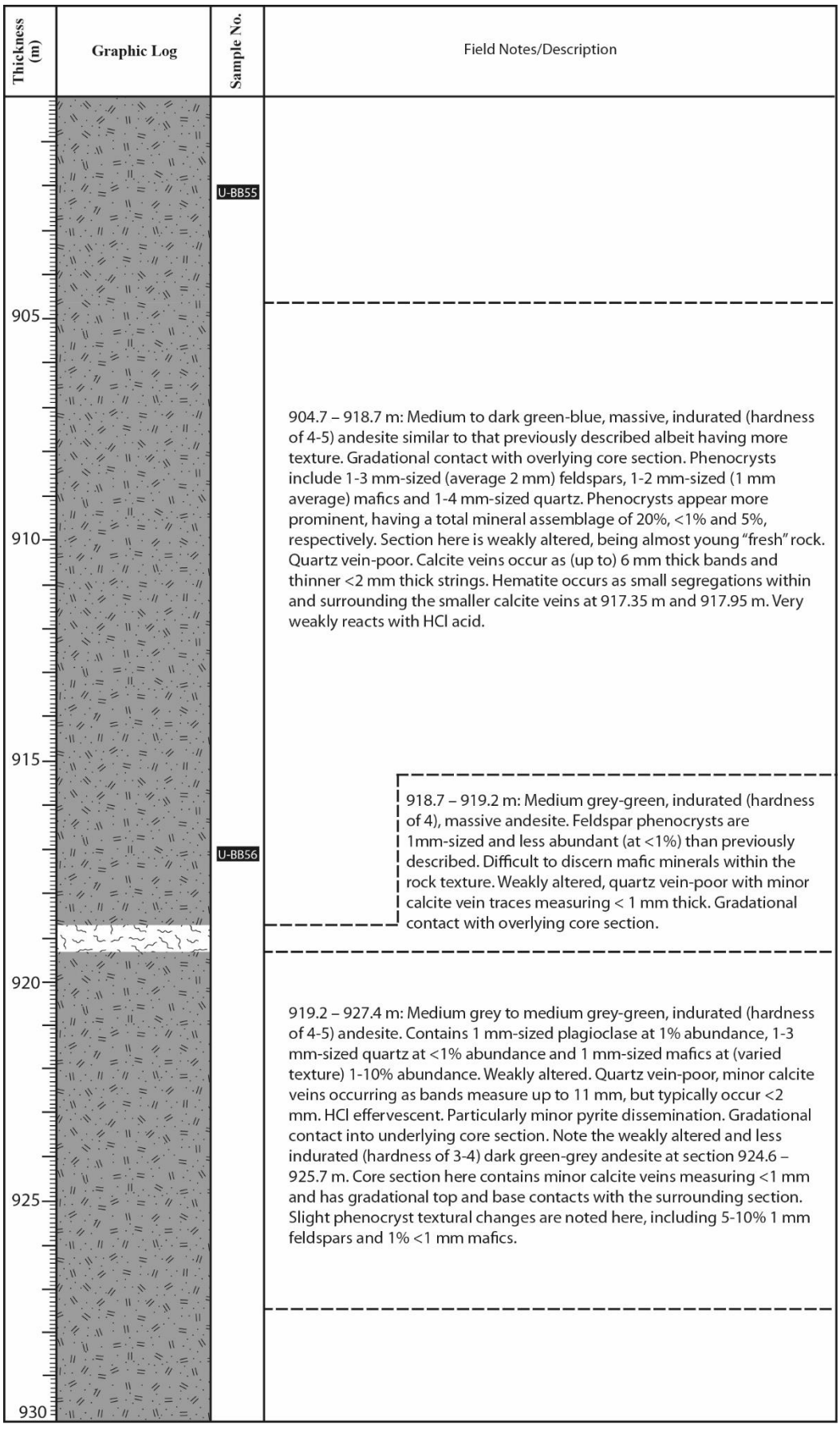
Thickness (m)
Graphic Log
Sample No.
Field Notes/Description
U-BB55
U-BB56
905
910
915
920
925
930
904.7 – 918.7 m: Medium to dark green-blue, massive, indurated (hardness of 4-5) andesite similar to that previously described albeit having more texture. Gradational contact with overlying core section. Phenocrysts include 1-3 mm-sized (average 2 mm) feldspars, 1-2 mm-sized (1 mm average) mafics and 1-4 mm-sized quartz. Phenocrysts appear more prominent, having a total mineral assemblage of 20%, <1% and 5%, respectively. Section here is weakly altered, being almost young "fresh" rock. Quartz vein-poor. Calcite veins occur as (up to) 6 mm thick bands and thinner <2 mm thick strings. Hematite occurs as small segregations within and surrounding the smaller calcite veins at 917.35 m and 917.95 m. Very weakly reacts with HCl acid.
918.7 – 919.2 m: Medium grey-green, indurated (hardness of 4), massive andesite. Feldspar phenocrysts are 1mm-sized and less abundant (at <1%) than previously described. Difficult to discern mafic minerals within the rock texture. Weakly altered, quartz vein-poor with minor calcite vein traces measuring < 1 mm thick. Gradational contact with overlying core section.
919.2 – 927.4 m: Medium grey to medium grey-green, indurated (hardness of 4-5) andesite. Contains 1 mm-sized plagioclase at 1% abundance, 1-3 mm-sized quartz at <1% abundance and 1 mm-sized mafics at (varied texture) 1-10% abundance. Weakly altered. Quartz vein-poor, minor calcite veins occurring as bands measure up to 11 mm, but typically occur <2 mm. HCl effervescent. Particularly minor pyrite dissemination. Gradational contact into underlying core section. Note the weakly altered and less indurated (hardness of 3-4) dark green-grey andesite at section 924.6 – 925.7 m. Core section here contains minor calcite veins measuring <1 mm and has gradational top and base contacts with the surrounding section. Slight phenocryst textural changes are noted here, including 5-10% 1 mm feldspars and 1% <1 mm mafics.

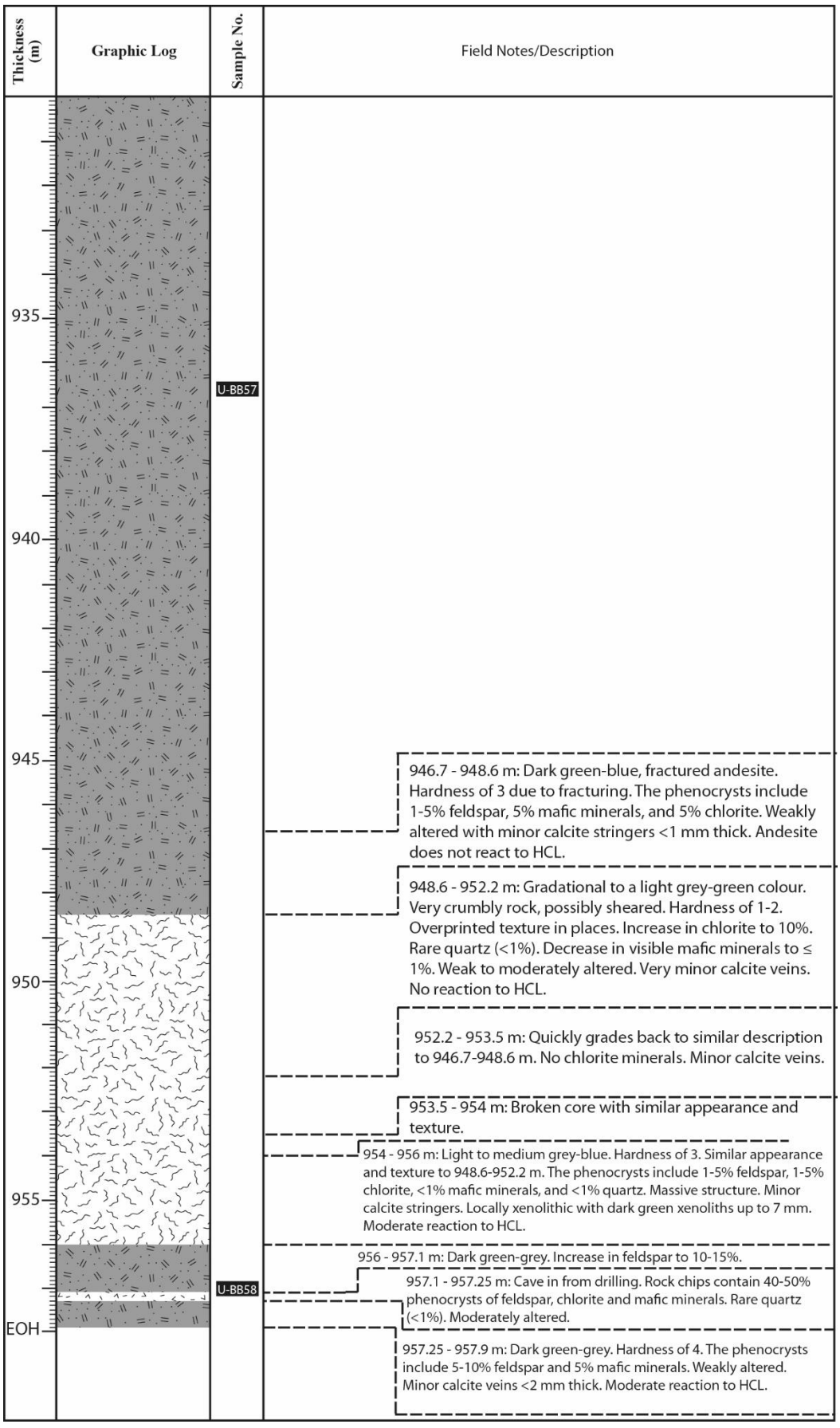
Thickness (m)
Graphic Log
Sample No.
Field Notes/Description
935
940
945
950
955
EOH
U-BB57
U-BB58
946.7 - 948.6 m: Dark green-blue, fractured andesite. Hardness of 3 due to fracturing. The phenocrysts include 1-5% feldspar, 5% mafic minerals, and 5% chlorite. Weakly altered with minor calcite stringers <1 mm thick. Andesite does not react to HCL.
948.6 - 952.2 m: Gradational to a light grey-green colour. Very crumbly rock, possibly sheared. Hardness of 1-2. Overprinted texture in places. Increase in chlorite to 10%. Rare quartz (<1%). Decrease in visible mafic minerals to ≤ 1%. Weak to moderately altered. Very minor calcite veins. No reaction to HCL.
952.2 - 953.5 m: Quickly grades back to similar description to 946.7-948.6 m. No chlorite minerals. Minor calcite veins.
953.5 - 954 m: Broken core with similar appearance and texture.
954 - 956 m: Light to medium grey-blue. Hardness of 3. Similar appearance and texture to 948.6-952.2 m. The phenocrysts include 1-5% feldspar, 1-5% chlorite, <1% mafic minerals, and <1% quartz. Massive structure. Minor calcite stringers. Locally xenolithic with dark green xenoliths up to 7 mm. Moderate reaction to HCL.
956 - 957.1 m: Dark green-grey. Increase in feldspar to 10-15%.
957.1 - 957.25 m: Cave in from drilling. Rock chips contain 40-50% phenocrysts of feldspar, chlorite and mafic minerals. Rare quartz (<1%). Moderately altered.
957.25 - 957.9 m: Dark green-grey. Hardness of 4. The phenocrysts include 5-10% feldspar and 5% mafic minerals. Weakly altered. Minor calcite veins <2 mm thick. Moderate reaction to HCL.

Drill hole SPO597 stratigraphic logs

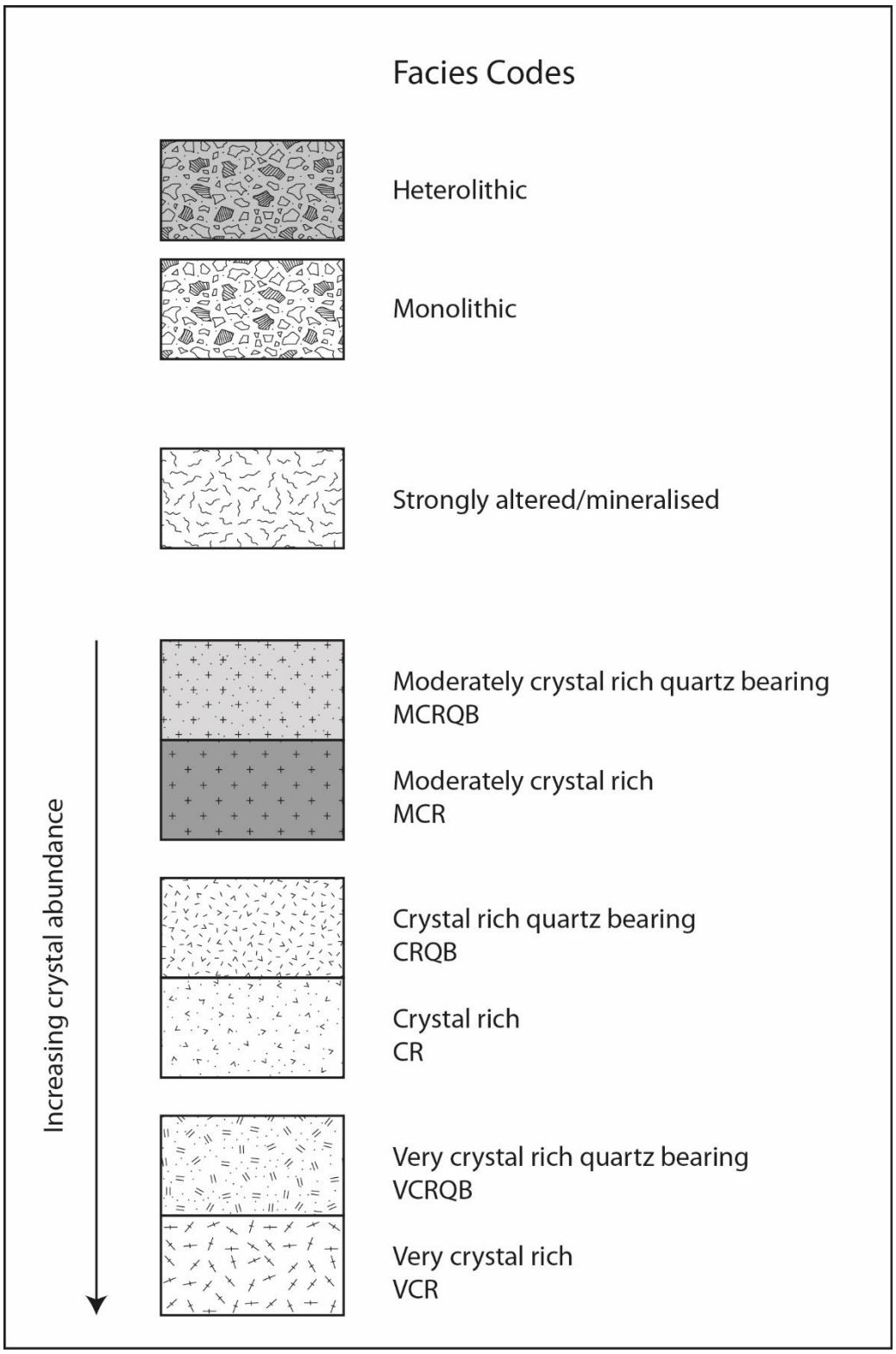

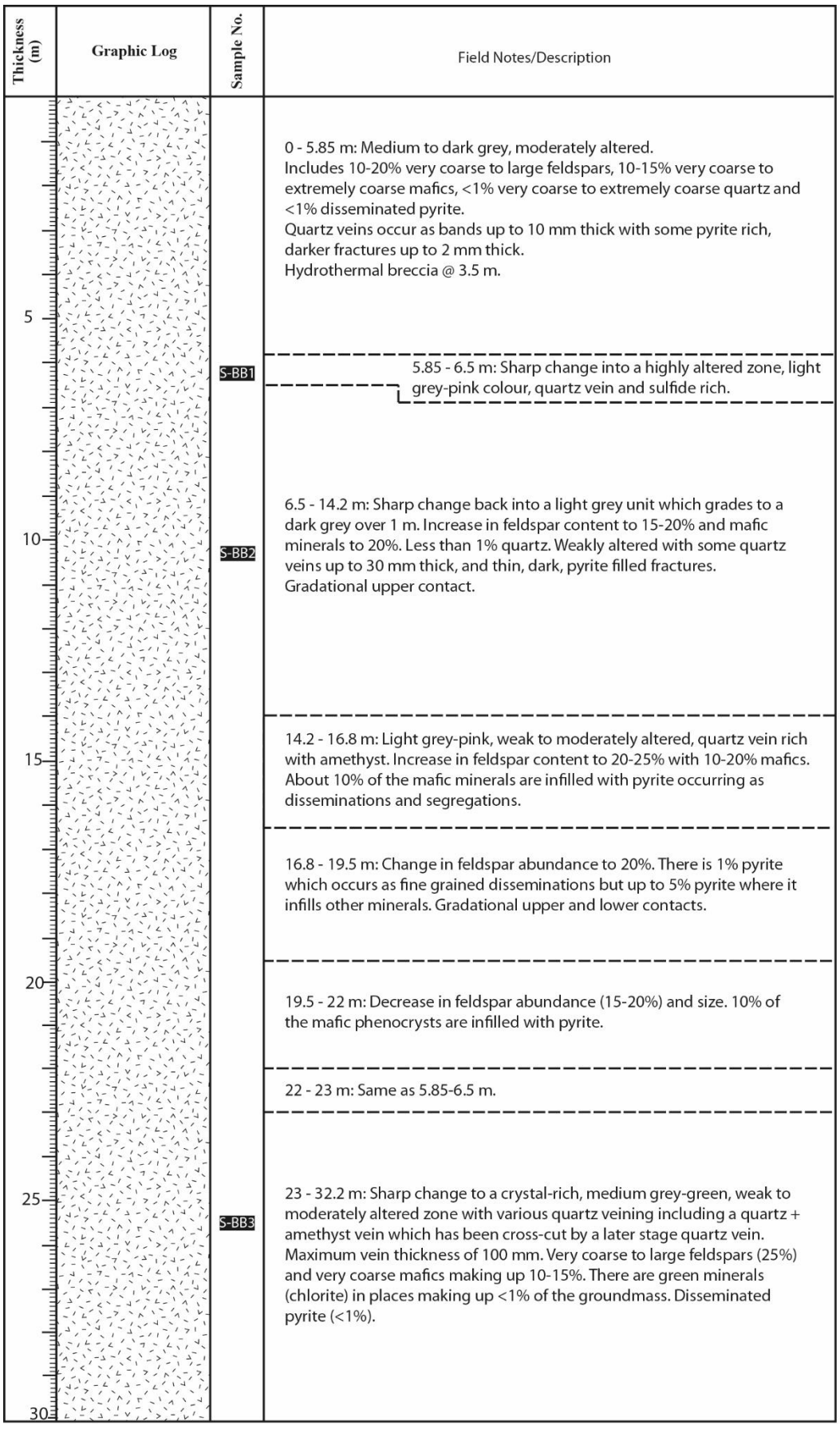
Thickness (m)
Graphic Log
Sample No.
Field Notes/Description
5
10
15
20
25
30
S-BB1
S-BB2
S-BB3
0 - 5.85 m: Medium to dark grey, moderately altered.
Includes 10-20% very coarse to large feldspars, 10-15% very coarse to extremely coarse mafics, <1% very coarse to extremely coarse quartz and <1% disseminated pyrite.
Quartz veins occur as bands up to 10 mm thick with some pyrite rich, darker fractures up to 2 mm thick.
Hydrothermal breccia @ 3.5 m.
5.85 - 6.5 m: Sharp change into a highly altered zone, light grey-pink colour, quartz vein and sulfide rich.
6.5 - 14.2 m: Sharp change back into a light grey unit which grades to a dark grey over 1 m. Increase in feldspar content to 15-20% and mafic minerals to 20%. Less than 1% quartz. Weakly altered with some quartz veins up to 30 mm thick, and thin, dark, pyrite filled fractures.
Gradational upper contact.
14.2 - 16.8 m: Light grey-pink, weak to moderately altered, quartz vein rich with amethyst. Increase in feldspar content to 20-25% with 10-20% mafics. About 10% of the mafic minerals are infilled with pyrite occurring as disseminations and segregations.
16.8 - 19.5 m: Change in feldspar abundance to 20%. There is 1% pyrite which occurs as fine grained disseminations but up to 5% pyrite where it infills other minerals. Gradational upper and lower contacts.
19.5 - 22 m: Decrease in feldspar abundance (15-20%) and size. 10% of the mafic phenocrysts are infilled with pyrite.
22 - 23 m: Same as 5.85-6.5 m.
23 - 32.2 m: Sharp change to a crystal-rich, medium grey-green, weak to moderately altered zone with various quartz veining including a quartz + amethyst vein which has been cross-cut by a later stage quartz vein. Maximum vein thickness of 100 mm. Very coarse to large feldspars (25%) and very coarse mafics making up 10-15%. There are green minerals (chlorite) in places making up <1% of the groundmass. Disseminated pyrite (<1%).

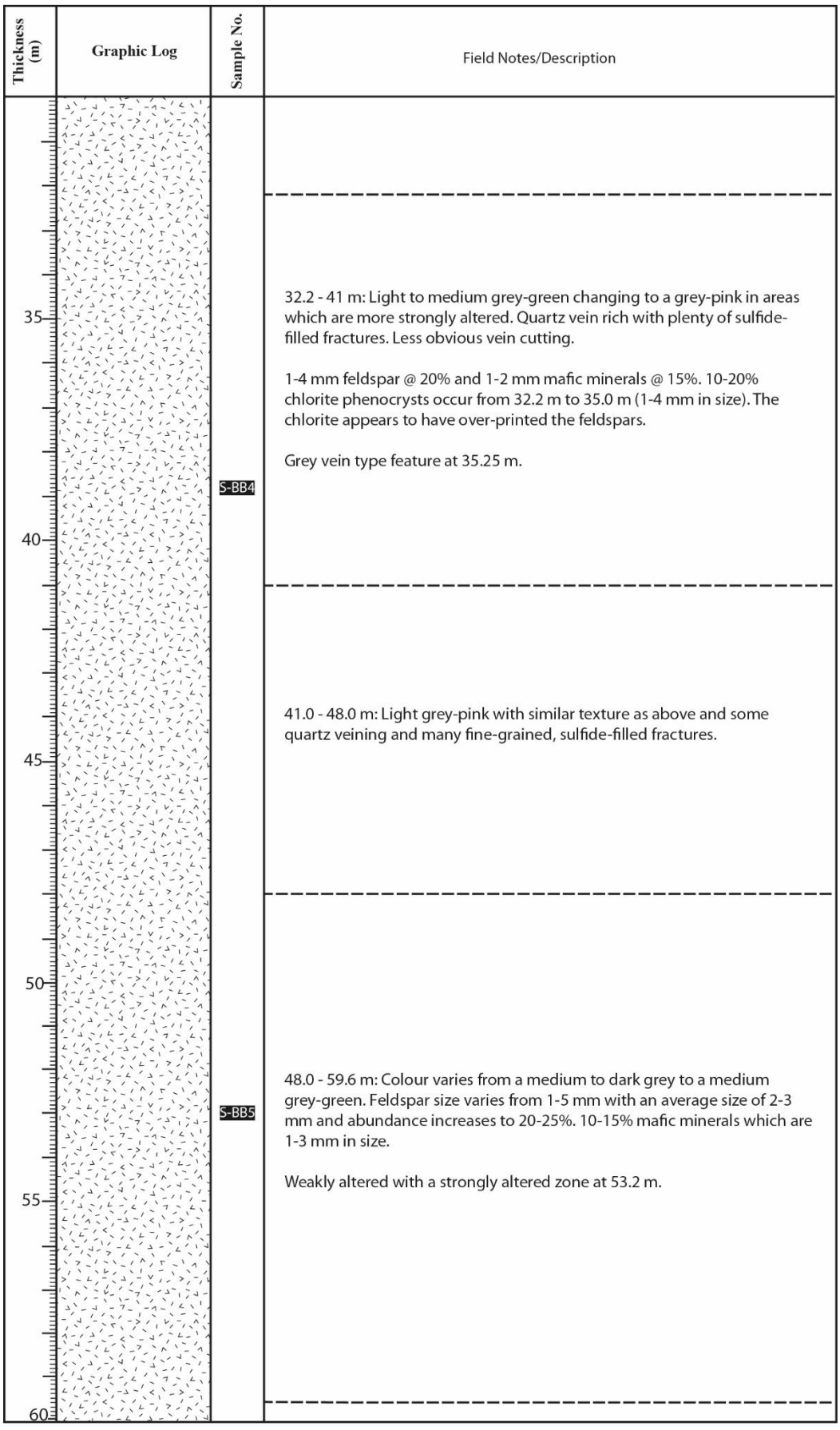
Thickness (m)
Graphic Log
Sample No.
Field Notes/Description
35
40
45
50
55
60
S-BB4
S-BB5
32.2 - 41 m: Light to medium grey-green changing to a grey-pink in areas which are more strongly altered. Quartz vein rich with plenty of sulfide-filled fractures. Less obvious vein cutting.
1-4 mm feldspar @ 20% and 1-2 mm mafic minerals @ 15%. 10-20% chlorite phenocrysts occur from 32.2 m to 35.0 m (1-4 mm in size). The chlorite appears to have over-printed the feldspars.
Grey vein type feature at 35.25 m.
41.0 - 48.0 m: Light grey-pink with similar texture as above and some quartz veining and many fine-grained, sulfide-filled fractures.
48.0 - 59.6 m: Colour varies from a medium to dark grey to a medium grey-green. Feldspar size varies from 1-5 mm with an average size of 2-3 mm and abundance increases to 20-25%. 10-15% mafic minerals which are 1-3 mm in size.
Weakly altered with a strongly altered zone at 53.2 m.

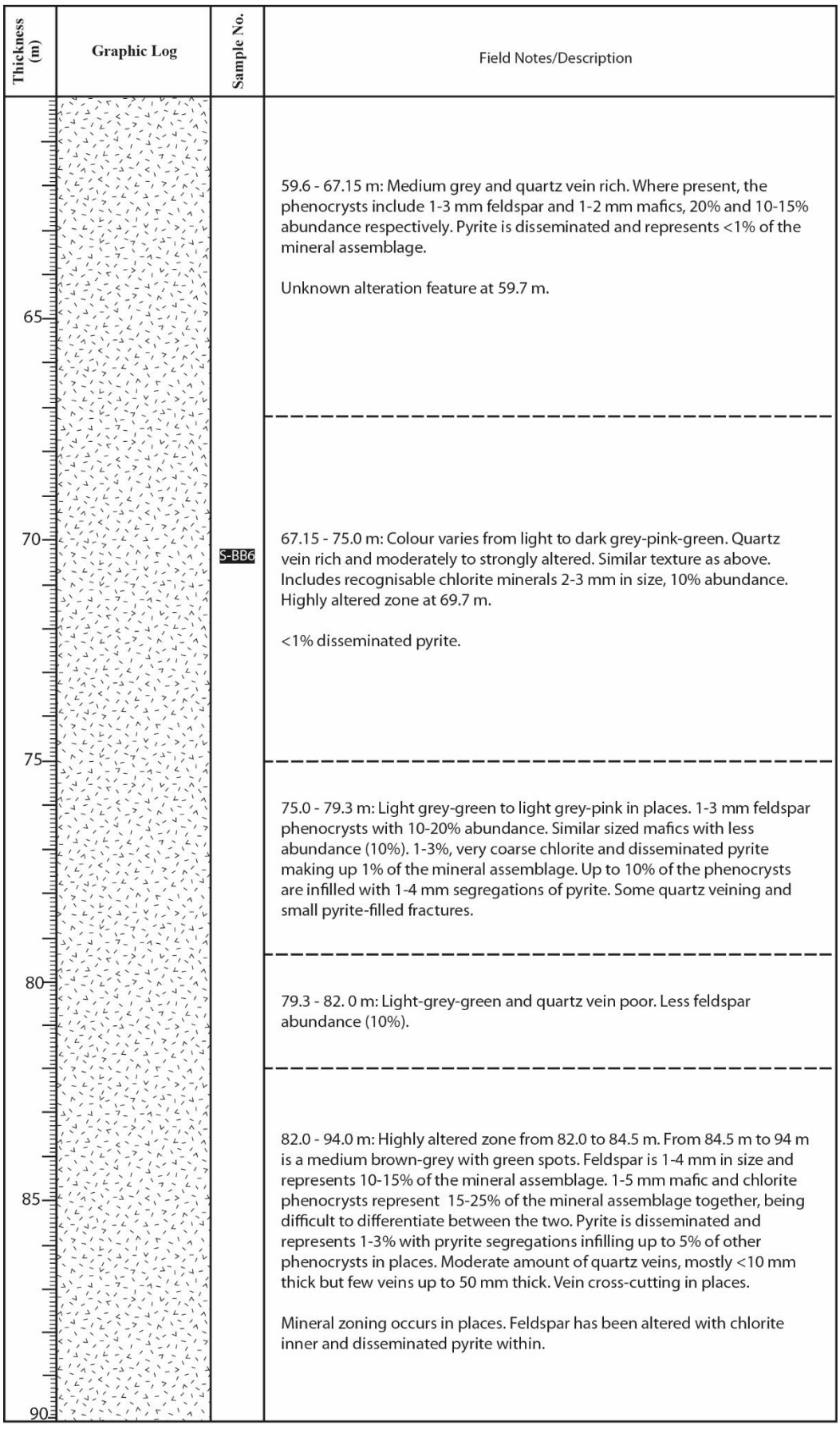
Thickness (m)
Graphic Log
Sample No.
Field Notes/Description
65
70
75
80
85
90
S-BB6
59.6 - 67.15 m: Medium grey and quartz vein rich. Where present, the phenocrysts include 1-3 mm feldspar and 1-2 mm mafics, 20% and 10-15% abundance respectively. Pyrite is disseminated and represents <1% of the mineral assemblage.
Unknown alteration feature at 59.7 m.
67.15 - 75.0 m: Colour varies from light to dark grey-pink-green. Quartz vein rich and moderately to strongly altered. Similar texture as above. Includes recognisable chlorite minerals 2-3 mm in size, 10% abundance. Highly altered zone at 69.7 m.
<1% disseminated pyrite.
75.0 - 79.3 m: Light grey-green to light grey-pink in places. 1-3 mm feldspar phenocrysts with 10-20% abundance. Similar sized mafics with less abundance (10%). 1-3%, very coarse chlorite and disseminated pyrite making up 1% of the mineral assemblage. Up to 10% of the phenocrysts are infilled with 1-4 mm segregations of pyrite. Some quartz veining and small pyrite-filled fractures.
79.3 - 82. 0 m: Light-grey-green and quartz vein poor. Less feldspar abundance (10%).
82.0 - 94.0 m: Highly altered zone from 82.0 to 84.5 m. From 84.5 m to 94 m is a medium brown-grey with green spots. Feldspar is 1-4 mm in size and represents 10-15% of the mineral assemblage. 1-5 mm mafic and chlorite phenocrysts represent 15-25% of the mineral assemblage together, being difficult to differentiate between the two. Pyrite is disseminated and represents 1-3% with pyrite segregations infilling up to 5% of other phenocrysts in places. Moderate amount of quartz veins, mostly <10 mm thick but few veins up to 50 mm thick. Vein cross-cutting in places.
Mineral zoning occurs in places. Feldspar has been altered with chlorite inner and disseminated pyrite within.

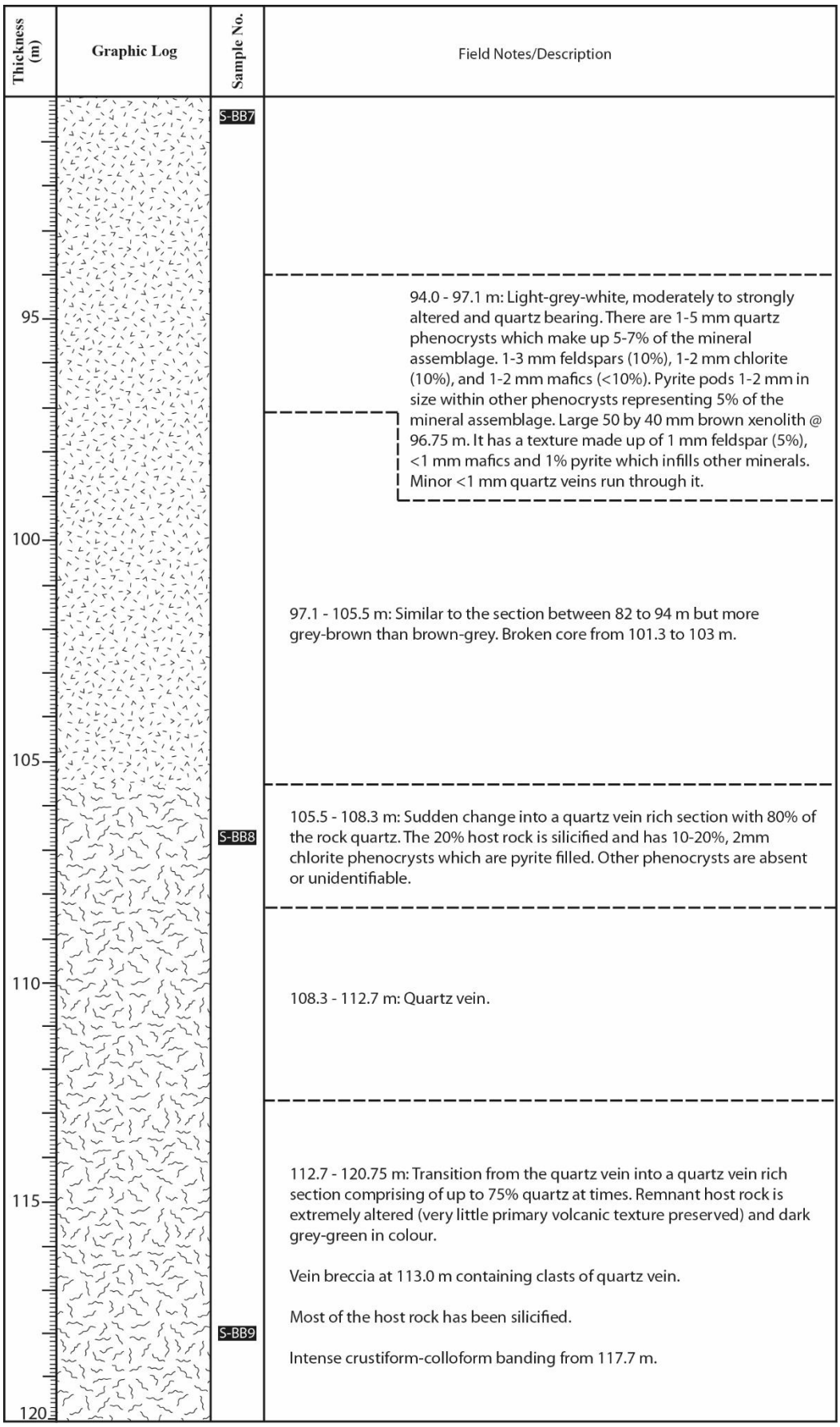
Thickness (m)
Graphic Log
Sample No.
Field Notes/Description
S-BB7
95
100
105
110
115
120
S-BB8
S-BB9
94.0 - 97.1 m: Light-grey-white, moderately to strongly altered and quartz bearing. There are 1-5 mm quartz phenocrysts which make up 5-7% of the mineral assemblage. 1-3 mm feldspars (10%), 1-2 mm chlorite (10%), and 1-2 mm mafics (<10%). Pyrite pods 1-2 mm in size within other phenocrysts representing 5% of the mineral assemblage. Large 50 by 40 mm brown xenolith @ 96.75 m. It has a texture made up of 1 mm feldspar (5%), <1 mm mafics and 1% pyrite which infills other minerals. Minor <1 mm quartz veins run through it.
97.1 - 105.5 m: Similar to the section between 82 to 94 m but more grey-brown than brown-grey. Broken core from 101.3 to 103 m.
105.5 - 108.3 m: Sudden change into a quartz vein rich section with 80% of the rock quartz. The 20% host rock is silicified and has 10-20%, 2mm chlorite phenocrysts which are pyrite filled. Other phenocrysts are absent or unidentifiable.
108.3 - 112.7 m: Quartz vein.
112.7 - 120.75 m: Transition from the quartz vein into a quartz vein rich section comprising of up to 75% quartz at times. Remnant host rock is extremely altered (very little primary volcanic texture preserved) and dark grey-green in colour.
Vein breccia at 113.0 m containing clasts of quartz vein.
Most of the host rock has been silicified.
Intense crustiform-colloform banding from 117.7 m.

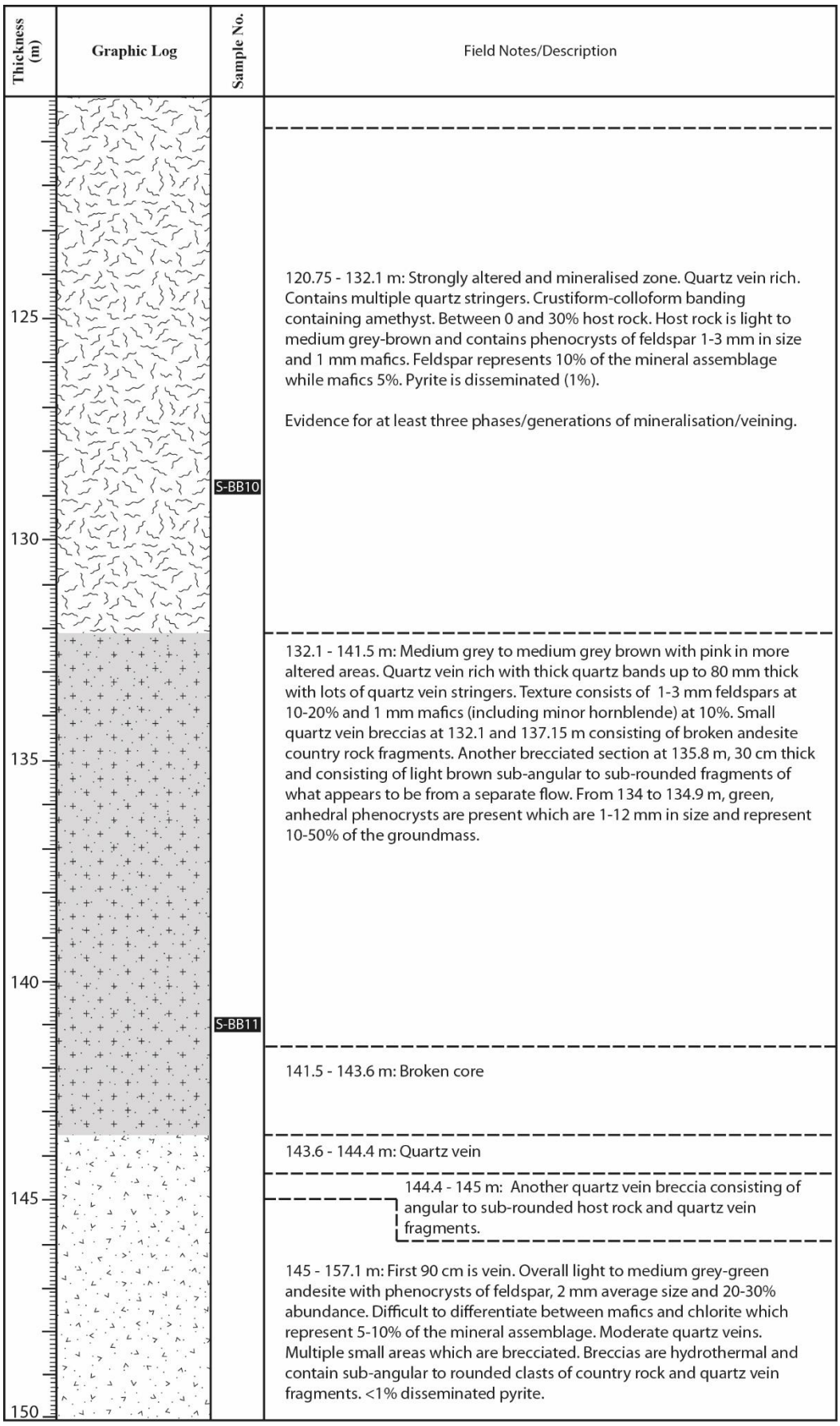
Thickness (m)
Graphic Log
Sample No.
Field Notes/Description
125
130
135
140
145
150
S-BB10
S-BB11
120.75 - 132.1 m: Strongly altered and mineralised zone. Quartz vein rich. Contains multiple quartz stringers. Crustiform-colloform banding containing amethyst. Between 0 and 30% host rock. Host rock is light to medium grey-brown and contains phenocrysts of feldspar 1-3 mm in size and 1 mm mafics. Feldspar represents 10% of the mineral assemblage while mafics 5%. Pyrite is disseminated (1%).
Evidence for at least three phases/generations of mineralisation/veining.
132.1 - 141.5 m: Medium grey to medium grey brown with pink in more altered areas. Quartz vein rich with thick quartz bands up to 80 mm thick with lots of quartz vein stringers. Texture consists of 1-3 mm feldspars at 10-20% and 1 mm mafics (including minor hornblende) at 10%. Small quartz vein breccias at 132.1 and 137.15 m consisting of broken andesite country rock fragments. Another brecciated section at 135.8 m, 30 cm thick and consisting of light brown sub-angular to sub-rounded fragments of what appears to be from a separate flow. From 134 to 134.9 m, green, anhedral phenocrysts are present which are 1-12 mm in size and represent 10-50% of the groundmass.
141.5 - 143.6 m: Broken core
143.6 - 144.4 m: Quartz vein
144.4 - 145 m: Another quartz vein breccia consisting of angular to sub-rounded host rock and quartz vein fragments.
145 - 157.1 m: First 90 cm is vein. Overall light to medium grey-green andesite with phenocrysts of feldspar, 2 mm average size and 20-30% abundance. Difficult to differentiate between mafics and chlorite which represent 5-10% of the mineral assemblage. Moderate quartz veins. Multiple small areas which are brecciated. Breccias are hydrothermal and contain sub-angular to rounded clasts of country rock and quartz vein fragments. <1% disseminated pyrite.

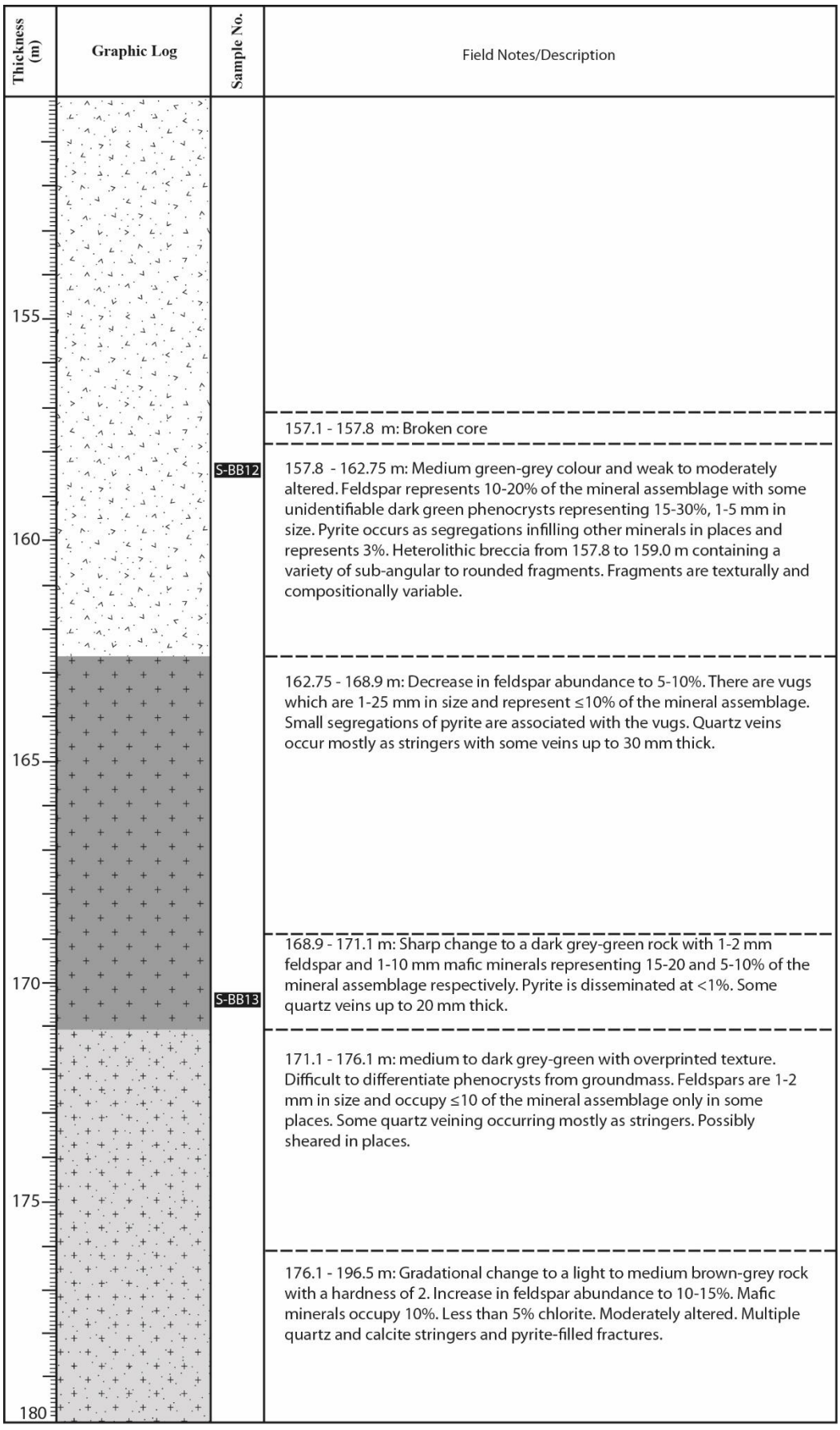
Thickness (m)
Graphic Log
Sample No.
Field Notes/Description
155
160
165
170
175
180
S-BB12
S-BB13
157.1 - 157.8 m: Broken core
157.8 - 162.75 m: Medium green-grey colour and weak to moderately altered. Feldspar represents 10-20% of the mineral assemblage with some unidentifiable dark green phenocrysts representing 15-30%, 1-5 mm in size. Pyrite occurs as segregations infilling other minerals in places and represents 3%. Heterolithic breccia from 157.8 to 159.0 m containing a variety of sub-angular to rounded fragments. Fragments are texturally and compositionally variable.
162.75 - 168.9 m: Decrease in feldspar abundance to 5-10%. There are vugs which are 1-25 mm in size and represent ≤10% of the mineral assemblage. Small segregations of pyrite are associated with the vugs. Quartz veins occur mostly as stringers with some veins up to 30 mm thick.
168.9 - 171.1 m: Sharp change to a dark grey-green rock with 1-2 mm feldspar and 1-10 mm mafic minerals representing 15-20 and 5-10% of the mineral assemblage respectively. Pyrite is disseminated at <1%. Some quartz veins up to 20 mm thick.
171.1 - 176.1 m: medium to dark grey-green with overprinted texture. Difficult to differentiate phenocrysts from groundmass. Feldspars are 1-2 mm in size and occupy ≤10 of the mineral assemblage only in some places. Some quartz veining occurring mostly as stringers. Possibly sheared in places.
176.1 - 196.5 m: Gradational change to a light to medium brown-grey rock with a hardness of 2. Increase in feldspar abundance to 10-15%. Mafic minerals occupy 10%. Less than 5% chlorite. Moderately altered. Multiple quartz and calcite stringers and pyrite-filled fractures.

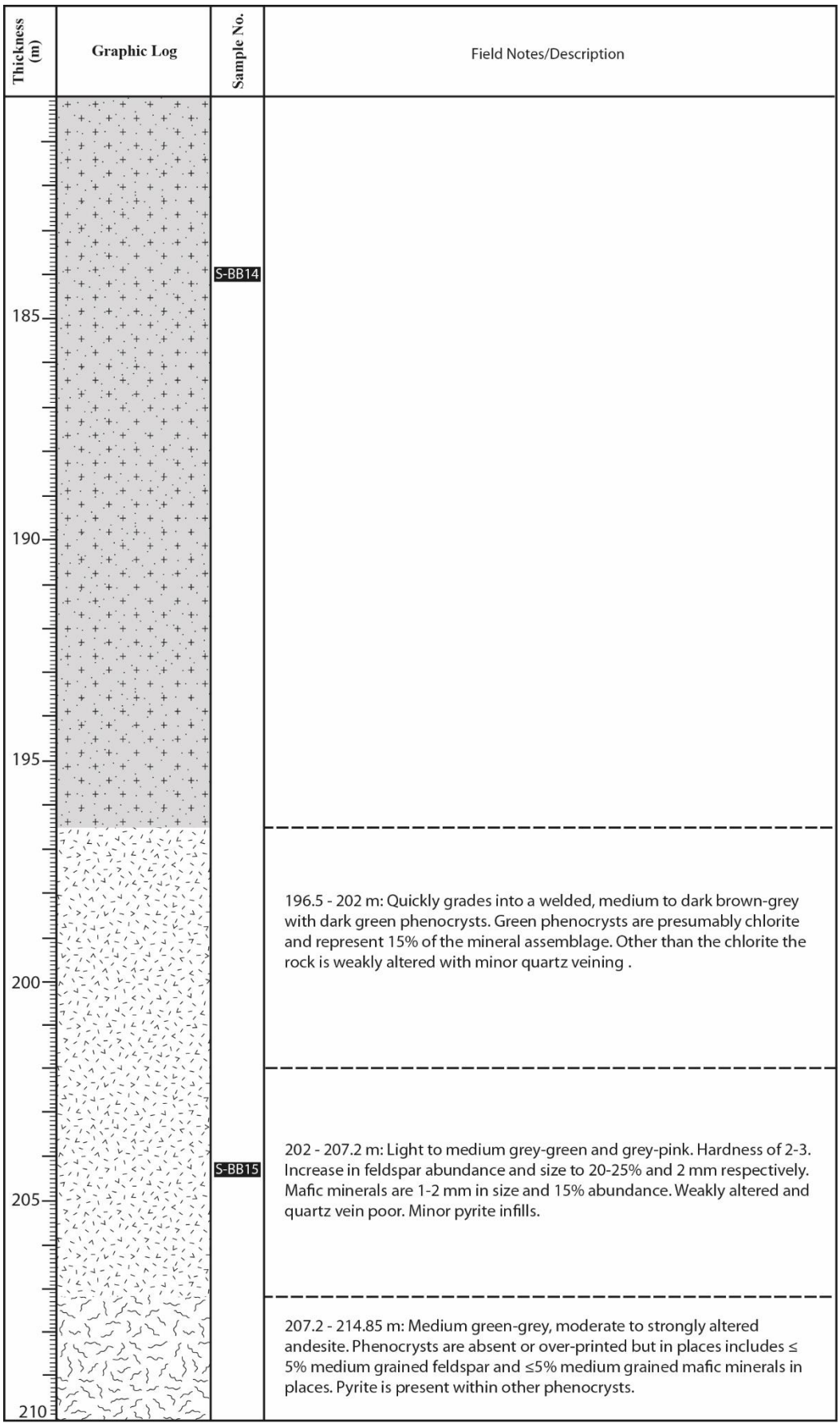
Thickness (m)
Graphic Log
Sample No.
Field Notes/Description
185
190
195
200
205
210
S-BB14
S-BB15
196.5 - 202 m: Quickly grades into a welded, medium to dark brown-grey with dark green phenocrysts. Green phenocrysts are presumably chlorite and represent 15% of the mineral assemblage. Other than the chlorite the rock is weakly altered with minor quartz veining .
202 - 207.2 m: Light to medium grey-green and grey-pink. Hardness of 2-3. Increase in feldspar abundance and size to 20-25% and 2 mm respectively. Mafic minerals are 1-2 mm in size and 15% abundance. Weakly altered and quartz vein poor. Minor pyrite infills.
207.2 - 214.85 m: Medium green-grey, moderate to strongly altered andesite. Phenocrysts are absent or over-printed but in places includes ≤ 5% medium grained feldspar and ≤5% medium grained mafic minerals in places. Pyrite is present within other phenocrysts.

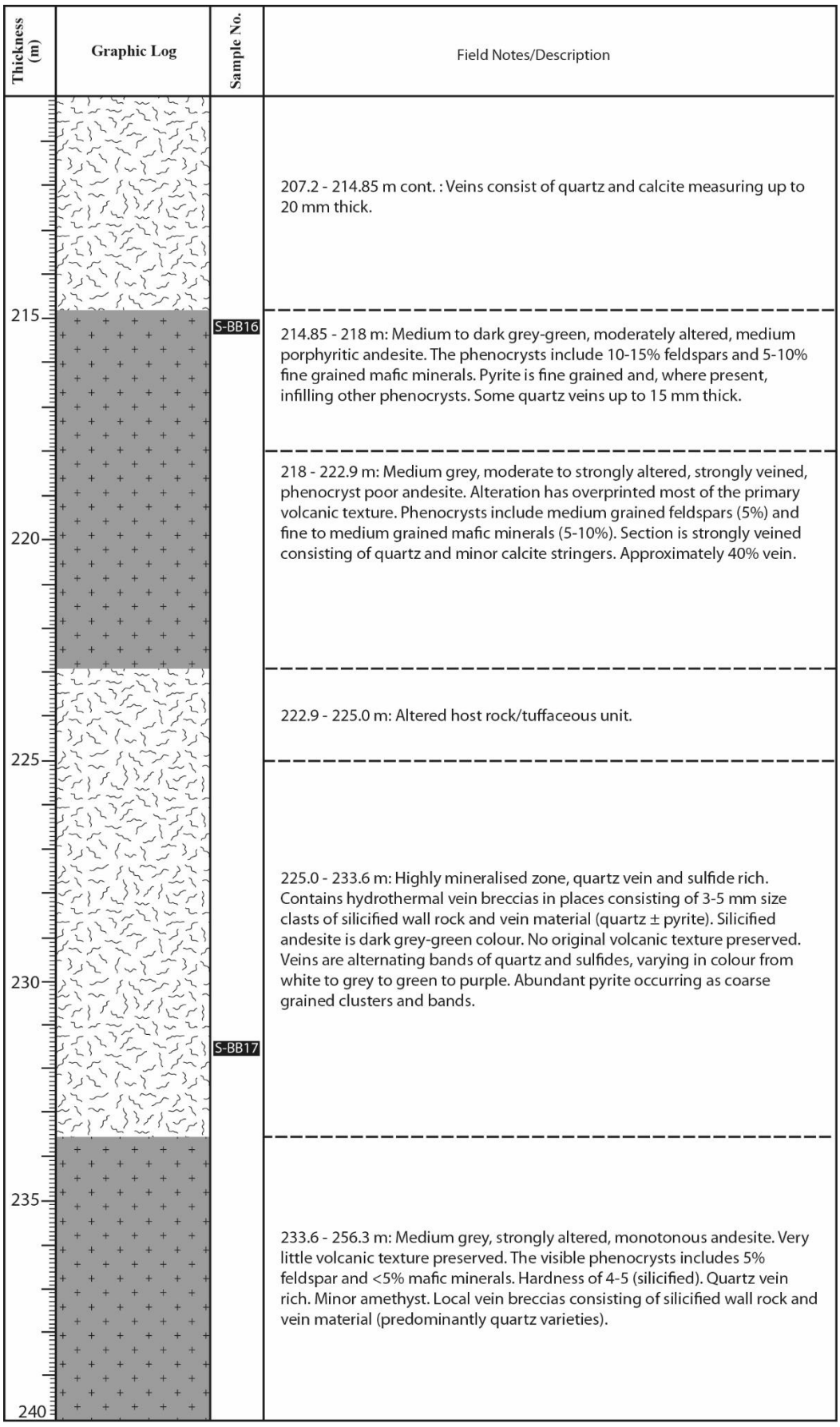
Thickness (m)
Graphic Log
Sample No.
Field Notes/Description
215
220
225
230
235
240
S-BB16
S-BB17
207.2 - 214.85 m cont. : Veins consist of quartz and calcite measuring up to 20 mm thick.
214.85 - 218 m: Medium to dark grey-green, moderately altered, medium porphyritic andesite. The phenocrysts include 10-15% feldspars and 5-10% fine grained mafic minerals. Pyrite is fine grained and, where present, infilling other phenocrysts. Some quartz veins up to 15 mm thick.
218 - 222.9 m: Medium grey, moderate to strongly altered, strongly veined, phenocryst poor andesite. Alteration has overprinted most of the primary volcanic texture. Phenocrysts include medium grained feldspars (5%) and fine to medium grained mafic minerals (5-10%). Section is strongly veined consisting of quartz and minor calcite stringers. Approximately 40% vein.
222.9 - 225.0 m: Altered host rock/tuffaceous unit.
225.0 - 233.6 m: Highly mineralised zone, quartz vein and sulfide rich. Contains hydrothermal vein breccias in places consisting of 3-5 mm size clasts of silicified wall rock and vein material (quartz ± pyrite). Silicified andesite is dark grey-green colour. No original volcanic texture preserved. Veins are alternating bands of quartz and sulfides, varying in colour from white to grey to green to purple. Abundant pyrite occurring as coarse grained clusters and bands.
233.6 - 256.3 m: Medium grey, strongly altered, monotonous andesite. Very little volcanic texture preserved. The visible phenocrysts includes 5% feldspar and <5% mafic minerals. Hardness of 4-5 (silicified). Quartz vein rich. Minor amethyst. Local vein breccias consisting of silicified wall rock and vein material (predominantly quartz varieties).

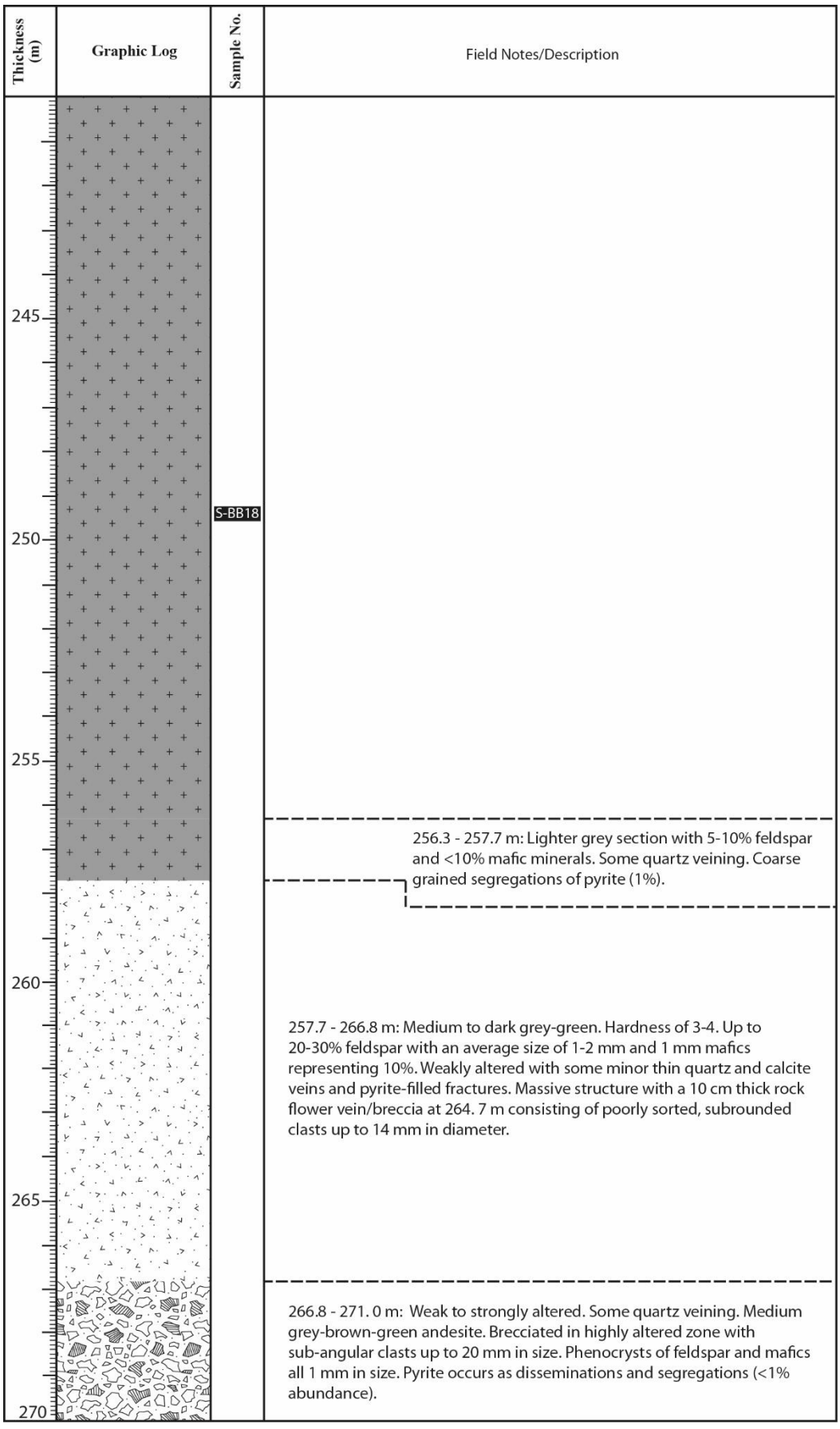
Thickness (m)
Graphic Log
Sample No.
Field Notes/Description
245
250
255
260
265
270
S-BB18
256.3 - 257.7 m: Lighter grey section with 5-10% feldspar and <10% mafic minerals. Some quartz veining. Coarse grained segregations of pyrite (1%).
257.7 - 266.8 m: Medium to dark grey-green. Hardness of 3-4. Up to 20-30% feldspar with an average size of 1-2 mm and 1 mm mafics representing 10%. Weakly altered with some minor thin quartz and calcite veins and pyrite-filled fractures. Massive structure with a 10 cm thick rock flower vein/breccia at 264. 7 m consisting of poorly sorted, subrounded clasts up to 14 mm in diameter.
266.8 - 271. 0 m: Weak to strongly altered. Some quartz veining. Medium grey-brown-green andesite. Brecciated in highly altered zone with sub-angular clasts up to 20 mm in size. Phenocrysts of feldspar and mafics all 1 mm in size. Pyrite occurs as disseminations and segregations (<1% abundance).

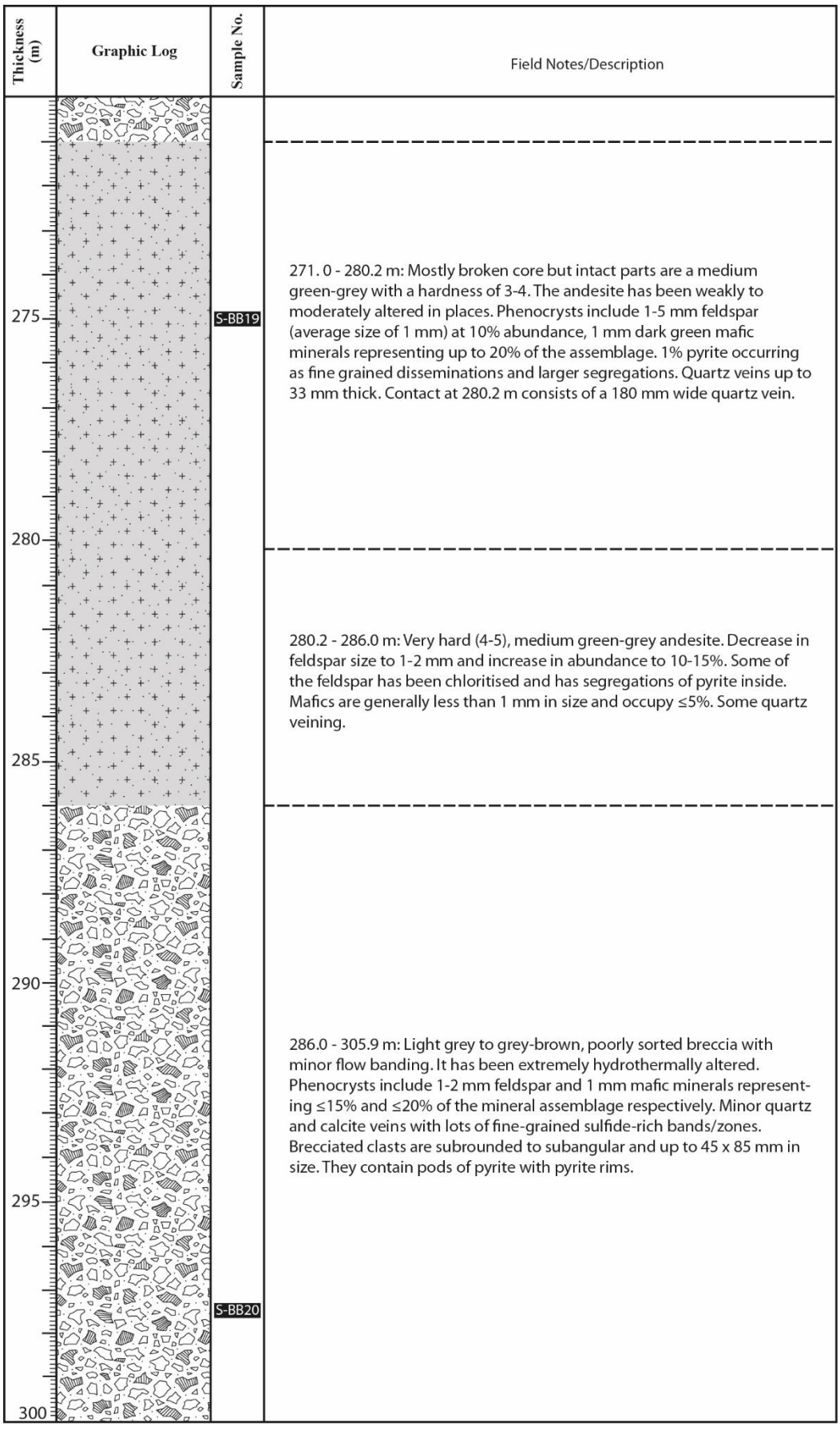
Thickness (m)
Graphic Log
Sample No.
Field Notes/Description
275
280
285
290
295
300
S-BB19
S-BB20
271. 0 - 280.2 m: Mostly broken core but intact parts are a medium green-grey with a hardness of 3-4. The andesite has been weakly to moderately altered in places. Phenocrysts include 1-5 mm feldspar (average size of 1 mm) at 10% abundance, 1 mm dark green mafic minerals representing up to 20% of the assemblage. 1% pyrite occurring as fine grained disseminations and larger segregations. Quartz veins up to 33 mm thick. Contact at 280.2 m consists of a 180 mm wide quartz vein.
280.2 - 286.0 m: Very hard (4-5), medium green-grey andesite. Decrease in feldspar size to 1-2 mm and increase in abundance to 10-15%. Some of the feldspar has been chloritised and has segregations of pyrite inside. Mafics are generally less than 1 mm in size and occupy ≤5%. Some quartz veining.
286.0 - 305.9 m: Light grey to grey-brown, poorly sorted breccia with minor flow banding. It has been extremely hydrothermally altered. Phenocrysts include 1-2 mm feldspar and 1 mm mafic minerals representing ≤15% and ≤20% of the mineral assemblage respectively. Minor quartz and calcite veins with lots of fine-grained sulfide-rich bands/zones. Brecciated clasts are subrounded to subangular and up to 45 x 85 mm in size. They contain pods of pyrite with pyrite rims.

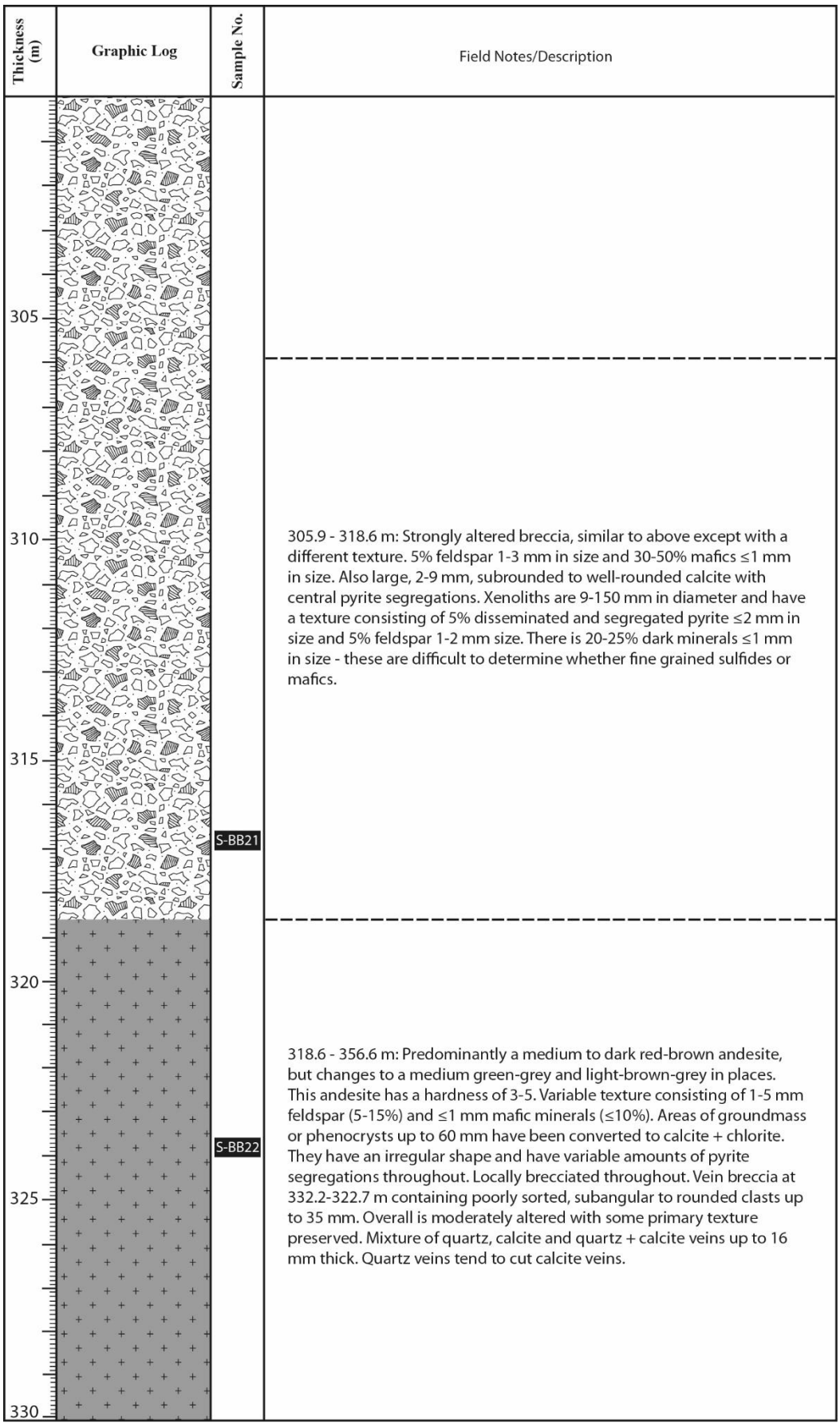
Thickness (m)
Graphic Log
Sample No.
Field Notes/Description
305
310
315
320
325
330
S-BB21
S-BB22
305.9 - 318.6 m: Strongly altered breccia, similar to above except with a different texture. 5% feldspar 1-3 mm in size and 30-50% mafics ≤1 mm in size. Also large, 2-9 mm, subrounded to well-rounded calcite with central pyrite segregations. Xenoliths are 9-150 mm in diameter and have a texture consisting of 5% disseminated and segregated pyrite ≤2 mm in size and 5% feldspar 1-2 mm size. There is 20-25% dark minerals ≤1 mm in size - these are difficult to determine whether fine grained sulfides or mafics.
318.6 - 356.6 m: Predominantly a medium to dark red-brown andesite, but changes to a medium green-grey and light-brown-grey in places. This andesite has a hardness of 3-5. Variable texture consisting of 1-5 mm feldspar (5-15%) and ≤1 mm mafic minerals (≤10%). Areas of groundmass or phenocrysts up to 60 mm have been converted to calcite + chlorite. They have an irregular shape and have variable amounts of pyrite segregations throughout. Locally brecciated throughout. Vein breccia at 332.2-322.7 m containing poorly sorted, subangular to rounded clasts up to 35 mm. Overall is moderately altered with some primary texture preserved. Mixture of quartz, calcite and quartz + calcite veins up to 16 mm thick. Quartz veins tend to cut calcite veins.

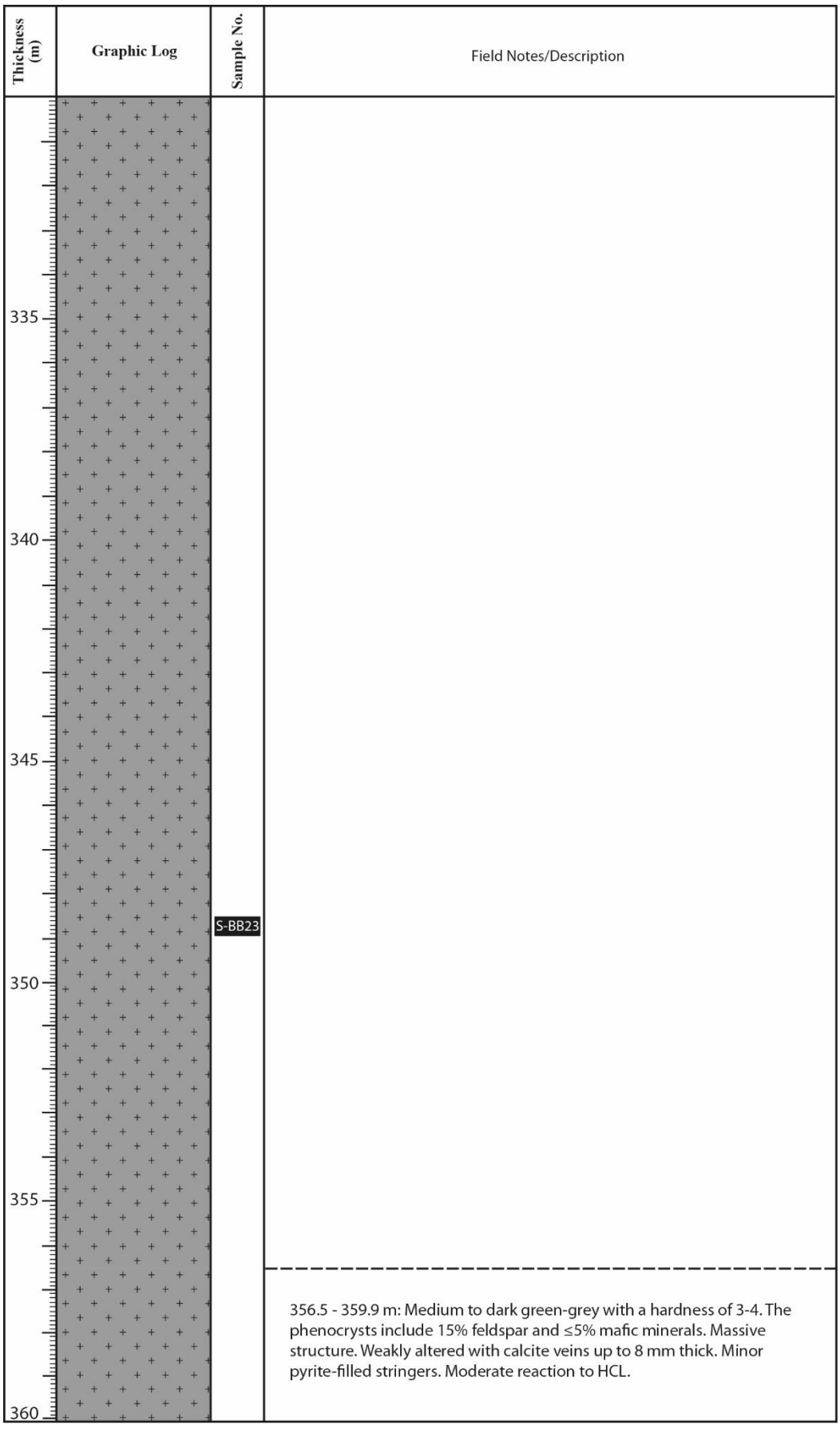
Thickness (m)
Graphic Log
Sample No.
Field Notes/Description
335
340
345
350
355
360
S-BB23
356.5 - 359.9 m: Medium to dark green-grey with a hardness of 3-4. The phenocrysts include 15% feldspar and ≤5% mafic minerals. Massive structure. Weakly altered with calcite veins up to 8 mm thick. Minor pyrite-filled stringers. Moderate reaction to HCL.

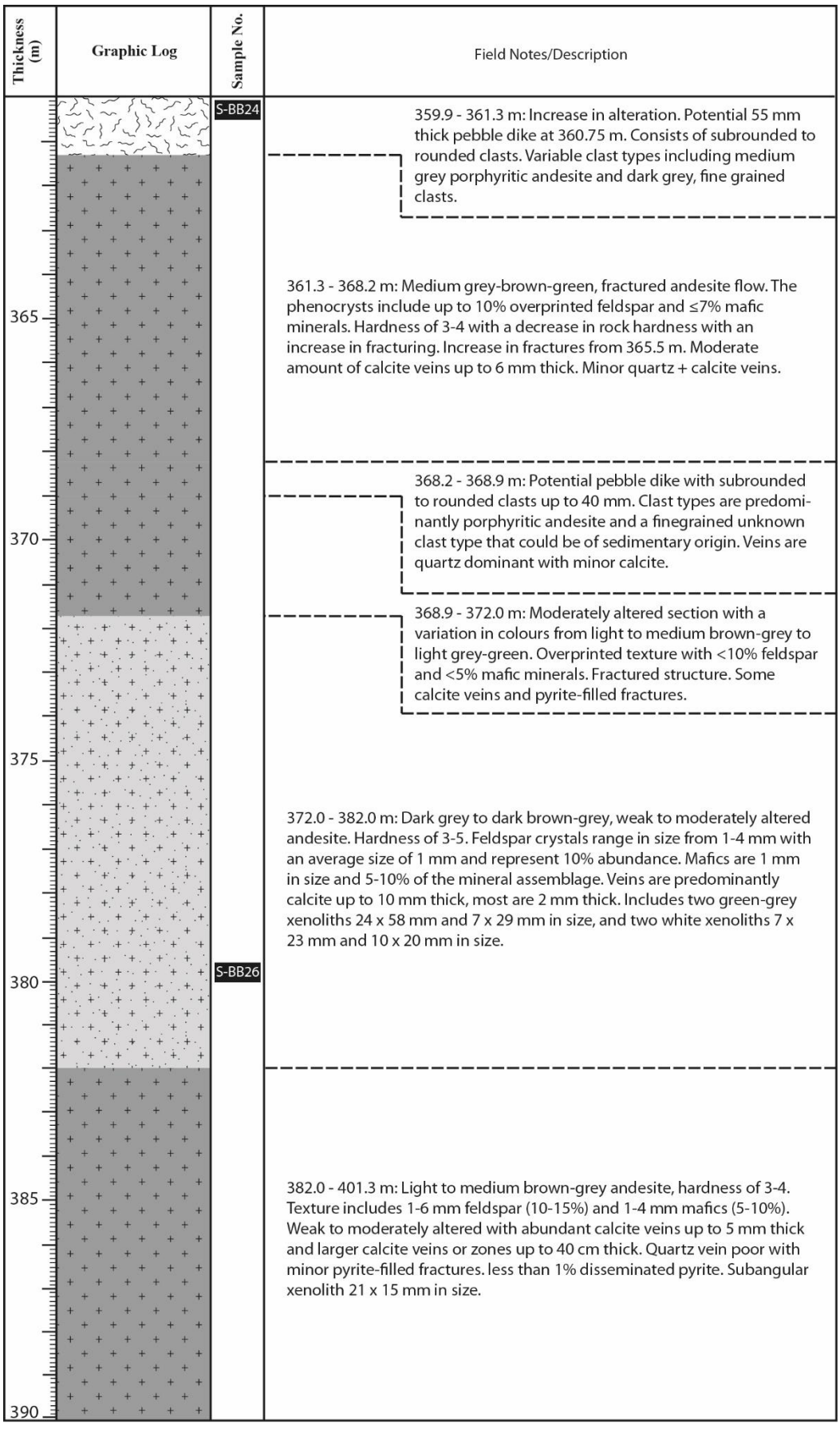
Thickness (m)
Graphic Log
Sample No.
Field Notes/Description
S-BB24
359.9 - 361.3 m: Increase in alteration. Potential 55 mm thick pebble dike at 360.75 m. Consists of subrounded to rounded clasts. Variable clast types including medium grey porphyritic andesite and dark grey, fine grained clasts.
361.3 - 368.2 m: Medium grey-brown-green, fractured andesite flow. The phenocrysts include up to 10% overprinted feldspar and ≤7% mafic minerals. Hardness of 3-4 with a decrease in rock hardness with an increase in fracturing. Increase in fractures from 365.5 m. Moderate amount of calcite veins up to 6 mm thick. Minor quartz + calcite veins.
365
368.2 - 368.9 m: Potential pebble dike with subrounded to rounded clasts up to 40 mm. Clast types are predominantly porphyritic andesite and a finegrained unknown clast type that could be of sedimentary origin. Veins are quartz dominant with minor calcite.
370
368.9 - 372.0 m: Moderately altered section with a variation in colours from light to medium brown-grey to light grey-green. Overprinted texture with <10% feldspar and <5% mafic minerals. Fractured structure. Some calcite veins and pyrite-filled fractures.
375
372.0 - 382.0 m: Dark grey to dark brown-grey, weak to moderately altered andesite. Hardness of 3-5. Feldspar crystals range in size from 1-4 mm with an average size of 1 mm and represent 10% abundance. Mafics are 1 mm in size and 5-10% of the mineral assemblage. Veins are predominantly calcite up to 10 mm thick, most are 2 mm thick. Includes two green-grey xenoliths 24 x 58 mm and 7 x 29 mm in size, and two white xenoliths 7 x 23 mm and 10 x 20 mm in size.
S-BB26
380
382.0 - 401.3 m: Light to medium brown-grey andesite, hardness of 3-4. Texture includes 1-6 mm feldspar (10-15%) and 1-4 mm mafics (5-10%). Weak to moderately altered with abundant calcite veins up to 5 mm thick and larger calcite veins or zones up to 40 cm thick. Quartz vein poor with minor pyrite-filled fractures. less than 1% disseminated pyrite. Subangular xenolith 21 x 15 mm in size.
385
390

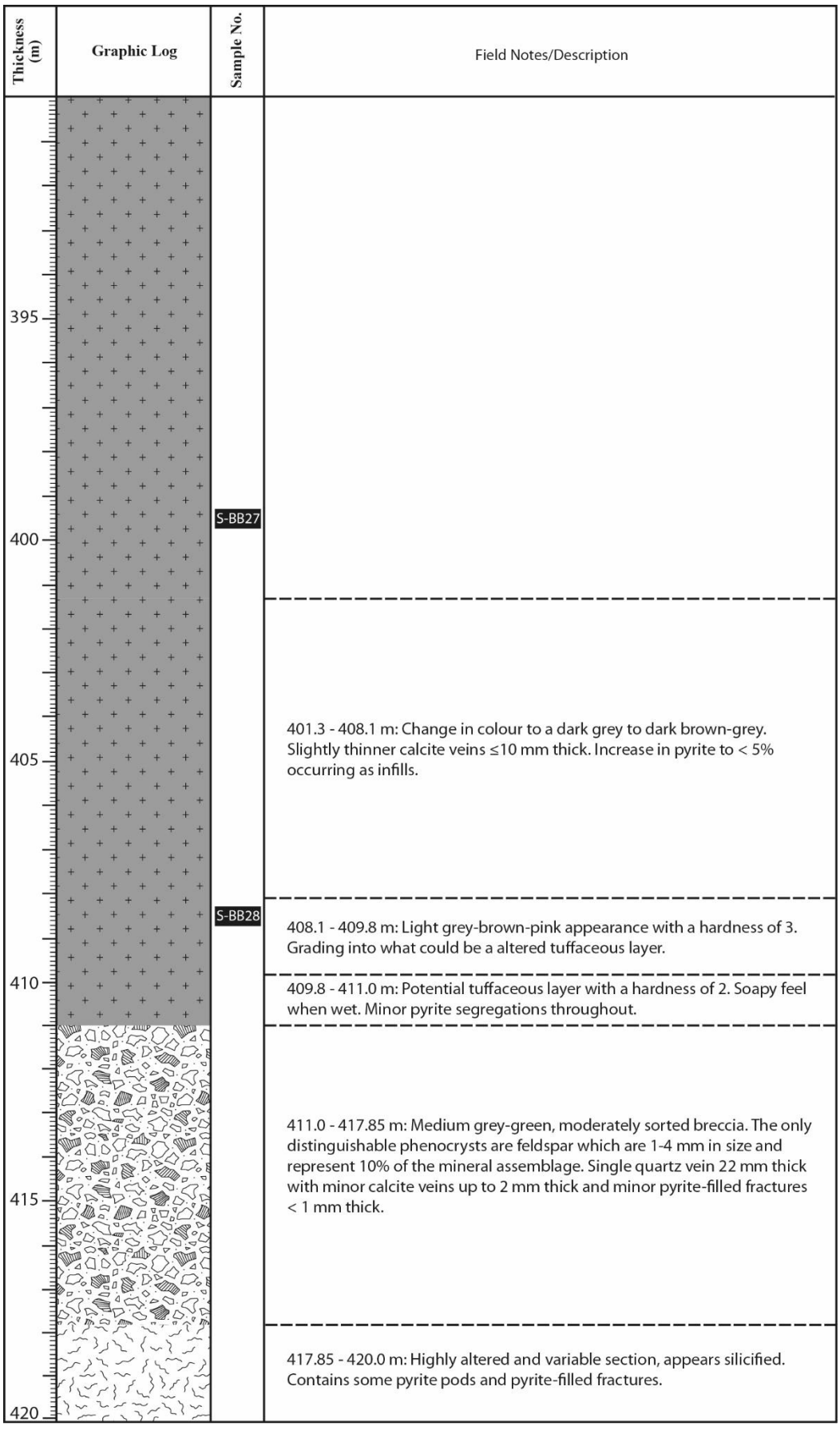
Thickness (m)
Graphic Log
Sample No.
Field Notes/Description
395
400
405
410
415
420
S-BB27
S-BB28
401.3 - 408.1 m: Change in colour to a dark grey to dark brown-grey. Slightly thinner calcite veins ≤10 mm thick. Increase in pyrite to < 5% occurring as infills.
408.1 - 409.8 m: Light grey-brown-pink appearance with a hardness of 3. Grading into what could be a altered tuffaceous layer.
409.8 - 411.0 m: Potential tuffaceous layer with a hardness of 2. Soapy feel when wet. Minor pyrite segregations throughout.
411.0 - 417.85 m: Medium grey-green, moderately sorted breccia. The only distinguishable phenocrysts are feldspar which are 1-4 mm in size and represent 10% of the mineral assemblage. Single quartz vein 22 mm thick with minor calcite veins up to 2 mm thick and minor pyrite-filled fractures < 1 mm thick.
417.85 - 420.0 m: Highly altered and variable section, appears silicified. Contains some pyrite pods and pyrite-filled fractures.

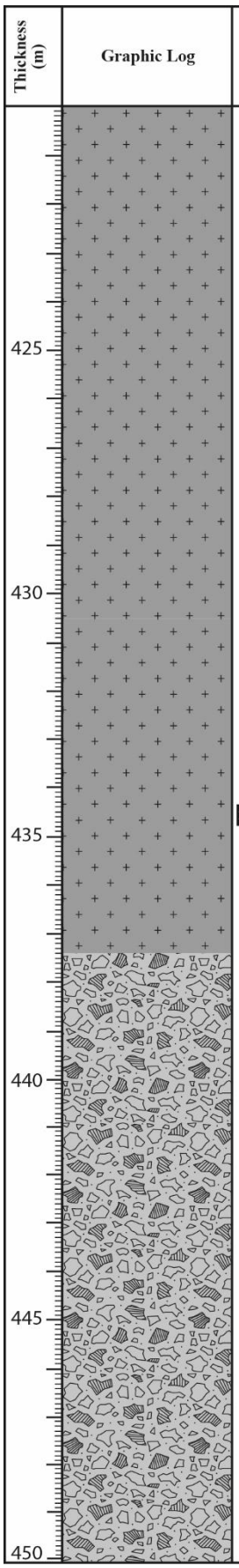

Thickness (m)	Graphic Log	Sample No.	Field Notes/Description
			420.0 - 430.5 m: Light grey-green, hardness of 3-4. Most of the texture has been overprinted. Some 1 mm feldspar with 10% abundance. Also includes large, green phenocrysts or altered groundmass of chlorite up to 16 mm in size. Quartz veins up to 7 mm thick and calcite veins up to 2mm thick. Some other dark green fractures with pyrite.
		S-BB29	430.5 - 437.5 m: Grades into a medium to dark grey-green. Hardness of 4-5 (darker coloured rock being the harder). Variable texture as it has been overprinted in places. Includes 1 mm feldspar with ≤10% abundance and ≤ 1mm mafics with ≤5% abundance. Weak to moderately altered. Veins are mostly quartz + calcite. Some dark fractures with and without pyrite. Minor pyrite infills.
			437.5 - 459.6 m: Gradational into a light to medium green-grey andesite. Brecciated in places and consisting of heterolithic subangular to subrounded clasts up to 15 x 15 mm in size, moderately sorted. Mineralogy includes 10% feldspar 1 mm in size. Difficult to distinguish other minerals because of host rock colour and degree of alteration. There is also large chloritised groundmass or inclusions up to 15 x 46 mm in size which are sometimes aligned.

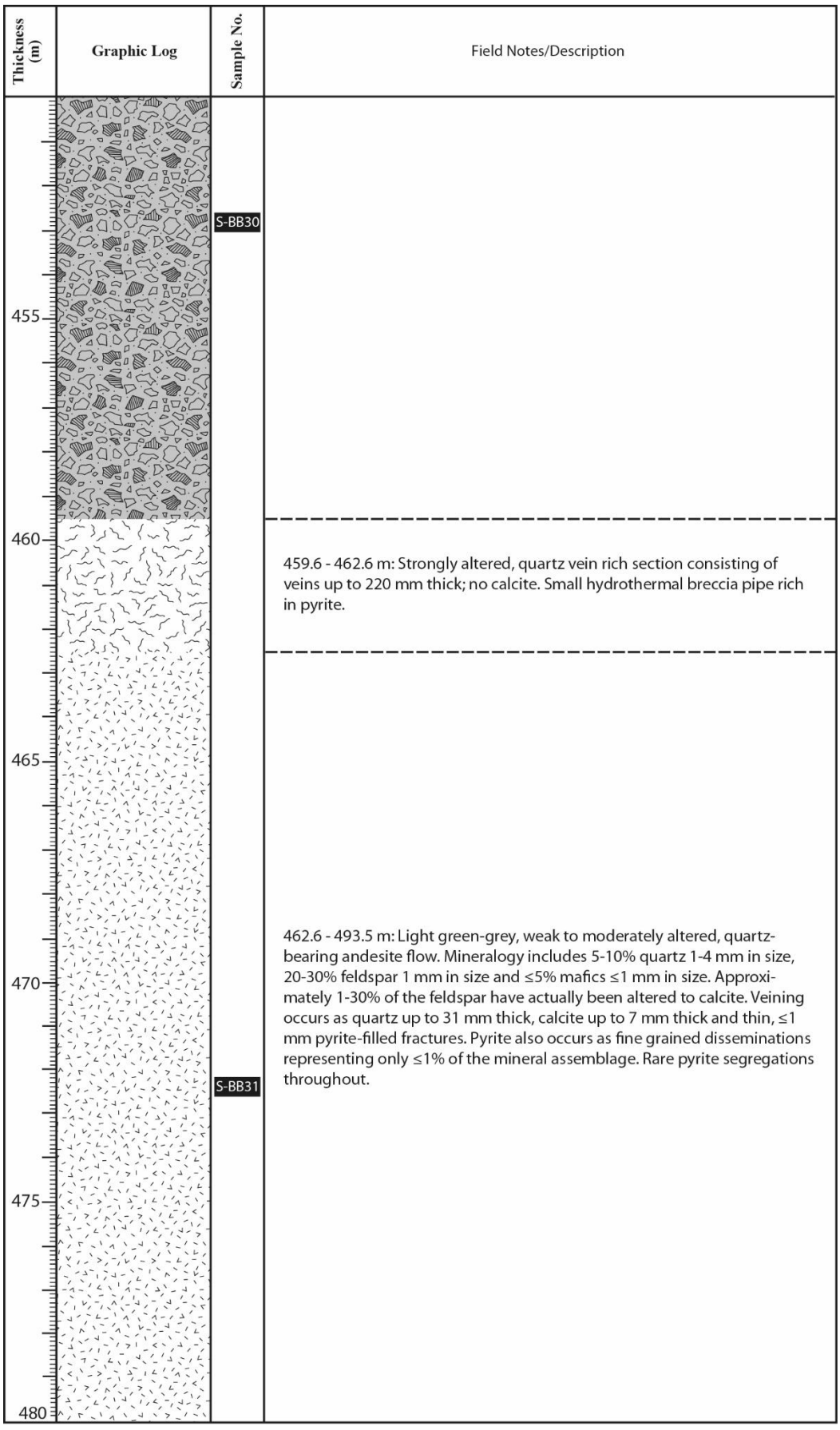
Thickness (m)
Graphic Log
Sample No.
Field Notes/Description
S-BB30
S-BB31
455
460
465
470
475
480
459.6 - 462.6 m: Strongly altered, quartz vein rich section consisting of veins up to 220 mm thick; no calcite. Small hydrothermal breccia pipe rich in pyrite.
462.6 - 493.5 m: Light green-grey, weak to moderately altered, quartz-bearing andesite flow. Mineralogy includes 5-10% quartz 1-4 mm in size, 20-30% feldspar 1 mm in size and ≤5% mafics ≤1 mm in size. Approximately 1-30% of the feldspar have actually been altered to calcite. Veining occurs as quartz up to 31 mm thick, calcite up to 7 mm thick and thin, ≤1 mm pyrite-filled fractures. Pyrite also occurs as fine grained disseminations representing only ≤1% of the mineral assemblage. Rare pyrite segregations throughout.

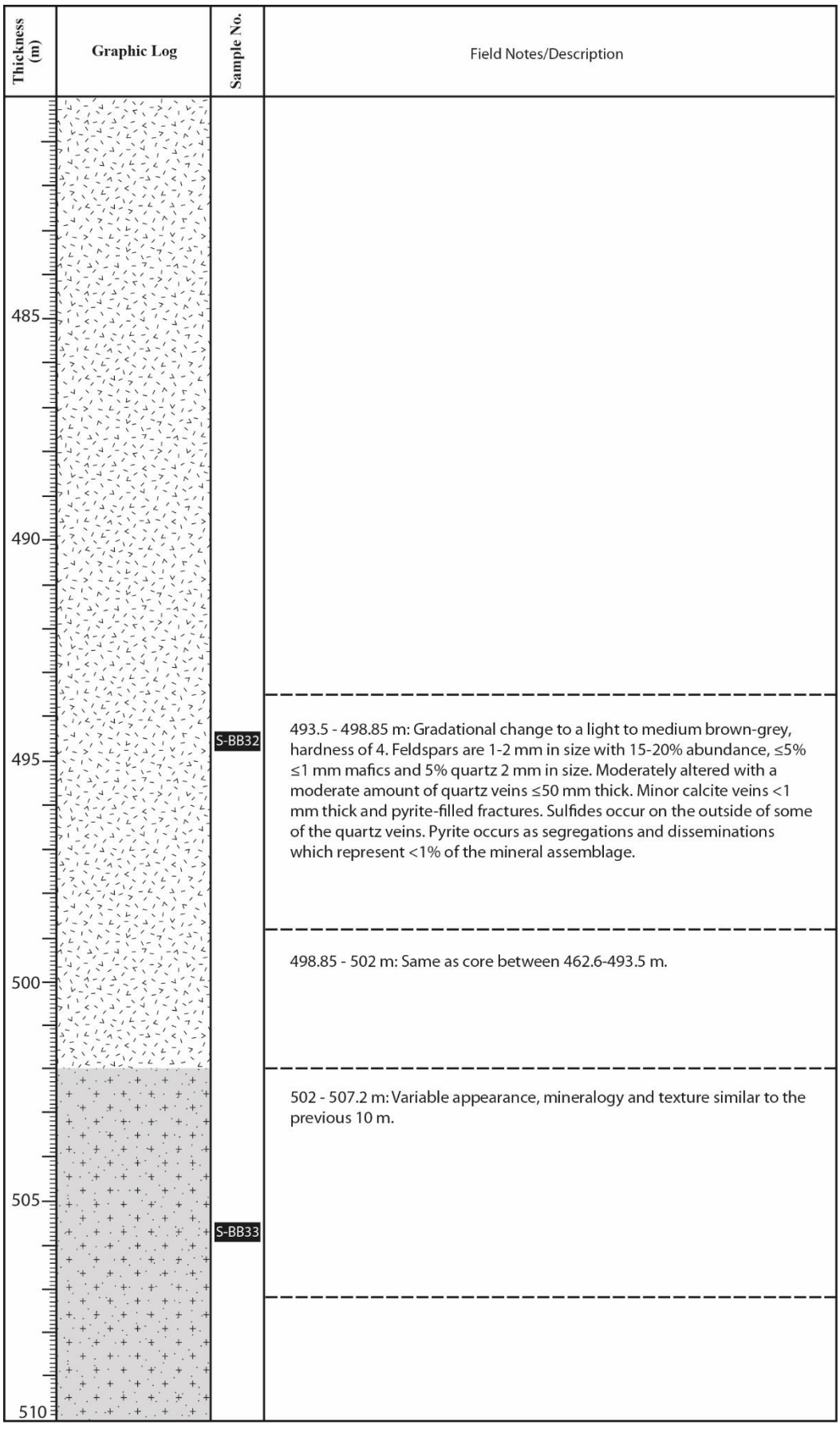
Thickness (m)
Graphic Log
Sample No.
Field Notes/Description
485
490
495
500
505
510
S-BB32
S-BB33
493.5 - 498.85 m: Gradational change to a light to medium brown-grey, hardness of 4. Feldspars are 1-2 mm in size with 15-20% abundance, ≤5% ≤1 mm mafics and 5% quartz 2 mm in size. Moderately altered with a moderate amount of quartz veins ≤50 mm thick. Minor calcite veins <1 mm thick and pyrite-filled fractures. Sulfides occur on the outside of some of the quartz veins. Pyrite occurs as segregations and disseminations which represent <1% of the mineral assemblage.
498.85 - 502 m: Same as core between 462.6-493.5 m.
502 - 507.2 m: Variable appearance, mineralogy and texture similar to the previous 10 m.

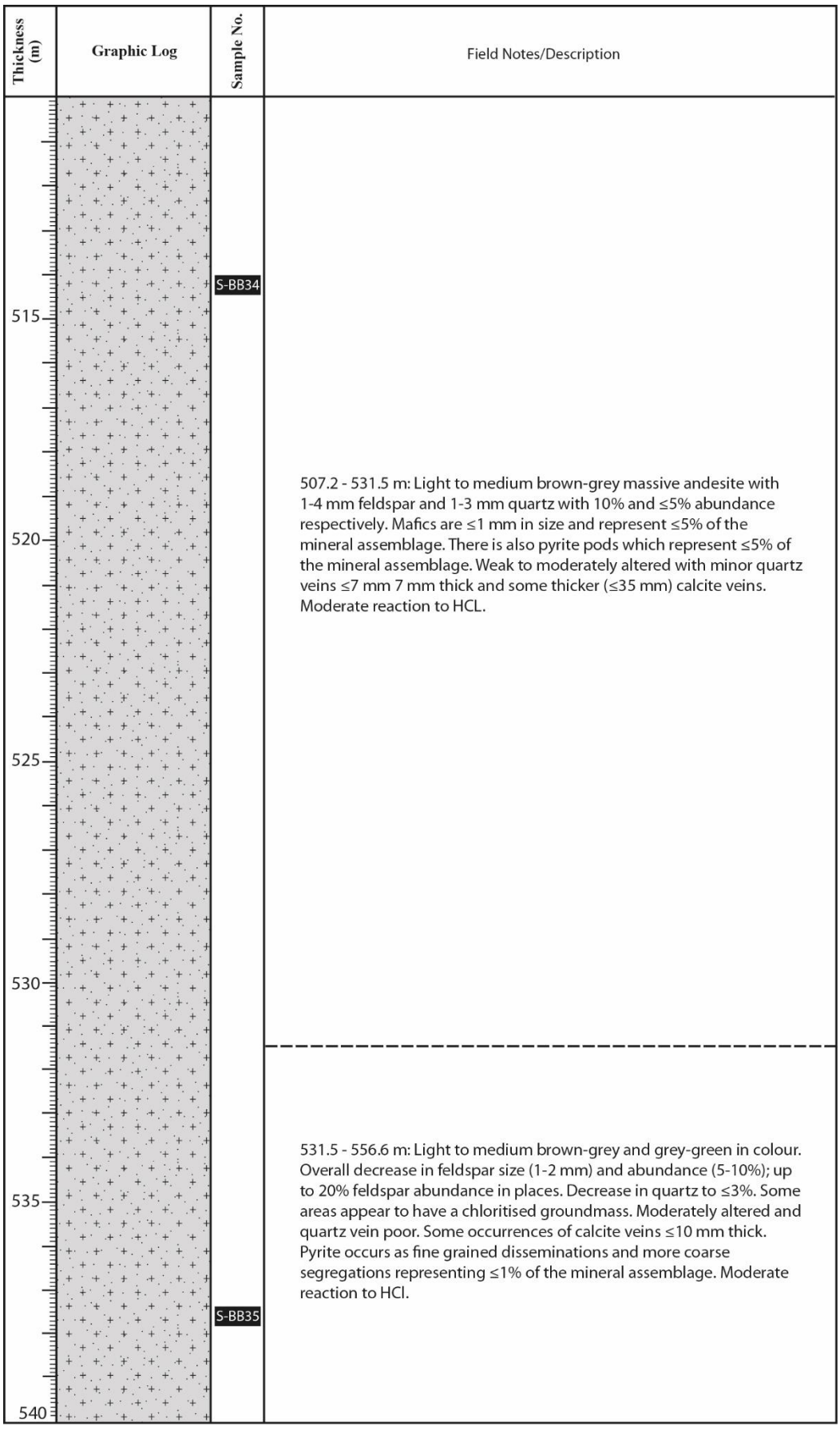
Thickness (m)
Graphic Log
Sample No.
Field Notes/Description
S-BB34
515
520
525
530
535
S-BB35
540
507.2 - 531.5 m: Light to medium brown-grey massive andesite with 1-4 mm feldspar and 1-3 mm quartz with 10% and ≤5% abundance respectively. Mafics are ≤1 mm in size and represent ≤5% of the mineral assemblage. There is also pyrite pods which represent ≤5% of the mineral assemblage. Weak to moderately altered with minor quartz veins ≤7 mm 7 mm thick and some thicker (≤35 mm) calcite veins. Moderate reaction to HCL.
531.5 - 556.6 m: Light to medium brown-grey and grey-green in colour. Overall decrease in feldspar size (1-2 mm) and abundance (5-10%); up to 20% feldspar abundance in places. Decrease in quartz to ≤3%. Some areas appear to have a chloritised groundmass. Moderately altered and quartz vein poor. Some occurrences of calcite veins ≤10 mm thick. Pyrite occurs as fine grained disseminations and more coarse segregations representing ≤1% of the mineral assemblage. Moderate reaction to HCl.

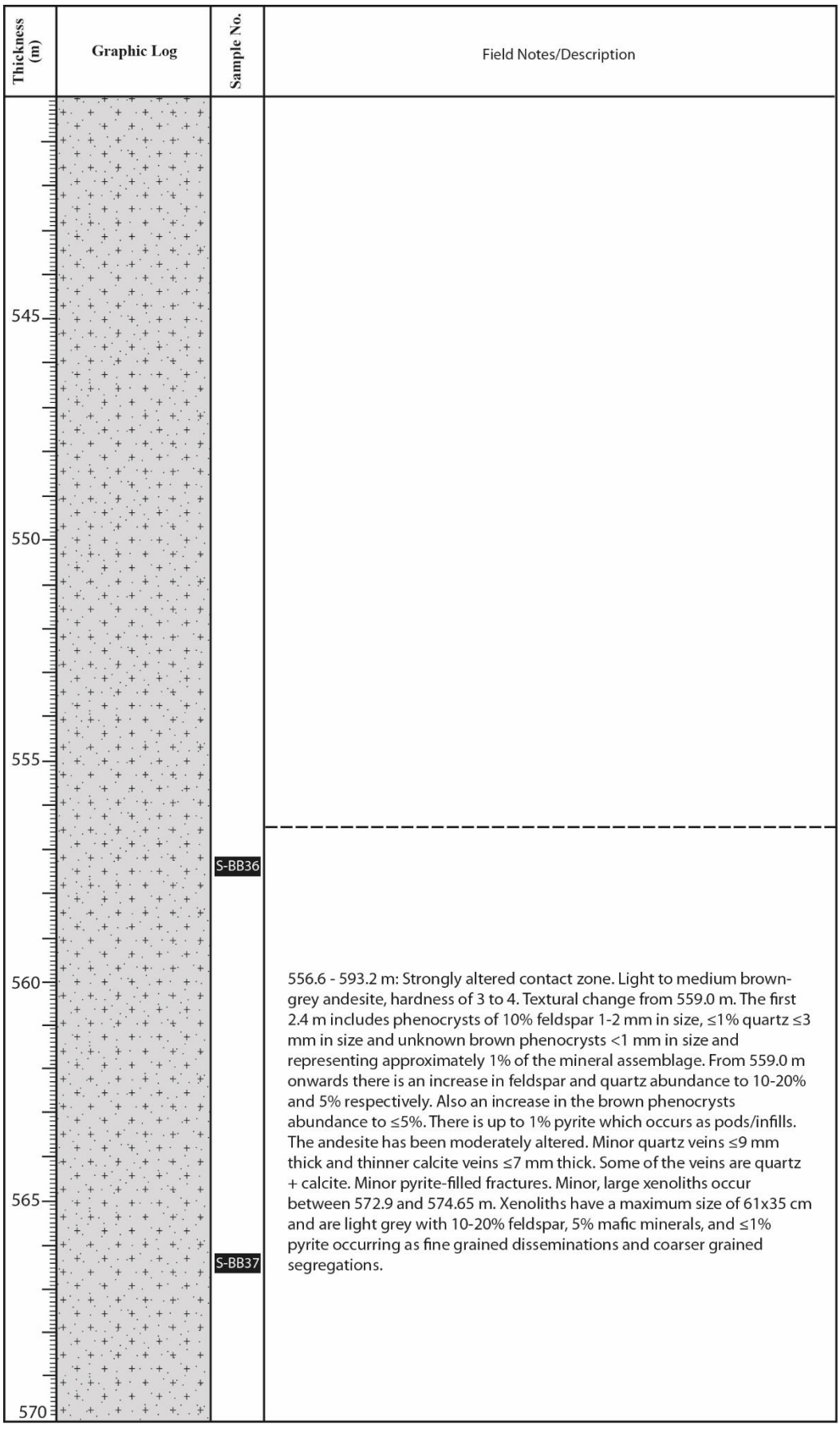
Thickness (m)
Graphic Log
Sample No.
Field Notes/Description
545
550
555
560
565
570
S-BB36
S-BB37
556.6 - 593.2 m: Strongly altered contact zone. Light to medium brown-grey andesite, hardness of 3 to 4. Textural change from 559.0 m. The first 2.4 m includes phenocrysts of 10% feldspar 1-2 mm in size, ≤1% quartz ≤3 mm in size and unknown brown phenocrysts <1 mm in size and representing approximately 1% of the mineral assemblage. From 559.0 m onwards there is an increase in feldspar and quartz abundance to 10-20% and 5% respectively. Also an increase in the brown phenocrysts abundance to ≤5%. There is up to 1% pyrite which occurs as pods/infills. The andesite has been moderately altered. Minor quartz veins ≤9 mm thick and thinner calcite veins ≤7 mm thick. Some of the veins are quartz + calcite. Minor pyrite-filled fractures. Minor, large xenoliths occur between 572.9 and 574.65 m. Xenoliths have a maximum size of 61x35 cm and are light grey with 10-20% feldspar, 5% mafic minerals, and ≤1% pyrite occurring as fine grained disseminations and coarser grained segregations.

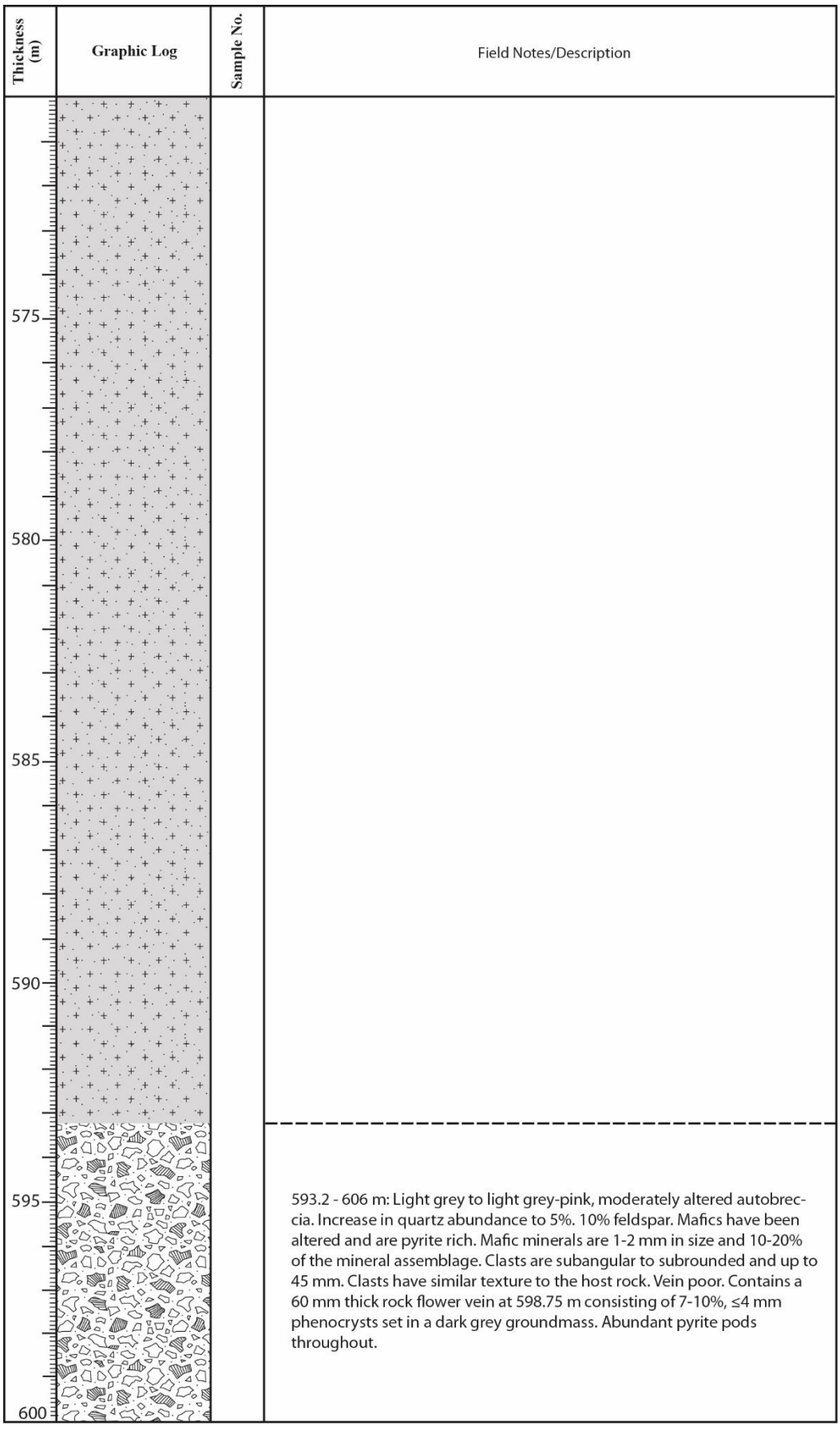
Thickness (m)
Graphic Log
Sample No.
Field Notes/Description
575
580
585
590
595
600
593.2 - 606 m: Light grey to light grey-pink, moderately altered autobrec-cia. Increase in quartz abundance to 5%. 10% feldspar. Mafics have been altered and are pyrite rich. Mafic minerals are 1-2 mm in size and 10-20% of the mineral assemblage. Clasts are subangular to subrounded and up to 45 mm. Clasts have similar texture to the host rock. Vein poor. Contains a 60 mm thick rock flower vein at 598.75 m consisting of 7-10%, ≤4 mm phenocrysts set in a dark grey groundmass. Abundant pyrite pods throughout.

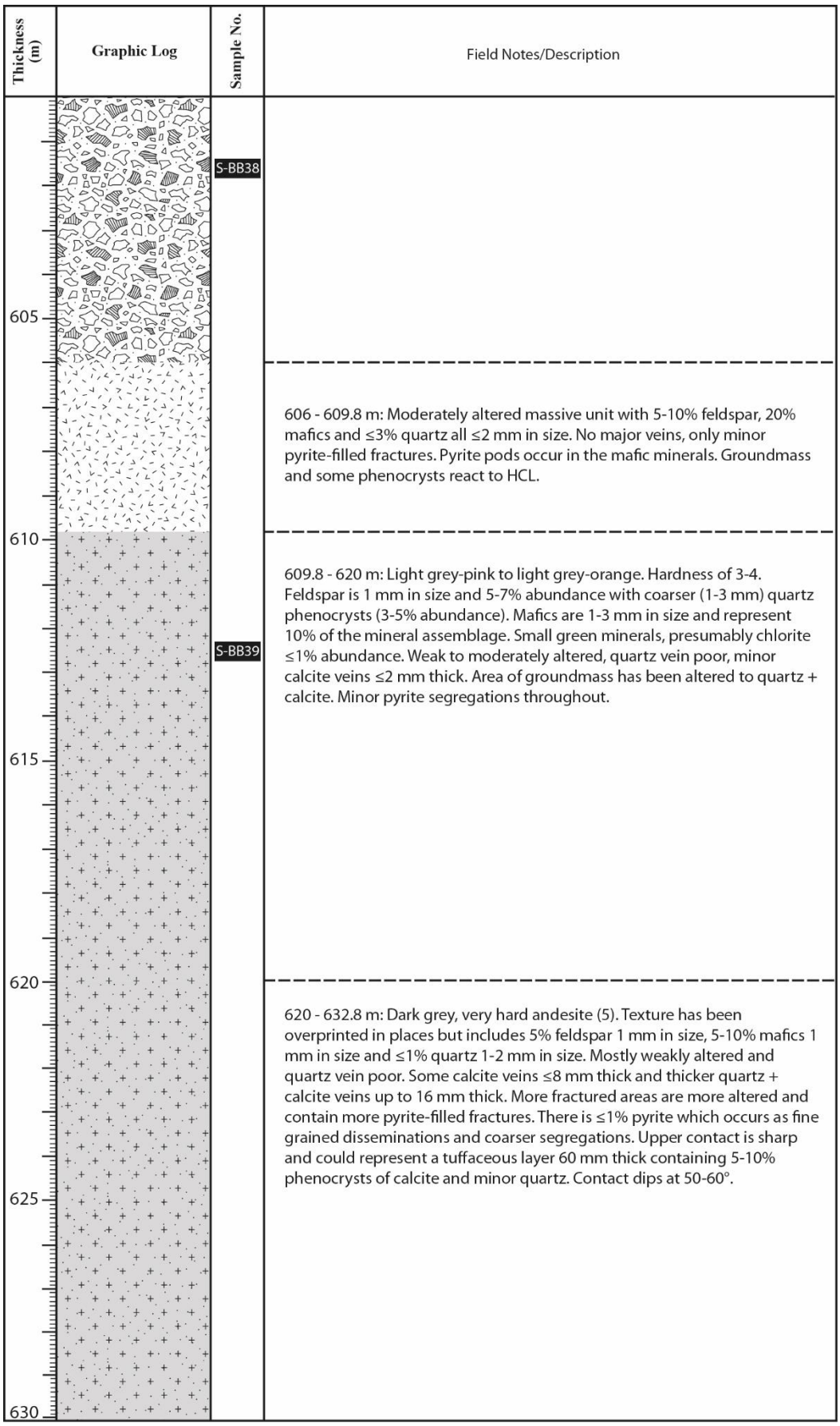
Thickness (m)
Graphic Log
Sample No.
Field Notes/Description
S-BB38
S-BB39
605
610
615
620
625
630
606 - 609.8 m: Moderately altered massive unit with 5-10% feldspar, 20% mafics and ≤3% quartz all ≤2 mm in size. No major veins, only minor pyrite-filled fractures. Pyrite pods occur in the mafic minerals. Groundmass and some phenocrysts react to HCL.
609.8 - 620 m: Light grey-pink to light grey-orange. Hardness of 3-4. Feldspar is 1 mm in size and 5-7% abundance with coarser (1-3 mm) quartz phenocrysts (3-5% abundance). Mafics are 1-3 mm in size and represent 10% of the mineral assemblage. Small green minerals, presumably chlorite ≤1% abundance. Weak to moderately altered, quartz vein poor, minor calcite veins ≤2 mm thick. Area of groundmass has been altered to quartz + calcite. Minor pyrite segregations throughout.
620 - 632.8 m: Dark grey, very hard andesite (5). Texture has been overprinted in places but includes 5% feldspar 1 mm in size, 5-10% mafics 1 mm in size and ≤1% quartz 1-2 mm in size. Mostly weakly altered and quartz vein poor. Some calcite veins ≤8 mm thick and thicker quartz + calcite veins up to 16 mm thick. More fractured areas are more altered and contain more pyrite-filled fractures. There is ≤1% pyrite which occurs as fine grained disseminations and coarser segregations. Upper contact is sharp and could represent a tuffaceous layer 60 mm thick containing 5-10% phenocrysts of calcite and minor quartz. Contact dips at 50-60°.

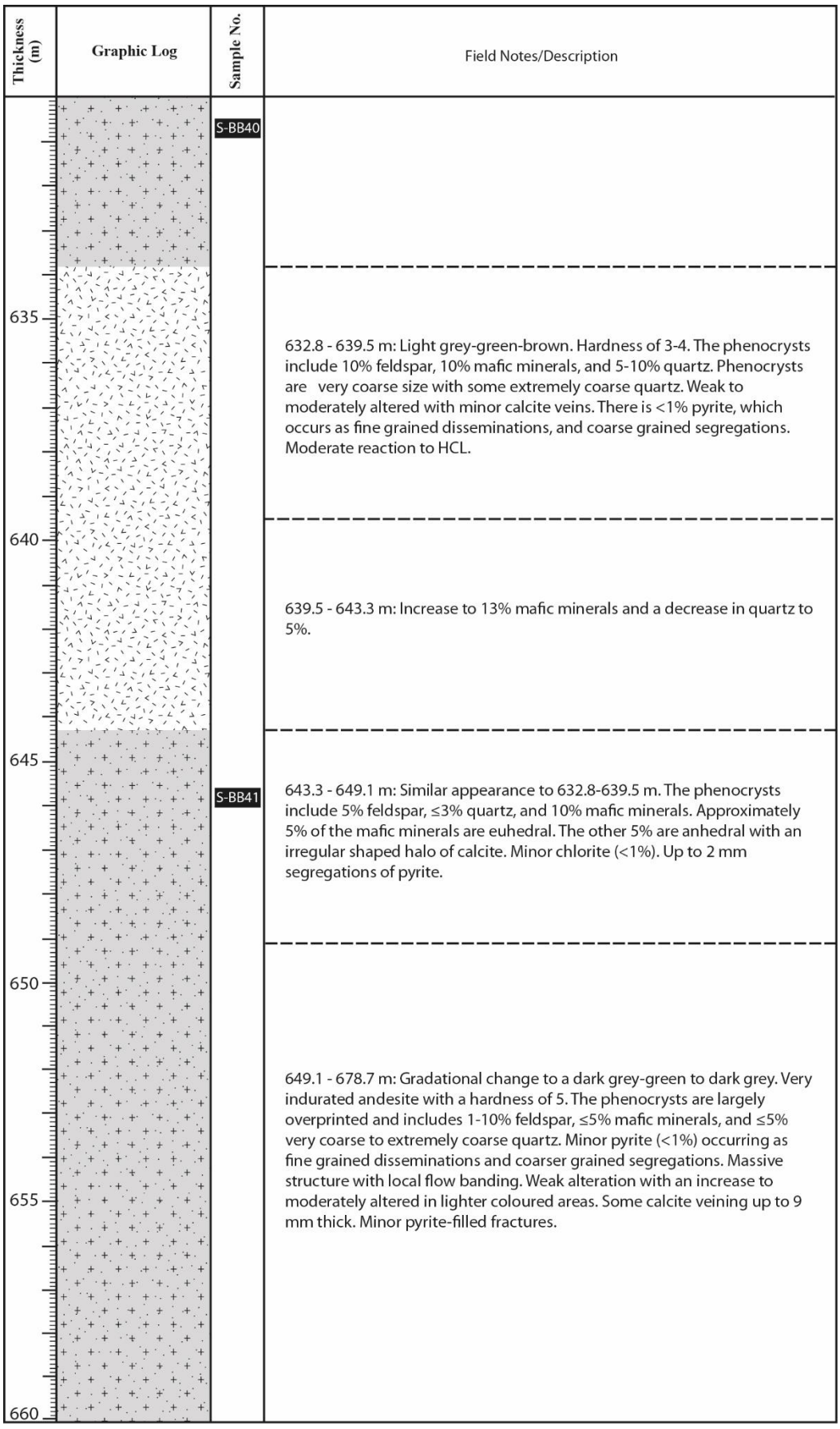
Thickness (m)
Graphic Log
Sample No.
Field Notes/Description
S-BB40
635
640
645
650
655
660
S-BB41
632.8 - 639.5 m: Light grey-green-brown. Hardness of 3-4. The phenocrysts include 10% feldspar, 10% mafic minerals, and 5-10% quartz. Phenocrysts are very coarse size with some extremely coarse quartz. Weak to moderately altered with minor calcite veins. There is <1% pyrite, which occurs as fine grained disseminations, and coarse grained segregations. Moderate reaction to HCL.
639.5 - 643.3 m: Increase to 13% mafic minerals and a decrease in quartz to 5%.
643.3 - 649.1 m: Similar appearance to 632.8-639.5 m. The phenocrysts include 5% feldspar, ≤3% quartz, and 10% mafic minerals. Approximately 5% of the mafic minerals are euhedral. The other 5% are anhedral with an irregular shaped halo of calcite. Minor chlorite (<1%). Up to 2 mm segregations of pyrite.
649.1 - 678.7 m: Gradational change to a dark grey-green to dark grey. Very indurated andesite with a hardness of 5. The phenocrysts are largely overprinted and includes 1-10% feldspar, ≤5% mafic minerals, and ≤5% very coarse to extremely coarse quartz. Minor pyrite (<1%) occurring as fine grained disseminations and coarser grained segregations. Massive structure with local flow banding. Weak alteration with an increase to moderately altered in lighter coloured areas. Some calcite veining up to 9 mm thick. Minor pyrite-filled fractures.

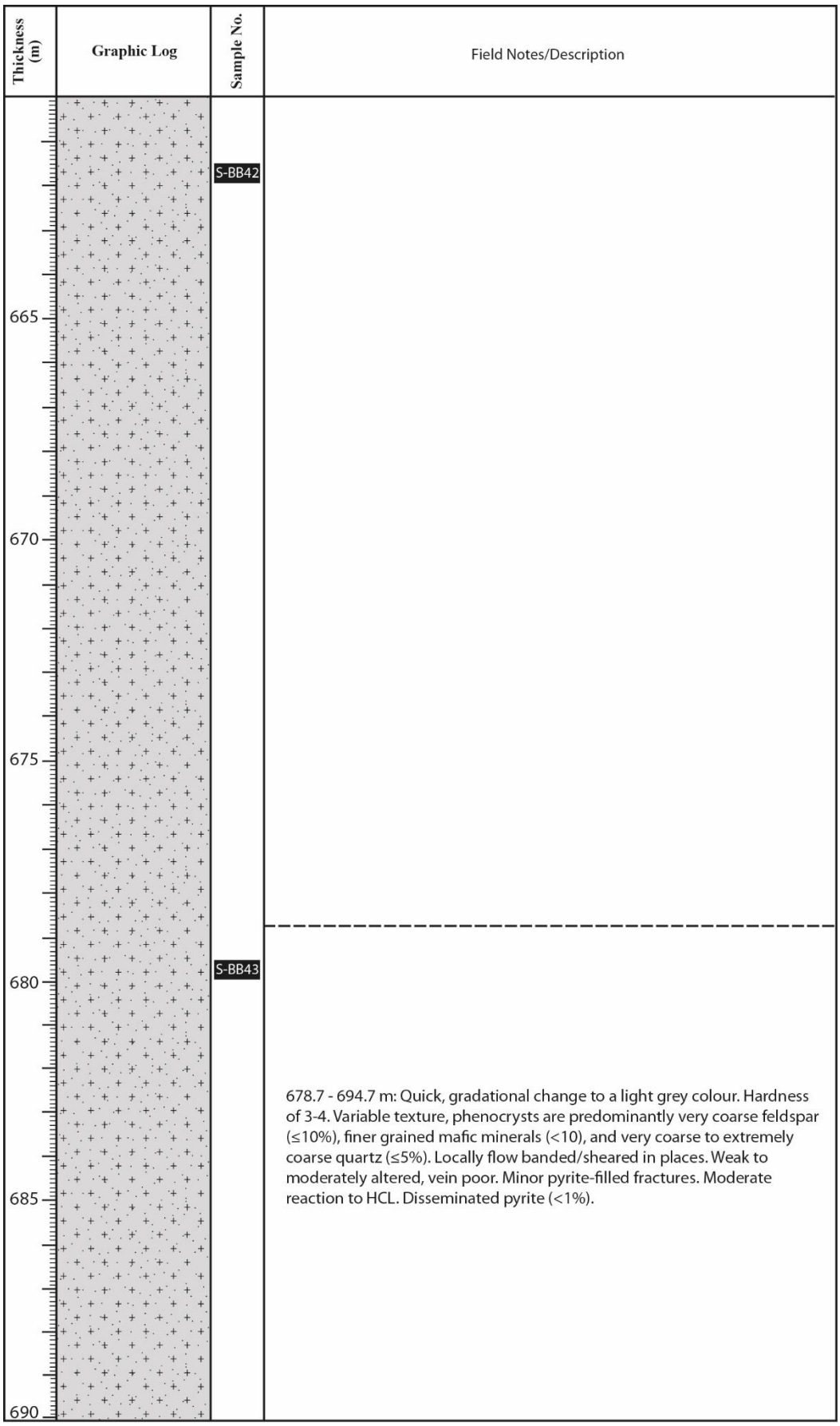
Thickness (m)
Graphic Log
Sample No.
Field Notes/Description
S-BB42
S-BB43
665
670
675
680
685
690
678.7 - 694.7 m: Quick, gradational change to a light grey colour. Hardness of 3-4. Variable texture, phenocrysts are predominantly very coarse feldspar (≤10%), finer grained mafic minerals (<10), and very coarse to extremely coarse quartz (≤5%). Locally flow banded/sheared in places. Weak to moderately altered, vein poor. Minor pyrite-filled fractures. Moderate reaction to HCL. Disseminated pyrite (<1%).

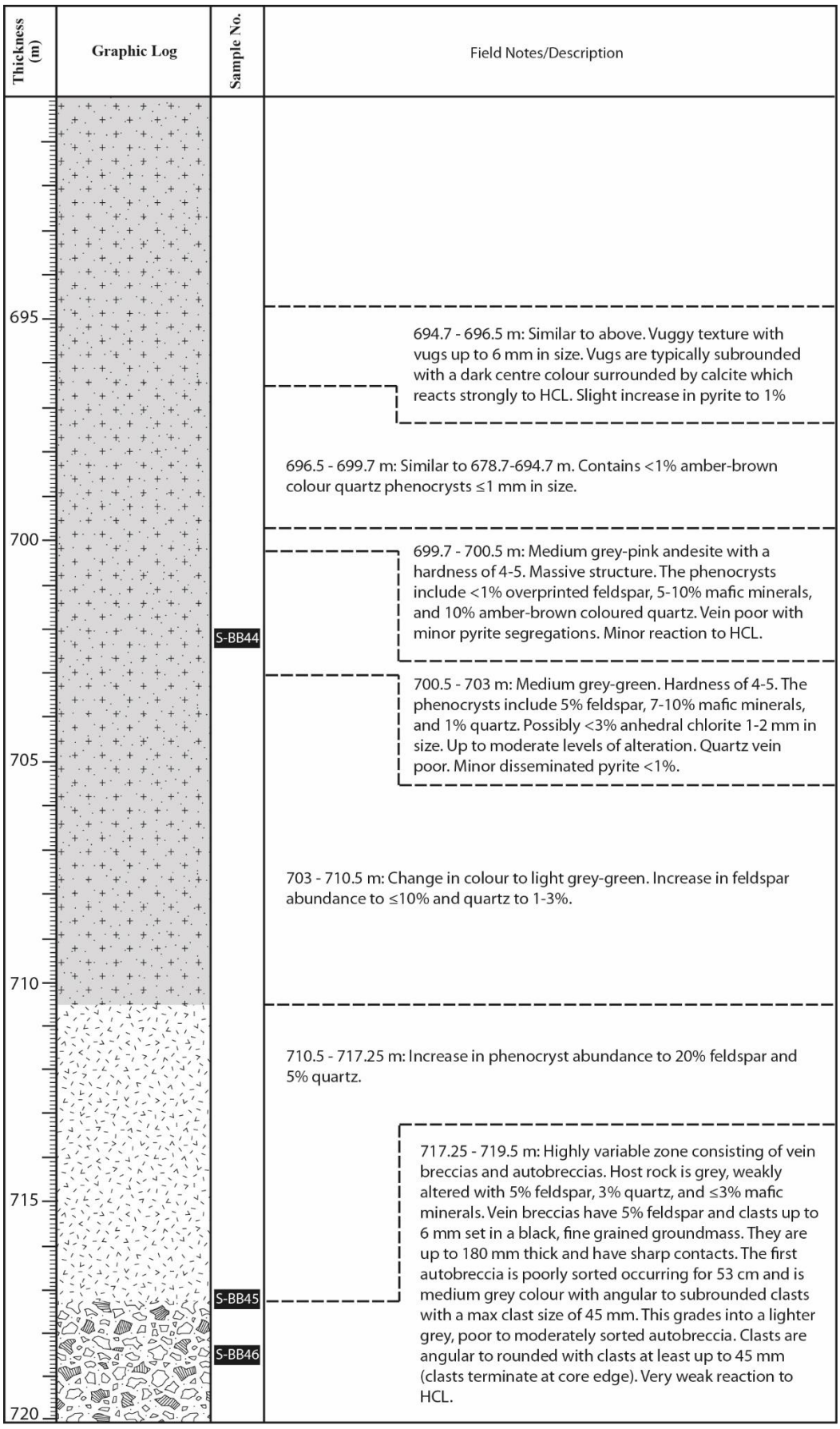
Thickness (m)
Graphic Log
Sample No.
Field Notes/Description
695
700
705
710
715
720
S-BB44
S-BB45
S-BB46
694.7 - 696.5 m: Similar to above. Vuggy texture with vugs up to 6 mm in size. Vugs are typically subrounded with a dark centre colour surrounded by calcite which reacts strongly to HCL. Slight increase in pyrite to 1%
696.5 - 699.7 m: Similar to 678.7-694.7 m. Contains <1% amber-brown colour quartz phenocrysts ≤1 mm in size.
699.7 - 700.5 m: Medium grey-pink andesite with a hardness of 4-5. Massive structure. The phenocrysts include <1% overprinted feldspar, 5-10% mafic minerals, and 10% amber-brown coloured quartz. Vein poor with minor pyrite segregations. Minor reaction to HCL.
700.5 - 703 m: Medium grey-green. Hardness of 4-5. The phenocrysts include 5% feldspar, 7-10% mafic minerals, and 1% quartz. Possibly <3% anhedral chlorite 1-2 mm in size. Up to moderate levels of alteration. Quartz vein poor. Minor disseminated pyrite <1%.
703 - 710.5 m: Change in colour to light grey-green. Increase in feldspar abundance to ≤10% and quartz to 1-3%.
710.5 - 717.25 m: Increase in phenocryst abundance to 20% feldspar and 5% quartz.
717.25 - 719.5 m: Highly variable zone consisting of vein breccias and autobreccias. Host rock is grey, weakly altered with 5% feldspar, 3% quartz, and ≤3% mafic minerals. Vein breccias have 5% feldspar and clasts up to 6 mm set in a black, fine grained groundmass. They are up to 180 mm thick and have sharp contacts. The first autobreccia is poorly sorted occurring for 53 cm and is medium grey colour with angular to subrounded clasts with a max clast size of 45 mm. This grades into a lighter grey, poor to moderately sorted autobreccia. Clasts are angular to rounded with clasts at least up to 45 mm (clasts terminate at core edge). Very weak reaction to HCL.

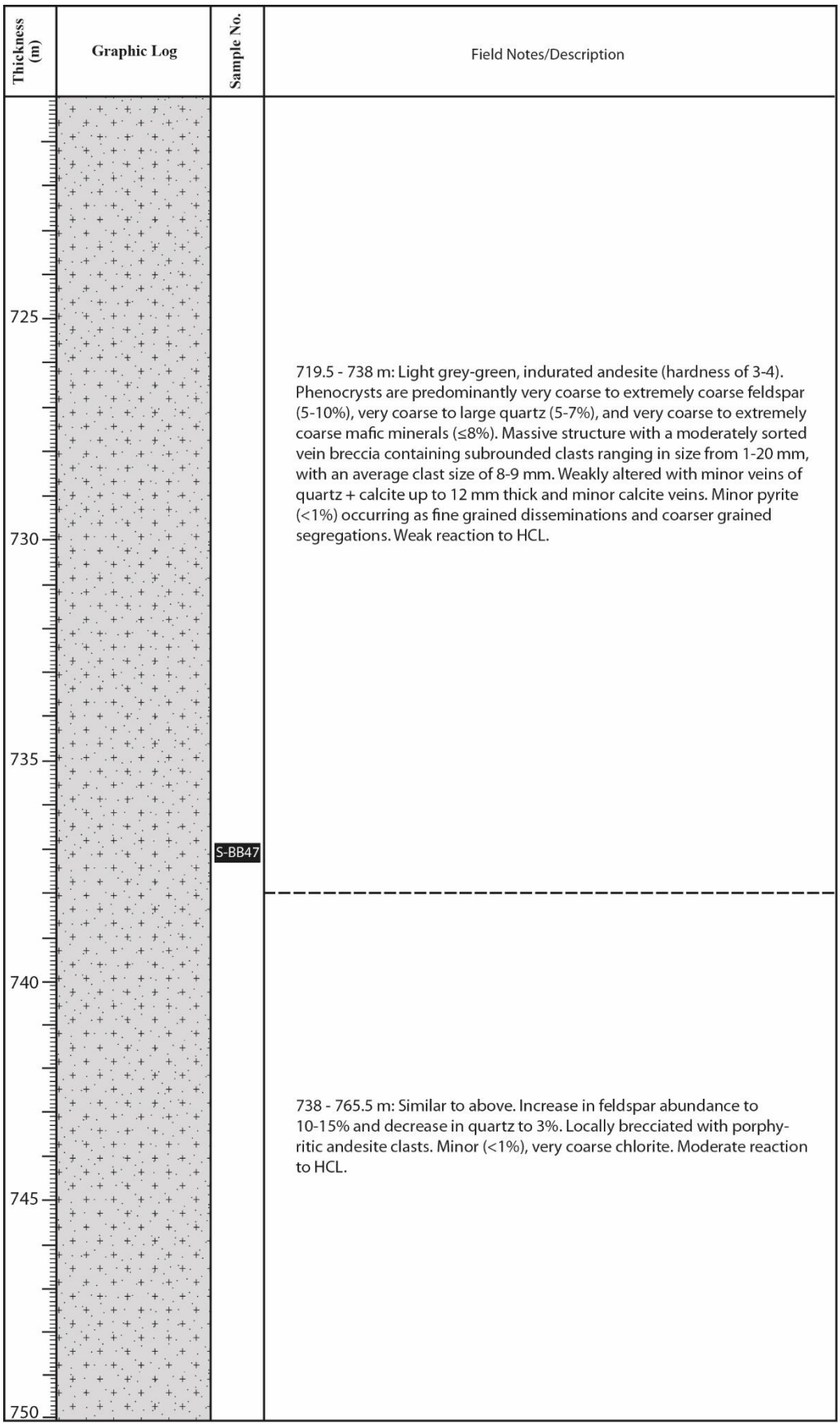
Thickness (m)
Graphic Log
Sample No.
Field Notes/Description
725
730
735
740
745
750
S-BB47
719.5 - 738 m: Light grey-green, indurated andesite (hardness of 3-4). Phenocrysts are predominantly very coarse to extremely coarse feldspar (5-10%), very coarse to large quartz (5-7%), and very coarse to extremely coarse mafic minerals (≤8%). Massive structure with a moderately sorted vein breccia containing subrounded clasts ranging in size from 1-20 mm, with an average clast size of 8-9 mm. Weakly altered with minor veins of quartz + calcite up to 12 mm thick and minor calcite veins. Minor pyrite (<1%) occurring as fine grained disseminations and coarser grained segregations. Weak reaction to HCL.
738 - 765.5 m: Similar to above. Increase in feldspar abundance to 10-15% and decrease in quartz to 3%. Locally brecciated with porphyritic andesite clasts. Minor (<1%), very coarse chlorite. Moderate reaction to HCL.

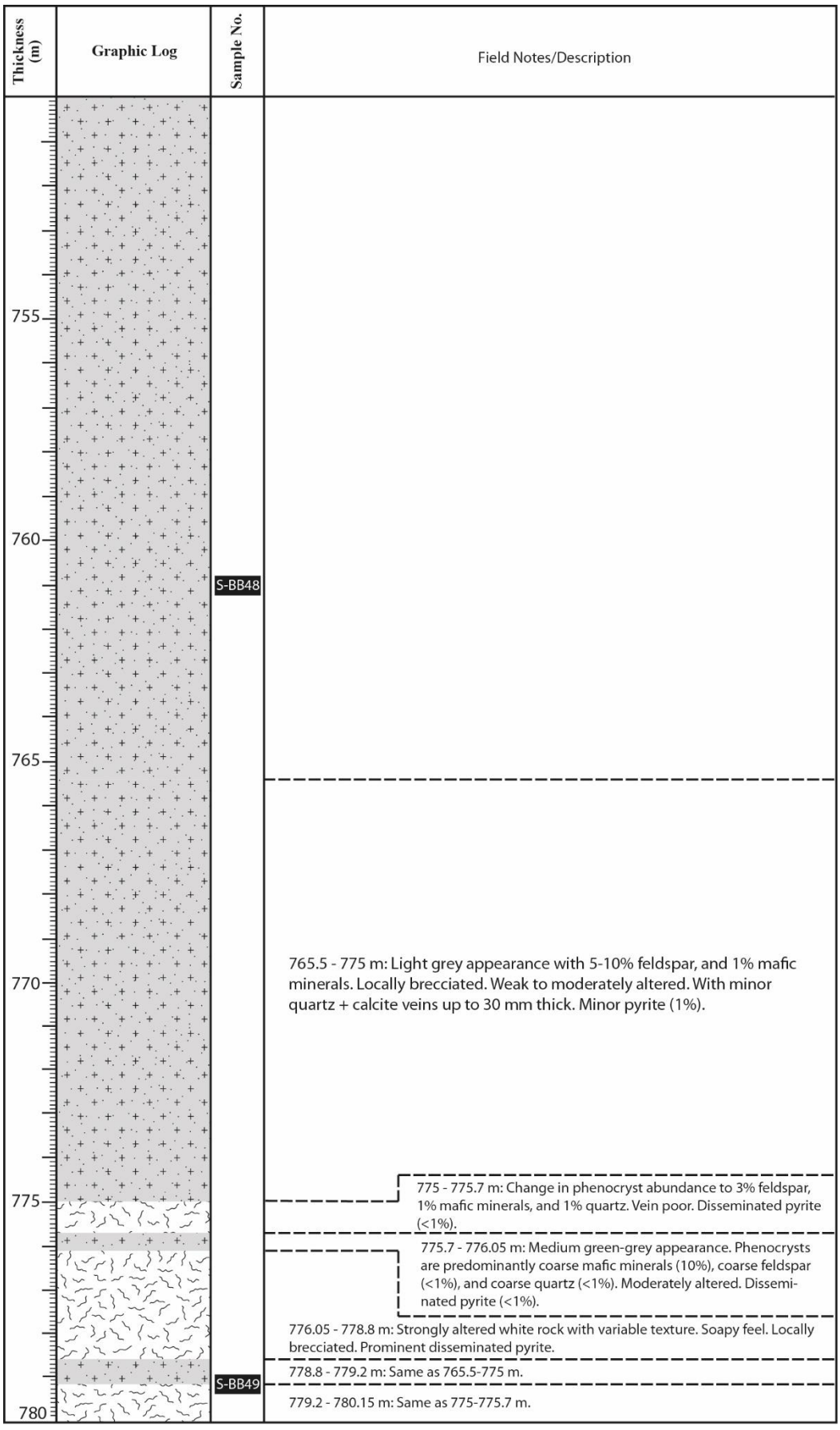
Thickness (m)
Graphic Log
Sample No.
Field Notes/Description
755
760
765
770
775
780
S-BB48
S-BB49
765.5 - 775 m: Light grey appearance with 5-10% feldspar, and 1% mafic minerals. Locally brecciated. Weak to moderately altered. With minor quartz + calcite veins up to 30 mm thick. Minor pyrite (1%).
775 - 775.7 m: Change in phenocryst abundance to 3% feldspar, 1% mafic minerals, and 1% quartz. Vein poor. Disseminated pyrite (<1%).
775.7 - 776.05 m: Medium green-grey appearance. Phenocrysts are predominantly coarse mafic minerals (10%), coarse feldspar (<1%), and coarse quartz (<1%). Moderately altered. Disseminated pyrite (<1%).
776.05 - 778.8 m: Strongly altered white rock with variable texture. Soapy feel. Locally brecciated. Prominent disseminated pyrite.
778.8 - 779.2 m: Same as 765.5-775 m.
779.2 - 780.15 m: Same as 775-775.7 m.

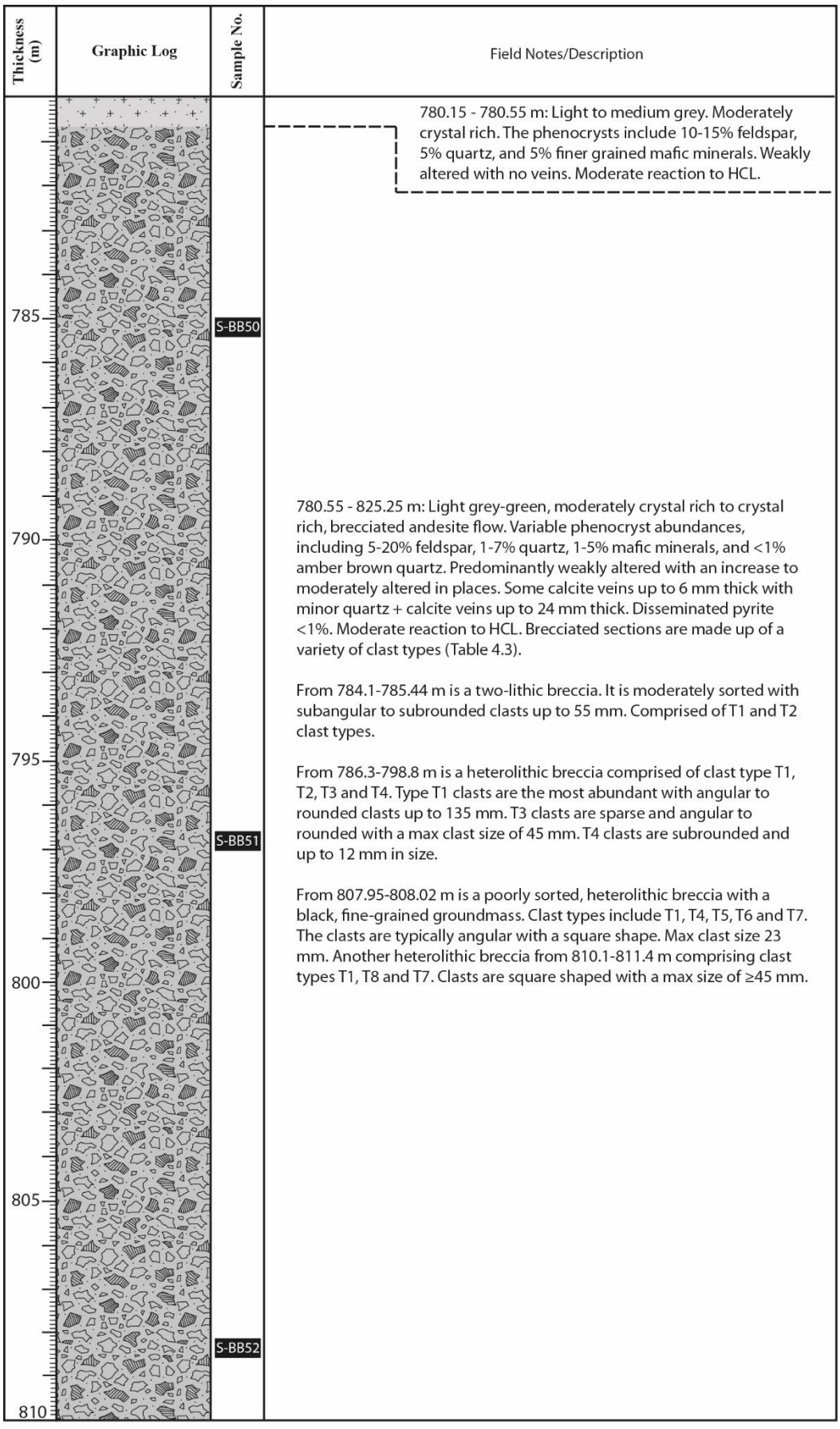
Thickness (m)
Graphic Log
Sample No.
Field Notes/Description
780.15 - 780.55 m: Light to medium grey. Moderately crystal rich. The phenocrysts include 10-15% feldspar, 5% quartz, and 5% finer grained mafic minerals. Weakly altered with no veins. Moderate reaction to HCL.
785
790
795
800
805
810
S-BB50
S-BB51
S-BB52
780.55 - 825.25 m: Light grey-green, moderately crystal rich to crystal rich, brecciated andesite flow. Variable phenocryst abundances, including 5-20% feldspar, 1-7% quartz, 1-5% mafic minerals, and <1% amber brown quartz. Predominantly weakly altered with an increase to moderately altered in places. Some calcite veins up to 6 mm thick with minor quartz + calcite veins up to 24 mm thick. Disseminated pyrite <1%. Moderate reaction to HCL. Brecciated sections are made up of a variety of clast types (Table 4.3).
From 784.1-785.44 m is a two-lithic breccia. It is moderately sorted with subangular to subrounded clasts up to 55 mm. Comprised of T1 and T2 clast types.
From 786.3-798.8 m is a heterolithic breccia comprised of clast type T1, T2, T3 and T4. Type T1 clasts are the most abundant with angular to rounded clasts up to 135 mm. T3 clasts are sparse and angular to rounded with a max clast size of 45 mm. T4 clasts are subrounded and up to 12 mm in size.
From 807.95-808.02 m is a poorly sorted, heterolithic breccia with a black, fine-grained groundmass. Clast types include T1, T4, T5, T6 and T7. The clasts are typically angular with a square shape. Max clast size 23 mm. Another heterolithic breccia from 810.1-811.4 m comprising clast types T1, T8 and T7. Clasts are square shaped with a max size of ≥45 mm.

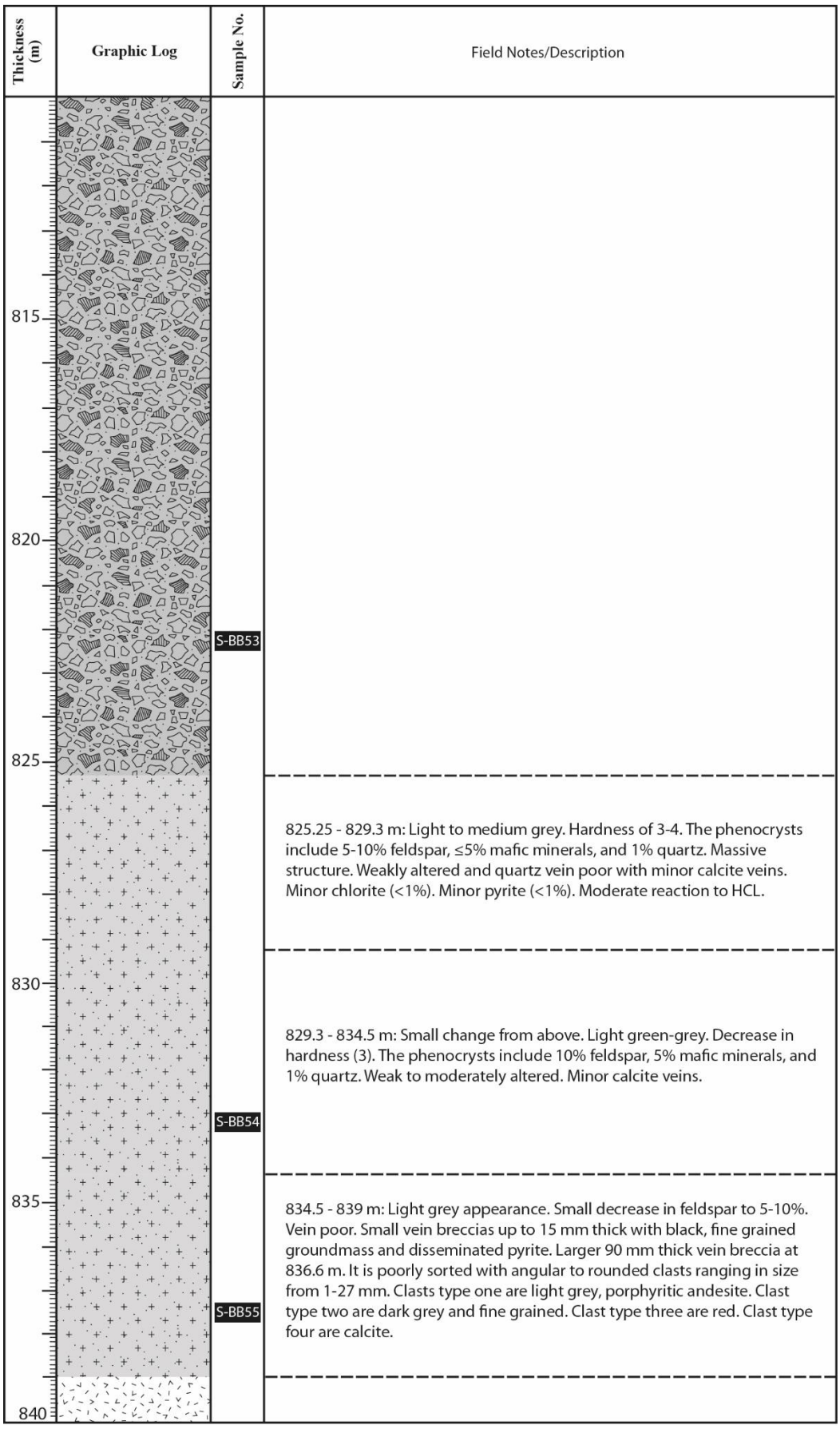
Thickness (m)
Graphic Log
Sample No.
Field Notes/Description
815
820
825
830
835
840
S-BB53
S-BB54
S-BB55
825.25 - 829.3 m: Light to medium grey. Hardness of 3-4. The phenocrysts include 5-10% feldspar, ≤5% mafic minerals, and 1% quartz. Massive structure. Weakly altered and quartz vein poor with minor calcite veins. Minor chlorite (<1%). Minor pyrite (<1%). Moderate reaction to HCL.
829.3 - 834.5 m: Small change from above. Light green-grey. Decrease in hardness (3). The phenocrysts include 10% feldspar, 5% mafic minerals, and 1% quartz. Weak to moderately altered. Minor calcite veins.
834.5 - 839 m: Light grey appearance. Small decrease in feldspar to 5-10%. Vein poor. Small vein breccias up to 15 mm thick with black, fine grained groundmass and disseminated pyrite. Larger 90 mm thick vein breccia at 836.6 m. It is poorly sorted with angular to rounded clasts ranging in size from 1-27 mm. Clasts type one are light grey, porphyritic andesite. Clast type two are dark grey and fine grained. Clast type three are red. Clast type four are calcite.

Thickness (m)	Graphic Log	Sample No.	Field Notes/Description
845 850 EOH	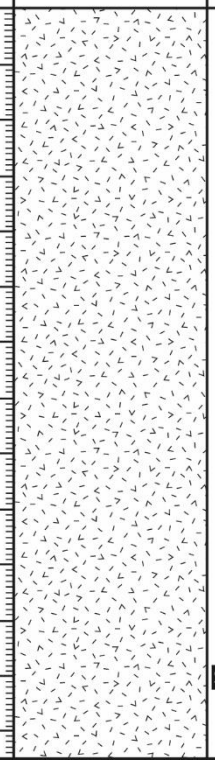	S-BB56	839 - 853.6 m: Light to medium grey, massive, crystal rich andesite. Hardness of 3-4. The phenocrysts include 15-20% feldspar, 5% quartz, and 5% mafic minerals. Weak to moderately altered with minor quartz + calcite veins. Minor dark coloured fractures with minor pyrite. There is <1% pyrite, which occurs as fine grained disseminations and coarse grained segregations. Moderate reaction to HCL. Vein breccia at 851.4 m, 65 cm thick. From 846.45 m for 75 cm the andesite grades into a dark grey and is indurated (hardness of 4-5) with 5% overprinted feldspar.

Appendix B – XRD processed spectra

S7

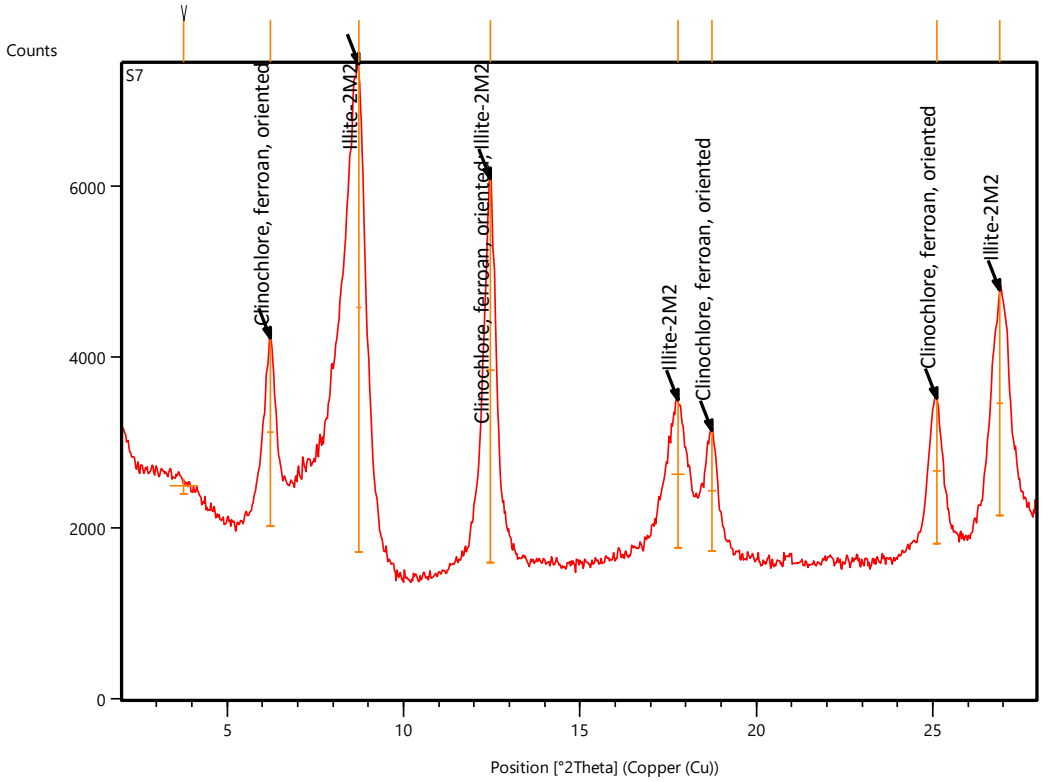

Pos. [°2Th.]	Height [cts]	FWHM Left [°2Th.]	d-spacing [Å]	Rel. Int. [%]
3.7578	191.16	0.8187	23.51358	3.35
6.2292	2206.29	0.2047	14.18909	38.61
8.7312	5714.06	0.1279	10.12789	100.00
12.4679	4497.54	0.2558	7.09962	78.71
17.7856	1730.87	0.3582	4.98711	30.29
18.7349	1406.14	0.2558	4.73650	24.61
25.1092	1699.63	0.2558	3.54666	29.74
26.9056	2637.85	0.2047	3.31381	46.16

S7_GLY

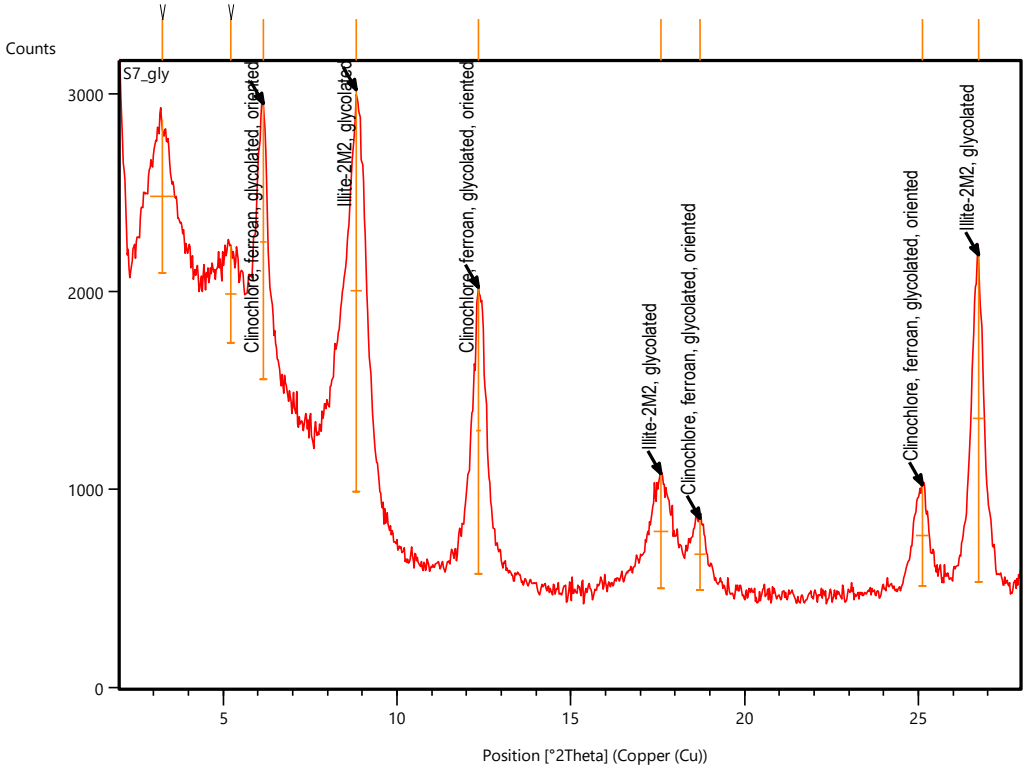

Pos. [°2Th.]	Height [cts]	FWHM Left [°2Th.]	d-spacing [Å]	Rel. Int. [%]
3.2494	770.00	0.7164	27.19124	37.91
5.2190	489.41	0.3070	16.93288	24.10
6.1526	1394.32	0.1791	14.36561	68.65
8.8383	2031.08	0.3326	10.00535	100.00
12.3390	1447.49	0.1279	7.17349	71.27
17.6057	579.47	0.4093	5.03764	28.53
18.7191	363.30	0.3070	4.74046	17.89
25.1246	510.96	0.3582	3.54452	25.16
26.7318	1650.42	0.3070	3.33495	81.26

S22

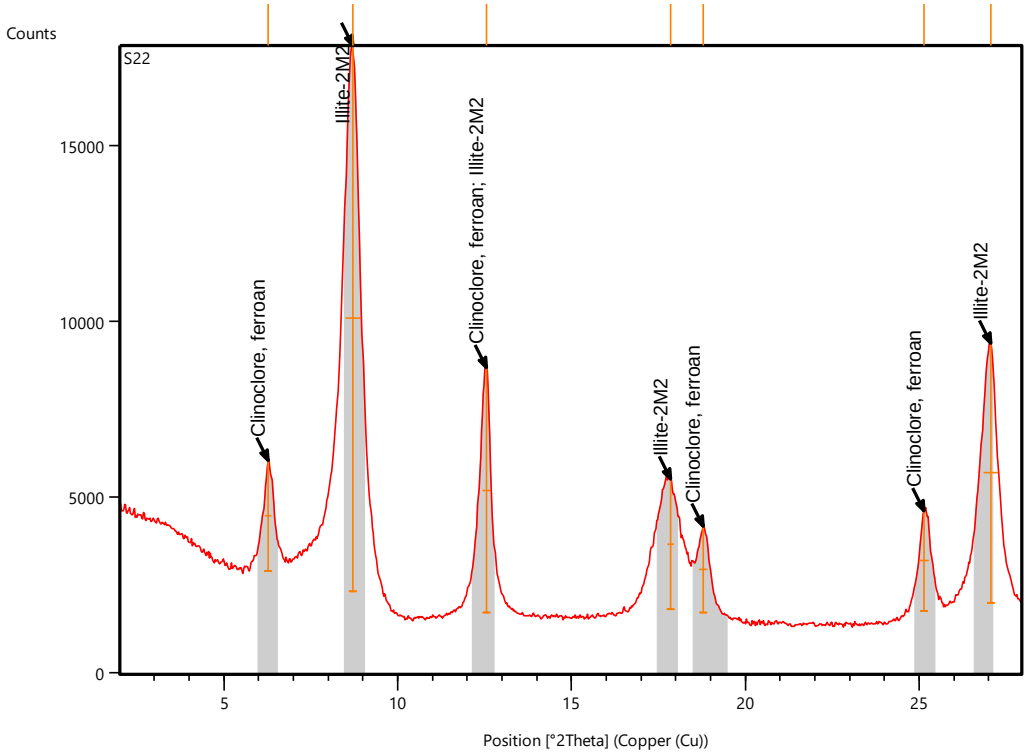

Pos. [°2Th.]	Height [cts]	FWHM Left [°2Th.]	d-spacing [Å]	Rel. Int. [%]
6.2855	3163.65	0.2047	14.06216	20.29
8.7063	15588.39	0.4093	10.15674	100.00
12.5632	6972.75	0.2303	7.04599	44.73
17.8441	3710.25	0.1791	4.97088	23.80
18.7806	2457.35	0.2303	4.72506	15.76
25.1492	2841.71	0.2814	3.54110	18.23
27.0611	7398.84	0.4093	3.29511	47.46

S22_GLY

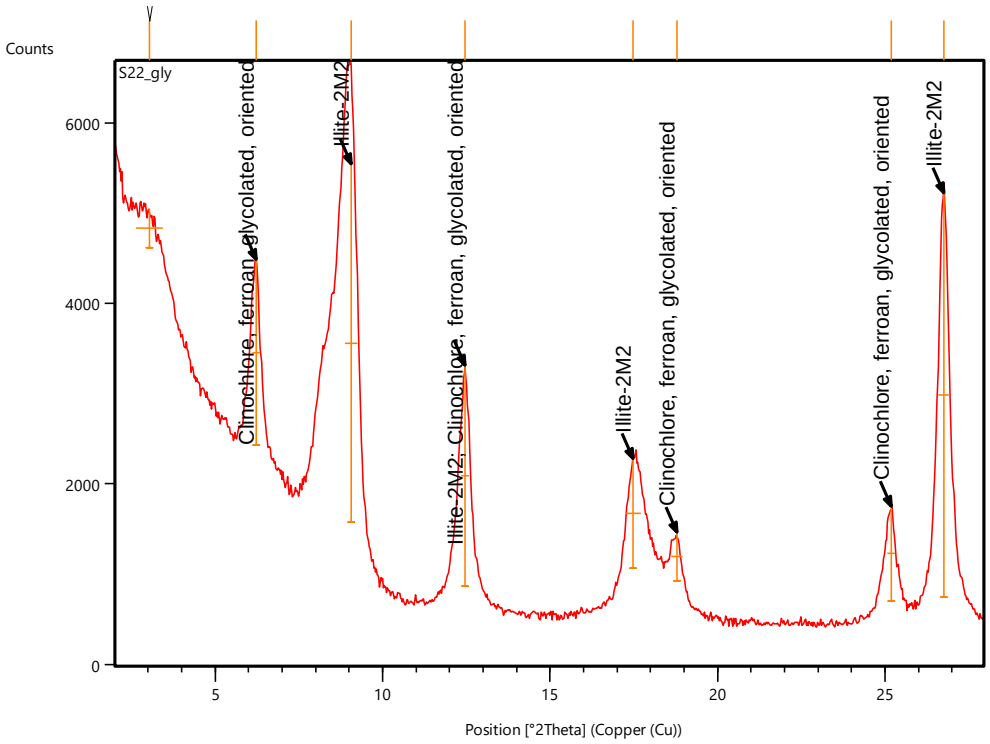

Pos. [°2Th.]	Height [cts]	FWHM Left [°2Th.]	d-spacing [Å]	Rel. Int. [%]
3.0438	430.33	0.8187	29.02718	9.61
6.2403	2058.39	0.2303	14.16383	45.99
9.0729	3965.14	0.3582	9.74716	88.59
12.4652	2447.48	0.2303	7.10116	54.68
17.4786	1210.82	0.4605	5.07399	27.05
18.7810	540.29	0.3070	4.72497	12.07
25.1962	1051.77	0.2303	3.53460	23.50
26.7519	4476.00	0.3070	3.33249	100.00

S36

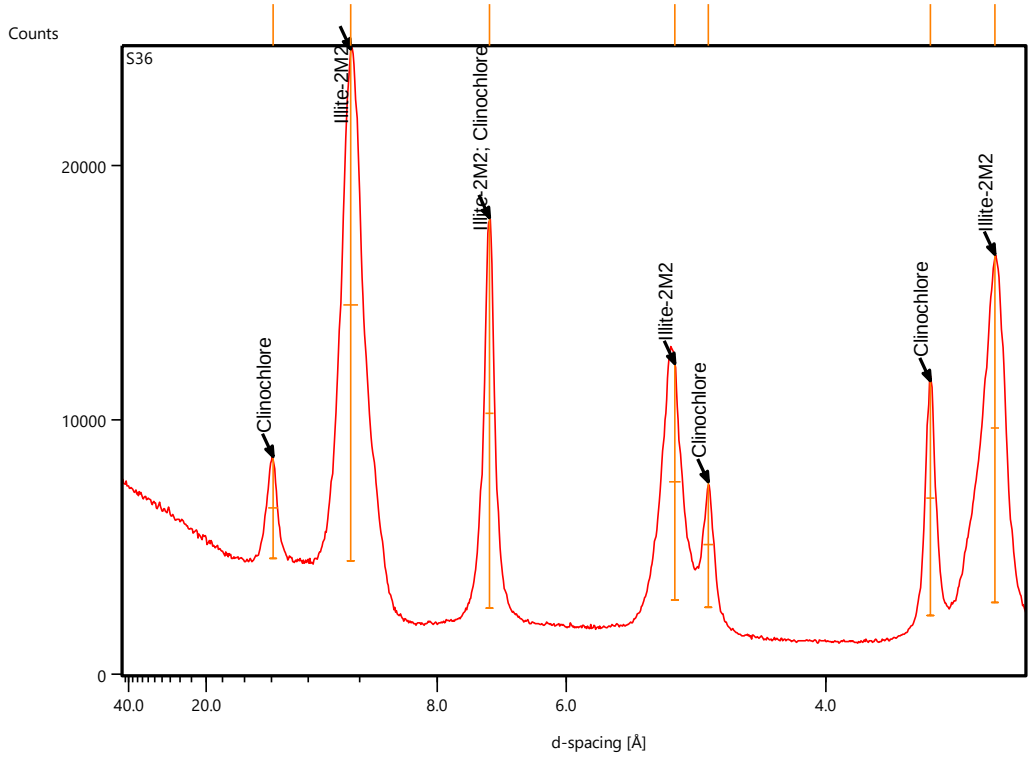

Pos. [°2Th.]	Height [cts]	FWHM Left [°2Th.]	d-spacing [Å]	Rel. Int. [%]
6.3368	4010.31	0.2814	13.94831	19.90
8.5667	20152.62	0.4349	10.32200	100.00
12.5671	15337.98	0.2558	7.04378	76.11
17.8781	9273.96	0.3070	4.96149	46.02
18.8492	4959.52	0.2814	4.70804	24.61
25.2227	9249.22	0.2558	3.53096	45.90
27.0659	13698.73	0.2558	3.29454	67.97

S36_GL Y

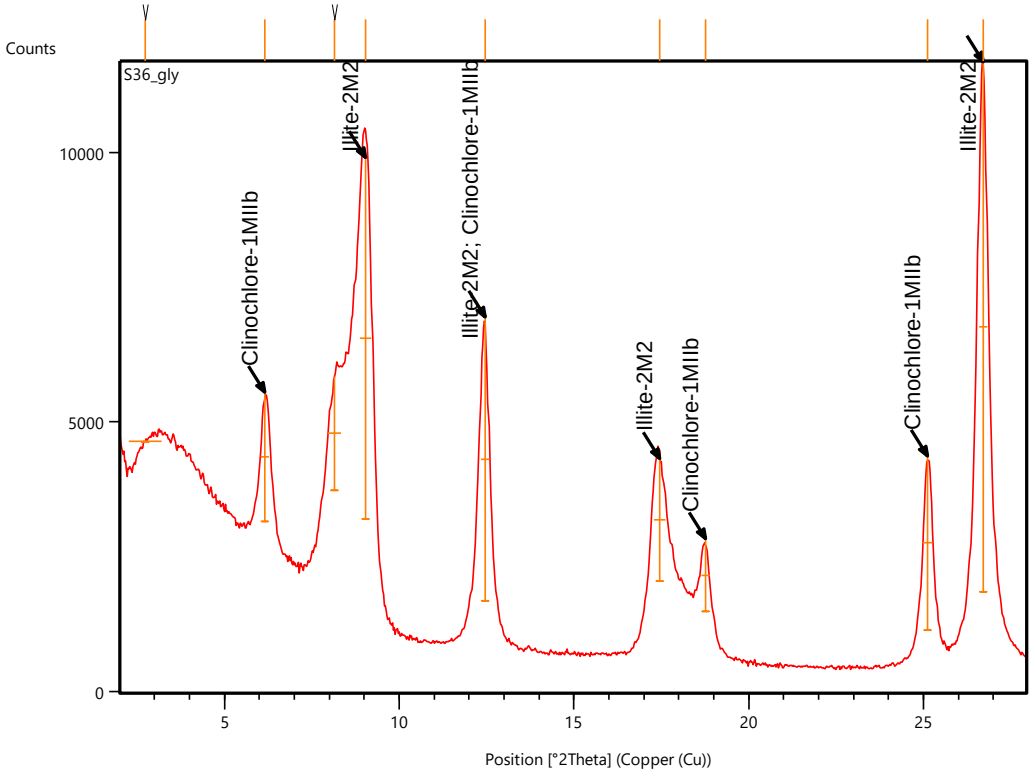

Pos. [°2Th.]	Height [cts]	FWHM Left [°2Th.]	d-spacing [Å]	Rel. Int. [%]
2.7450	23.40	0.9210	32.18612	0.24
6.1505	2404.20	0.2558	14.37048	24.45
8.1452	2107.96	0.3582	10.85508	21.44
9.0337	6705.87	0.3326	9.78936	68.20
12.4632	5266.37	0.2558	7.10229	53.56
17.4597	2288.32	0.3070	5.07944	23.27
18.7759	1341.00	0.2303	4.72625	13.64
25.1259	3227.71	0.2814	3.54435	32.83
26.7112	9832.33	0.2558	3.33748	100.00

S43

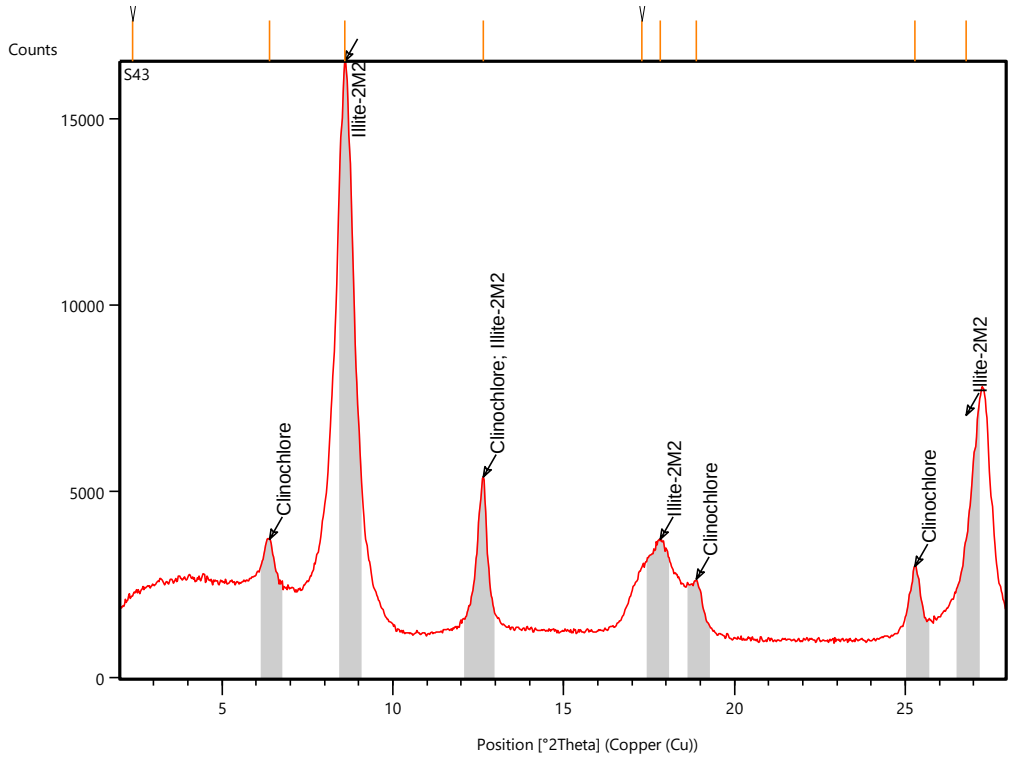

Pos. [°2Th.]	Height [cts]	FWHM Left [°2Th.]	d-spacing [Å]	Rel. Int. [%]
2.3755	272.55	0.5117	37.19255	1.84
6.3979	1507.38	0.2558	13.81534	10.15
8.6012	14845.39	0.3582	10.28070	100.00
12.6540	4082.49	0.2047	6.99560	27.50
17.2876	1664.36	0.5628	5.12962	11.21
17.8409	2446.91	0.3582	4.97177	16.48
18.8856	1456.69	0.1791	4.69903	9.81
25.2846	1641.73	0.1791	3.52246	11.06
26.7857	5234.01	0.2303	3.32836	35.26

S43_GLY

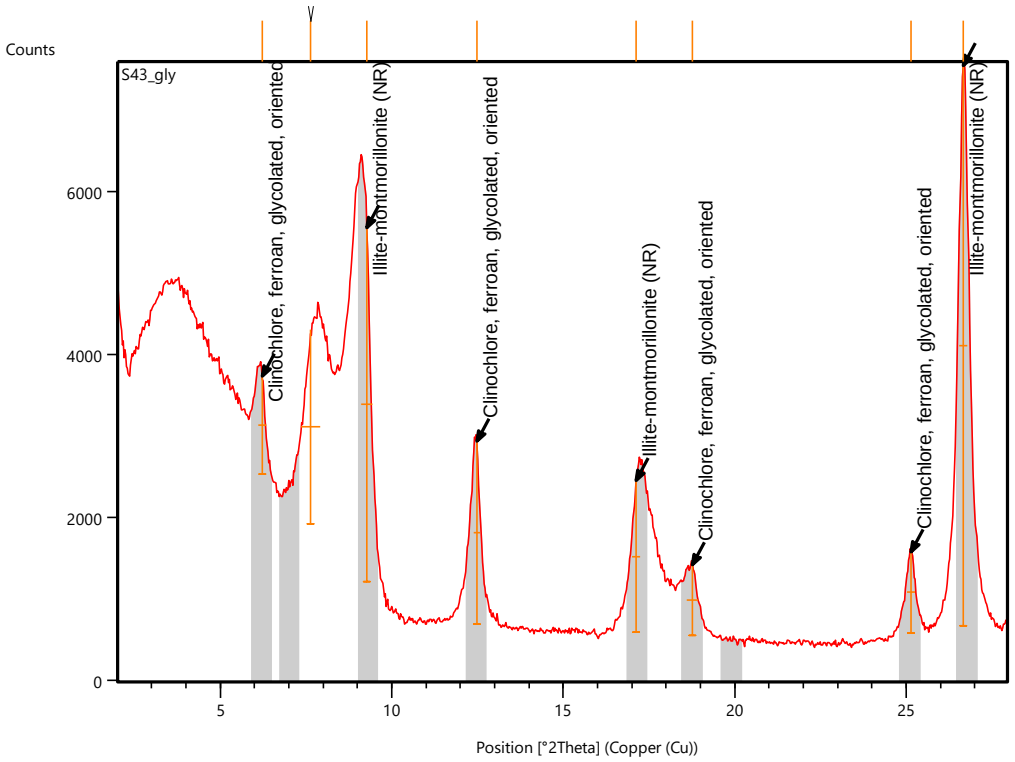

Pos. [°2Th.]	Height [cts]	FWHM Left [°2Th.]	d-spacing [Å]	Rel. Int. [%]
6.2250	1201.29	0.2303	14.19865	17.46
7.6471	2380.24	0.5628	11.56101	34.59
9.2689	4354.31	0.3070	9.54152	63.27
12.4843	2249.01	0.2047	7.09032	32.68
17.1179	1863.38	0.2303	5.18010	27.08
18.7748	862.51	0.3070	4.72653	12.53
25.1450	994.57	0.2558	3.54169	14.45
26.6673	6882.08	0.2558	3.34287	100.00

S47

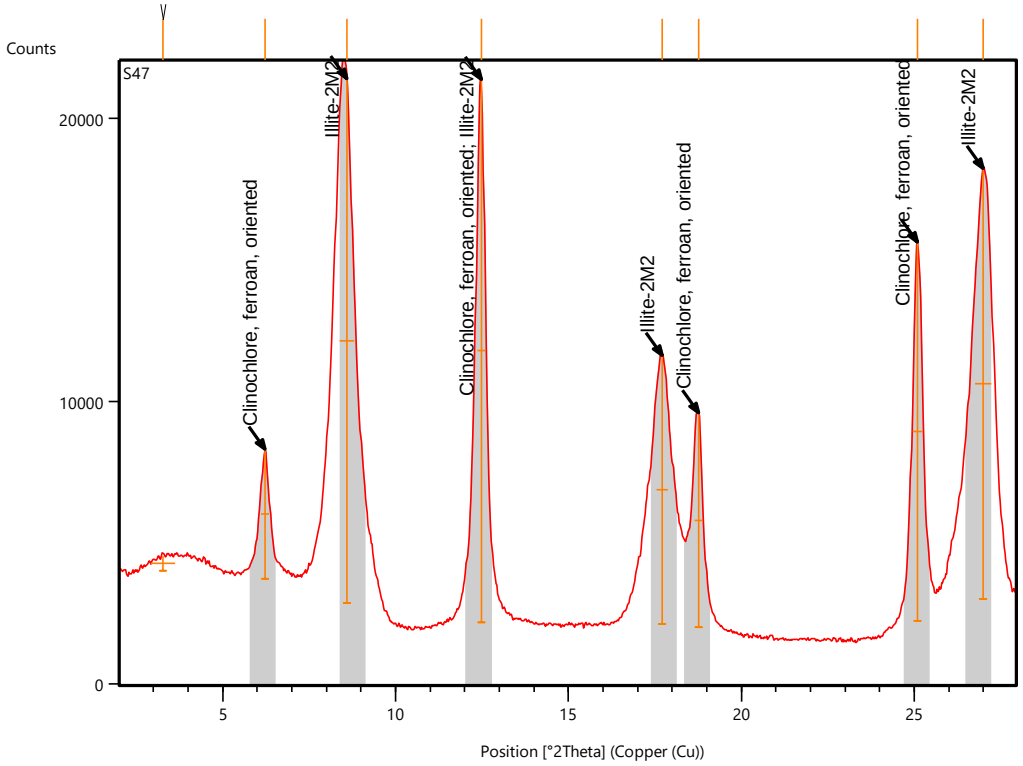

Pos. [°2Th.]	Height [cts]	FWHM Left [°2Th.]	d-spacing [Å]	Rel. Int. [%]
3.2651	515.95	0.7164	27.06069	2.68
6.2273	4584.94	0.2303	14.19327	23.86
8.6017	18573.34	0.4093	10.28001	96.64
12.4764	19218.57	0.2558	7.09480	100.00
17.7122	9517.22	0.3070	5.00759	49.52
18.7608	7584.54	0.2303	4.73001	39.46
25.0861	13397.75	0.2814	3.54987	69.71

S47_GLY

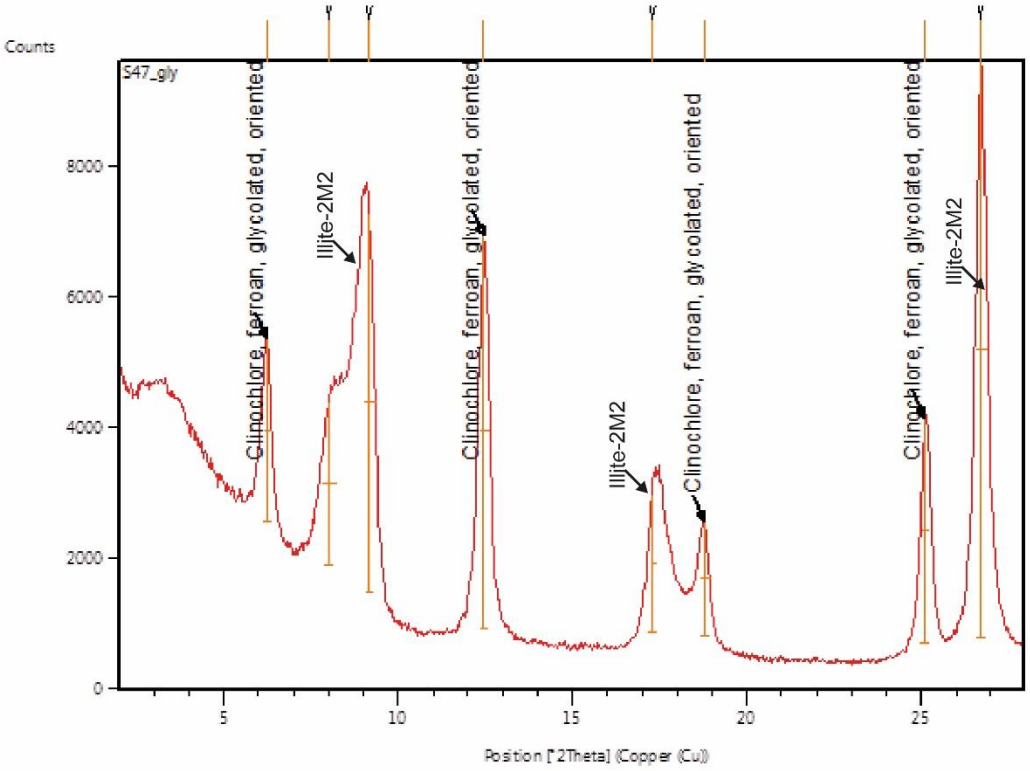

Pos. [°2Th.]	Height [cts]	FWHM Left [°2Th.]	d-spacing [Å]	Rel. Int. [%]
6.2583	2806.76	0.2303	14.12314	31.80
8.0020	2500.22	0.4093	11.04902	28.33
9.1906	5806.65	0.3838	9.62259	65.79
12.4690	6024.19	0.2814	7.09902	68.25
17.2836	2126.99	0.1535	5.13080	24.10
18.7989	1759.02	0.3070	4.72050	19.93
25.1066	3455.80	0.2558	3.54702	39.15
26.7093	8826.24	0.2814	3.33771	100.00

S49

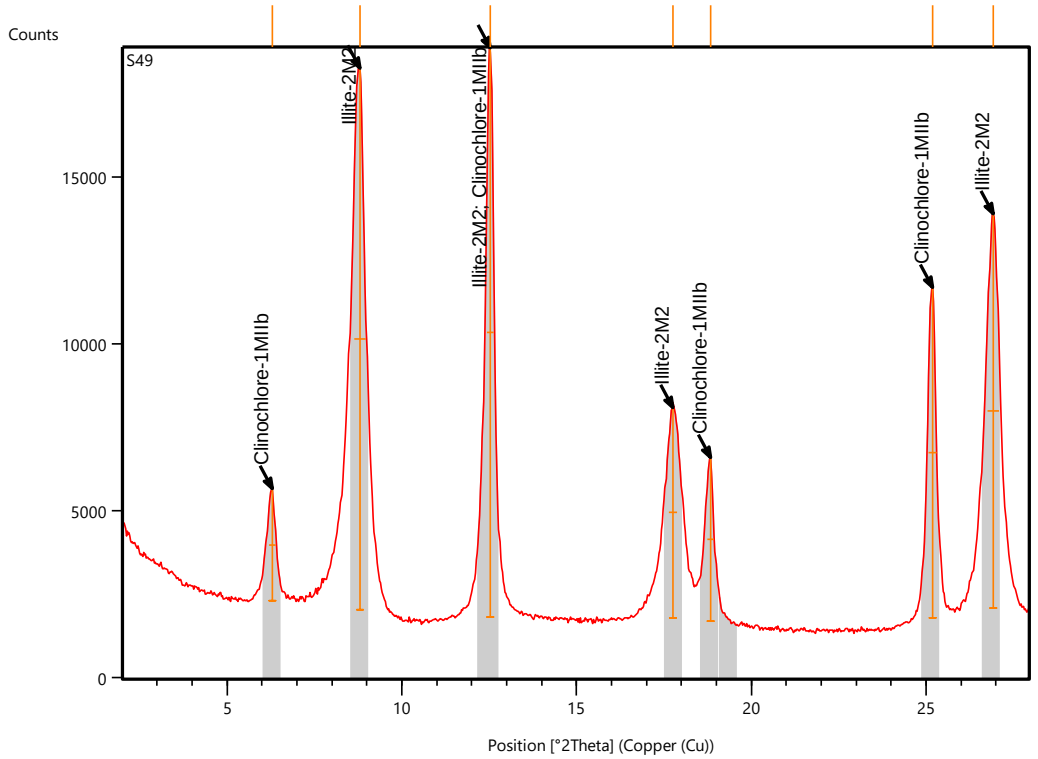

Pos. [°2Th.]	Height [cts]	FWHM Left [°2Th.]	d-spacing [Å]	Rel. Int. [%]
6.2995	3356.40	0.2047	14.03091	19.66
8.8023	16205.19	0.3070	10.04621	94.91
12.5396	17073.58	0.2047	7.05919	100.00
17.7507	6288.50	0.2303	4.99683	36.83
18.8323	4882.12	0.2047	4.71221	28.59
25.1797	9912.20	0.2303	3.53688	58.06
26.9210	11801.43	0.3326	3.31194	69.12

S49_GLY

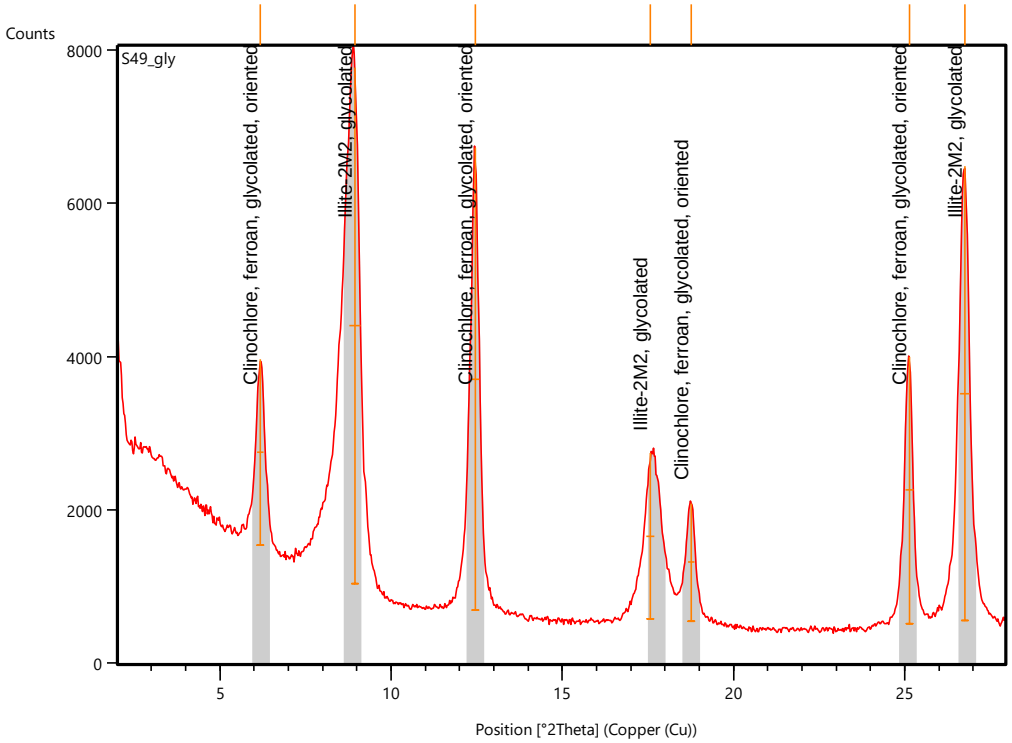

Pos. [°2Th.]	Height [cts]	FWHM Left [°2Th.]	d-spacing [Å]	Rel. Int. [%]
6.1849	2423.93	0.2047	14.29049	36.00
8.9488	6732.24	0.3070	9.88209	100.00
12.4521	6039.80	0.2303	7.10862	89.71
17.5826	2169.82	0.2558	5.04421	32.23
18.7601	1537.40	0.2047	4.73018	22.84
25.1320	3489.26	0.2303	3.54350	51.83
26.7612	5933.27	0.2814	3.33136	88.13

S51

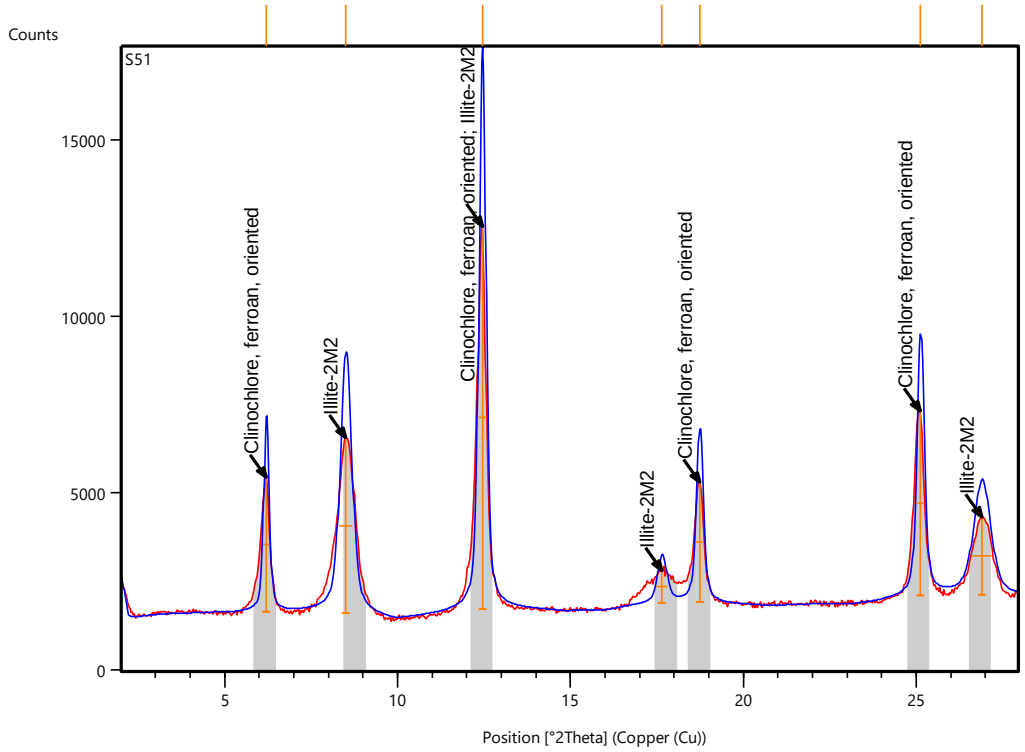

Pos. [°2Th.]	Height [cts]	FWHM Left [°2Th.]	d-spacing [Å]	Rel. Int. [%]
6.2098	3806.98	0.1791	14.23337	35.13
8.5120	4948.43	0.3838	10.38812	45.66
12.4540	10836.49	0.2303	7.10753	100.00
17.6479	908.55	0.3070	5.02571	8.38
18.7334	3390.27	0.2303	4.73686	31.29
25.1140	5232.45	0.2303	3.54600	48.29
26.8915	2186.76	0.5628	3.31551	20.18

S51_GLY

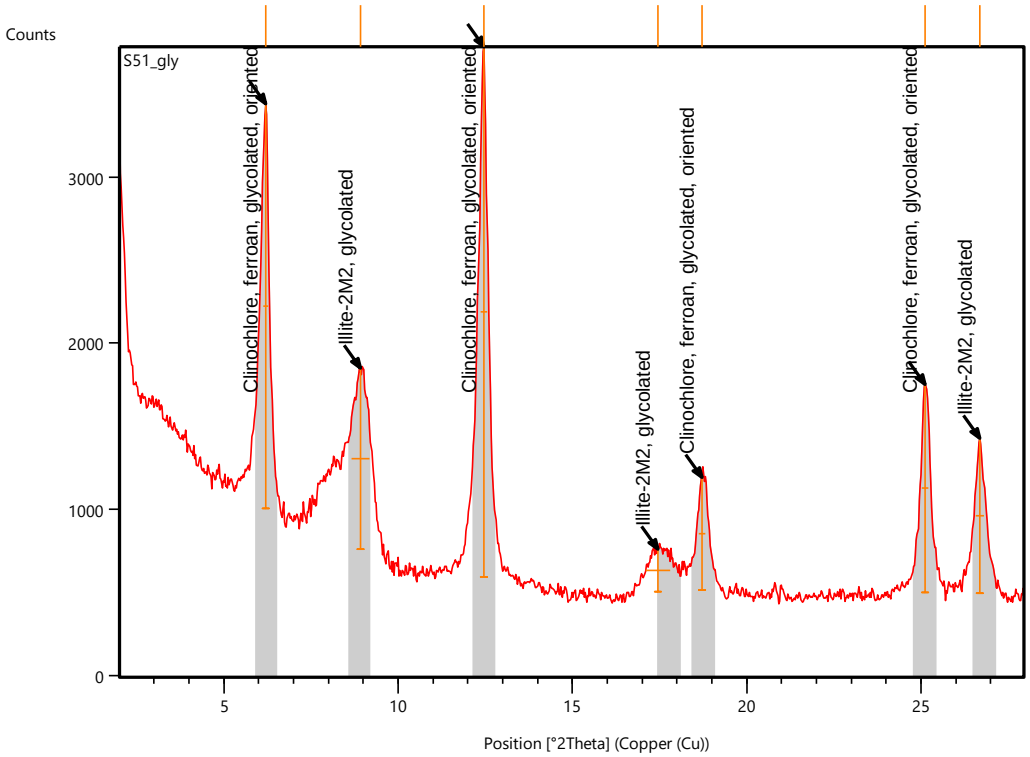

Pos. [°2Th.]	Height [cts]	FWHM Left [°2Th.]	d-spacing [Å]	Rel. Int. [%]
6.2074	2431.00	0.1535	14.23892	76.01
8.9357	1085.57	0.5117	9.89658	33.94
12.4674	3198.12	0.2047	7.09991	100.00
17.4611	257.37	0.7164	5.07905	8.05
18.7126	673.62	0.2047	4.74209	21.06
25.1098	1253.28	0.2047	3.54657	39.19
26.6892	931.38	0.2303	3.34018	29.12

S53

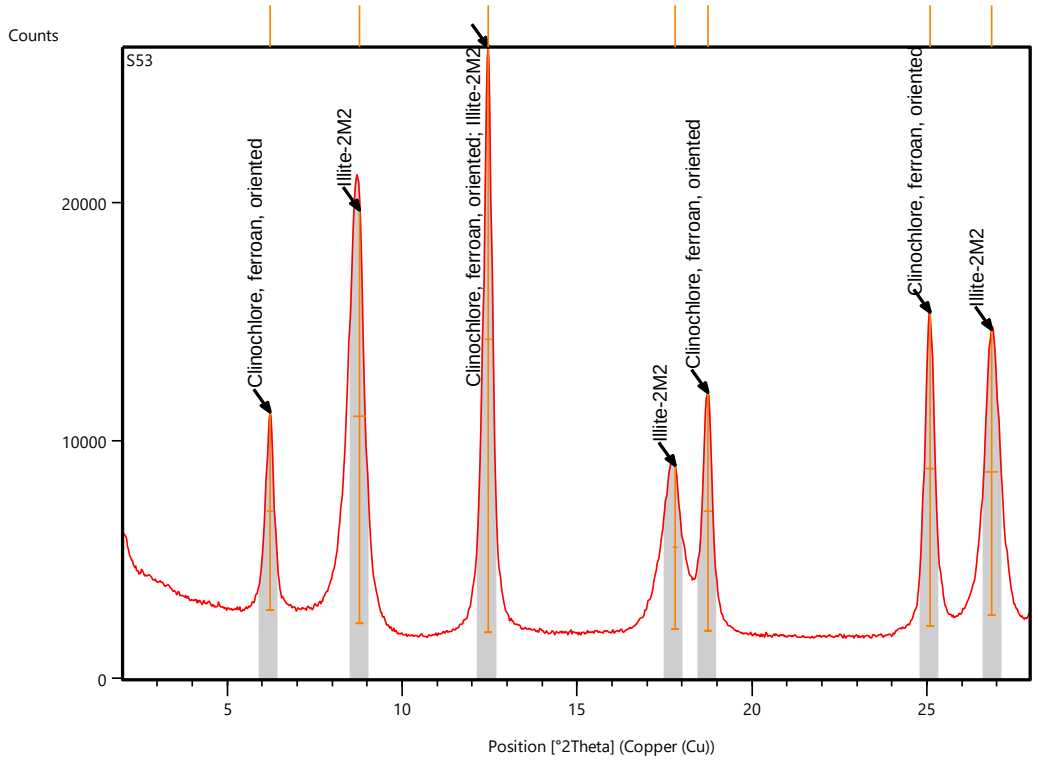

Pos. [°2Th.]	Height [cts]	FWHM Left [°2Th.]	d-spacing [Å]	Rel. Int. [%]
6.2367	8353.32	0.2047	14.17207	33.90
8.7954	17418.96	0.3582	10.05404	70.69
12.4699	24641.49	0.2047	7.09848	100.00
17.8019	6914.53	0.1535	4.98258	28.06
18.7367	10024.24	0.2303	4.73604	40.68
25.0968	13178.35	0.2558	3.54839	53.48
26.8439	12023.24	0.3838	3.32128	48.79

S53_GLY

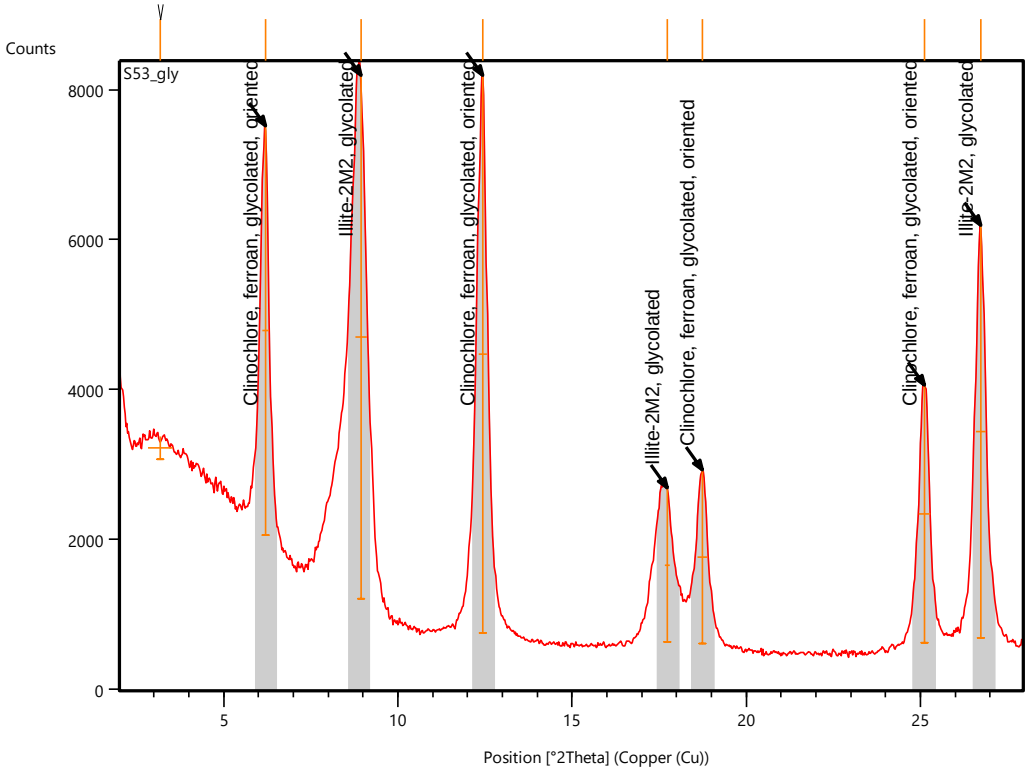

Pos. [°2Th.]	Height [cts]	FWHM Left [°2Th.]	d-spacing [Å]	Rel. Int. [%]
3.1766	304.11	0.7164	27.81379	4.09
6.1976	5466.84	0.2047	14.26126	73.47
8.9435	6979.33	0.3070	9.88789	93.80
12.4397	7440.65	0.2558	7.11568	100.00
17.7410	2052.30	0.1535	4.99953	27.58
18.7392	2320.11	0.2814	4.73542	31.18
25.1160	3442.14	0.3326	3.54572	46.26

S54

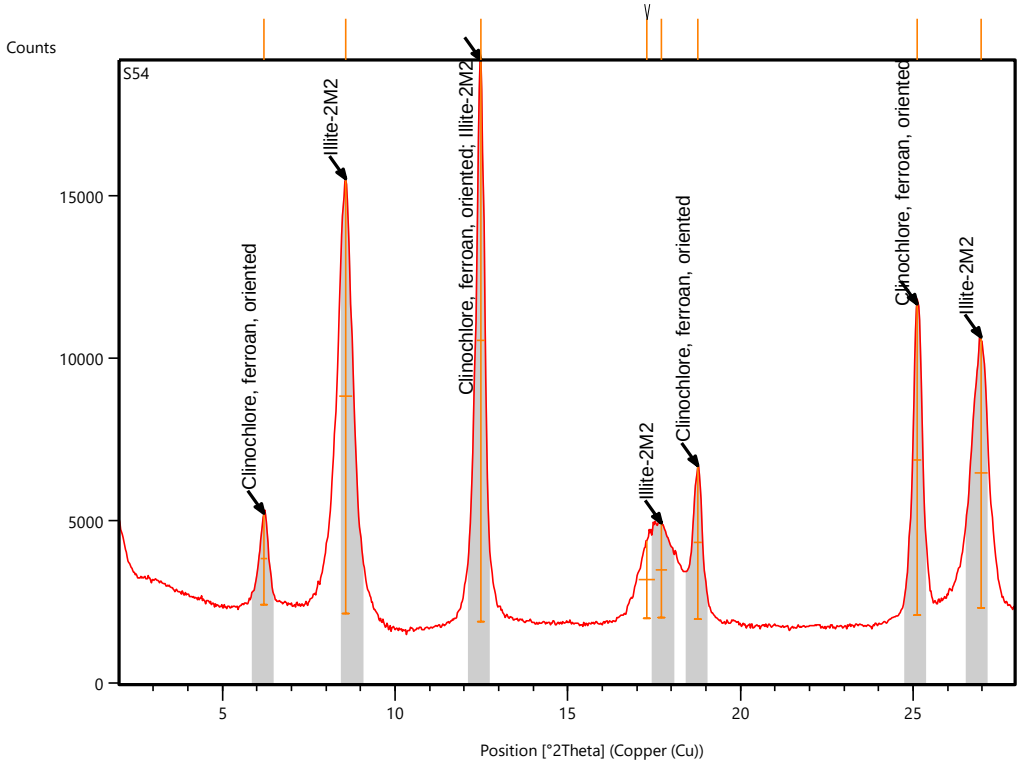

Pos. [°2Th.]	Height [cts]	FWHM Left [°2Th.]	d-spacing [Å]	Rel. Int. [%]
6.2043	2800.53	0.2047	14.24601	16.12
8.5672	13381.88	0.3582	10.32133	77.04
12.4893	17369.51	0.2303	7.08753	100.00
17.2896	2381.07	0.4605	5.12903	13.71
17.7218	2917.36	0.3070	5.00492	16.80
18.7736	4720.06	0.2303	4.72680	27.17
25.1133	9561.90	0.2303	3.54609	55.05

S54_GLY

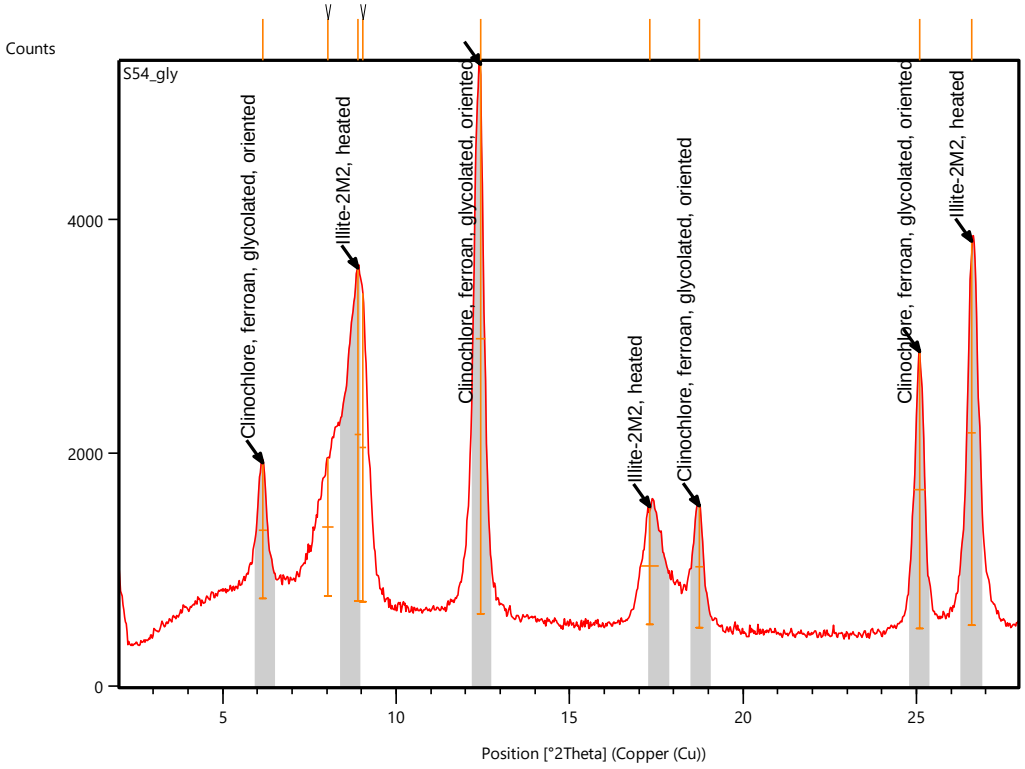

Pos. [°2Th.]	Height [cts]	FWHM Left [°2Th.]	d-spacing [Å]	Rel. Int. [%]
6.1699	1165.40	0.2303	14.32533	24.76
8.0447	1183.10	0.3070	10.99050	25.14
8.8909	2853.95	0.1791	9.94633	60.63
9.0394	2642.85	0.1791	9.78318	56.15
12.4322	4706.82	0.2814	7.11992	100.00
17.3248	1009.43	0.5117	5.11870	21.45
18.7336	1045.46	0.2558	4.73682	22.21
25.0971	2371.87	0.3326	3.54834	50.39
26.6007	3291.40	0.2558	3.35109	69.93

S56

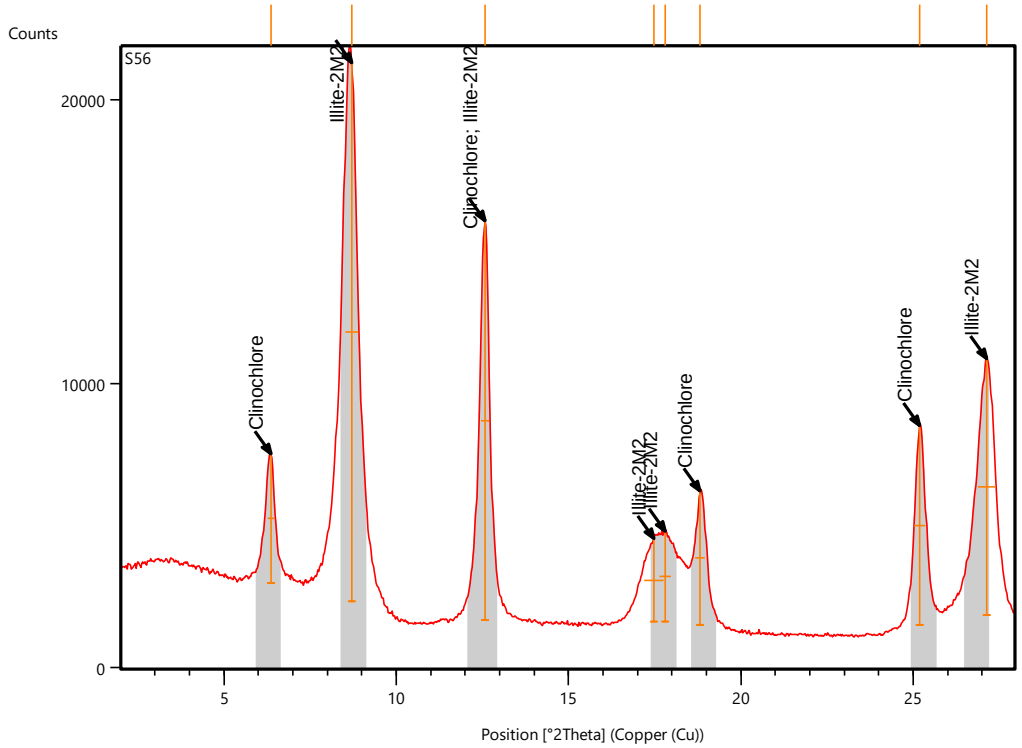

Pos. [°2Th.]	Height [cts]	FWHM Left [°2Th.]	d-spacing [Å]	Rel. Int. [%]
6.3694	4558.07	0.2047	13.87711	24.02
8.7167	18974.41	0.3838	10.14463	100.00
12.5789	14059.06	0.2303	7.03722	74.09
17.4823	2914.89	0.5628	5.07294	15.36
17.8145	3182.05	0.3070	4.97907	16.77
18.8239	4734.26	0.2814	4.71430	24.95
25.2006	7031.93	0.3326	3.53400	37.06
27.1302	9038.95	0.5117	3.28688	47.64

S56_GLY

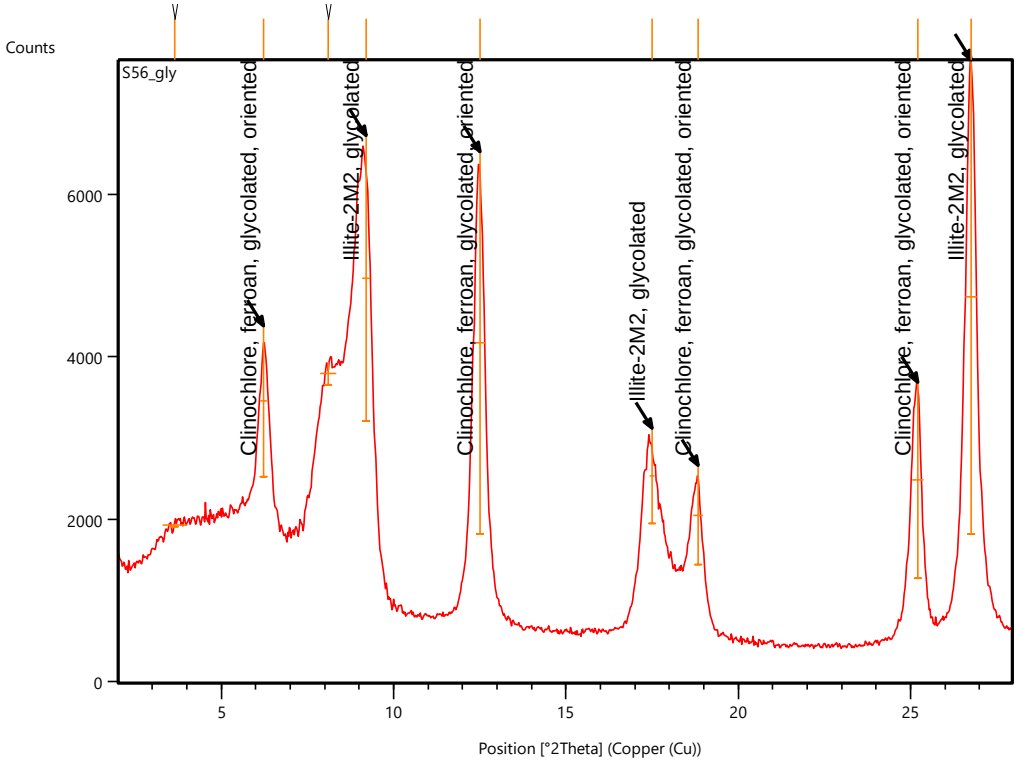

Pos. [°2Th.]	Height [cts]	FWHM Left [°2Th.]	d-spacing [Å]	Rel. Int. [%]
3.6459	26.08	0.7164	24.23494	0.44
6.2290	1859.89	0.2047	14.18949	31.32
8.1058	271.46	0.4605	10.90778	4.57
9.2149	3516.66	0.2303	9.59728	59.22
12.5073	4706.99	0.3070	7.07737	79.27
17.5031	1165.21	0.1535	5.06696	19.62
18.8331	1218.76	0.2814	4.71200	20.52
25.2095	2418.31	0.3326	3.53278	40.73
26.7642	5938.04	0.3326	3.33099	100.00

UW462 samples

U7

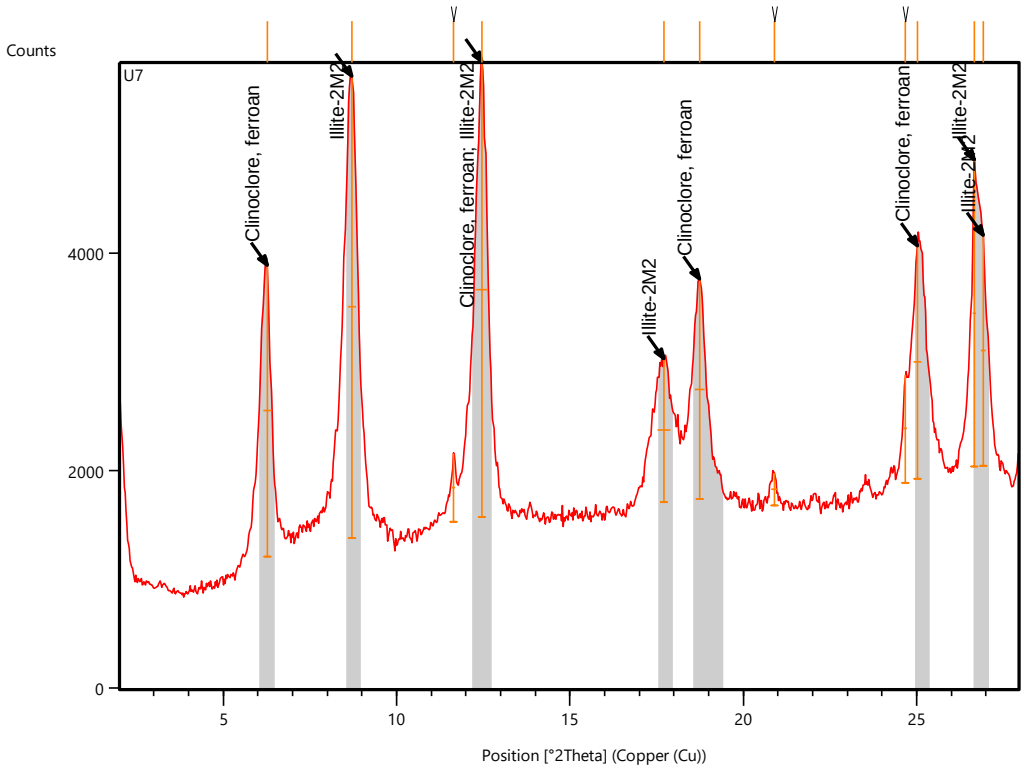

Pos. [°2Th.]	Height [cts]	FWHM Left [°2Th.]	d-spacing [Å]	Rel. Int. [%]
6.2679	2684.20	0.2558	14.10156	63.17
8.7181	4249.21	0.2558	10.14308	100.00
11.6528	624.49	0.0768	7.59435	14.70
12.4670	4186.85	0.3326	7.10011	98.53
17.7191	1320.66	0.3582	5.00565	31.08
18.7429	2023.47	0.2814	4.73449	47.62
20.8955	298.20	0.1791	4.25137	7.02
24.6782	989.47	0.0768	3.60762	23.29
25.0231	2136.87	0.2303	3.55867	50.29
26.6600	2823.87	0.1023	3.34376	66.46
26.9129	2122.58	0.1535	3.31292	49.95

U7_GLY

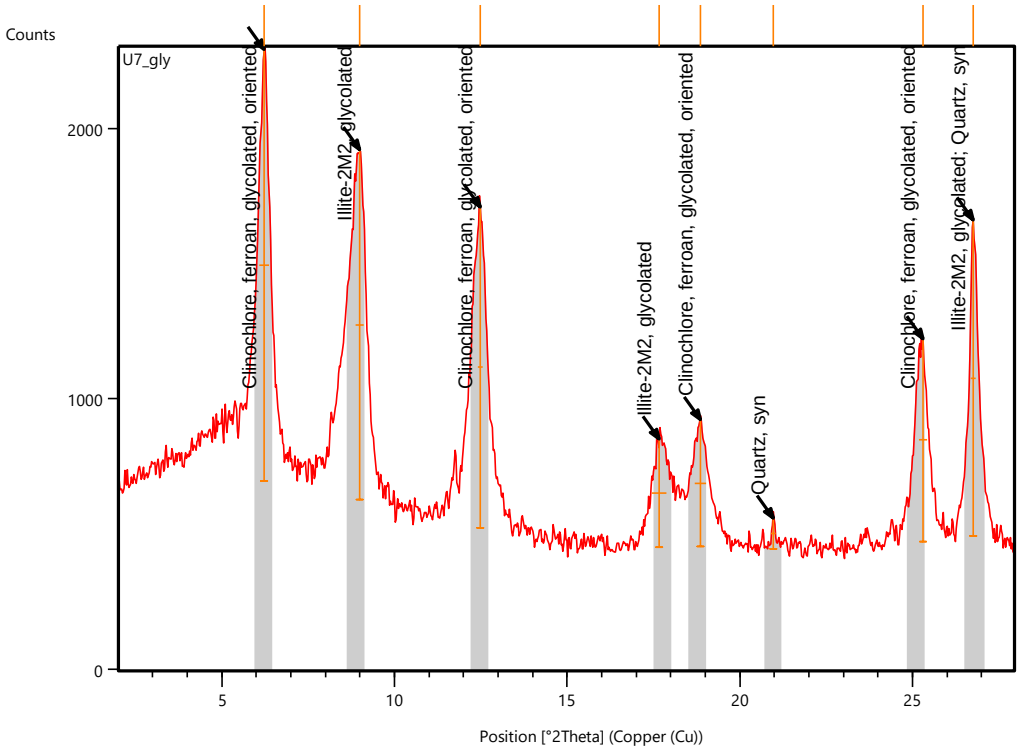

Pos. [°2Th.]	Height [cts]	FWHM Left [°2Th.]	d-spacing [Å]	Rel. Int. [%]
6.2366	1597.27	0.2814	14.17231	100.00
8.9982	1294.98	0.2558	9.82795	81.07
12.4946	1187.50	0.1279	7.08450	74.35
17.6754	401.61	0.4093	5.01796	25.14
18.8568	470.43	0.3070	4.70614	29.45
20.9787	113.06	0.1535	4.23469	7.08
25.3080	749.81	0.2558	3.51925	46.94
26.7538	1171.02	0.1535	3.33226	73.31

U20

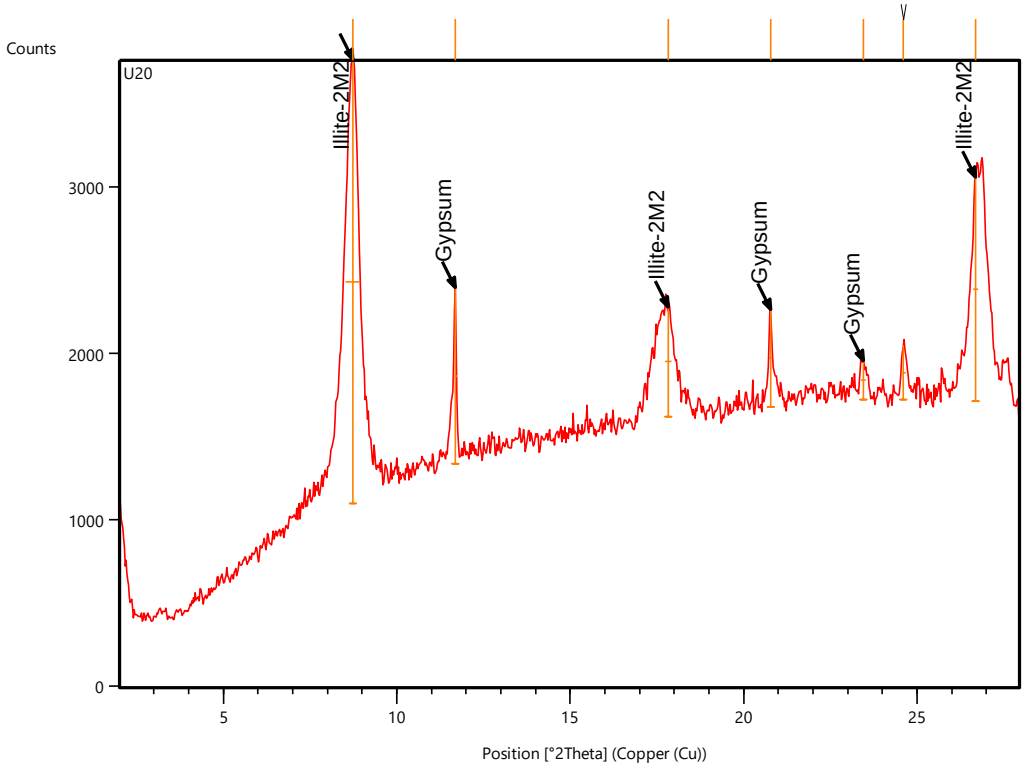

Pos. [°2Th.]	Height [cts]	FWHM Left [°2Th.]	d-spacing [Å]	Rel. Int. [%]
8.7416	2670.78	0.4349	10.11589	100.00
11.6821	1054.66	0.0768	7.57538	39.49
17.8406	660.57	0.2047	4.97184	24.73
20.7772	582.72	0.0768	4.27530	21.82
23.4525	231.78	0.1535	3.79330	8.68
24.6143	325.89	0.1279	3.61683	12.20
26.6851	1348.07	0.1535	3.34069	50.47

U20_GLY

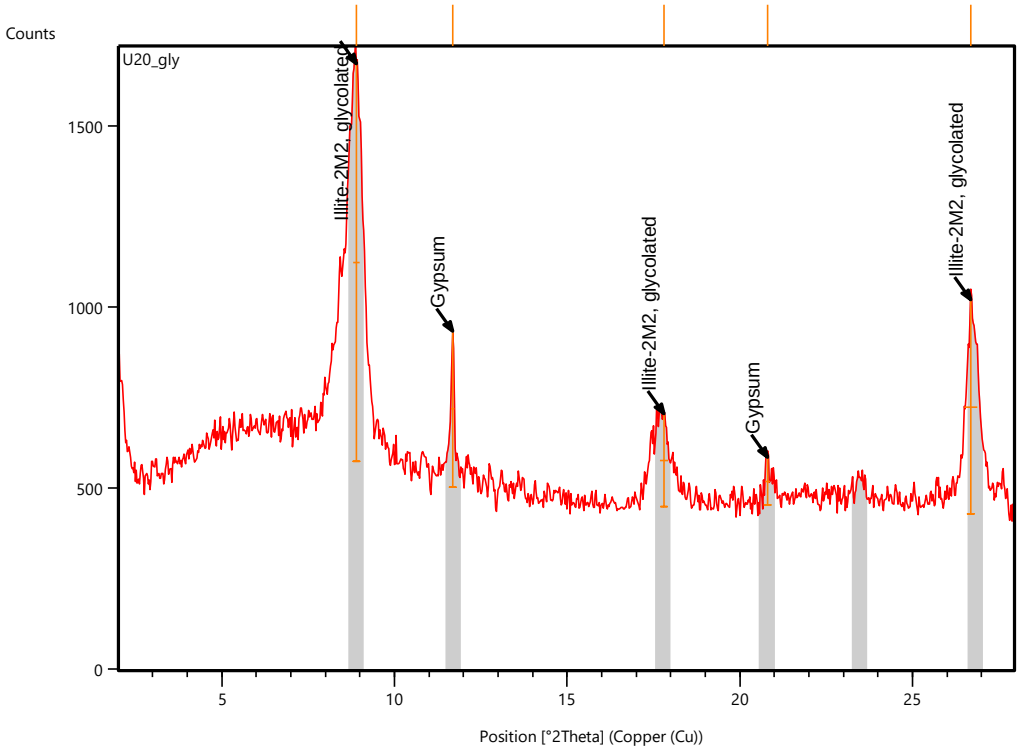

Pos. [°2Th.]	Height [cts]	FWHM Left [°2Th.]	d-spacing [Å]	Rel. Int. [%]
8.9038	1097.78	0.2047	9.93194	100.00
11.6889	430.30	0.1023	7.57099	39.20
17.8020	255.00	0.2558	4.98255	23.23
20.8147	132.25	0.1535	4.26769	12.05
26.6980	591.60	0.3582	3.33910	53.89

U27

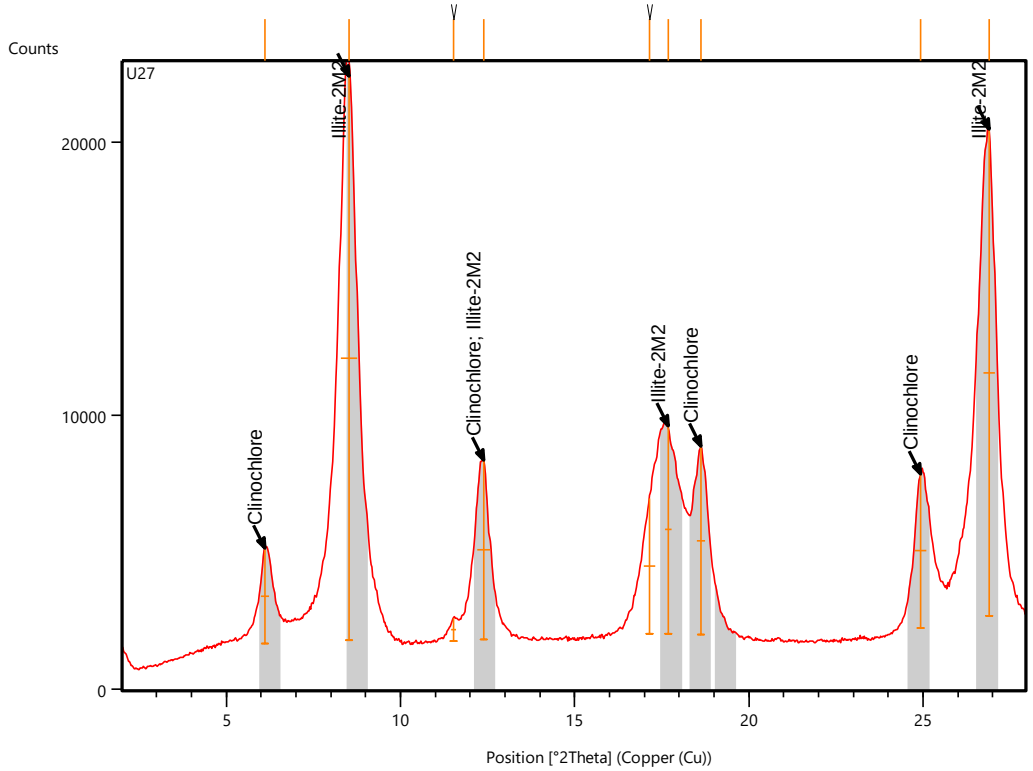

Pos. [°2Th.]	Height [cts]	FWHM Left [°2Th.]	d-spacing [Å]	Rel. Int. [%]
6.1154	3476.16	0.2558	14.45278	16.86
8.5235	20621.99	0.4605	10.37420	100.00
11.5246	832.90	0.1535	7.67853	4.04
12.3884	6566.93	0.3582	7.14499	31.84
17.1435	4959.67	0.3070	5.17242	24.05
17.6855	7603.81	0.1791	5.01511	36.87
18.6207	6905.09	0.2558	4.76527	33.48
24.9289	5631.53	0.3326	3.57191	27.31
26.8918	17788.37	0.3326	3.31548	86.26

U27_GLY

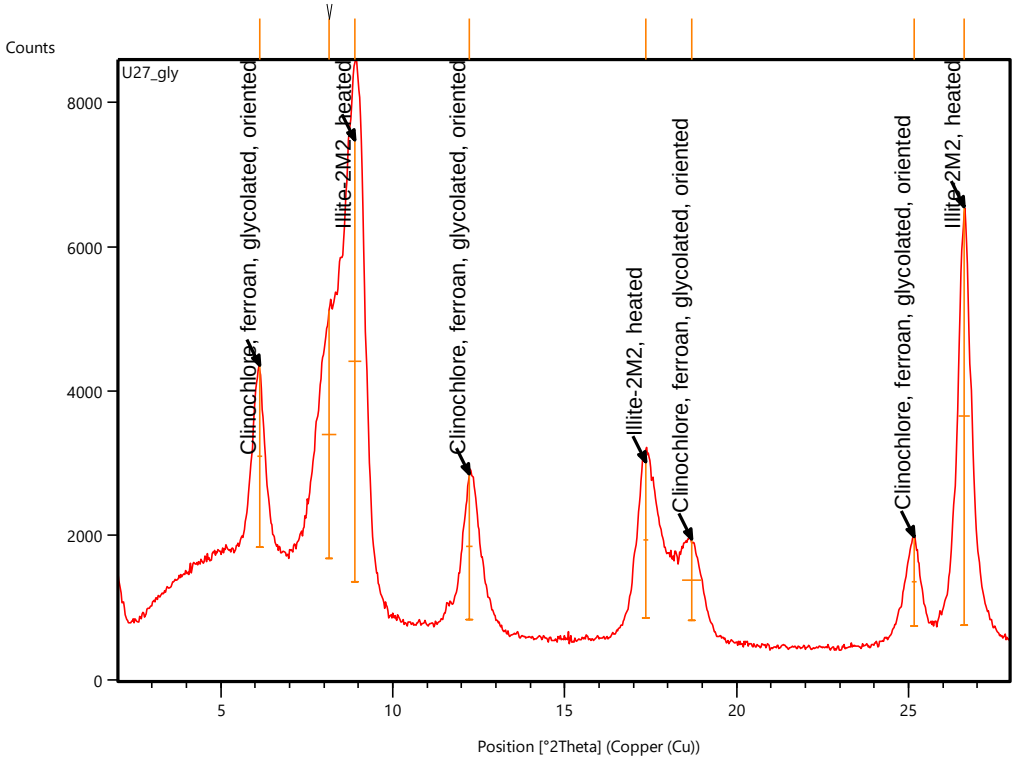

Pos. [°2Th.]	Height [cts]	FWHM Left [°2Th.]	d-spacing [Å]	Rel. Int. [%]
6.1267	2215.88	0.1279	14.42625	42.65
8.1408	1878.58	0.4093	10.86100	36.16
9.0898	5074.99	0.3582	9.72909	97.68
12.2387	1469.73	0.2047	7.23209	28.29
17.2704	1354.88	0.1279	5.13471	26.08
18.6914	518.51	0.5628	4.74742	9.98
25.1556	1000.93	0.1535	3.54022	19.26

U31

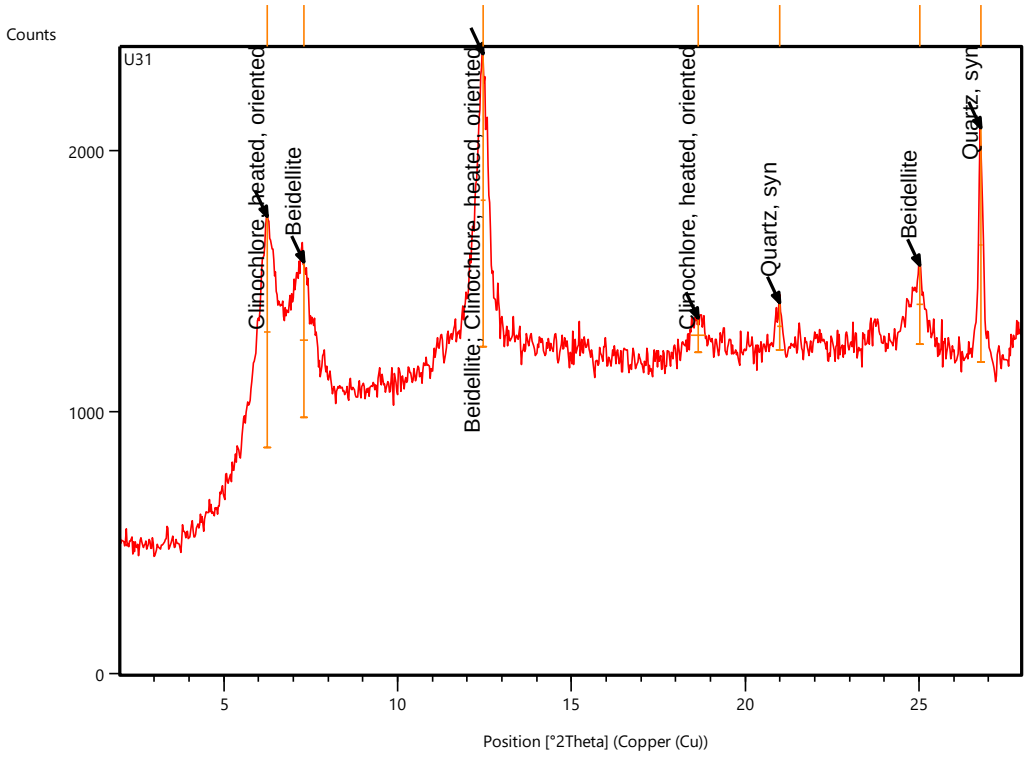

Pos. [°2Th.]	Height [cts]	FWHM Left [°2Th.]	d-spacing [Å]	Rel. Int. [%]
6.2484	883.39	0.2047	14.14560	78.88
7.3019	595.81	0.2558	12.10677	53.20
12.4577	1119.96	0.1535	7.10543	100.00
18.6600	128.71	0.4093	4.75533	11.49
20.9848	179.63	0.1535	4.23347	16.04
25.0342	301.69	0.2047	3.55711	26.94
26.7728	894.88	0.1023	3.32994	79.90

U31_GLY

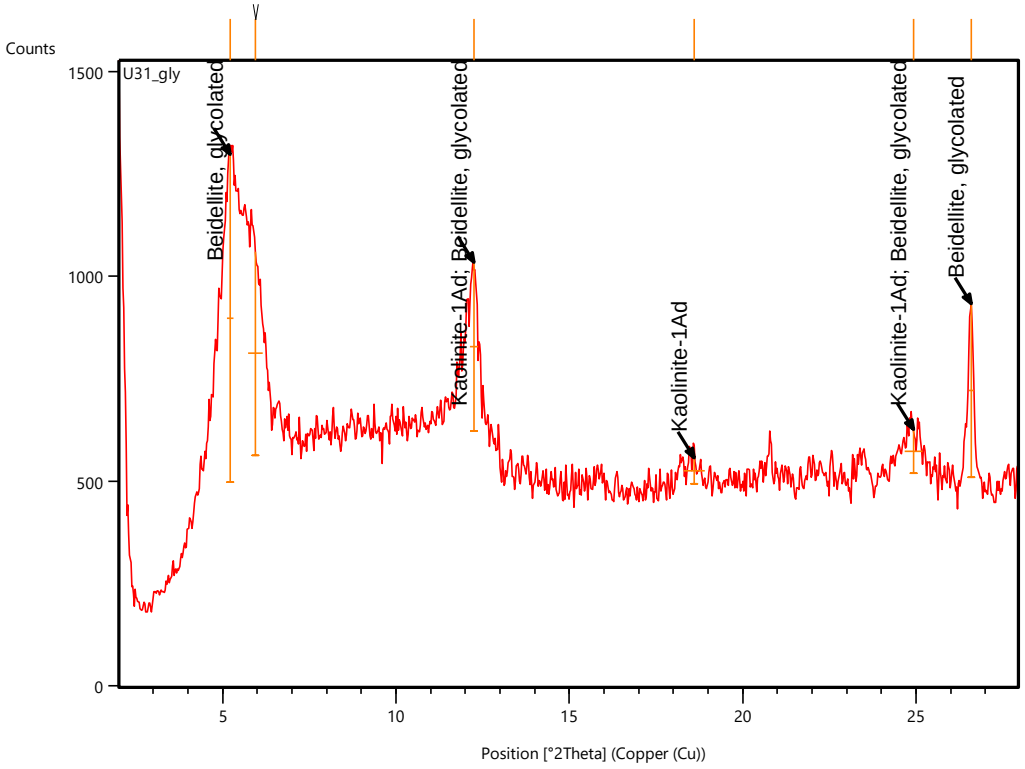

Pos. [°2Th.]	Height [cts]	FWHM Left [°2Th.]	d-spacing [Å]	Rel. Int. [%]
5.2128	800.92	0.1791	16.95323	100.00
5.9529	496.65	0.4093	14.84699	62.01
12.2540	413.82	0.2558	7.22308	51.67
18.6123	63.08	0.6140	4.76741	7.88
24.9395	107.37	0.5117	3.57040	13.41
26.5850	423.43	0.1279	3.35303	52.87

U37

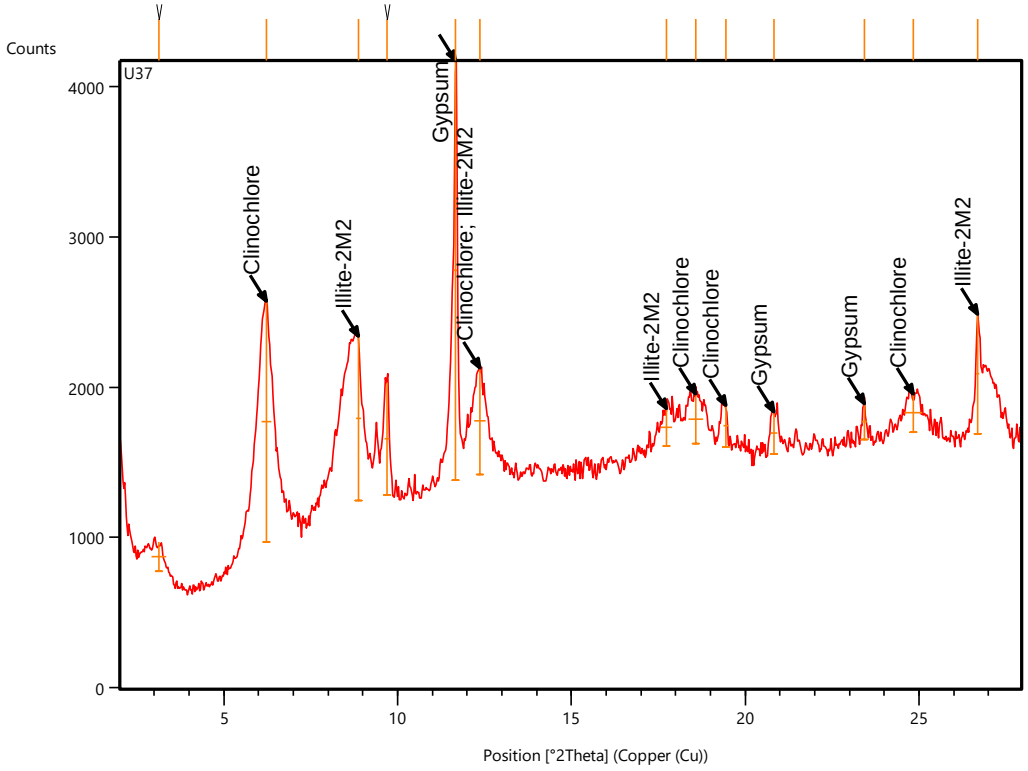

Pos. [°2Th.]	Height [cts]	FWHM Left [°2Th.]	d-spacing [Å]	Rel. Int. [%]
3.1274	196.15	0.4093	28.25127	6.85
6.2224	1602.13	0.2814	14.20459	55.98
8.8676	1091.01	0.1535	9.97235	38.12
9.6895	747.98	0.1279	9.12824	26.13
11.6769	2862.09	0.0768	7.57870	100.00
12.3585	709.65	0.3070	7.16225	24.79
17.7397	250.73	0.3070	4.99991	8.76
18.5815	332.12	0.4093	4.77523	11.60
19.4377	274.89	0.1535	4.56679	9.60
20.8313	279.42	0.2047	4.26431	9.76

23.4316	235.04	0.1535	3.79665	8.21
24.8342	253.73	0.5117	3.58530	8.87
26.6966	798.30	0.1023	3.33927	27.89

U37_GLY

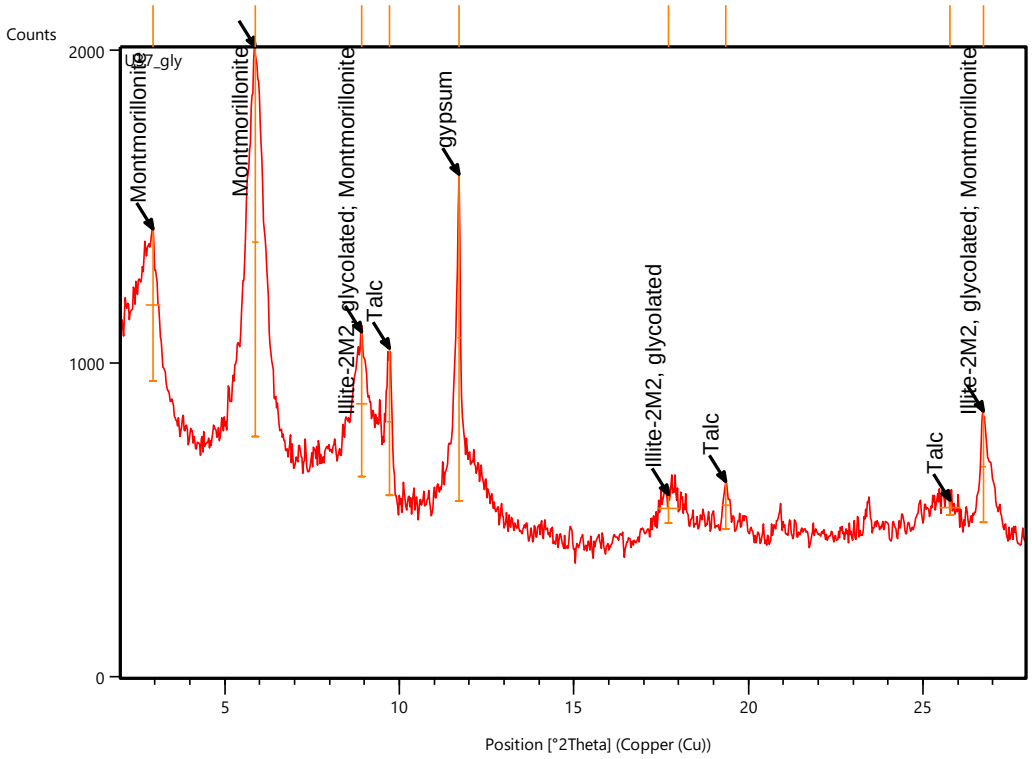

Pos. [°2Th.]	Height [cts]	FWHM Left [°2Th.]	d-spacing [Å]	Rel. Int. [%]
2.9509	485.57	0.4093	29.94052	38.91
5.8726	1248.01	0.2047	15.04971	100.00
8.9176	460.81	0.3070	9.91664	36.92
9.7310	468.16	0.1535	9.08944	37.51
11.7083	1042.49	0.1023	7.55846	83.53
17.7082	90.18	0.6140	5.00872	7.23
19.3570	149.09	0.1791	4.58566	11.95
25.7821	46.31	0.6140	3.45560	3.71
26.7257	355.67	0.1279	3.33570	28.50

U47

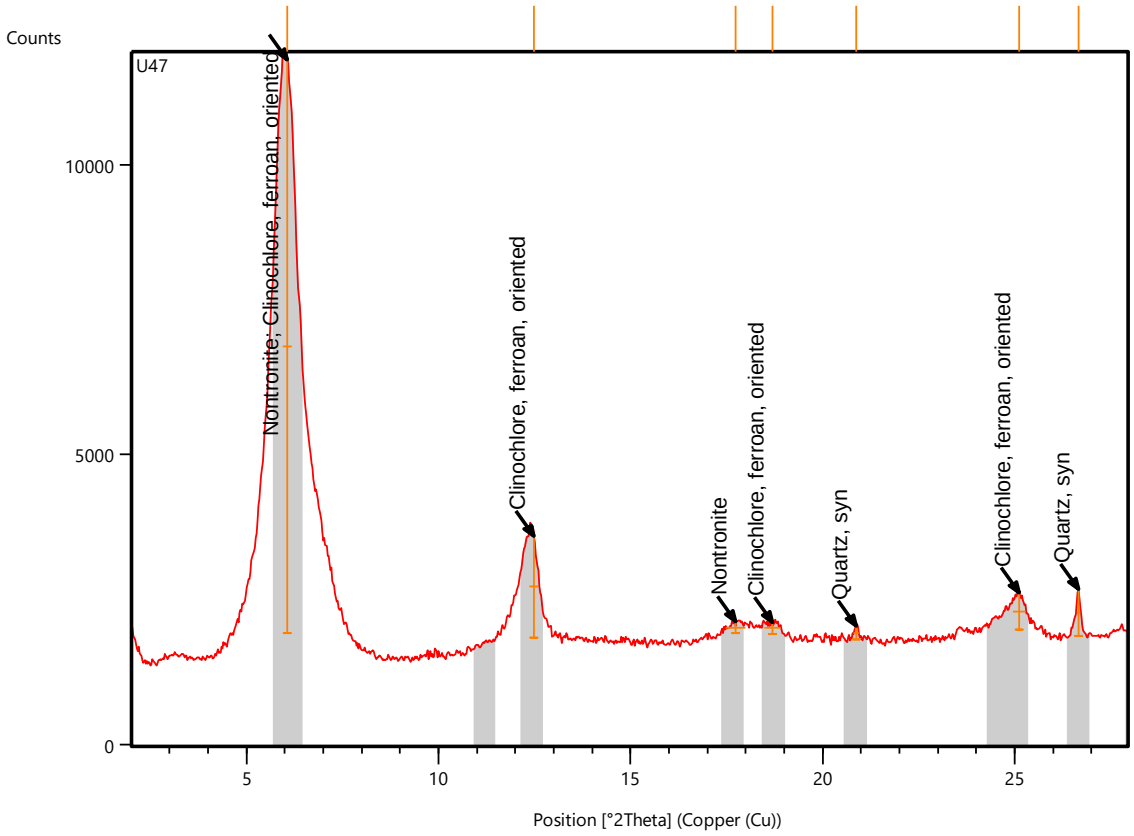

Pos. [°2Th.]	Height [cts]	FWHM Left [°2Th.]	d-spacing [Å]	Rel. Int. [%]
6.0765	9890.75	0.2303	14.54519	100.00
12.4913	1737.10	0.2303	7.08635	17.56
17.7375	210.43	0.5117	5.00053	2.13
18.7057	202.47	0.4093	4.74381	2.05
20.8782	232.42	0.1535	4.25485	2.35
25.1126	628.71	0.3070	3.54619	6.36
26.6577	801.03	0.1023	3.34405	8.10

U47_GLY

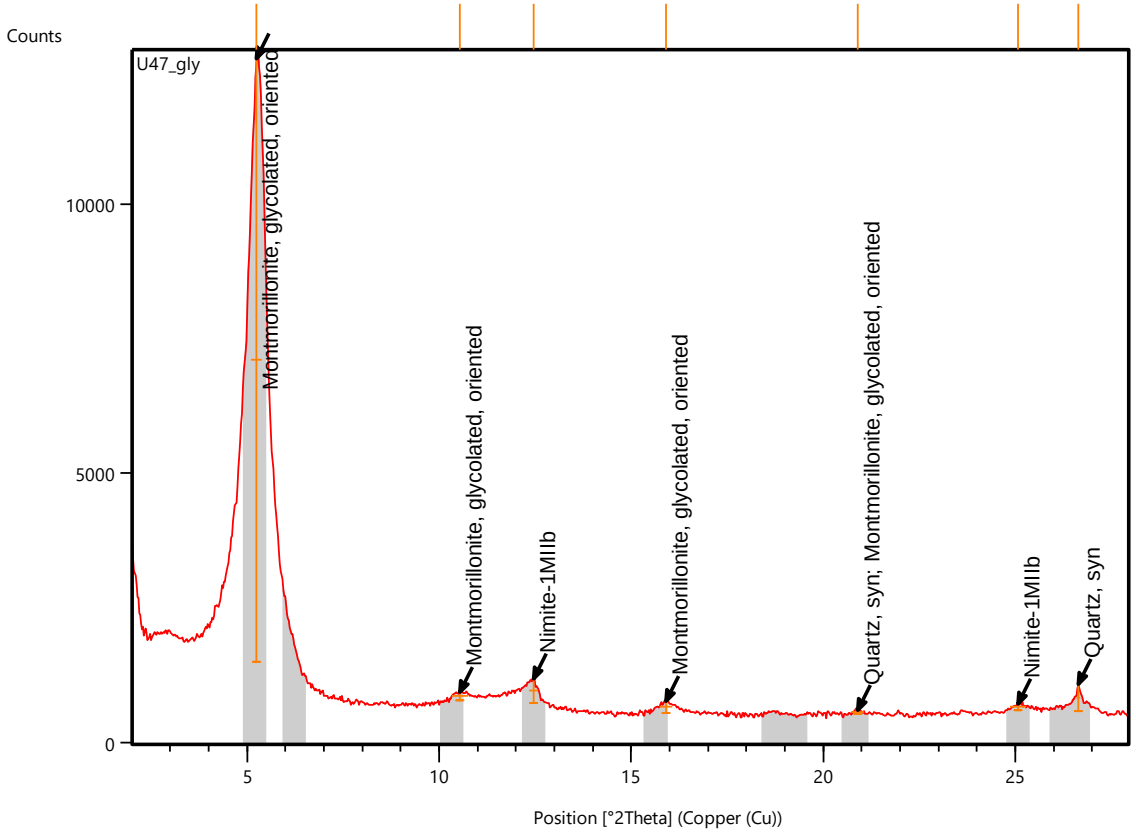

Pos. [°2Th.]	Height [cts]	FWHM Left [°2Th.]	d-spacing [Å]	Rel. Int. [%]
5.2469	11199.95	0.2814	16.84303	100.00
10.5455	160.33	0.4093	8.38912	1.43
12.4649	451.82	0.2558	7.10131	4.03
15.9038	213.38	0.3070	5.57269	1.91
20.8918	77.43	0.3070	4.25211	0.69
25.0837	119.31	0.4093	3.55020	1.07
26.6468	494.15	0.1023	3.34540	4.41

U51

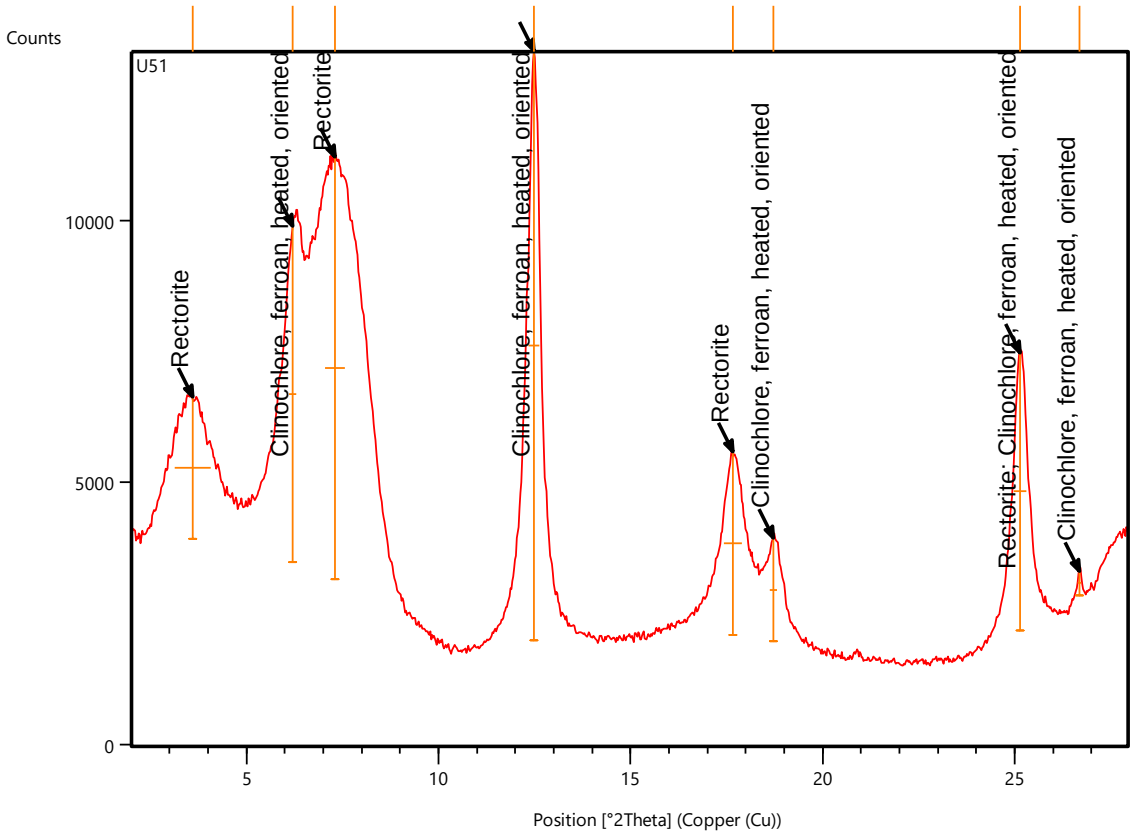

Pos. [°2Th.]	Height [cts]	FWHM Left [°2Th.]	d-spacing [Å]	Rel. Int. [%]
3.6015	2704.20	0.9210	24.53348	24.03
6.1989	6413.99	0.1791	14.25825	57.00
7.3157	8054.83	0.5117	12.08396	71.58
12.4926	11252.30	0.2814	7.08563	100.00
17.6706	3506.71	0.4605	5.01930	31.16
18.7149	1973.63	0.1791	4.74150	17.54
25.1349	5300.23	0.3070	3.54309	47.10
26.6958	463.39	0.1023	3.33937	4.12

U51_GLY

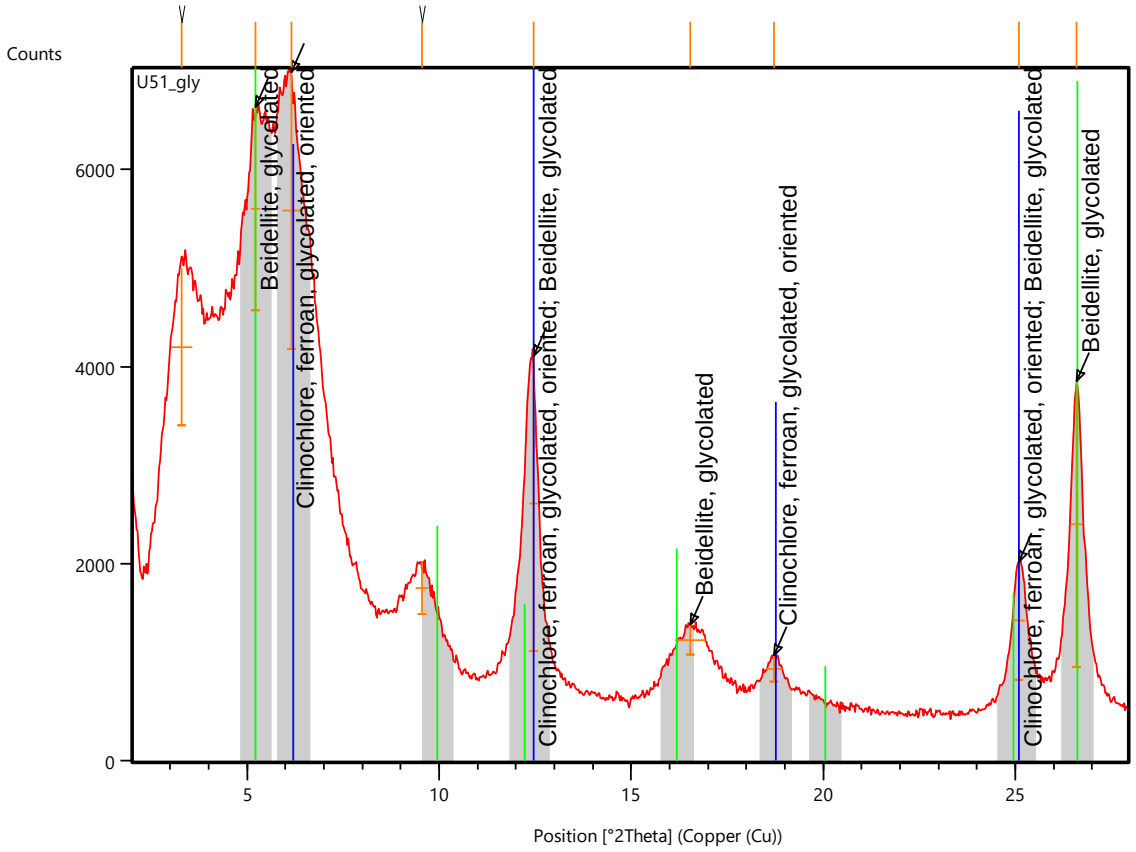

Pos. [°2Th.]	Height [cts]	FWHM Left [°2Th.]	d-spacing [Å]	Rel. Int. [%]
3.3101	1598.97	0.5628	26.69222	53.44
5.2130	2059.44	0.2558	16.95237	68.84
6.1534	2820.09	0.4605	14.36371	94.26
9.5493	530.94	0.3070	9.26196	17.75
12.4569	2991.81	0.2558	7.10586	100.00
16.5393	297.10	0.8187	5.35997	9.93
18.7320	266.49	0.4093	4.73721	8.91
25.0850	1202.30	0.3326	3.55002	40.19
26.6048	2903.98	0.2814	3.35058	97.06

U55

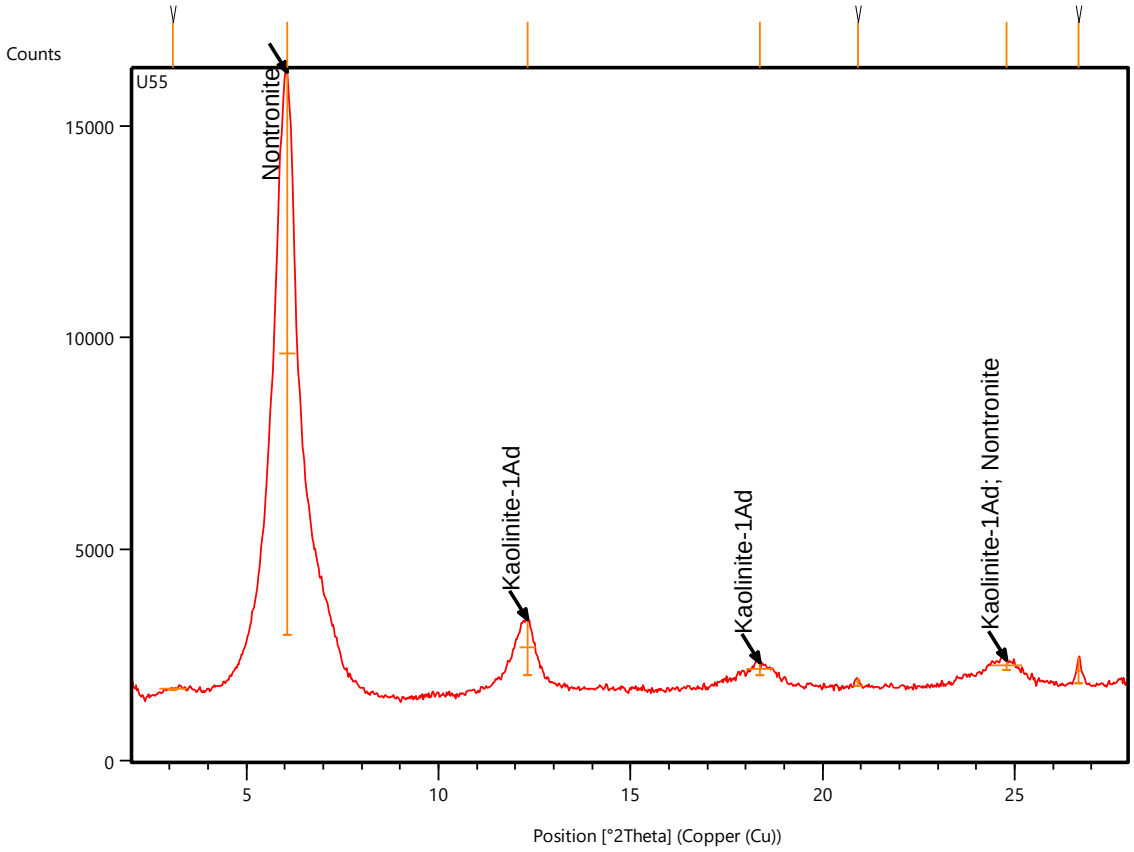

Pos. [°2Th.]	Height [cts]	FWHM Left [°2Th.]	d-spacing [Å]	Rel. Int. [%]
3.0937	31.53	0.7164	28.55899	0.24
6.0723	13301.99	0.4093	14.55543	100.00
12.3257	1310.70	0.4093	7.18123	9.85
18.3639	308.41	0.7164	4.83135	2.32
20.9136	188.01	0.1535	4.24772	1.41
24.7941	226.75	0.8187	3.59102	1.70
26.6695	625.17	0.1279	3.34260	4.70

U55-GLY

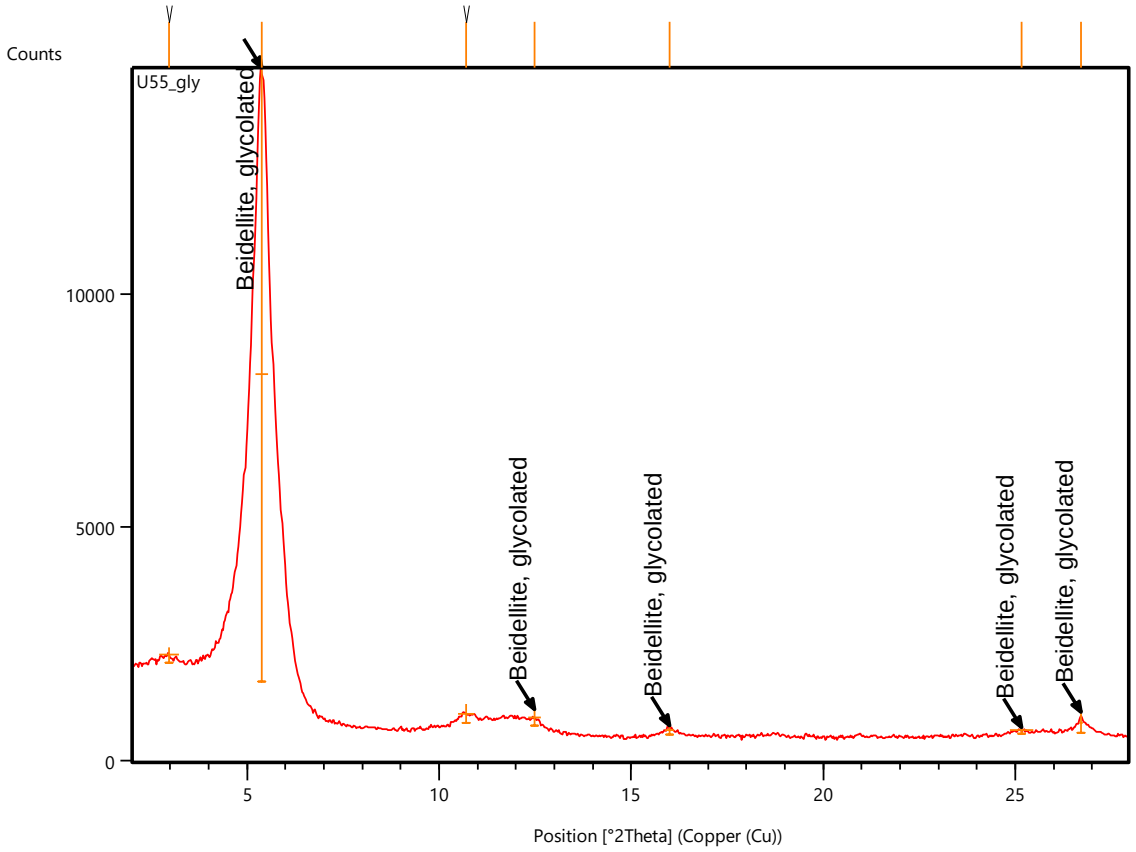

Pos. [°2Th.]	Height [cts]	FWHM Left [°2Th.]	d-spacing [Å]	Rel. Int. [%]
2.9604	330.47	0.5117	29.84454	2.44
5.3797	13567.27	0.3070	16.42768	100.00
10.7133	390.28	0.4093	8.25809	2.88
12.4784	351.38	0.3070	7.09368	2.59
15.9938	208.05	0.2558	5.54156	1.53
25.1637	130.88	0.6140	3.53910	0.96
26.7142	436.66	0.1023	3.33710	3.22

U58

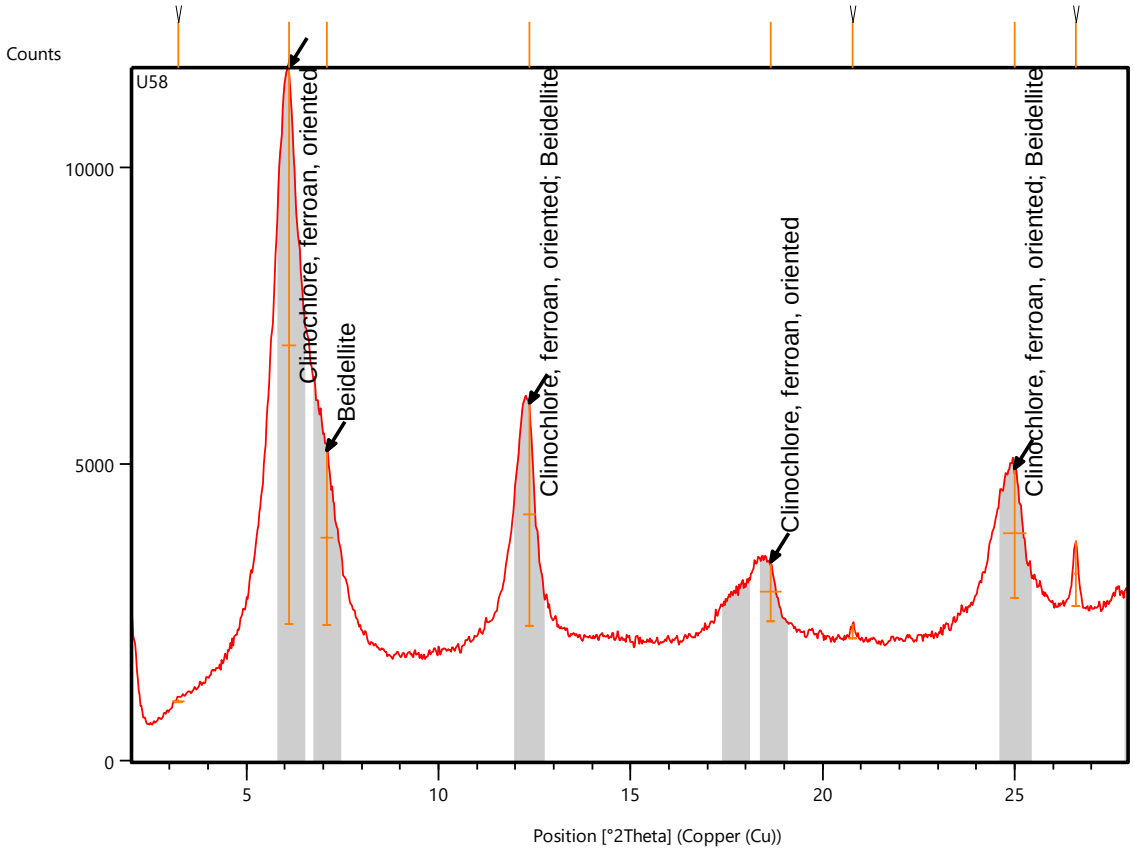

Pos. [°2Th.]	Height [cts]	FWHM Left [°2Th.]	d-spacing [Å]	Rel. Int. [%]
3.2393	48.83	0.3070	27.27566	0.52
6.1006	9411.37	0.3838	14.48775	100.00
7.0953	2934.47	0.3070	12.45882	31.18
12.3638	3750.48	0.3326	7.15916	39.85
18.6409	1002.51	0.5628	4.76017	10.65
20.7940	246.42	0.1535	4.27189	2.62
25.0087	2190.58	0.6140	3.56068	23.28
26.5907	1094.05	0.1023	3.35233	11.62

U58_GLY

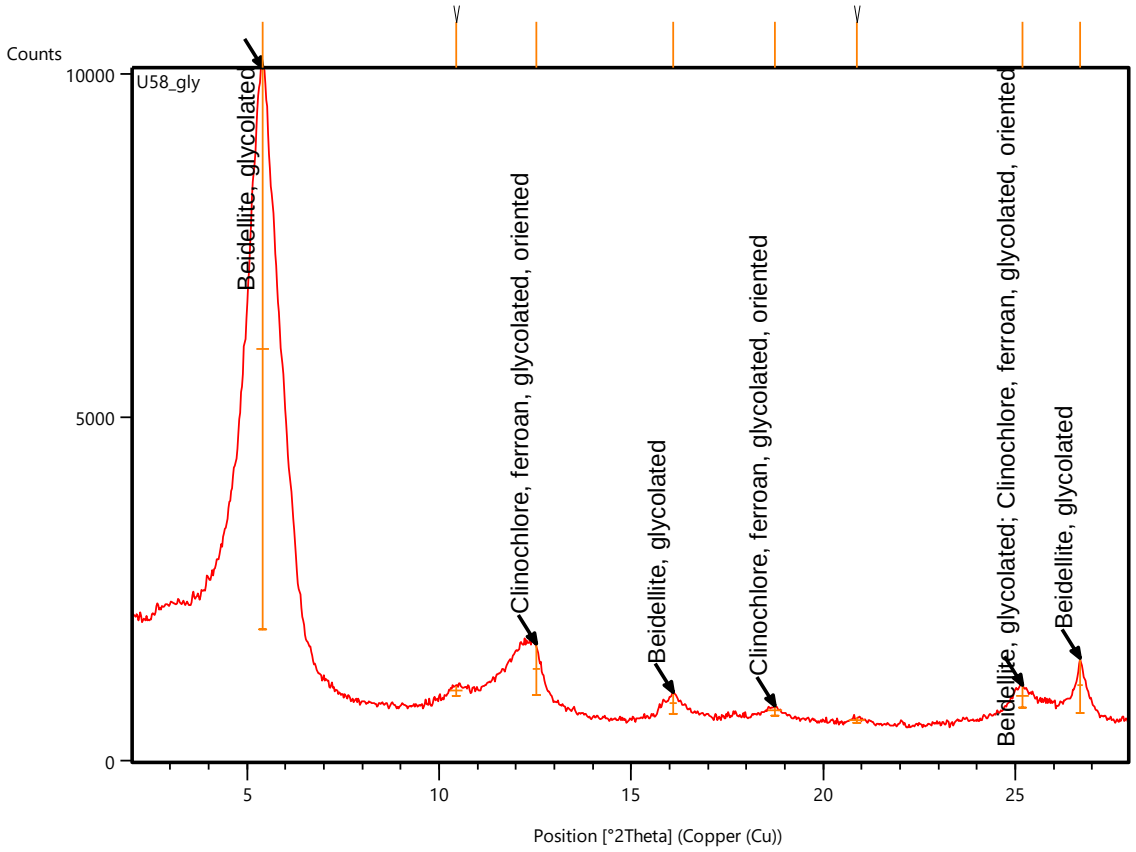

Pos. [°2Th.]	Height [cts]	FWHM Left [°2Th.]	d-spacing [Å]	Rel. Int. [%]
5.4173	8218.76	0.3070	16.31372	100.00
10.4563	141.37	0.3070	8.46055	1.72
12.5351	744.39	0.2047	7.06174	9.06
16.1053	310.28	0.2047	5.50344	3.78
18.7444	150.83	0.3582	4.73411	1.84
20.8736	73.18	0.4093	4.25578	0.89
25.1928	327.56	0.3070	3.53508	3.99
26.6990	800.62	0.1535	3.33897	9.74

Appendix C – X-ray fluorescence results

Major elements

Hole ID	Sample ID	Major elements (wt %)									
		Na_2O	MgO	Al_2O_3	SiO_2	P_2O_5	K_2O	CaO	TiO_2	MnO	Fe_2O_3
SPO597	S-BB01	0.88	0.65	8.67	52.37	0.07	7.38	9.81	0.24	0.11	10.57
	S-BB02	1.68	3.63	13.25	57.65	0.09	3.04	3.74	0.58	0.17	5.88
	S-BB03	2.36	4.98	14.98	57.25	0.09	2.83	2.41	0.58	0.24	6.36
	S-BB04	0.42	2.49	15.00	70.17	0.12	5.38	0.47	0.58	0.05	3.49
	S-BB05	0.02	3.03	15.94	56.37	0.09	3.39	4.66	0.54	0.13	5.17
	S-BB06	0.16	2.89	15.08	61.18	0.10	3.71	3.30	0.63	0.07	4.89
	S-BB07	1.97	3.22	13.69	56.93	0.09	2.06	5.22	0.61	0.13	7.11
	S-BB08	0.02	0.01	1.73	32.43	0.00	1.63	28.56	0.00	0.20	0.05
	S-BB10	0.94	2.02	12.44	74.97	0.16	4.49	0.46	0.62	0.12	5.47
	S-BB11	1.08	3.35	12.85	60.85	0.11	3.98	2.29	0.61	0.16	6.28
	S-BB12	1.28	2.51	17.43	58.88	0.12	4.37	1.44	0.55	0.14	6.87
	S-BB13	1.01	2.46	15.80	57.36	0.07	3.67	3.59	0.58	0.09	5.21
	S-BB14	0.44	3.43	13.99	57.63	0.09	2.85	3.70	0.64	0.21	5.90
	S-BB15	0.44	1.87	16.16	61.24	0.08	3.92	2.41	0.57	0.10	4.10
	S-BB16	1.66	4.75	12.30	60.89	0.11	4.44	0.57	0.56	0.32	6.63
	S-BB18	1.69	1.77	15.79	59.13	0.12	4.45	2.48	0.87	0.06	4.89

	S-BB19	2.84	4.33	14.29	57.96	0.11	2.71	3.20	0.62	0.10	6.21
	S-BB20	0.95	4.21	15.04	65.10	0.08	3.43	3.13	0.59	0.12	5.18
	S-BB21	1.01	4.25	16.89	59.73	0.09	3.76	4.21	0.68	0.15	7.04
	S-BB22	0.59	4.19	15.29	58.99	0.09	3.24	3.53	0.61	0.19	6.19
	S-BB23	0.30	2.70	14.84	57.94	0.07	3.04	4.80	0.57	0.12	4.59
	S-BB24	1.07	2.22	17.00	60.11	0.12	3.82	4.10	0.64	0.07	4.20
	S-BB26	1.11	1.52	15.83	58.65	0.09	3.28	6.54	0.46	0.07	5.63
	S-BB27	0.60	2.14	17.75	58.63	0.09	4.27	4.52	0.55	0.08	3.70
	S-BB28	0.43	1.79	17.37	61.87	0.08	3.89	5.15	0.50	0.10	2.98
	S-BB29	1.55	2.45	12.72	51.22	0.08	1.50	7.46	0.57	0.19	7.14
	S-BB30	1.25	2.22	17.52	63.29	0.14	5.71	3.25	0.54	0.15	4.34
	S-BB31	1.94	1.35	15.66	71.09	0.12	4.21	0.38	0.40	0.04	2.14
	S-BB32	1.69	1.55	15.68	63.49	0.10	3.50	3.28	0.46	0.07	3.49
	S-BB33	0.23	1.84	16.60	59.67	0.07	3.93	4.50	0.48	0.09	3.83
	S-BB34	0.12	2.56	17.25	62.84	0.08	3.95	2.40	0.48	0.09	4.09
	S-BB35	0.14	2.33	15.10	57.90	0.08	3.11	5.59	0.48	0.14	5.80
	S-BB36	0.19	1.86	16.91	67.03	0.09	3.72	1.54	0.39	0.08	3.47
	S-BB37	0.06	1.57	15.67	61.62	0.09	3.41	4.52	0.44	0.08	2.89
	S-BB38	2.54	1.92	17.61	62.49	0.11	2.49	3.91	0.55	0.06	2.55
	S-BB39	3.03	2.47	16.56	61.29	0.09	2.12	5.01	0.47	0.08	3.49
	S-BB40	2.48	2.69	13.42	58.34	0.09	1.09	4.73	0.45	0.08	6.00
	S-BB41	1.97	3.37	15.23	55.90	0.07	2.06	4.79	0.42	0.10	5.42

	S-BB42	2.36	2.96	12.39	58.51	0.08	0.77	4.99	0.44	0.09	5.57
	S-BB43	2.63	1.98	14.85	57.29	0.08	2.11	4.61	0.45	0.07	3.48
	S-BB44	2.56	2.56	13.79	57.90	0.08	1.88	5.51	0.45	0.08	5.00
	S-BB45	3.26	2.73	17.11	60.19	0.07	3.04	0.25	0.58	0.10	7.54
	S-BB46	3.94	1.95	17.47	62.63	0.07	2.41	1.01	0.51	0.06	4.47
	S-BB47	3.13	1.44	17.00	68.15	0.09	2.76	0.77	0.44	0.04	3.17
	S-BB48	2.85	1.54	14.02	62.32	0.08	2.15	4.96	0.35	0.09	3.07
	S-BB49	2.34	1.34	16.98	64.12	0.04	3.49	2.77	0.52	0.05	2.95
	S-BB50	2.87	1.84	15.20	64.92	0.07	2.12	2.15	0.44	0.06	3.28
	S-BB51	2.71	1.41	14.95	64.75	0.06	2.30	2.65	0.46	0.05	3.48
	S-BB52	1.72	1.58	16.58	60.98	0.16	3.29	2.75	0.66	0.06	6.21
	S-BB53	1.95	1.52	16.26	54.53	0.08	3.27	7.72	0.41	0.09	3.17
	S-BB54	1.87	1.66	14.65	62.03	0.05	2.30	3.24	0.38	0.09	5.50
	S-BB55	1.98	1.65	15.34	65.13	0.10	2.77	3.07	0.45	0.06	4.37
	S-BB56	1.57	1.60	14.74	62.44	0.06	2.66	4.16	0.39	0.07	4.43
UW462	U-BB01	1.91	2.96	12.61	60.88	0.09	4.63	1.05	0.53	0.85	5.79
	U-BB02	2.11	3.58	12.58	57.20	0.08	2.31	4.68	0.46	0.17	6.01
	U-BB03	1.70	1.97	15.30	70.02	0.12	6.33	0.45	0.56	0.05	4.58
	U-BB04	2.33	2.59	13.40	67.27	0.11	5.25	1.59	0.46	0.07	4.44
	U-BB05	3.09	2.05	15.98	68.42	0.14	5.60	0.44	0.64	0.05	5.50
	U-BB06	1.82	3.34	13.89	61.71	0.09	3.39	1.25	0.53	0.07	5.74
	U-BB07	1.27	2.61	14.89	64.66	0.13	4.05	0.75	0.50	0.06	5.30

	U-BB08	2.29	2.96	13.45	59.92	0.10	3.58	3.27	0.53	0.12	4.88
	U-BB09	3.01	3.54	12.48	59.40	0.08	2.43	3.48	0.41	0.10	5.78
	U-BB10	0.84	1.22	17.79	70.32	0.14	4.75	0.78	0.67	0.03	4.88
	U-BB11	0.25	3.45	15.85	64.04	0.12	3.81	1.04	0.55	0.11	6.82
	U-BB12	0.59	2.50	16.60	58.07	0.08	3.78	6.23	0.56	0.18	4.25
	U-BB13	2.18	3.56	12.71	58.32	0.09	4.44	3.31	0.48	0.11	5.54
	U-BB14	2.09	3.40	12.86	56.77	0.08	3.17	3.60	0.41	0.14	5.74
	U-BB15	2.71	3.01	12.71	59.47	0.10	2.80	3.94	0.48	0.10	5.23
	U-BB16	1.78	1.67	14.33	62.99	0.11	4.64	4.21	0.47	0.10	5.48
	U-BB17	1.90	2.42	13.50	62.39	0.10	4.75	2.87	0.45	0.08	4.54
	U-BB18	1.94	2.42	13.14	58.55	0.10	4.50	4.65	0.48	0.13	5.18
	U-BB19	0.54	1.58	16.84	59.81	0.12	12.17	0.66	0.67	0.07	5.43
	U-BB20	1.09	0.75	13.91	70.47	0.13	4.84	0.25	0.45	0.01	6.79
	U-BB21	3.26	2.50	13.28	57.19	0.09	3.67	3.98	0.54	0.12	5.66
	U-BB22	1.09	1.01	18.29	70.21	0.11	4.50	0.40	0.56	0.01	4.57
	U-BB23	0.74	2.41	14.16	62.57	0.08	4.33	4.24	0.55	0.08	3.98
	U-BB24	0.17	2.22	14.52	57.01	0.10	3.01	5.96	0.50	0.06	3.77
	U-BB25	0.63	1.65	15.63	61.46	0.11	3.36	4.90	0.52	0.05	4.33
	U-BB26	0.63	1.86	16.30	66.51	0.08	3.67	2.93	0.49	0.09	3.81
	U-BB27	0.88	1.98	17.80	69.67	0.11	3.90	1.46	0.56	0.05	4.68
	U-BB28	0.81	1.91	16.74	65.24	0.13	3.67	2.85	0.49	0.04	4.10
	U-BB29	2.64	2.56	12.40	63.99	0.10	1.63	4.85	0.55	0.09	5.97

	U-BB30/1	0.65	2.93	20.55	55.38	0.12	4.86	5.14	0.68	0.16	6.22
	U-BB30/2	0.69	1.93	16.74	69.02	0.13	3.72	2.65	0.56	0.07	3.95
	U-BB31	3.54	2.37	12.40	63.21	0.11	1.60	5.34	0.54	0.09	6.12
	U-BB32	0.93	3.44	19.88	65.23	0.14	2.46	2.27	0.57	0.06	4.08
	U-BB33	0.31	2.32	14.65	56.28	0.09	1.47	5.99	0.49	0.13	6.20
	U-BB34	1.07	3.19	14.79	51.73	0.13	1.82	8.47	0.61	0.12	8.68
	U-BB35	4.30	3.05	12.66	67.08	0.11	1.56	4.08	0.54	0.07	4.56
	U-BB36	3.39	3.78	12.34	66.46	0.12	1.50	3.23	0.48	0.07	6.06
	U-BB37	2.33	2.96	15.59	62.90	0.09	2.36	4.13	0.52	0.05	6.17
	U-BB38	2.91	2.30	11.99	64.73	0.09	1.62	4.41	0.45	0.08	5.57
	U-BB39	2.28	2.47	13.77	64.17	0.12	2.04	4.09	0.60	0.07	5.10
	U-BB40	1.99	2.61	12.34	58.75	0.09	1.87	4.95	0.50	0.12	6.47
	U-BB41	0.76	1.55	16.38	60.71	0.11	1.42	3.49	0.56	0.06	5.48
	U-BB42	0.57	2.44	15.94	61.08	0.09	0.67	4.25	0.57	0.06	5.11
	U-BB43	0.58	1.96	15.66	63.52	0.09	1.90	3.38	0.54	0.04	3.14
	U-BB44	0.81	2.43	14.10	62.02	0.10	1.80	3.07	0.60	0.09	6.60
	U-BB45	0.53	2.41	13.95	59.03	0.09	1.88	3.43	0.52	0.06	5.02
	U-BB46	1.56	2.63	17.28	70.16	0.09	1.70	3.89	0.54	0.06	4.39
	U-BB47	2.26	1.82	13.02	63.10	0.10	2.07	4.31	0.48	0.05	4.67
	U-BB48	1.14	0.83	14.44	78.01	0.10	2.21	0.70	0.42	0.01	8.65
	U-BB49	0.35	1.95	14.68	57.24	0.08	1.85	5.22	0.49	0.09	4.98
	U-BB50	0.08	2.11	13.70	53.57	0.06	1.01	6.52	0.45	0.11	6.04

	U-BB51	1.25	1.57	15.66	63.14	0.08	2.15	0.85	0.48	0.04	6.02
	U-BB52	0.29	2.18	13.51	52.51	0.06	0.90	7.93	0.48	0.07	6.28
	U-BB53	0.99	1.39	13.67	59.00	0.09	1.74	5.37	0.48	0.08	4.39
	U-BB54	1.55	2.54	12.57	60.34	0.09	1.74	4.53	0.43	0.09	5.47
	U-BB55	2.15	3.82	12.53	63.26	0.09	2.15	3.44	0.47	0.07	5.35
	U-BB56	0.85	2.64	12.36	53.59	0.07	1.36	6.94	0.46	0.11	5.83
	U-BB57	1.86	3.45	12.81	60.26	0.08	1.83	3.83	0.49	0.07	6.08
	U-BB58	2.03	3.10	12.75	60.47	0.08	2.01	4.06	0.51	0.09	6.30

Trace elements (ppm)

	Sample ID									
	S-BB01	S-BB02	S-BB03	S-BB04	S-BB05	S-BB06	S-BB07	S-BB08	S-BB10	S-BB11
S	47600	3871	3035	13030	4447	8960	6576	167.7	22340	15100
Cl	12.3	58.2	74	50	37	44.5	67	< 2.6	57	47
V	41	142	162	172	145	159	166	< 2.4	84	186
Cr	73	155	147	209	158	258	232	< 1.3	15	177
Co	76	38	31	36	33	32	39	13	45	34
Ni	36	35	33	30	30	55	31	2.8	< 1.1	12.9
Cu	10.4	13.8	27	< 0.5	9.1	13	14	< 0.6	205	6.8
Zn	78	48	71	41	44	47	89	17	3421	51
Ga	7.7	16.6	17	17.3	17.4	18.1	16.3	2.4	12.2	15.5
Ge	< 1.2	0.7	1	< 0.6	< 0.5	1	0.4	1.2	0.6	1
As	29	41	33	62	17.9	13.9	12.6	< 0.4	237	32
Se	9.6	1.9	1.4	3.3	2.3	2.8	1.6	1.9	3.6	3
Br	1	0.4	0.6	0.5	0.3	0.7	0.2	0.9	< 0.4	0.3
Rb	264	159	137	261	151	176	119	78	178	192
Sr	171	141	107	72	69	41	166	191	60	126
Y	30	17.6	18.8	24	17.9	20	17.5	4.3	12.7	18.3
Zr	43	110	114	110	103	112	99	4	89	104
Nb	4.2	6.4	6.2	5.8	6.1	6.3	6.3	2.6	6.2	6
Mo	3.1	1.8	1.7	1.9	1.6	2	1.6	0.9	2.2	1.7
Sn	2.6	3.8	1.4	2.6	2.7	1.5	2.1	< 0.7	2.2	3.3
Sb	4.9	1.7	2	2.5	1.9	1.9	1.6	2.4	11.9	2.4
Te	4.2	1.5	2	2.3	2.1	1.6	1.9	< 1.2	2.7	1.4
Ba	612.3	460.8	282.2	520.3	463	416.1	259.4	120.8	857.5	641.7
La	< 4.9	8.5	10.1	13.9	25.7	9.9	7.8	< 4.9	< 4.9	6.7
Ce	12.9	19.1	20	29.3	43.2	23.6	18.5	< 5.8	13	20.8
Nd	< 10	10.6	< 10	14.5	20.5	< 10	< 10	< 10	< 10	< 10
Hf	3.8	7.4	6.6	7.3	7.8	6.1	6.8	3	< 4.3	6.8

Ta	3.9	4.9	8.9	6.2	4.7	4.7	6.2	4.6	< 7.1	3.3
W	477.6	130.3	112.7	138.7	92.4	64.7	46.9	288.1	280.9	143.4
Tl	8.1	3.7	4	5.3	4	3.8	3.4	4.1	0.8	4.2
Pb	41.5	10.7	10.5	9.2	8.2	8.8	8.8	11.3	900.6	12.2
Bi	7.1	2.1	1.8	2.3	2.5	2.2	2.7	2.2	< 1.4	2.6
Th	9.8	10.8	10.3	10.7	11.5	12	10.2	7.2	13.2	10.8
U	13.3	9.6	8.5	9.7	10.6	11.2	8.9	9.4	8.8	8

	Sample ID									
	S-BB12	S-BB13	S-BB14	S-BB15	S-BB16	S-BB18	S-BB19	S-BB20	S-BB21	S-BB22
S	12780	1124	3911	5331	12010	3702	6535	16020	24300	8260
Cl	43.1	33.8	161	49	< 2.7	16.8	101	76	41	45
V	123	117	160	131	150	113	179	172	234	161
Cr	56	126	188	245	218	35	170	138	214	174
Co	28	27	35	28	44	28	32	33	40	35
Ni	14	36	41	32	29	13.6	14.7	15.4	11.7	27.5
Cu	20	32	31	< 0.5	60	2.3	7.2	< 0.5	2.1	10.9
Zn	61	42	74	57	63	45	49	72	101	100
Ga	18.1	17.4	14.8	17.2	14.5	18.5	15.9	15.9	17.3	16.1
Ge	0.8	1.3	0.5	0.5	< 0.6	1.2	1.6	0.8	0.7	0.9
As	145	14.1	26	6.8	40	22	148	3.6	8.8	46
Se	2.9	1.2	1.9	4.9	5.2	2.2	2.1	5.8	2.2	2
Br	0.9	0.5	0.2	0.3	0.4	0.4	1.1	0.7	0.4	0.6
Rb	169	158	167	220	202	213	143	186	209	165
Sr	58	61	40	43	165	215	93	44	66	66
Y	15.6	22	22	22	16.9	22	16.2	17.1	18	18.9
Zr	132	117	120	125	88.6	149	96.9	88.1	116	119
Nb	6.9	7	6.2	6.9	5.4	9.2	5.9	5.6	6	6.2

Mo	2.5	2.1	1.2	1.4	2.6	2.7	2	2	2.3	2.1
Sn	2.9	2.1	3.2	4.7	5.9	3.3	2.1	3.9	3.7	2
Sb	3.7	1.9	1.2	1.4	4.5	2.1	2.6	2.2	3	1.9
Te	2.5	2.6	1.7	1.7	2.1	1.8	2	2	1.7	1.6
Ba	797.9	539	307.3	393.5	618	579.9	218.8	235.5	206.2	315.6
La	13.5	15.1	10.2	17.9	4.5	14.8	8.7	8.2	8.1	11.3
Ce	29.2	29.4	23.5	35	14.2	32.4	17.8	21.3	21.6	23
Nd	10.3	11.6	< 10	10.8	< 10	11.8	< 10	< 10	< 10	< 10
Hf	7.9	6.7	7.6	6.5	7	7.4	7.5	7.1	6.4	6.7
Ta	4.7	7.7	8.6	4.6	6.4	4.5	6.8	5.9	7.4	5.6
W	115	79.1	55.1	61.4	150.3	84.8	91.5	80.6	56.6	98.1
Tl	4.3	3.7	3.3	5	7.6	4.7	3.7	4.4	4.4	4.1
Pb	24.4	11.6	10.5	25.7	8.6	10.8	10.6	20.7	19.5	15.5
Bi	2.1	1.9	2.2	1.5	1.4	1.1	3.6	4.5	2.5	7.6
Th	13.1	11.9	11.3	12.6	9.7	15	11	10.7	11.4	13.2
U	10.3	9.4	10.3	11.8	9.9	11.5	9.9	11.3	12.1	11.6

	Sample ID									
	S-BB23	S-BB24	S-BB26	S-BB27	S-BB28	S-BB29	S-BB30	S-BB31	S-BB32	S-BB33
S	3559	6738	12650	7214	4942	2805	7781	4321	5261	3087
Cl	45	42	98	136	83	6.3	15	67	78	29.7
V	139	150	81	82	127	167	99	71	80	135
Cr	153	173	47	41	104	40	105	41	27	133
Co	22	31	35	31	29	32	36	25	32	35
Ni	9.1	13.8	9.8	12.6	17.1	15.5	16.2	12	10.1	34
Cu	2	7.1	0.6	16.2	< 0.5	9.7	0.3	1.9	4.9	24.1
Zn	54	56	109	65	56	66	39	37	25	22
Ga	13.3	16.8	14.8	14	16.1	16.4	16.7	14.4	16.4	16.2

Ge	1	1	1.2	< 0.6	0.8	0.8	0.7	1.4	0.6	1.7
As	2.3	14.4	28	5.3	4.1	14.5	13.9	23	16.5	35
Se	2.3	1.4	1.2	1.5	1.4	1.1	1.7	1.6	1.6	1
Br	0.3	0.6	0.6	0.6	0.5	0.4	0.6	0.9	0.8	0.6
Rb	149	186	139	228	189	86	281	186	168	190
Sr	95	58	66	55	50	163	79	78	77	40
Y	21	18.8	18.2	27	18.6	21	28	17.8	19.6	17.6
Zr	91.3	120	102	131	109	97	120	106	125	107
Nb	6.2	6.6	5.1	6.1	6.4	6.3	6.3	6.7	7.5	6
Mo	1.8	3.9	1.9	1.7	1.6	2.1	1.8	2.2	3.3	5
Sn	2.5	3.3	4.6	5.2	2.5	1.3	5.4	4	7.5	4.4
Sb	1.5	2.7	2.3	2.1	1.9	1.7	3.7	2.6	2.6	1.5
Te	1.5	2.1	2	2.8	2.1	1.4	2.7	2.8	2.1	1.5
Ba	402.3	370.8	462.7	462.3	266.9	292.9	846.7	611.1	381.2	286.9
La	12	12.1	7.6	18.1	13.9	7.1	15.8	19.9	16.5	13.3
Ce	24.1	23.5	18.2	35.9	29.1	19.8	32.9	34.7	35.2	25.5
Nd	< 10	< 10	< 10	< 10	14.7	< 10	12.2	12.3	13.3	13.9
Hf	6.9	8.2	7	8.4	6.7	6.3	7.9	7.4	7.7	6.4
Ta	4.7	5.7	5.9	7.8	5.7	5.9	5.9	6	4.2	5.2
W	107.8	84.7	106	156.3	124.5	74.5	178.6	266.4	275.9	104.7
Tl	3.7	4.3	4	4.3	4.1	3	5.2	4.4	4.7	4.2
Pb	9	10.2	25.5	13.9	14.3	8.1	13.4	13	8.7	6.2
Bi	1.1	2.2	2.4	2.2	2.2	1.9	2.2	1.6	2.1	2.1
Th	12	12.1	11.8	12.9	13.5	11.3	13.6	14.3	15.7	12.3
U	12.2	10.7	11.3	11.3	11.5	11.3	11.9	11.6	12	10

	Sample ID									
	S-BB34	S-BB35	S-BB36	S-BB37	S-BB38	S-BB39	S-BB40	S-BB41	S-BB42	S-BB43
S	4113	6533	4898	3592	9466	8448	5910	1132	1349	6243
Cl	136	111	89	57	44	94	47	44	7.7	< 2.2
V	177	132	74	78	127	116	133	125	125	130
Cr	170	131	19	22	128	113	153	130	136	148
Co	35	34	20	19	27	47	42	28	34	25
Ni	46	32	6.1	7	21	23	47	34	36	28
Cu	40	21	0.3	< 0.4	4.7	6.4	13.5	13.5	11.7	19.6
Zn	23	144	50	68	41	58	42	26	60	25
Ga	16.1	14.8	15.5	16.1	18.4	16.1	16.1	16.4	16.3	15.4
Ge	0.5	0.7	< 0.6	0.6	< 0.6	0.7	0.6	0.5	0.8	0.9
As	79	51	18	5.5	3.1	2.2	6.9	37	8.2	5.9
Se	1.1	5.6	1.8	1.1	0.8	0.8	0.9	0.5	0.6	0.6
Br	0.6	0.3	0.3	0.3	0.3	0.3	0.3	< 0.2	0.2	0.4
Rb	189	134	160	141	81	71	42	73	28	75
Sr	28	64	45	80	164	154	320	138	275	168
Y	15.8	15	16.1	17.1	19.5	15.3	17.4	16.7	16.5	19.3
Zr	90	87	108	123	122	109	105	106	108	104
Nb	4.4	4.8	5.7	6.4	6.3	5.6	5.7	5.3	5.7	5.7
Mo	2.4	1.8	1.3	1.7	1.3	1.3	1.4	0.9	1.2	1.8
Sn	3.5	3.6	3.6	1.8	1.3	0.6	3	0.8	< 0.7	< 0.7
Sb	1.1	< 0.9	< 0.9	< 0.9	< 0.9	< 0.9	< 0.9	< 0.9	< 0.9	< 0.9
Te	0.7	0.7	< 1.2	< 1.2	< 1.2	1	0.8	< 1.2	< 1.2	< 1.2
Ba	264.3	426.2	385.2	442	463	316.8	383.1	370.6	374.9	388.5
La	14.9	9	11.7	18	14.8	13	7	11.8	10	11.5
Ce	30.1	16.5	26.2	36	30.7	24.6	18.2	25.2	23.3	25.7
Nd	18.5	< 10	< 10	13.4	11.4	9.8	< 10	9	11.2	< 10
Hf	3.9	3.7	4.7	4.9	5.4	3.6	4.6	3.9	3.5	4.3
Ta	< 3.4	4.6	3.1	3.7	4.1	< 2.5	< 2.9	< 2.7	3.3	3.9

W	137.2	171.3	178	232	142.9	240.8	161.6	115.2	163.9	149.2
Tl	2.8	2.7	2.9	2.9	2	1.9	1.5	1.2	1.5	1.6
Pb	3.4	13.6	8.3	9.8	8.5	6.6	7.3	6.5	8.7	1.5
Bi	0.7	0.9	1	1.2	1.3	1.6	2.3	1	0.7	0.8
Th	8.7	9.4	11.7	13.2	12.1	10.4	10.1	9.9	10.1	10.2
U	6.8	6.6	6.4	7.3	5.8	5.4	4.8	5.6	4.8	6.1

	Sample ID									
	S-BB44	S-BB45	S-BB46	S-BB47	S-BB48	S-BB49	S-BB50	S-BB51	S-BB52	S-BB53
S	4637	844.1	442.3	2345	3398	2034	959	1831	21240	5054
Cl	< 2.2	35		3.8	2.1	< 2.7	< 1.8	1.8	31	< 2.4
V	118	141	86	72	65	194	81	78	134	72
Cr	153	140	64	65	28	107	77	79	79	15.6
Co	30	40	34	31	25	21	24	24	36	29
Ni	33	52	18.9	13	10.4	14.1	14.4	11.3	22	5.3
Cu	9.3	38	8.4	1.2	< 0.5	11.5	7.5	4.1	18.3	2.7
Zn	60	91	52	53	34	38	63	44	89	43
Ga	16.2	20	18.8	17.8	14.9	23	16	15.7	19.9	21
Ge	0.4	1	1.2	1.4	0.8	0.7	0.8	0.8	0.6	0.4
As	6.9	5.8	4.6	5.1	4.1	2.2	1.4	2.4	32	10.9
Se	0.5	1.2	1.1	1.4	1.4	1.3	0.8	0.8	1.6	0.9
Br	0.2	< 0.2	0.9	0.6	0.8	0.6	0.3	0.5	0.6	0.7
Rb	61	168	81	86	72	163	72	87	123	155
Sr	307	85	178	113	214	130	163	194	102	166
Y	18.4	24	20	14.5	21	26	16.2	13.9	24	23
Zr	100	112	138	112	117	148	120	122	158	131
Nb	5.5	6.3	8.1	7.2	7.1	8.8	6.4	6.5	7.6	7
Mo	1.3	1.6	1.8	3.1	2.3	1.4	1	1.1	3.5	2.2
Sn	< 0.7	3.5	2.2	2	2.2	3	1	0.9	2.2	2.3
Sb	< 0.9	1.4	1.5	2.1	1.7	1.3	< 0.9	< 0.9	1.6	< 0.9

Te	< 1.2	2	2.6	2.5	2.2	2.2	0.7	0.8	1.4	< 1.2
Ba	636.4	374.3	543.6	506.5	450.7	470.1	534.9	542.6	543.8	356.1
La	10.4	14.6	21.9	22.2	19.3	30.8	24.6	23.9	19.2	15.6
Ce	23.3	26.5	34.6	35	35.5	53.6	43.1	40.1	40.6	34
Nd	< 10	< 10	14.3	15.9	12.8	20.7	21.9	18.5	19.8	< 10
Hf	4	7.6	9.3	7	7.4	8.5	5.2	5.4	5.7	5.7
Ta	4.1	7.1	7	4.9	2.3	4.7	4.5	5.1	3.6	3.2
W	127.7	101.8	254.4	215.6	259.4	193.2	233.6	234.5	158.3	292
Tl	1.4	3.3	3.3	2.9	3.3	3	1.7	1.5	2.1	2.4
Pb	7.7	17.3	12.4	10.2	7.6	7.4	8.5	9	26.2	7.8
Bi	0.9	1.7	2.2	2.2	2.6	2	1.2	1	3.4	1
Th	10.2	9.9	16.4	15	16.4	14.9	12.4	13.2	12	14.4
U	5.1	10.5	9.1	10.2	9.4	11	6	5.7	7	7.6

	Sample ID		
	S-BB54	S-BB55	S-BB56
S	1943	15300	10520
Cl	103	< 2.9	4.1
V	67	93	75
Cr	26	40	34
Co	32	31	31
Ni	12.1	9.9	8.5
Cu	5.1	7	1.5
Zn	49	114	49
Ga	16.9	16	15.6
Ge	0.5	< 0.7	1.1
As	19.4	56	24.8
Se	0.7	1.9	0.7
Br	0.2	0.4	0.4
Rb	83	101	97

	118	125	137
Sr	16.5	17	17.6
Y	124	116	123
Zr	6.5	6.8	6.2
Nb	0.9	6	6.8
Mo	< 0.7	< 0.7	1
Sn	< 0.9	0.9	0.5
Sb	< 1.2	< 1.2	0.7
Te	465.8	537.2	604.9
Ba	16	18.3	16.1
La	31.6	33.7	30.2
Ce	9.5	13.1	< 10
Nd	4.9	4.9	5
Hf	4.4	3.6	3.9
Ta	289.5	232.7	227.7
W	2.1	2.2	2
Tl	9.3	16.1	12.4
Pb	1.1	1.3	1.3
Bi	12.1	12.1	11.8
Th	6.7	7.8	6
U			